STRUCTURE AND FUNCTION OF THE ALPHA3BETA4 NICOTINIC ACETYLCHOLINE RECEPTOR

APPROVED BY SUPERVISORY COMMITTEE

Ryan E. Hibbs, Ph.D.

Youxing Jiang, Ph.D.

Xuewu Zhang, Ph.D.

Xiaochen Bai, Ph.D.

DEDICATION

This work is dedicated to all of the family, friends, and colleagues who have supported me throughout my graduate studies.

STRUCTURE AND FUNCTION OF THE ALPHA3BETA4 NICOTINIC ACETYLCHOLINE RECEPTOR

by

ANANT VISHWANATH GHARPURE

DISSERTATION

Presented to the Faculty of the Graduate School of Biomedical Sciences

The University of Texas Southwestern Medical Center at Dallas

In Partial Fulfillment of the Requirements

For the Degree of

DOCTOR OF PHILOSOPHY

The University of Texas Southwestern Medical Center at Dallas

Dallas, Texas

December, 2020

STRUCTURE AND FUNCTION OF THE ALPHA3BETA4 NICOTINIC ACETYLCHOLINE RECEPTOR

Publication No. _____

Anant Vishwanath Gharpure

The University of Texas Southwestern Medical Center at Dallas, 2020

Supervising Professor: Ryan E. Hibbs, Ph.D.

Nicotinic acetylcholine receptors are pentameric ligand-gated ion channels that are essential for the proper function of the central and peripheral nervous systems. The α3β4 subtype is highly expressed in the autonomic ganglia, where it contributes to signal transduction from the central nervous system to the periphery. Moreover, α3β4 receptors are found in key brain regions that modulate reward circuits and have therefore been identified as potential targets for anti-addiction therapeutics. Given the physiological importance of this protein, I sought to understand the molecular mechanisms underlying ligand recognition, channel gating, and ion permeation in the α3β4 nicotinic acetylcholine receptor.

Paramount to this goal was the pursuit of a high-resolution structure of the α3β4 subtype. I initially attempted to determine a crystal structure of this receptor before taking advantage of recent technological advances in cryo-electron microscopy. Using this method, I solved the first structure of the α3β4 nicotinic receptor, which was also the first high-resolution structure of any nicotinic acetylcholine receptor in a lipidic environment. By obtaining structural information of the protein bound to a non-selective nicotinic agonist as well as an α3β4-selective ligand, I was able to draw conclusions regarding ligand-selectivity in the nicotinic receptor family. Furthermore, these structures provided a detailed view of the ordered regions of the intracellular domain for the first time, giving insight into the full ion permeation pathway of these channels. This work also provided a blueprint to examine other outstanding questions in the field. Specifically, I used structural and functional approaches to begin to understand the consequences of accessory subunit incorporation, the role of multivalent cations in the desensitization of nicotinic receptors, and the role of the intracellular domain in ion selectivity and rectification.

ACKNOWLEDGEMENTS

They say it takes a village to raise a child- this proverb also holds true for writing a dissertation. A body of work of this length would not have been possible without the efforts, guidance, and support of many individuals and I am extremely thankful for all of them.

First, I would like to thank my mentor, Dr. Ryan Hibbs. I will always be grateful to Ryan for allowing me to join his lab despite my immense gaps in knowledge in molecular biology, biochemistry, and structural biology at the start of my graduate studies. In those early days, Ryan put me in a position to learn and grow as a graduate student. As I matured, Ryan's mentorship style shifted slightly to grant me more freedom in my scientific pursuits, which instilled in me an invaluable sense of confidence. I believe this speaks to his unique ability to understand and cater to his mentees' needs. A terrific investigator and (perhaps more importantly) a great guy, Ryan is as good of a role model as any young scientist could hope for.

Next, I would like to thank all of the current and former members of the Hibbs Lab. I am especially indebted to the three scientists who were in the lab prior to my arrival: Dr. Colleen Noviello, Dr. Claudio Morales-Perez, and Dr. Richard Walsh. They not only taught me many of the scientific skills that I know today, but they also showed me what it would take to be successful as a graduate student. The intensity and excitement that pervaded our small group helped cultivate my passion for science and I will forever cherish that early period in the lab. I would also like to thank the current members of the lab: Dr. Shaotong Zhu, Rico Cabuco, Dr. Guipeun Kang, Dagim Legesse, Dr. Jinfeng Teng, Dr. JJ Kim, Dr.

Mahfuz Rahman, Umang Goswami, and Leah Baxter. It has been a pleasure working alongside this wonderful group of people who have helped make graduate school an enjoyable experience.

I would like to thank everyone who helped make my dissertation project possible. I am deeply grateful to Colleen for the many hours she spent in the microscope room screening grids and collecting data on α3β4 and Jinfeng for the liposome patch experiments. I would also like to thank our collaborators in Sweden: Yuxuan Zhuang, Dr. Rebecca Howard, and Dr. Erik Lindahl for performing the molecular dynamics simulations.

I would like to thank my committee members, Dr. Youxing Jiang, Dr. Xiaochen Bai, and Dr. Xuewu Zhang for their support and advice, as well as other members of the UT Southwestern community including Dr. Daniel Rosenbaum, Dr. Luke Rice, Dr. Ruhma Syeda, Dr. Diana Tomchick, Dr. Chad Brautigam, Dr. Zhe Chen, Dr. Ege Kavalali, Dr. Said Kourrich, and Dr. Amelia Eisch for their valuable feedback over the years. I am also grateful to my undergraduate mentor, Dr. Julie Kauer, for providing me with the opportunity to experience working in a research lab and encouraging me to pursue a graduate degree in the biomedical sciences.

Members of the Rosenbaum and Jiang labs, specifically Dr. Lindsay Clark and Dr. Nam Nguyen, have been incredibly helpful with advice on membrane protein biochemistry, crystallization, and cryo-EM. Dr. Daniel Stoddard and Dr. Xiaochen Bai have also been essential in facilitating and troubleshooting EM data collection and data processing.

Perhaps the most important support system that I have had throughout graduate school has been my friends. The friends I have made during my time in Texas, as well as

friends from past lives in New Jersey and Rhode Island have kept me from fully slipping into insanity.

Finally, I would like to thank my family. I would not be here without the endless love and support from my parents, Anjani and Vishwanath. Along with my sister Radhika, they pushed me to pursue whatever I was passionate about and to strive for excellence, and for that I am truly grateful.

TABLE OF CONTENTS

PRIOR PUBLICATIONS

Kim JJ, **Gharpure A**, Teng J, Zhuang Y, Howard RJ, Zhu S, Noviello CM, Walsh RM, Lindahl E, Hibbs RE. "Shared structural mechanisms of general anesthetics and benzodiazepines." Accepted in *Nature*.

Gharpure A, Noviello CM, Hibbs RE. "Progress in nicotinic receptor structural biology." *Neuropharmacology* 2020:171:108086.

Brams M, Govaerts C, Kambara K, Price K, Spurny R, **Gharpure A**, Pardon E, Evans GL, Bertrand D, Lummis SCR, Hibbs RE, Steyaert J, Ulens C. "Modulation of the *Erwinia* Ligand-Gated Ion Channel (ELIC) and the 5-HT_3 Receptor via a Common Vestibule Site." *eLife* 2020:9:e51511.

Mann N, Kause F, Henze EK, **Gharpure A**, Shril S, Connaughton DM, Nakayama M, Klämbt V, Majmundar AJ, Wu CW, Kolvenbach CM, Dai R, Chen J, van der Ven AT, Ityel H, Tooley MJ, Kari JA, Bownass L, El Desoky S, De Franco E, Shalaby M, Tasic V, Bauer SB, Lee RS, Beckel JM, Yu W, Mane SM, Lifton RP, Reutter H, Ellard S, Hibbs RE, Kawate T, Hildebrandt F. "CAKUT and Autonomic Dysfunction Caused by Acetylcholine Receptor Mutations." *American Journal of Human Genetics* 2019:105(6):1286-1293.

Gharpure A, Teng J, Zhuang Y, Noviello CM, Walsh RM, Cabuco R, Howard RJ, Zaveri NT, Lindahl E, Hibbs RE. "Agonist Selectivity and Ion Permeation in the α3β4 Ganglionic Nicotinic Receptor." *Neuron* 2019:104(3):501-511.

Walsh RM*, Roh SH*, **Gharpure A**, Morales-Perez CL, Teng J, Hibbs RE. "Structural principles of distinct assemblies of the human α4β2 nicotinic receptor." *Nature* 2018: 557(7704):261-265. * Equal contribution

LIST OF FIGURES

LIST OF TABLES

LIST OF APPENDICES

LIST OF ABBREVIATIONS

5-HT_3 – Serotonin type 3

ACh – Acetylcholine

AChBP – Acetylcholine-binding protein

AMPA – α-amino-3-hydroxy-5-methyl-4-isoxazolepropionic acid

APS – Advanced Photon Source

BacMam – Baculovirus gene transfer into mammalian cells

BFP – Blue fluorescent protein

BRIL – Apocytochrome b(562)RIL

C10E6 – Hexaethylene glycol monodecyl ether

C11M – n-undecyl-β-D-maltopyranoside

CHAPS – 3-[(3-cholamidopropyl)dimethylammonio]-1-propanesulfonate

CHAPSO – 3-[(3-cholamidopropyl)dimethylammonio]-2-hydroxy-1-propanesulfonate

CHS – Cholesteryl hemisuccinate

Cymal-5 – 5-cyclohexyl-1-pentyl-β-D-maltoside

Cymal-6 – 6-cyclohexyl-1-hexyl-β-D-maltoside

cryo-EM – Cryo-electron microscopy

DDM – n-dodecyl-β-D-maltoside

DM – n-decyl-β-D-maltopyranoside

DMEM – Dulbecco's modified Eagle medium

DMPC – 1,2-dimyristoyl-sn-glycero-3-phosphocholine

EC_{50} – Half maximal excitatory concentration

ECD – Extracellular domain

EGTA – Ethylene glycol tetraacetic acid

ELIC – *Erwinia* ligand-gated ion channel

EM – Electron microscopy

EndoH – Endoglycosidase H

Fab – Antigen-binding fragment

FBS – Fetal bovine serum

FSC- Fourier shell correlation

FSEC – Fluorescence-detection size exclusion chromatography

$GABA_A$ – γ-aminobutyric acid type A

GDN – Glyco-diosgenin

GFP – Green fluorescent protein

GLIC – *Gloebacter* ligand-gated ion channel

GluCl – Glutamate-activated chloride channel

GnTI – N-acetylglucosaminyltransferase I

HEK – Human embryonic kidney

HEPES – 2-[4-(2-hydroxyethyl)piperazin-1-yl]ethanesulfonic acid

IC_{50} – Half maximal inhibitory concentration

ICD – Intracellular domain

K_d – Dissociation constant

K_i – Inhibitory constant

LDAO – Dodecyldimethylamine oxide

LMNG – 2,2-didecylpropane-1,3-bis-β-D-maltopyranoside

mAb – Monoclonal antibody

MD – Molecular dynamics

MSP – Membrane scaffold protein

nAChR – Nicotinic acetylcholine receptor

n_H – Hill coefficient

PAGE – Polyacrylamide gel electrophoresis

pCa – Permeability of calcium

PCR – Polymerase chainreaction

PEG – Polyethylene glycol

PMSF – Phenylmethylsulfonyl fluoride

pNa – Permeability of sodium

PNCC – Pacific Northwest Center for Cryo-EM

POPC – 1-palmitoyl-2-oleoyl-sn-glycero-3-phosphocholine

SDS – Sodium dodecyl sulfate

SEC – Size exclusion chromatography

Sf9 – *Spodoptera frugiperda* 9

TBS – Tris-buffered saline

TCEP – Tris(2-carboxyethyl) phosphine

T_m – Melting temperature

TMD – Transmembrane domain

WT – Wild type

ZAC – Zinc-activated ion channel

AMINO ACID RESIDUES

Ala or A – Alanine

Arg or R – Arginine

Asn or N – Asparagine

Asp or D – Aspartate

Cys or C – Cysteine

Glu or E – Glutamate

Gln or Q – Glutamine

Gly or G – Glycine

His or H – Histidine

Ile or I – Isoleucine

Lys or K – Lysine

Leu or L – Leucine

Met or M – Methionine

Phe or F – Phenylalanine

Pro or P – Proline

Ser or S – Serine

Thr or T – Threonine

Trp or W – Tryptophan

Tyr or Y – Tyrosine

Val or V - Valine

CHAPTER ONE

Nicotinic acetylcholine receptors

(Modified from Gharpure A, Noviello CM, Hibbs RE. "Progress in nicotinic receptor structural biology." *Neuropharmacology* 2020:171:108086.)

The nicotinic acetylcholine receptor has played a prominent role in numerous landmark studies since the turn of the 20th century. As the subject of John Newport Langley's revolutionary theory on "receptive substances" (Langley, 1905), the nicotinic receptor provided a foundation for modern pharmacological research. Electrophysiological studies on nicotinic receptors at the neuromuscular junction contributed to the initial discovery of postsynaptic potentials (Göpfert and Schaefer, 1938, Eccles et al., 1941, Eccles and O'Connor, 1939, Fatt and Katz, 1950). Furthermore, these receptors were the first ion channels to be purified (Meunier et al., 1971, Karlsson et al., 1972, Klett et al., 1973, Miledi et al., 1971, Olsen et al., 1972, Changeux et al., 1970), cloned (Claudio et al., 1983, Noda et al., 1983, Devillers-Thiery et al., 1983), and studied on a single-channel level (Neher and Sakmann, 1976). It is thus difficult to overstate the impact that the nicotinic receptor has had throughout the history of neuroscience. One discipline in which research on these proteins has lagged is structural biology. Until recently, high-resolution information on intact nicotinic receptors was absent, forcing the field to rely on structures of homologous proteins and lower-resolution electron microscopy (EM) reconstructions for insights. Over the past few years, several structures of neuronal nicotinic receptors have emerged that provide a blueprint for a more comprehensive understanding of the molecular mechanisms underlying

their function. Recent advances in structure determination with single particle cryo-EM, as well as tomography, will undoubtedly assist in resolving further outstanding questions. In this introductory chapter, I will discuss the role of nicotinic receptors in important discoveries in neuroscience, subunit and subtype diversity in the Cys-loop receptor superfamily and nicotinic receptor family, and advances in the pursuit of structural information.

Acetylcholine and the discovery of neurotransmission

The history of acetylcholine and nicotinic acetylcholine receptors is intimately tied to the discovery of chemical neurotransmission through the work of notable scientists such as Claude Bernard, John Newport Langley, Otto Loewi, and Henry Dale. Some of the earliest experiments that suggested the presence of neurotransmitters came from Claude Bernard, a French scientist who was fascinated by poisonous substances. In the 19th century, Bernard was investigating the mechanism of action of curare, a potent alkaloid that was commonly used as an arrow poison by the indigenous people of Central and South America and is now known to be a nicotinic receptor antagonist. Following the insertion of a small sample of dried curare under the skin of a frog, he noticed that the frog slowly went limp and lost activity. After opening up the frog, Bernard found that electrical stimulation of the muscles still led to contractions, whereas stimulation of the nerves innervating those muscles produced no activity, leading him to believe that curare acted primarily on motor neurons (Black, 1999). This work was followed up on by John Newport Langley, who looked at the physiological effects of curare and another natural alkaloid, nicotine. When Langley applied

nicotine to the skeletal muscles of an anesthetized fowl, he saw that muscles contracted. The activation by nicotine could be blocked by pre-administration of curare (Langley, 1905). This finding was similar to the antagonistic actions of pilocarpine and atropine he had previously observed in the sub-maxillary gland (Langley, 1880). These observations led Langley to conclude that neither nicotine nor curare were directly acting on the "contractile substance" of the muscle, but rather on "accessory" or "receptive substances" (Langley, 1905, Maehle, 2004), which we now know to be cell-surface receptors.

While Bernard and Langley took the first steps toward identifying neurotransmitter receptors, Henry Dale and Otto Loewi helped materialize the concept of chemical neurotransmission by identifying acetylcholine as a neurotransmitter. In the 1910's Dale found that a preparation from ergot of rye was capable of producing effects similar to that of muscarine (Tansey, 1991). A colleague of his, Arthur Ewins, was able to isolate the active compound and showed that this compound was identical to acetylcholine (Ewins, 1914). In turn, Dale showed that acetylcholine had two primary physiological effects- one mirroring that of muscarine (through action on metabotropic muscarinic receptors), and the other similar to that of nicotine (through action on ionotropic nicotinic receptors) (Dale, 1914). While these results were striking, there was little evidence that acetylcholine was physiologically relevant at this point. In 1921, Otto Loewi provided some credence to this possibility with his now iconic experiment. Loewi dissected hearts out of two frogs. After stimulating the vagus nerve of one heart, he found that the heart stopped beating. Loewi then collected the fluid surrounding that heart and found that the second heart stopped beating upon application of the fluid. From these results, Loewi concluded that there was a chemical

compound, which he named Vagusstoff, that was released by the vagus nerve that caused the hearts to stop beating (Loewi, 1921). Loewi and colleagues later found that Vagusstoff was very similar to acetylcholine, and shortly after that Dale confirmed that acetylcholine was naturally present in mammals and acted as a neurotransmitter in the peripheral nervous system (Tansey, 1991).

It is now common knowledge that acetylcholine and nicotinic receptors are involved in fast synaptic transmission in the autonomic ganglia and at the neuromuscular junction. Acetylcholine also plays an important role in the central nervous system through action on muscarinic receptors, which are G-protein coupled receptors, and on nicotinic receptors. Cholinergic neurons can be projection neurons, originating in nuclei throughout the brain, including the medial habenula and basal forebrain, or they can be local interneurons, which play important roles in the striatum and nucleus accumbens (Picciotto et al., 2012). Typically, in the central nervous system, acetylcholine acts as a modulator and contributes to vital processes such as addiction, reward, attention, food intake, and stress (Picciotto et al., 2012).

Cys-loop receptors

Nicotinic acetylcholine receptors belong to a superfamily of pentameric ligand-gated ion channels, commonly referred to as Cys-loop receptors. In humans, this superfamily also includes the γ-aminobutyric acid type A ($GABA_A$) receptor, glycine receptor, serotonin type 3 ($5\text{-}HT_3$) receptor and the zinc-activated ion channel (ZAC) (Nemecz et al., 2016). Cys-loop receptor homologs are also prevalent in prokaryotes and invertebrates (Tasneem et al., 2005).

Notable examples include ion channels from *Erwinia chrysanthemi* (ELIC), *Gloebacter violaceus* (GLIC), and a glutamate-activated chloride channel from *Caenorhabditis elegans* (GluCl). These members have been studied extensively through X-ray crystallography and provided initial high-resolution insights into the overall topology, pore profiles, and allosteric gating mechanisms within the family (Hilf and Dutzler, 2009, Hilf and Dutzler, 2008, Bocquet et al., 2009, Althoff et al., 2014, Hibbs and Gouaux, 2011, Sauguet et al., 2014, Sauguet et al., 2013, Nemecz et al., 2016).

Cys-loop receptors form homo- or heteropentameric assemblies with five subunits arranged in an approximately symmetric manner about the central channel axis (Fig. I.1). Individual subunits share a modular design with a large N-terminal extracellular domain (ECD) where orthosteric ligands bind, a transmembrane domain (TMD) that surrounds the ion-conducting pore, and an intracellular domain (ICD) of variable length and secondary structure (Fig. I.2) (Thompson et al., 2010). Remarkably, within the constraints of this generally conserved architecture, members of this family have evolved differential selectivities for cations and anions (Cymes and Grosman, 2016). Accordingly, Cys-loop receptors represent the only family of ion channels that facilitate both excitatory and inhibitory signaling, allowing them to perform a wide range of important physiological functions. In vertebrates, anionic members such as $GABA_A$ and glycine receptors mediate the majority of fast inhibitory neurotransmission in the central nervous system (Bowery and Smart, 2006). In contrast, cationic members of the family, including 5-HT_3 and nicotinic receptors, largely play a modulatory role in the brain (Wonnacott, 1997, Miquel et al., 2002,

Picciotto et al., 2012) and are directly involved in fast excitatory synaptic transmission in the periphery (Skok, 2002, Browning, 2015, Lummis, 2012).

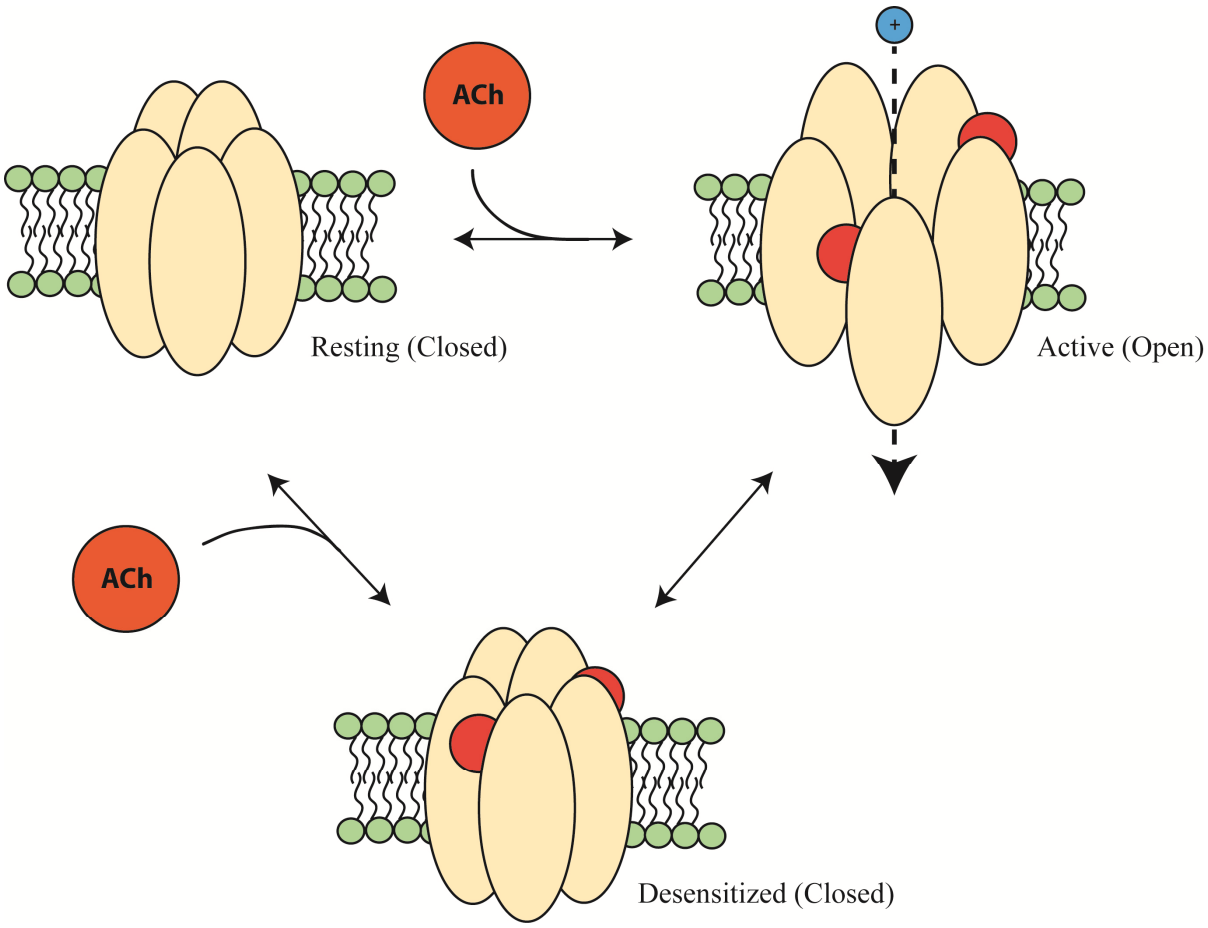

Fig. I.1 Conformational cycle of Cys-loop receptors
Cartoon diagram of a pentameric ligand-gated ion channel illustrating the allosteric gating mechanism. In the absence of agonist, receptors will primarily be in the resting state. Upon agonist (depicted as acetylcholine) binding, channels will open before entering an energetically favorable desensitized conformation.

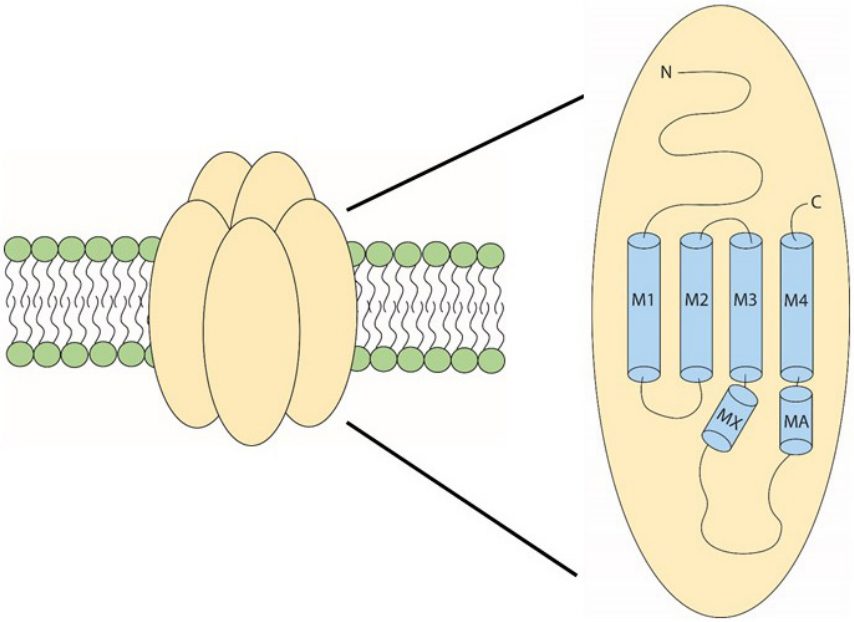

Fig. I.2 Subunit architecture
Cartoon representation of the subunit architecture of a nicotinic acetylcholine receptor.

Subtype diversity of nicotinic receptors

The nicotinic receptor family consists of 17 subunits (α1-α10, β1-β4, γ, δ, and ε) that can assemble in limited combinations to generate a large but restricted number of distinct pentameric subtypes (Albuquerque et al., 2009) (Fig. I.3). Broadly, nicotinic receptors can be divided into two main classes, muscle-type and neuronal-type, based on subunit composition and physiological function. Muscle-type receptors are found on the motor endplate at the neuromuscular junction, and activation of these receptors produces depolarizing end plate potentials that lead to muscle contraction. Neuronal nicotinic receptors are expressed throughout the central and peripheral nervous systems and play important roles in cognition (Maskos et al., 2005, Levin, 2002, Ohno et al., 1993, Ji et al., 2001, Picciotto et al., 1995),

addiction (Azam et al., 2002, Leslie et al., 2013, Berrettini et al., 2008, Picciotto et al., 1998), and homeostatic function of the autonomic nervous system (Skok, 2002, Zoli et al., 2015).

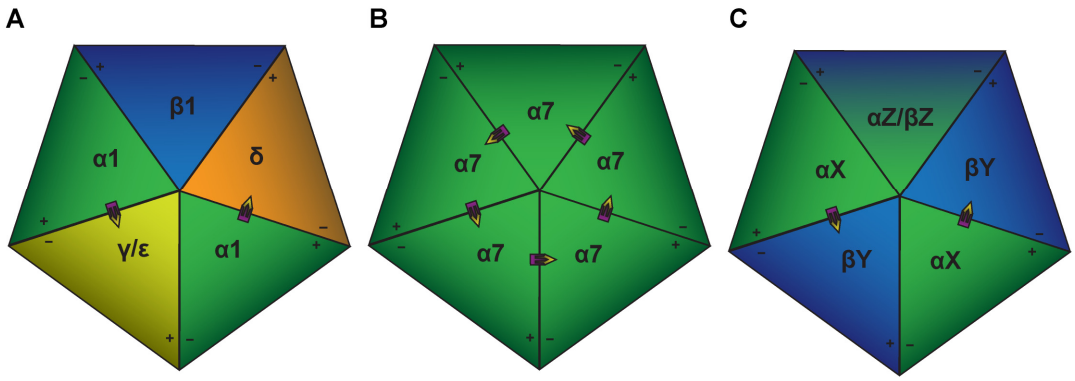

Fig. I.3 Nicotinic acetylcholine receptor subunit assemblies
(A) Subunit arrangement of the muscle-type nicotinic receptor. Orthosteric binding sites are denoted by arrows at α1-γ/ε and α1-δ interfaces. (B) Subunit arrangement of a homomeric neuronal nicotinic receptor, α7. α9 can also form homomers. (C) Subunit arrangement of heteromeric neuronal nicotinic receptors. αX positions can be occupied by α2, α3, α4, or α6 subunits, βY positions can be occupied by β2 or β4 subunits, and the last position (αZ/βZ) can be occupied by any of the above as well as α5 and β3.

Muscle-type nicotinic receptors form heteromers with a stoichiometry of $\alpha1_2\beta1\gamma\delta$ (Karlin et al., 1983) (Fig. I.3A). In adult human muscle, the γ subunit is replaced by an ε subunit to form $\alpha1_2\beta1\varepsilon\delta$ assemblies (Mishina et al., 1986). While γ and ε protomers share high sequence identity (Table I.1), receptor subtypes containing either subunit display varying functional properties (Mishina et al., 1986, Sakmann and Brenner, 1978) and contribute differently to neuromuscular development and maintenance (Witzemann et al., 1996, Takahashi et al., 2002, Koenen et al., 2005, Liu et al., 2008). Muscle-type receptors have classically served as the prototype not just for nicotinic receptors, but for all ligand-

gated ion channels, due to their abundance at muscle fiber endplates and in other natural sources such as the electrocytes of electric fish (Nachmansohn et al., 1941). Historical perspectives on this receptor subtype and its involvement in significant breakthroughs in neuroscience have been discussed in great detail in (Changeux, 2012, Unwin, 2013, Karlin, 2002).

Neuronal-type receptors are composed of various combinations of α2-α10 and β2-β4 subunits (Zoli et al., 2015, Dani and Bertrand, 2007). The large diversity in subunits in this class produces an apparently overwhelming number of possible permutations of neuronal-type assemblies. However, these subunits can be further grouped into clades that dictate the permitted subtypes they can form, greatly limiting the number of potential subtypes. α7 and α9 subunits typically assemble as homopentamers (Seguela et al., 1993, Elgoyhen et al., 1994) (Fig. I.3B), although α9-containing receptors can also incorporate α10 subunits (Elgoyhen et al., 2001, Sgard et al., 2002), and there is growing evidence of an α7β2 subtype expressed in restricted tissues (Liu et al., 2009, Moretti et al., 2014). In contrast, α2-α6 and β2-β4 subunits form obligate heteromers. Ligand binding sites in these subtypes require contributions from a principal α (α2, α3, α4, or α6) subunit and a complementary β (β2 or β4) subunit (Le Novere et al., 2002). Thus, neuronal assemblies consist of at least two α subunits and two β subunits. The fifth subunit in the pentamer does not directly contribute to the classical agonist binding site and thus its identity is not as restricted (Fig. I.3C). Due to tissue-dependent expression differences, certain assemblies are more prevalent than others. Receptors containing α4 and β2 subunits constitute the most abundant subtype in the central nervous system and serve as the major high-affinity binding site for nicotine (Flores et al.,

1992, Wada et al., 1989, Whiting and Lindstrom, 1988). α3β4-containing receptors are the predominant nicotinic receptors in the autonomic ganglia (Fig. I.4) (Conroy and Berg, 1995, Vernallis et al., 1993) and adrenal medulla (Campos-Caro et al., 1997, Free et al., 2002) and are also expressed in abundance in certain brain areas that modulate reward, such as the medial habenula and the interpeduncular nucleus (Grady et al., 2009, Mulle et al., 1991, Quick et al., 1999). Both α4β2 and α3β4 are expected to co-assemble with accessory subunits such as α5 (Conroy et al., 1992, Boulter et al., 1990, Ramirez-Latorre et al., 1996) and β3 (Grady et al., 2009, Broadbent et al., 2006, Jain et al., 2016), although the extent and functional consequences of accessory subunit incorporation remain unclear. Differential incorporation of accessory subunits may allow for further diversity and fine-tuning of functional responses in different brain regions.

	α1	α2	α3	α4	α5	α6	α7	α9	α10	β1	β2	β3	β4	γ	δ
α1															
α2	48														
α3	49	57													
α4	49	70	67												
α5	44	52	48	53											
α6	45	53	65	54	47										
α7	35	39	36	38	35	35									
α9	35	34	34	34	34	35	35								
α10	34	36	35	36	34	35	40	55							
β1	36	38	37	40	36	36	30	29	32						
β2	42	49	46	51	41	46	34	30	35	42					
β3	43	53	48	54	69	47	35	33	34	37	42				
β4	42	49	46	48	42	44	36	31	37	41	65	43			
γ	33	35	33	36	32	34	30	29	31	40	37	31	38		
δ	36	38	38	37	34	38	31	29	34	41	41	37	40	46	
ε	31	36	35	33	32	35	29	28	32	39	36	33	36	51	46

Table I.1 Sequence identities of human nicotinic receptor subunits
Sequence identity matrix of all human nicotinic receptor subunits. α8 is not found in mammals and is not included. Principal α subunits are indicated in green, complementary β subunits in blue, complementary muscle-type subunits in yellow and orange, and auxiliary subunits in teal. Highlighted boxes show sequence identities between interchangeable subunits.

The vast diversity in nicotinic receptors produces subtypes with subtly different functional properties. Whether or not these differences are physiologically significant is debatable (Le Novere et al., 2002); however, these differences can provide insight into the molecular determinants of certain properties, as they allow researchers to tie changes in sequence to changes in function. Here, I will briefly discuss some of the distinctive biophysical properties of α3β4 nicotinic receptors and compare them to other well-studied neuronal subtypes, such as α4β2 and α7.

One notable property of non-selective cation channels is relative calcium permeability. Calcium is very important physiologically, acting as a second messenger in many signaling pathways. Neuronal nicotinic receptors are relatively more calcium-permeable than muscle-type receptors. Among neuronal receptors, heteromeric subtypes, such as α3β4 and α4β2 tend to have lower calcium permeabilities (pCa/pNa ~1) than homomeric receptors such as α7 (pCa/pNa ~ 10) (Fucile, 2004). The molecular basis for this property is believed to be due to the identity of the M2 20′ residue. In α subunits, this residue tends to be acidic, whereas in β subunits it tends to be basic. Thus, pentamers with more copies of α subunits will be better suited for the passage of a multivalent cation such as calcium (Tapia et al., 2007, Walsh et al., 2018). Another interesting property of α3β4 receptors is their desensitization rate. This subtype desensitizes slower than α3β2, α4β2, and α4β4 subtypes (Cachelin and Jaggi, 1991, Fenster et al., 1997, Quick and Lester, 2002). This slow desensitization may be a function of the β4 subunit, as α4β4 receptors will also desensitize slower than α3β2 and α4β2 (Fenster et al., 1997). α7 receptors are among the fastest desensitizing subtypes (Peng et al., 1994). Finally, α3β4 receptors display a lower

affinity for many classical nicotinic receptor agonists than α4β2 receptors. These include the endogenous ligand acetylcholine, as well as high affinity α4β2 agonists such as nicotine and epibatidine (Eaton et al., 2003, Xiao et al., 1998). One of the main focuses of this dissertation project was to provide insight into this phenomenon and this will be discussed in detail in chapter three.

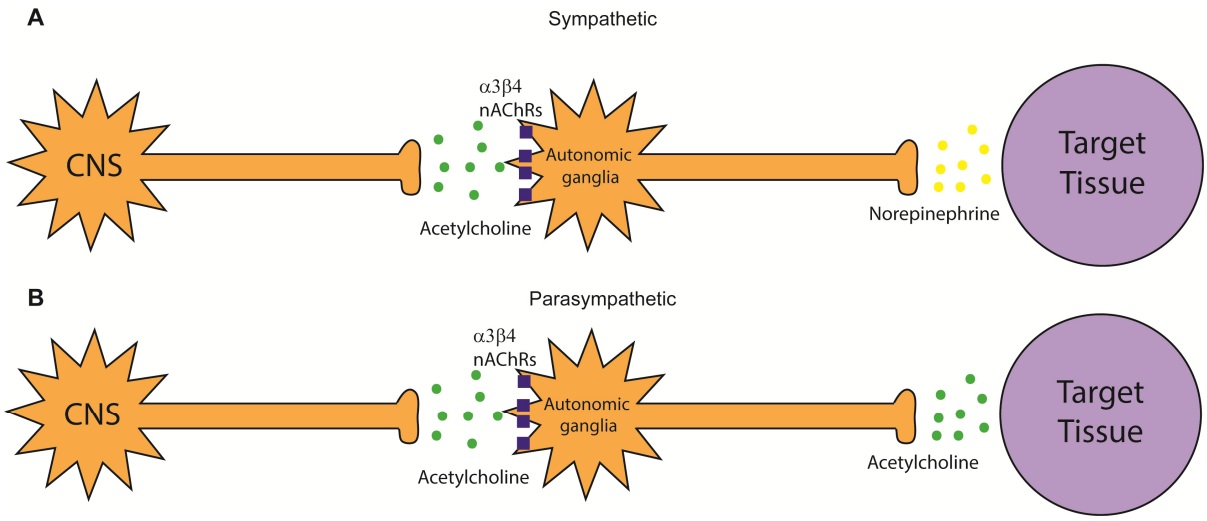

Fig. I.4 Disynaptic architecture in the autonomic nervous system
(A) Cartoon diagram showing the arrangement of the sympathetic branch. The ganglionic synapse relies on acetylcholine and α3β4 nicotinic receptors for fast synaptic transmission. Ganglionic neurons in turn release norepinephrine that act on adrenergic receptors. (B) Cartoon diagram showing the arrangement of the parasympathetic branch. The ganglionic synapse relies on acetylcholine and α3β4 nicotinic receptors for fast synaptic transmission. Ganglionic neurons in turn release acetylcholine that primarily act on muscarinic receptors.

A brief history of structural studies

Structural studies on the nicotinic receptor date back to the 1970's. Negatively-stained electron micrographs of purified receptors and subsynaptic membranes from *Torpedo marmorata* and *Torpedo californica* electrocytes revealed distinct rosettes 80-90 Å in diameter (Klymkowsky and Stroud, 1979, Cartaud et al., 1973, Cartaud et al., 1980). Later, Unwin and colleagues were able to coax membrane fragments containing a high density of receptors into forming well-ordered tubular crystals that were then suitable for examination through electron crystallography (Brisson and Unwin, 1984). Early attempts at structure determination through this method yielded relatively low-resolution reconstructions that provided an initial glimpse at the overall architecture of the receptor (Fig. I.5A) (Brisson and Unwin, 1985, Toyoshima and Unwin, 1988, Toyoshima and Unwin, 1990, Unwin et al., 1988). Systematic improvements in data quality through averaging (Unwin, 1993), correction of image distortions by computational segmentation of tubular crystals (Beroukhim and Unwin, 1997), and advances in electron microscope hardware led to substantial enhancement of map quality (Unwin, 2005, Miyazawa et al., 2003). However, the overall resolutions of reconstructions attained from this work were still insufficient for accurate atomic modeling of the entire receptor, limiting the detailed molecular insights that could be gleaned. This review will mainly focus on recently determined higher-resolution structures; however, a thorough examination of this transformative series of *Torpedo* receptor studies can be found in (Unwin, 2013).

The dawn of the new millennium provided the opportunity for higher-resolution information on the ligand-binding site of the nicotinic receptor with the identification of a

synaptic protein released by glial cells in mollusks (Fig. I.5B) (Smit et al., 2001). This molecule, appropriately dubbed the acetylcholine-binding protein (AChBP), is structurally homologous to the extracellular domain of nicotinic receptors, sharing 24% sequence identity with the N-terminal region of the α7 nicotinic receptor subunit. The relatively small size (~120 kDa pentamer) and soluble nature of this protein make it particularly amenable to crystallization (Brejc et al., 2001). Consequently, numerous X-ray structures of AChBPs, mostly from *Lymnaea stagnalis* and *Aplysia californica*, have been determined, ranging in resolutions from 4.2 Å – 1.75 Å (Rucktooa et al., 2009, Shahsavar et al., 2016, Brejc et al., 2001). Further progress was made with the design of chimeras between AChBP and the human α7 subunit (Li et al., 2011, Nemecz and Taylor, 2011, Delbart et al., 2018). A couple of these humanized receptors share >60% sequence identity with the α7 ECD, with the ligand-binding site and surrounding regions entirely consisting of α7 residues. Structures of AChBP and the related chimeras as well as emerging crystal structures of isolated extracellular domains of human α1 (Fig. I.5C) (Dellisanti et al., 2007, Noridomi et al., 2017), α9 (Zouridakis et al., 2014, Zouridakis et al., 2019), and α2 (Kouvatsos et al., 2016) provided unprecedented structural insights into the fold of the extracellular domain and local conformational changes in the ligand-binding site upon binding of agonists and antagonists that rationalized prior biochemical studies (Hansen et al., 2005, Celie et al., 2004, Bourne et al., 2005, Damle and Karlin, 1980, Karlin, 1969). However, these structures came with several limitations. AChBP is not functionally coupled to a pore domain (Bouzat et al., 2004); therefore, these structures could not elucidate how the conformational changes seen in the binding pocket are propagated to the transmembrane domain. The isolated nicotinic

receptor extracellular domains, on the other hand, did not form pentamers, except in the case of α2, which is not thought to assemble physiologically as a homopentamer. Perhaps the most glaring issue was the lack of transmembrane and intracellular domains, thus precluding any conclusions that could be drawn about these regions.

The need for high-resolution structural information on intact nicotinic receptors was thus apparent. A recent series of structures of α4β2 (Morales-Perez et al., 2016b, Walsh et al., 2018) and α3β4 (Gharpure et al., 2019) subtypes have begun to address outstanding questions about these proteins, including detailed examinations into structural bases for ion permeation, lipidic interactions, and differences in ligand affinity, as well as queries into the nature of heteromeric assemblies. The remainder of this review will describe the technical developments required to achieve these structures, and then highlight key findings from them in the context of earlier biochemical and functional studies.

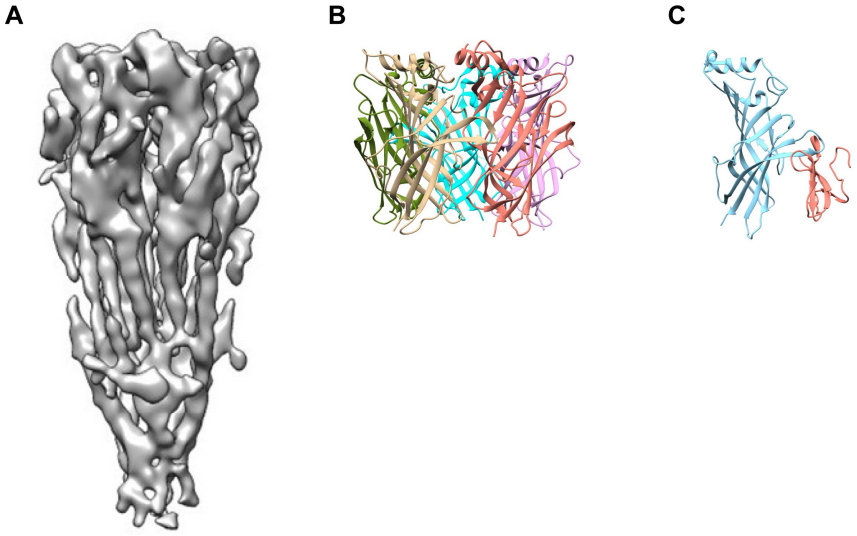

Fig. I.5 Early structural studies of nicotinic acetylcholine receptors
(A) Reconstruction of the Torpedo nicotinic receptor (EMDB: EMD-2071). (B)Atomic model of the acetylcholine binding protein from *L. stagnalis* (PDB: 1I9B). (C) Atomic model of a monomeric α1 subunit ECD (blue) bound to α-bungarotoxin (salmon) (PDB: 2QC1).

Technical hurdles

Several technical difficulties thwarted attempts to obtain high-resolution structures of intact nicotinic receptors for many years. These receptors, like many other membrane proteins, suffer from low expression in heterologous systems and poor biochemical stability when extracted from the plasma membrane. Nicotinic receptors are also heavily glycosylated, which can impede traditional structural approaches such as X-ray crystallography, as the flexible and chemically heterogeneous sugar moieties can hinder growth of well-ordered crystals. Furthermore, the heteromeric nature of the vast majority of physiologically relevant subtypes presents important problems for structure determination. Heteropentamers can often assemble in multiple stoichiometries (usually as 2α:3β or 3α:2β) (Nelson et al., 2003), complicating the isolation of a homogeneous sample required for crystallography. Heteromeric assemblies are also inherently pseudo-symmetric, with nearly identical tertiary structure between different subunits in a pentamer. This pseudosymmetry can pose a significant challenge in structural biology by making difficult the correct assignment of subunits.

Advances in membrane protein biochemistry and cell biology contributed to overcoming these obstacles associated with expression, purification, and structure determination of nicotinic receptors. Concurrent developments of an HEK 293-derived cell line deficient in N-acetylglucosaminyltransferase I ($GnTI^-$) (Reeves et al., 2002), and technology utilizing baculovirus mediated gene transfer in mammalian cells (BacMam expression system) (Dukkipati et al., 2008, Goehring et al., 2014), allowed for overexpression of human membrane proteins containing homogeneous N-linked glycans that

could be more efficiently cleaved by endoglycosidases. Rapid and cost-efficient biochemical screening in order to identify tractable constructs and optimal conditions for receptor stability was enabled by the popularization of fluorescence-detection size exclusion chromatography (FSEC) (Kawate and Gouaux, 2006). By attaching a fluorophore such as GFP to the protein of interest, hundreds of constructs and solubilization conditions could be screened in a matter of days, requiring only minute quantities of protein, circumventing the need for purification in the initial optimization of sample biochemistry. A related approach was used to address the mixed stoichiometry problem and streamline titration of the viruses used to express the heteromer (Morales-Perez et al., 2016a). Fusion of different fluorescent proteins to α4 and β2 genes allowed for optimization of expression conditions to bias production of one heteromeric assembly of α4β2, which was a critical step in determining the initial crystal structure of this subtype (Morales-Perez et al., 2016b).

Perhaps the most powerful and far-reaching developments in high-resolution structure determination were associated with the "resolution revolution" in cryo-EM (Cheng, 2015, Cheng et al., 2015, Cao, 2020). Improvements in direct electron detectors and related data-processing software that could correct beam-induced motions of individual particles resulted in a substantial increase in achievable resolutions through single-particle analysis. This new technology has been a boon for structural biology by removing the requirement of crystallization, which is often the rate-limiting step in structural studies of membrane proteins. Single-particle cryo-EM has now become the preferred method for studies on integral membrane proteins and large complexes and structural information for such proteins is being uncovered at an unprecedented rate. However, as mentioned above, pseudo-

symmetric molecules such as nicotinic receptors are not ideal specimens for this technique. 3D reconstructions of cryo-EM maps rely on low-resolution information for initial particle alignment (Henderson et al., 2011, Scheres, 2016), and in heteromeric nicotinic receptors, subunit identities may not be obvious at low resolutions. To resolve this problem, subtype-specific Fab fragments were used as fiducial markers to distinguish subunits in the initial stages of particle alignment. This method enabled the determination of both stoichiometries of α4β2 from a single heterogeneous sample (Walsh et al., 2018), as well as the 2α:3β stoichiometry of α3β4 (Gharpure et al., 2019) which will be discussed in detail in the next two chapters.

CHAPTER TWO

The pursuit of structural information

Introduction

The primary objective of my dissertation project was to determine high-resolution structures of the α3β4 nicotinic acetylcholine receptor. The emergence of single-particle cryo-EM as a viable method in structural biology was instrumental to the success of this goal. However, prior to the popularization of this technique and the opening of the cryo-EM facility at UT Southwestern, the vast majority of my work on this project was spent trying to grow crystals that would diffract sufficiently well to determine an X-ray structure. While these efforts were ultimately fruitless, the lessons I learned and insights I gained about membrane protein biochemistry and structural biology undoubtedly contributed to the success of this project. In this chapter, I will briefly summarize key experiments from my attempts at determining a crystal structure of the α3β4 receptor, as well as the cryo-EM sample optimization that led to the completion of this project.

Results

Identification of α3β4 as a candidate for structural studies

As highlighted in the previous chapter, the α3β4 nicotinic receptor plays important roles in physiology and is thus an attractive subject for structural studies. To test the biochemical feasibility of this project, I created GFP-fusion constructs for human α3 and β4 subunits by placing GFP in the M3-M4 loop, a common site for fusion partner incorporation

in Cys-loop receptors (Morales-Perez et al., 2016a). I first wanted to confirm that α3 and β4 subunits, when expressed alone in HEK cells, would not assemble as pentamers. Individually transfected α3-GFP and β4-GFP constructs did produce a minor peak at a similar size as the control α7-GFP (which is expected to assemble as a homopentamer), however the fluorescence intensity for α3 and β4 was considerably lower than that of the control, indicating less efficient expression (Fig. II.1A).

Next, I wanted to see if co-expression of α3 and β4 subunits would improve pentamer formation. When α3-GFP and β4-WT were co-transfected in HEK cells, a more monodisperse peak in the pentamer region (as defined by the control, α7-GFP) was seen in the resultant FSEC trace; however, the fluorescence intensity was once again substantially lower than the control. A similar result was seen with the co-transfection of α3-WT and β4-GFP (Fig. II.1B). The lower fluorescence intensity seen for α3β4 in these experiments could be explained in a few different ways. First, heteropentamers containing only one species of GFP-tagged subunits would be expected to contain one to four copies of GFP, as opposed to the five copies in a homopentameric assembly. Thus, the fluorescence would be apparently lower for the same protein yield. However, the α3β4 FSEC traces were roughly 8-fold lower than the control, so this likely would not account for the entire difference. Second, the inclusion of WT subunits without any soluble fusion partners (such as GFP) could hinder biochemical stability and lower the protein yield. Finally, α3β4 may inherently express worse than α7.

To address this issue, I next co-transfected α3-GFP and β4-GFP and the FSEC trace showed a nice monodisperse peak in the pentamer region, that was ~50% of the control peak

(Fig. II.1C). Although further construct optimization appeared necessary to reduce aggregation and other impurities, human α3β4 looked to be a good lead for structural studies.

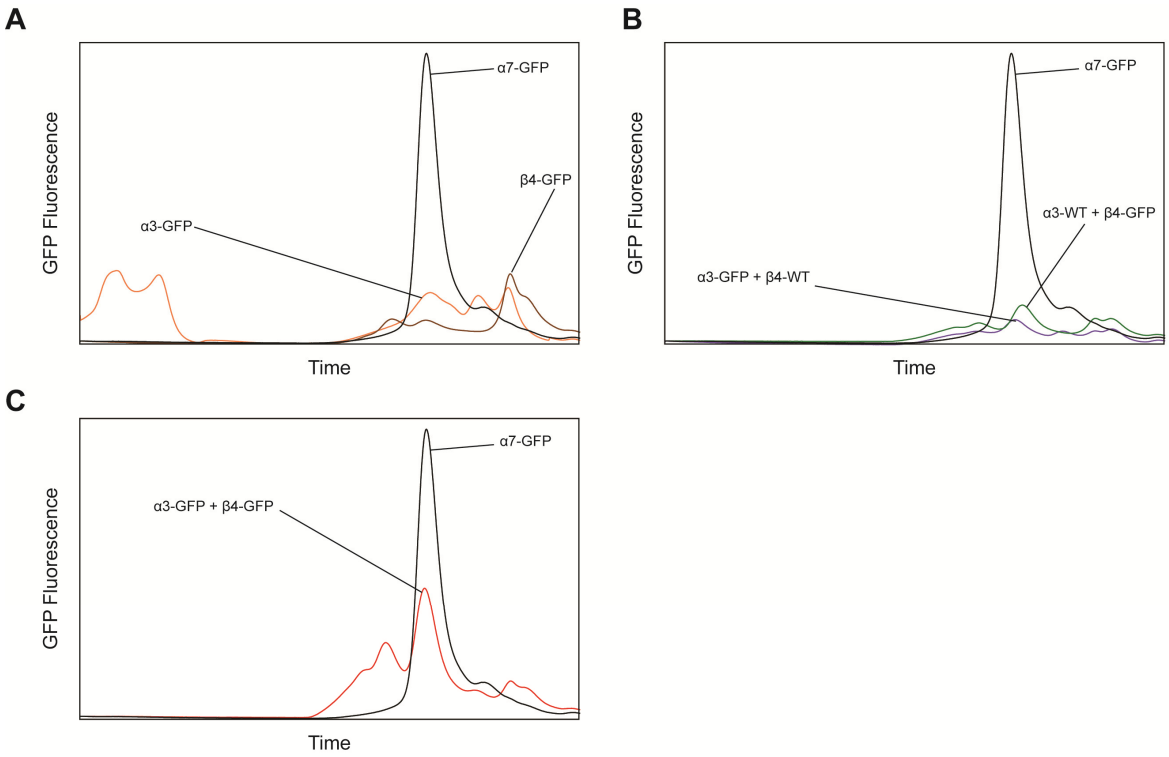

Fig. II.1 Initial α3β4 FSEC screening
(A) FSEC trace of α3-GFP (orange) and β4-GFP fusion (brown) constructs transfected individually. α7-GFP is included as a control (black). (B) FSEC results of co-transfections of α3-GFP and β4-WT (blue) and α3-WT and β4-GFP (green). (C) FSEC trace of co-transfection of α3-GFP and β4-GFP (red).

In an attempt to increase yield and produce a more homogeneous population of protein, I made a large deletion in the M3-M4 loop and replaced this region with BRIL, creating similar constructs to those that had originally worked to grow crystals of the α4β2 subtype (Morales-Perez et al., 2016a). I added a Strep-tag (Schmidt and Skerra, 2007) to the C-terminus of the β4 subunit to enable affinity purification. I chose to add this modification

to β4 as opposed to α3 because the expected stoichiometry for this receptor is $(\alpha3)_2(\beta4)_3$, meaning that there would likely be more copies of the affinity tag in the pentamer, the C-terminus of β4 is longer than that of α3, providing more room for the affinity tag, and the lower propensity for β4 to form homomers. I used these new modified constructs (which will be referred to as Del1-BRIL) to transfect adherent HEK GnTI- cells and performed a small-scale purification. The resulting FSEC trace showed a nice monodisperse peak, indicating that these constructs were suitable for initial crystallization studies (Fig. II.2A).

Initial large-scale purifications (800 mL of suspension HEK GnTI- cells) using these constructs produced protein with good purity and yield. The buffer conditions for these purifications were selected based on what had originally worked in the small-scale tests I described earlier, as well as what had worked for the α4β2 subtype. I used dodecylmaltoside (DDM) as the detergent for solubilization, affinity purification, and size-exclusion chromatography. I also included nicotine, a non-selective agonist of nicotinic acetylcholine receptors, throughout the purification. I purified protein in the presence of cholesteryl hemisuccinate (CHS), a more soluble cholesterol analog commonly used in structural studies of membrane proteins. The protein was treated with Endoglycosidase H (EndoH) following affinity purification and prior to gel-filtration to reduce heterogeneity in glycosylation in the final sample. I used the protein from these preps to set up crystallization screens. Despite the good quality of protein attained from these purifications (Fig. II.2B-C), I did not see any crystals. The complete absence of hits, even in the form of microcrystals, suggested that modifications in purification conditions and/or constructs would likely be required for crystal growth.

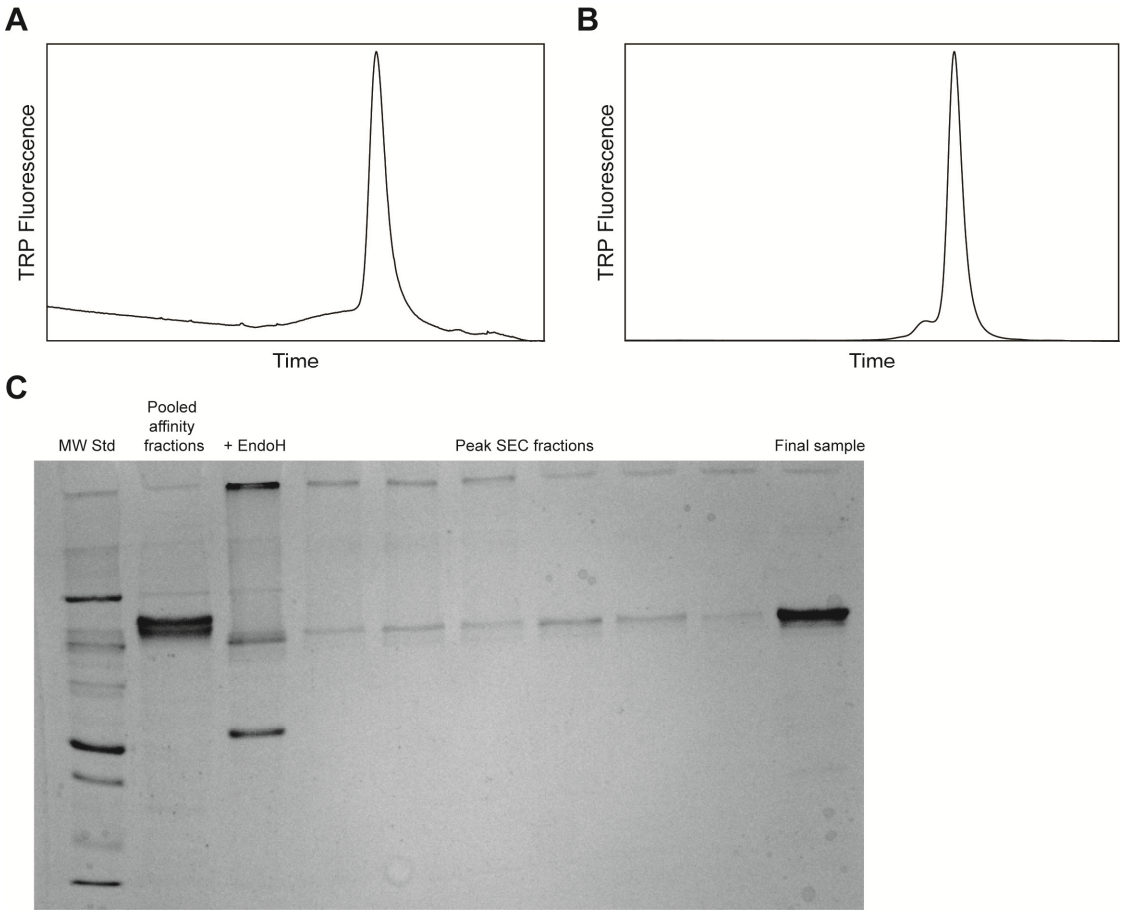

Fig. II.2 Purification of α3β4 Del1-BRIL protein
(A) FSEC trace of small-scale batch purification test of Del1-BRIL constructs. (B) Final product FSEC trace of initial large-scale purification. (C) SDS-PAGE gel indicating homogeneity in the final sample used for crystallization.

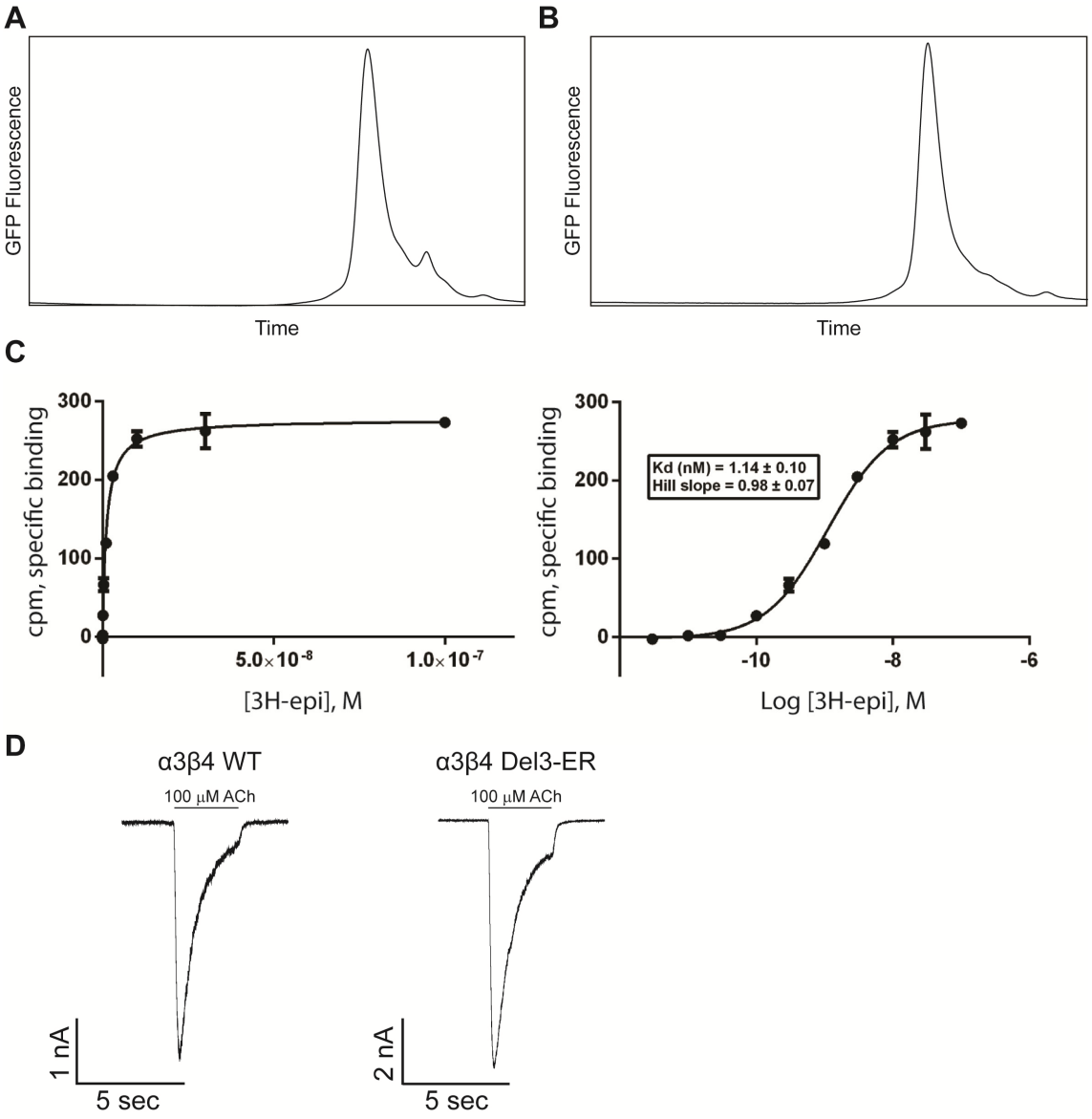

Fig. II.3 FSEC and functional tests of Del3-ER constructs
(A) FSEC trace of co-transfected α3-GFP and β4-Del3-ER, measuring GFP fluorescence. (B) FSEC trace of co-transfected α3-Del3-ER and β4-GFP, measuring GFP fluorescence. (C) Preliminary saturation radioligand binding assay using Del3-ER protein and tritiated epibatidine shows a K_d of ~1 nM. (D) Whole-cell recordings of wild type and Del3-ER α3β4 show the modified protein is qualitatively similar to unmodified receptors.

Around this time, other members of the lab showed that removal of BRIL from the M3-M4 loop did not negatively affect the biochemical quality of the α7 subtype and produced better-diffracting crystals of α4β2. I decided to follow suit and created constructs of α3 and β4 without BRIL and with a more aggressive deletion than before with 5 more residues taken out of the intracellular loop. I also included a two amino acid long charged linker (glutamate-arginine) in the M3-M4 loop that had been beneficial for α4β2 crystallization. Initial FSEC results showed good monodispersity (Fig. II.3A-B), and preliminary whole-cell recordings (Fig. II.3D) and radioligand binding assays (Fig. II.3C) confirmed that these constructs were functional, so I decided to move forward with these constructs, which will be referred to as Del3-ER.

Stoichiometry optimization

Another possible explanation for the lack of crystal growth could be related to a form of sample heterogeneity that would be difficult to detect by FSEC analysis or SDS-PAGE. As a heteromeric protein, α3β4 is believed to assemble in multiple stoichiometries- mostly as $(\alpha3)_2(\beta4)_3$ and $(\alpha3)_3(\beta4)_2$ (Covernton et al., 1994, Grishin et al., 2010, Krashia et al., 2010). A sample that is stoichiometrically heterogeneous would likely not be successful in crystallization trials. To remediate this potential issue, I utilized a fluorescence-based assay that was developed for and used to grow crystals of the α4β2 subtype (Fig. II.4B) (Morales-Perez et al., 2016a).

For this assay, I needed α3 and β4 subunits to be tagged with different fluorescent markers. Since I already had GFP fusions for both subunits, I also made an α3-mCherry

fusion construct (Fig. II.4A). I transduced an 800 mL culture with MOIs of 1 for both α3-mCherry and β4-GFP and allowed 72 hours for protein expression. I collected the SEC fractions from this prep and calculated the molar concentration of α3-mCherry and β4-GFP subunits in the sample by using Beer's law. The measured absorbance of GFP (488 nm) and mCherry (587 nm) was divided by the extinction coefficient for the respective fluorophore. Using this approach, I was able to determine that in this sample, where a 1:1 ratio of virus was used for protein expression, I had a nearly perfect 0.67 molar ratio of α3 subunits to β4, indicating a 2α:3β stoichiometry. To provide further confidence to these results, I ran these fractions through FSEC to determine a scale factor to correlate the known molar concentration of a subunit to the observed fluorescence intensity. These scale factors would then allow me to conduct small-scale experiments in which I could alter expression conditions and look for changes in sample stoichiometry by measuring fluorescence intensity in FSEC.

To this end, I transduced 1 mL of suspension HEK cells with various ratios of α3-mCherry virus and β4-GFP virus ranging from 1:10 to 10:1. There was a high level of mCherry background noise after solubilization which might have caused an overestimation of mCherry fluorescence. To address this, I performed an additional step of purification using strep resin, and the resulting FSEC profiles were much cleaner (Fig. II.5). After measuring the peak intensities of mCherry and GFP fluorescence for the different ratios, I found that a 1:1 viral ratio provides a molar ratio of α3:β4 of ~0.64, indicating a population with fixed stoichiometry, confirming the results from the large-scale experiment (Fig. II.4C, Table II.1). Another conclusion of this experiment was that altering the viral ratio enabled me to change

the molar ratio of α3:β4, although I was not able to get that ratio to 1.5 (indicating a mostly pure $(\alpha3)_3(\beta4)_2$ stoichiometry) even with viral ratios as high as 10α:1β. Interestingly, shifting the viral ratio in the other direction, with more β4 virus, produced samples with molar ratios below 0.67. This result suggested that stoichiometries of 1α:4β may be being expressed; however, this is likely just an artifact of overexpression. The overall conclusion from this set of experiments was that a 1:1 viral ratio would produce a mostly homogenous population of protein containing 2α:3β pentamers.

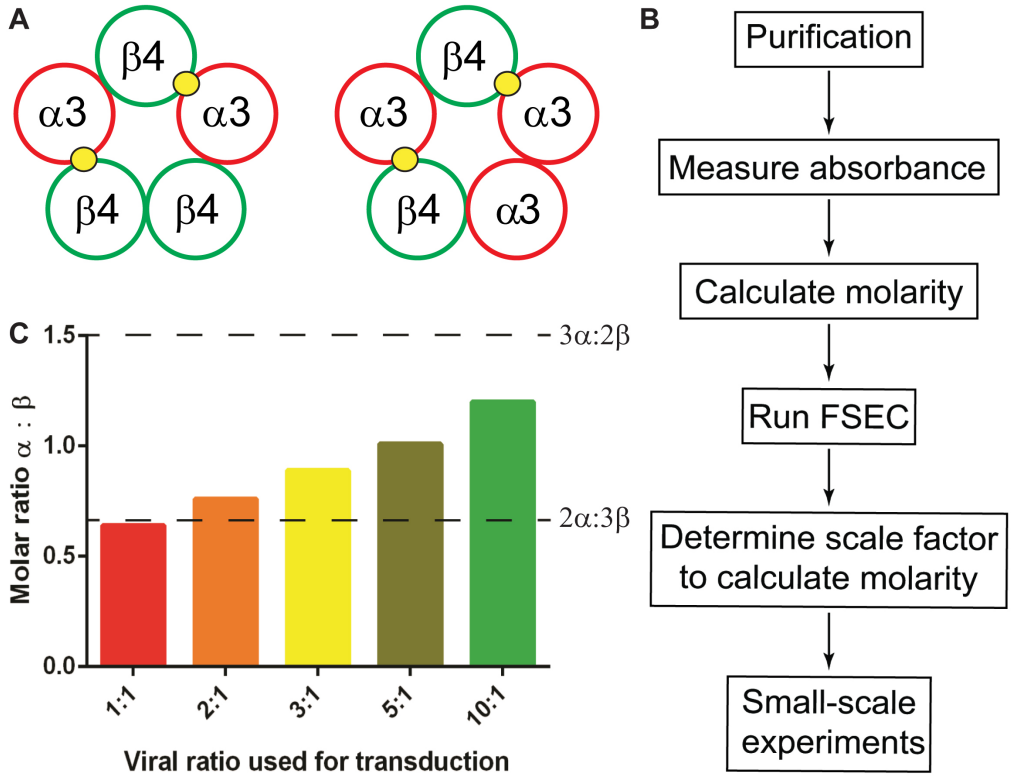

Fig. II.4 Fluorescent stoichiometry assay
(A) α3β4 receptors can assemble in two functional stoichiometries. For this assay, α3 subunits were labeled with mCherry and β4 subunits were labeled with GFP. (B) Flow-chart diagram of assay to determine amount of each subunit in a given sample. (C) Increasing amount of α virus to β virus results in a higher α:β subunit ratio in the sample.

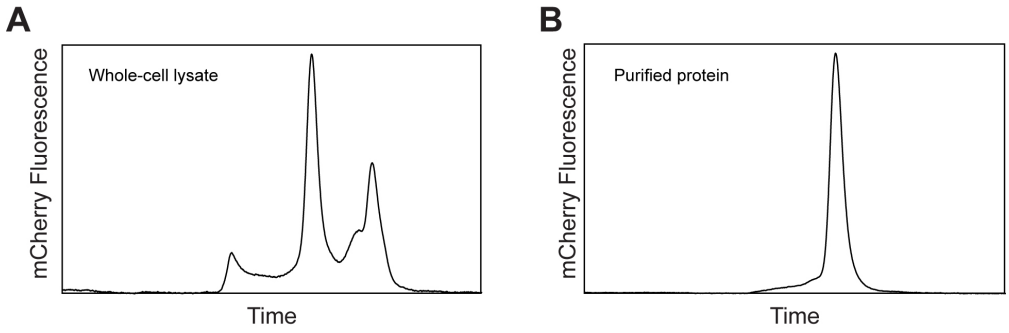

Fig. II.5 mCherry signal before and after purification
(A) FSEC trace showing mCherry fluorescence signal following whole-cell solubilization. (B) FSEC trace showing mCherry fluorescence signal after an additional purification step.

Viral ratio (α:β)	Molar ratio (α:β) before purification	Molar ratio (α:β) after purification
1:1	0.69	0.64
1:2	0.56	0.54
1:3	0.53	0.50
1:5	0.52	0.48
1:10	0.49	0.44
2:1	0.83	0.76
3:1	0.99	0.89
5:1	1.26	1.01
10:1	1.76	1.20

Table II.1 Stoichiometry assay results
Calculated molar ratios from small-scale transductions of varying viral ratios before and after batch affinity purification.

Thermostability assay to screen detergents and additives

Another important aspect of growing protein crystals is screening a large number of conditions. For membrane proteins (and specifically ligand-gated ion channels), this usually means setting up crystallization screens in the presence of different detergents, ligands, and other additives. Specifically, reagents that promote stability of the protein may have a greater chance of resulting in crystal growth. Up until this point, I had identified one detergent (DDM), one ligand (nicotine), and only a couple additives (TCEP, CHS) that resulted in successful purification of α3β4. To identify reagents that may be more optimal than the ones I had been using, I employed an FSEC-based thermostability assay that was developed by the Gouaux lab (Hattori et al., 2012).

The basic principle of this assay is to incubate small (nanogram) quantities of protein at various temperatures and then test them by FSEC. The results provide a denaturation curve that can be used as a proxy for a melting temperature (T_m). By incubating the protein at this temperature in control conditions, and in the presence of other detergents, ligands, and additives, it is possible to identify reagents that may have a thermostabilizing effect on the protein of interest. To conduct this experiment, I took purified α3β4 Del3-ER protein in DDM and incubated it at 4, 20, 30, 40, 50, 60, 70, 80, and 90°C for 10 minutes before pelleting insoluble material and testing by FSEC (Fig. II.6A). These results suggested that the T_m (where the peak height is 50% of the maximum) was approximately 65°C (Fig. II.6B).

I next tried purifying the protein in a variety of different detergents, including dodecyldimethylamine oxide (LDAO), n-decyl-β-D-maltopyranoside (DM), hexaethylene glycol monodecyl ether (C10E6), n-undecyl-β-D-maltopyranoside (C11M), 6-cyclohexyl-1-

hexyl-β-D-maltoside (Cymal-6), 5-cyclohexyl-1-pentyl-β-D-maltoside (Cymal-5), and 2,2-didecylpropane-1,3-bis-β-D-maltopyranoside (LMNG). I also used additives and ligands in the background of control conditions (DDM) to see if they had a protective effect. These samples were incubated at 65°C for 10 minutes, before being tested by FSEC. The results from these experiments showed that α3β4 is very sensitive to the detergent used for extraction and purification (Fig. II.6C). Detergents such as LDAO and C10E6 caused almost all of the protein to crash out, whereas other detergents such as C10M and Cymal-5 resulted in a >50% reduction of peak height. However, this assay did help identify C11M, Cymal-6, and LMNG as suitable alternatives to DDM. As for the ligands (I tested the non-selective agonists nicotine and epibatidine, as well as the α3β4-selective antagonist SR-16584) and other additives (mostly lipids to form mixed micelles), none of these had substantial protective or detrimental effects (Fig. II.6D). Ultimately, these experiments helped me expand my arsenal of detergents, ligands, and lipids that could be used in crystallization trials.

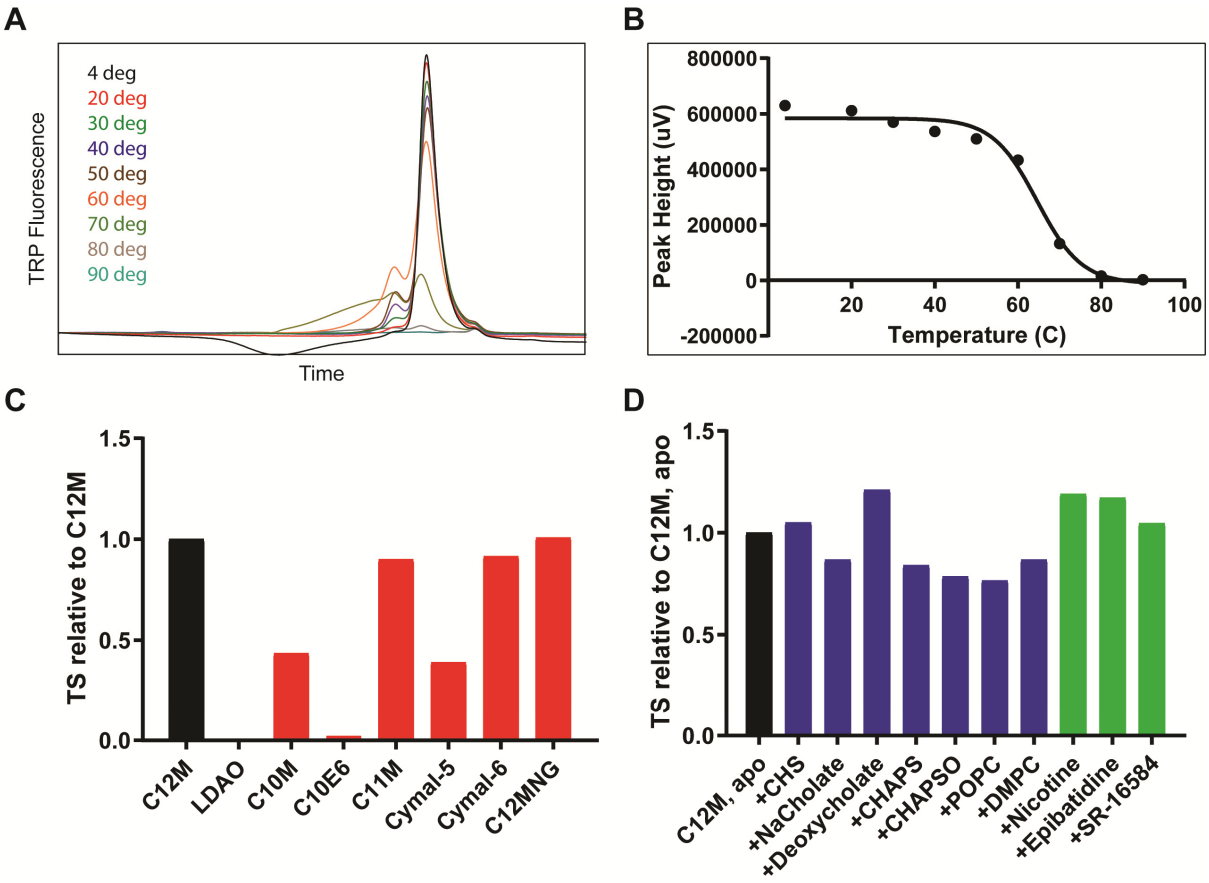

Fig. II.6 Thermostability assay to screen detergents and additives
(A) FSEC traces of α3β4 Del3-ER protein heated at different temperatures. (B) Resulting thermostability curve. T_m was approximately 65°C. (C) Thermostability of α3β4 in different detergents. (D) Thermostability of α3β4 with added lipids and ligands.

Crystallization of α3β4

Having identified a viable crystallization construct, expression conditions to produce a stoichiometrically homogeneous protein population, and a panel of detergents and additives that could be used during purification, I set out to a screen a wide variety of conditions for crystallization hits. I first purified the Del3-ER protein in the presence of 1 mM DDM, 0.2 mM CHS, 1 mM nicotine, and 1 mM TCEP. The final product of this protein prep was very stable for at least 12 days, as shown by FSEC (Fig. II.7A). Using this protein, I was able to set up many crystallization screens tailored for membrane proteins at 4 and 14°C. From these screens, I began to see several hits for the first time. Many of these produced small blobby diamonds less than 50 microns in length (Fig. II.7B-C). I fished and froze a handful of these crystals and sent them to the APS23 IDD beamline to test diffraction quality. These crystals diffracted to ~25 Å, which was an exciting first step, but not too promising (Fig. II.7D). Attempts at optimizing these crystals were ineffective.

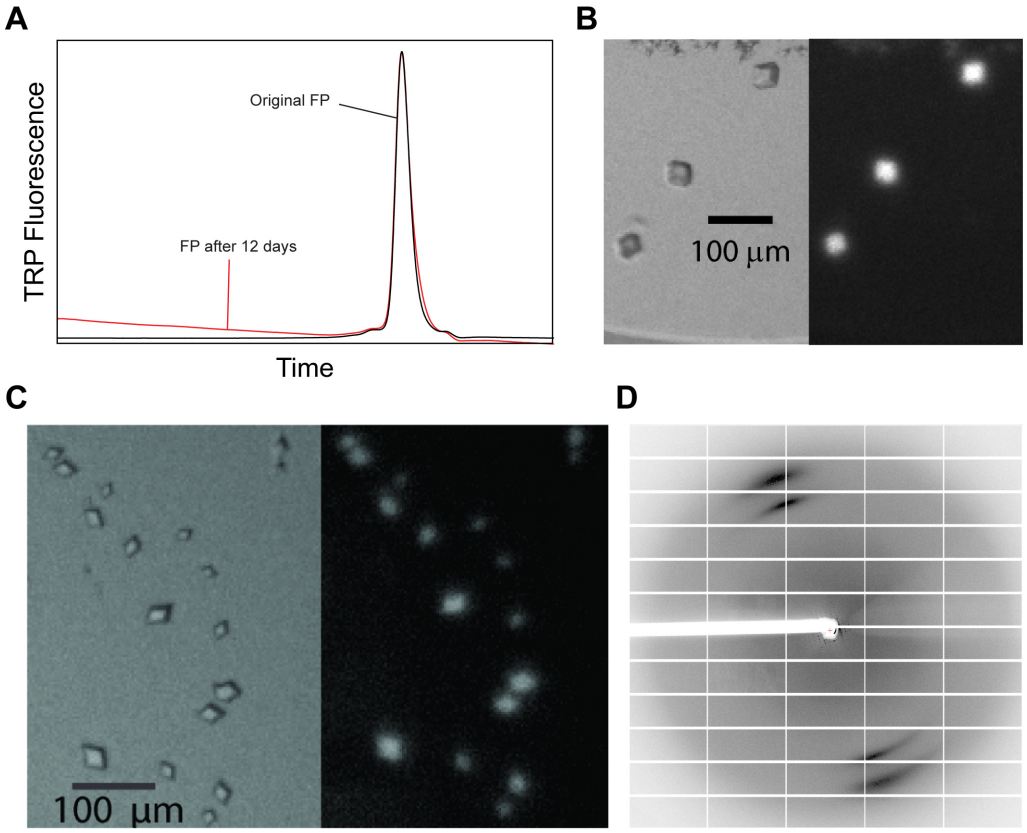

Fig. II.7 Initial crystallization hits
(A) FSEC traces comparing final product (FP) on the day of purification (black) and 12 days later (red). (B-C) First crystallization hits showing visible light images and UV fluorescence (to indicate protein content) side-by-side. (D) First diffraction pattern, with reflections going out to ~25 Å.

I next turned to C11M as the primary detergent for purification to see if this would help crystal growth and order. Preps using this (and detergents other than DDM) used DDM for membrane solubilization and affinity purification, before exchanging into the final detergent during SEC. Once again, the final product was very monodisperse. After roughly 10 days of setting up crystallization screens, I began to see several hits with bar-like crystals (Fig. II.8A). Although there were many hits, the conditions that produced these crystals were

all very similar- they all were at neutral pH values (between 6 and 8) and contained PEG 3350 or PEG 4000. Initial diffraction tests showed that these crystals diffracted to ~20-14 Å, a marked improvement over the DDM crystals, so I decided to optimize these conditions.

By increasing the protein concentration and protein:reservoir ratio in the drops, I was able to grow larger crystals, with bars growing up to 200-300 μM in length (Fig. II.8B). From these crystals, I collected a full dataset to 9.3 Å. Further improvement in crystal quality was achieved by increasing the drop size. I set up 600 nL drops using the mosquito with a 2 protein: 1 reservoir ratio. While this change yielded less hits and more precipitate, some conditions grew bars with lengths of 200-300 μm. From the best diffracting crystal in this setup, I was able to collect a full dataset to 7.8 Å (Fig. II.8C).

All datasets collected from these bar-like crystals were indexed and consistently gave similar unit cell dimensions (Table II.2). The space group was $P2_1$ and the unit cell dimensions were 127 x 304 x 198 (Å). Full diffraction statistics from the best collected dataset are shown in Table II.2. Molecular replacement using α4β2 as a model was successful for the 9.3 Å dataset, but not the 7.8 Å dataset. Phaser found 3 copies of the pentamer in the asymmetric unit suggesting a very high solvent content for these crystals, which is not ideal for diffraction quality (Fig. II.8D). The TFZ score was 19.9 and the LLG was 600.694 and a round of refinement dropped the R-free value to 0.43, indicating a correct solution.

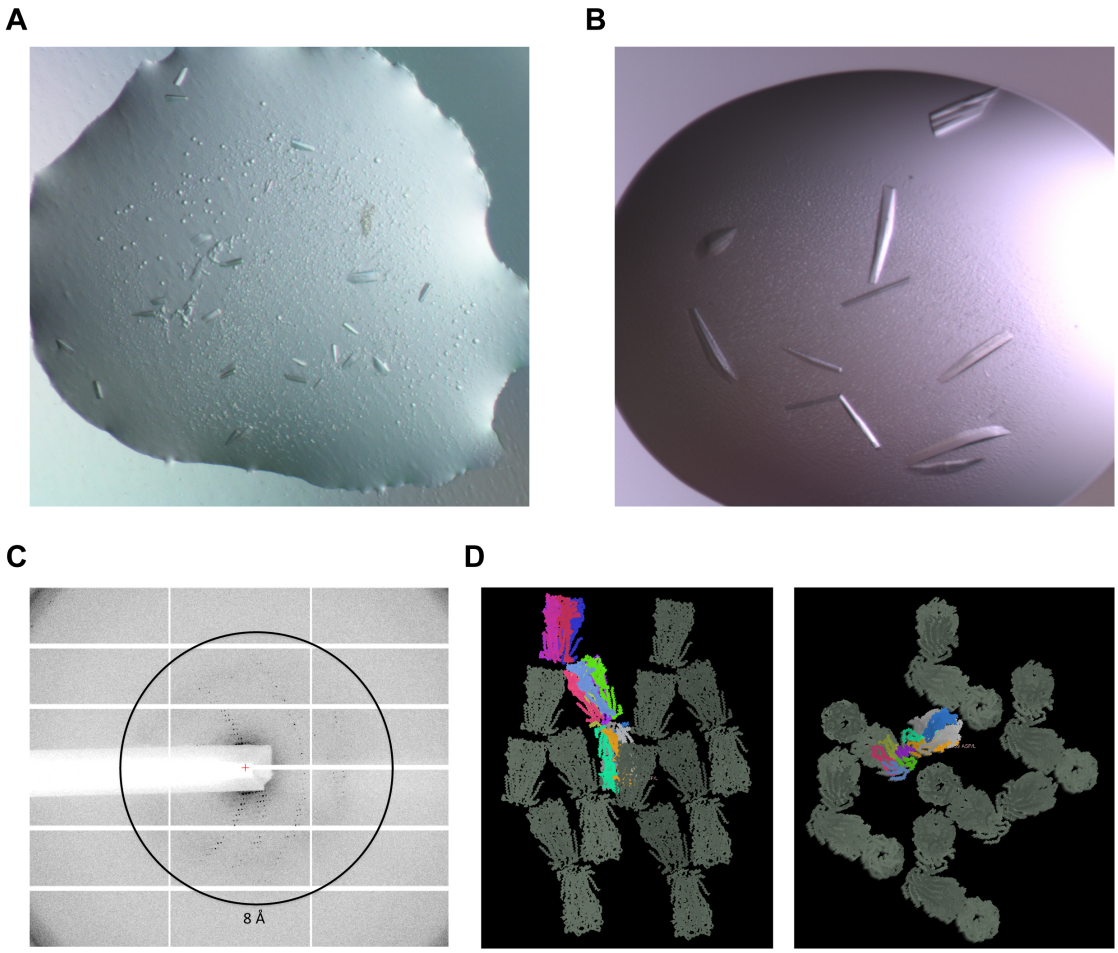

Fig. II.8 Crystal optimization and diffraction
(A) Bar-like crystal hits from protein purified in C11M. (B) Optimized crystal bars, roughly 200-300 µm in length. (C) Representative diffraction image with visible reflections approaching 8 Å. (D) Molecular replacement solution for the 9.3 Å dataset shows three copies of α3β4 in the asymmetric unit and high solvent content.

Parameter	Dataset 1	Dataset 2
Space group	$P2_1$	$P2_1$
Unit cell dimensions (Å)	127, 304, 198	128, 308, 200
Unit cell angles (deg)	90, 102, 90	90, 102, 90
Resolution range (Å)	40.00-9.30 (9.46-9.30)	50.00-7.80 (8.08-7.80)
Multiplicity	3.5 (2.9)	3.1 (2.7)
Data completeness (%)	99.6 (99.0)	96.8 (91.1)
$\langle I \rangle / \langle \sigma \rangle$	11.75 (1.06)	15.33 (1.00)
Copies in asymmetric unit	3	-
Matthews coefficient (Å3/Da)	5.54	-
Solvent content (%)	78	-

Table II.2 Diffraction statistics for two best datasets
Diffraction statistics. A molecular replacement solution was found for dataset 1, but not dataset 2.

Further optimization attempts of crystals from these conditions were largely unsuccessful. I tried varying the pH, the buffer molecule, the cations and anions in the salt, and the salt concentration in hopes of improving diffraction quality. Given the high predicted solvent content of these crystals, I also tried dehydrating the crystals. While many of these optimization trays did produce crystals that looked similar to the original crystals, I never saw diffraction data that went past 7.8 Å.

The crystals grown in C11M with added CHS, nicotine, and TCEP gave hope that well-ordered crystals of α3β4 could be grown, and that with the right conditions, these crystals may diffract past 4 Å. I decided to screen more conditions, either by changing the

detergent (which my results had shown would drastically change crystal quality) or by changing the ligand (which may change the protein conformation). LMNG was one of the detergents that I had identified as a possible candidate in my initial thermostability screen. Exchanging into LMNG during SEC resulted in significant aggregation, but once again this was not seen in the final product. I set up several screens which resulted in only a few hits, none of which were as encouraging as hits seen with C11M. I next decided to try glyco-diosgenin (GDN), a detergent similar to digitonin. Initial experiments showed that this detergent did not harm my protein and had a protecting effect at the T_m, so I proceeded to use it in a large-scale prep. SEC traces after exchanging into 0.5 mM GDN looked fine, and I set up at 4 and 14°C. From these screens, I saw hits in similar conditions as with C11M preps, however the crystals were either blobby or diamond shaped (Fig. II.9A). I was very excited about the diamond crystals despite their relatively small size (<50 um), but disappointingly, they did not diffract. Based on this result, I moved back to using C11M as the primary detergent for preps.

Changing detergents had a significant effect on crystal growth and quality, so I wanted to see if using different ligands would have a similar effect. I first turned to SR-16584, a selective α3β4 antagonist with a K_d of ~500 nM. These preps were mostly done apo and I added ligand to a concentration of 100 μM to peak SEC fractions. There was significant aggregation, which may have been caused by trying to purify apo protein or may have been because the affinity fractions were concentrated to a very high concentration (A280 = 7.7). Regardless, the final product was monodisperse and was used to set up crystal trays. One condition, composed of HEPES 7.5, 0.2 M NaCl, and PEG 4000, produced crystals that

looked like hexagonal plates (Fig. II.9B). These plates diffracted well, and I collected an incomplete dataset to ~9 Å. Optimization produced crystals that diffracted past 7 Å but did not improve beyond that.

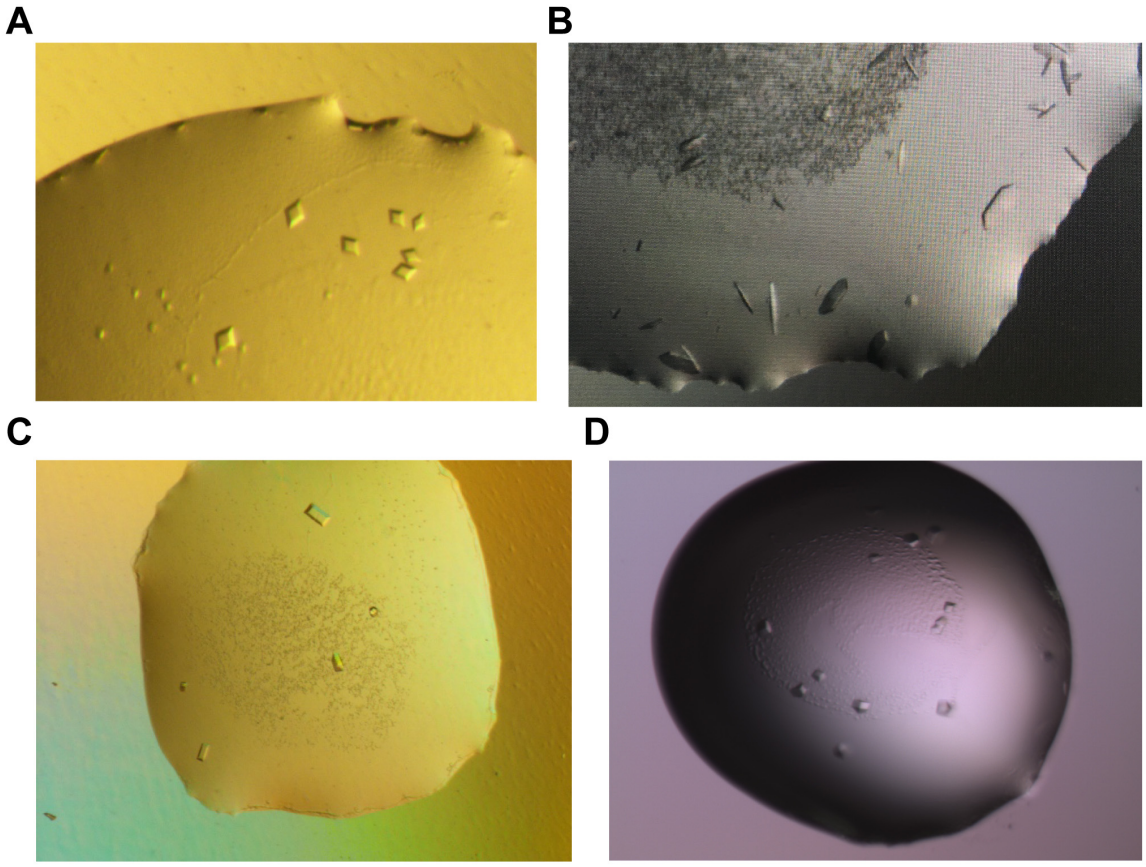

Fig. II.9 Other α3β4 crystals
(A) Diamond-shaped crystals from α3β4 in GDN. These crystals did not diffract. (B) Hexagonal plates grown with α3β4 in C11M with SR-16584 as the ligand. These crystals produced reflections out to ~7 Å. (C-D) Crystals of other morphologies grown with SR-16584 as the ligand. These crystals did not diffract well.

Electron microscopy of α3β4

With such few conditions that enabled crystallization of α3β4 and no signs of diffraction beyond 6 Å, I turned to the rapidly emerging field of cryo-EM for structural studies. As mentioned before, hardware and software advancements in single-particle cryo-EM had made the determination of high-resolution protein structures possible. This was especially beneficial for membrane proteins that were recalcitrant to well-ordered crystal growth, such as α3β4.

In order to get an initial sense of what the receptor would look like under an electron microscope, I first prepared some samples for negative-stain imaging. After optimizing sample preparation, I discovered that using a very small amount of protein (A280 ~0.02) and staining with 2% uranyl acetate produced nice images (Fig. II.10). Particle density in these images was good, but I only saw top views of the receptor, thus preventing me from attempting to create a low-resolution reconstruction. However, this was still a rather exciting result for me as the top views showed distinct pentameric receptors that were reminiscent of the “rosettes” seen in early electron micrographs from the 70’s and 80’s (Cartaud et al., 1973, Cartaud et al., 1980, Klymkowsky and Stroud, 1979).

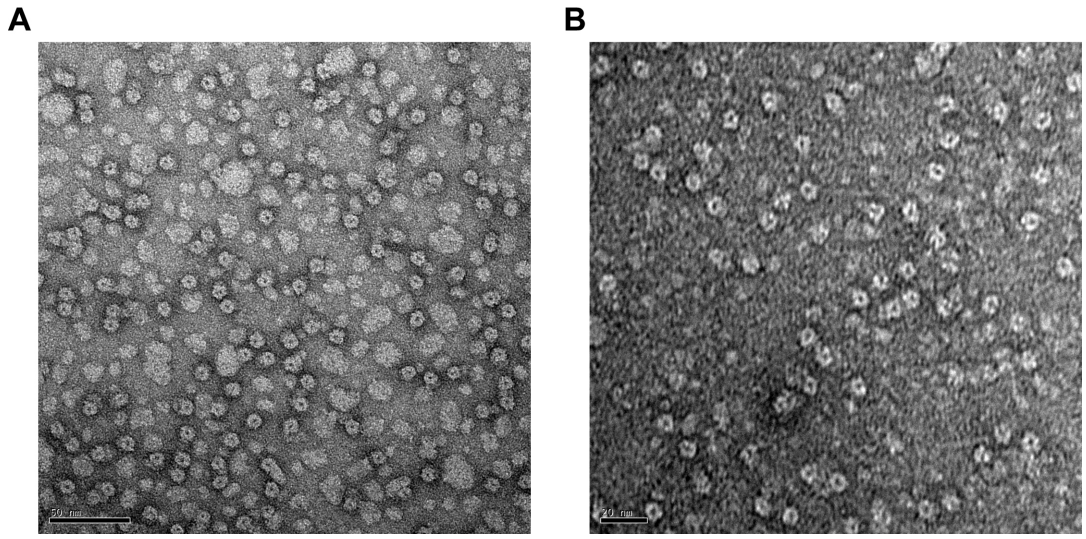

Fig. II.10 Negative stain micrographs of α3β4
(A) Negative stain image of α3β4 showing many top views resembling the rosettes seen by the Stroud and Changeux groups in the 70's. (B) Higher magnification image shows pentameric assembly of the receptor.

For my first attempt at cryo-EM, I returned to the Del1-BRIL construct that I had used in my initial attempts at crystallography. This was done because including BRIL in the M3-M4 loop greatly increases the yield (about threefold) and stability (very little aggregation prior to SEC and purified protein looks good by FSEC for over two months). For this prep, I used a buffer containing 1 mM DDM, 0.2 mM CHS, 1 mM TCEP and 1 mM nicotine in TBS throughout affinity and size exclusion chromatography. My peak fraction had an A280 of ~1.34, and this fraction was concentrated two-fold to reach a final A280 of ~2.66.

Over the course of a weekend, Dr. Colleen Noviello collected about 1000 images on this sample. This was my first time processing cryo-EM data and the steps I took are detailed here. From the first few images, I manually picked about 50 particles and sorted them into

five 2D classes. Two of these classes were used as templates for autopicking on the full dataset. Relion autopicked about 150,000 particles, but after going through images individually and throwing out bad images and obvious false positives, I was left with about 67,000 particles. These particles were then subjected to multiple rounds of 2D classification, with increasing resolution cutoffs and decreasing number of classes, to better judge data quality and throw out junk particles. After the third round of 2D classification, I was left with 19,000 particles in 12 classes. A handful of these showed clearly defined features in the ECD and had visible ordered density in the detergent micelle, which was encouraging (Fig.II.11A). I then proceeded to 3D classification and sorted these particles into 4 classes. 2 of these classes (containing 65% or 12,728 particles) closely resembled a pentameric channel surrounded by a detergent micelle. I selected the particles in these classes and continued on to 3D refinement. Because of the low number of particles, I imposed C5 symmetry at this stage in an attempt to increase the signal. After the first round of refinement, I saw what appeared to be an empty micelle, but after increasing the contour level, I saw some density in the TM region. I then created a mask that would focus on just the ECD and TMD (no micelle). After including this mask in refinement, I got a ~20 Å model that vaguely resembled a nicotinic receptor (Fig. II.11B).

Although this was a promising first dataset, there were still a few issues that had to be addressed. Most importantly, it was not possible to distinguish subunit identities as α3 and β4 subunits looked identical. The final refinement was done using C5 symmetry, which would naturally merge and average the subunits, but even in C1 symmetry it was not possible to see clear differences between the two subunits. One way to solve this problem would be to use

large markers for one kind of subunit, that would help the processing software discriminate between the subunit types at low resolutions. To do this, I turned to subunit-specific antibodies.

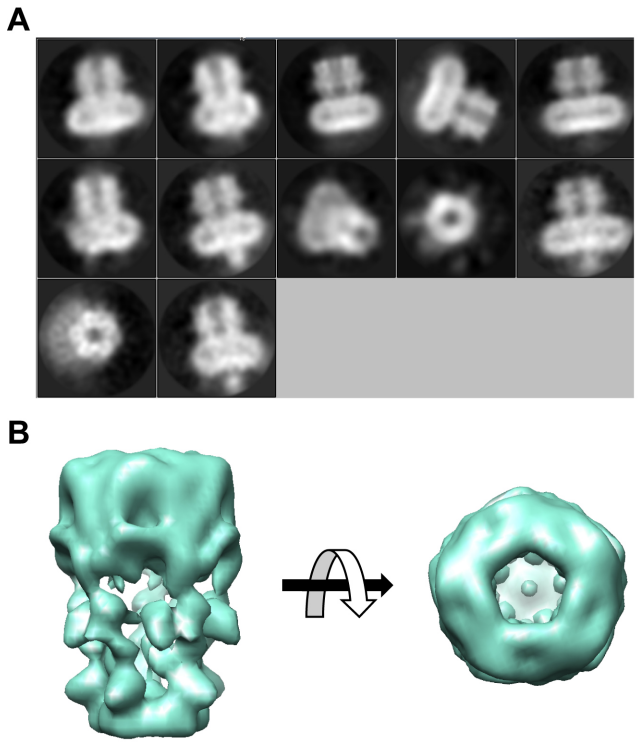

Fig. II.11 First cryo-EM dataset without Fabs
(A) 2D classes showing features in ECD and helical lines in TMD. (B) Final 3D reconstruction from this dataset using C5 symmetry.

I sent purified α3β4 protein to Dan Cawley at the Oregon Health & Science University to raise monoclonal antibodies (mAbs). I received 28 mAbs to test for further studies. Ideally, antibodies used for cryo-EM should recognize folded but not denatured protein. I set out to identify which of the mAbs would meet these criteria through FSEC and western blot experiments. To look at binding to folded protein, I incubated each of the mAbs with GFP tagged protein and tested them by FSEC. I looked for a second peak at a lower elution time which would indicate a mAb/receptor complex (Fig. II.12A). This experiment narrowed down the number of potential candidates from 28 to 12. Next, I wanted to see if these 12 antibodies would bind to denatured protein, so I performed a western blot using the mAbs as the primary antibody (Fig. II.12B). After some western blot troubleshooting, I found that only 1 of the 12 candidates bound to denatured protein. Of the 11 remaining mAbs, I selected 1A12 to be ordered on a large scale.

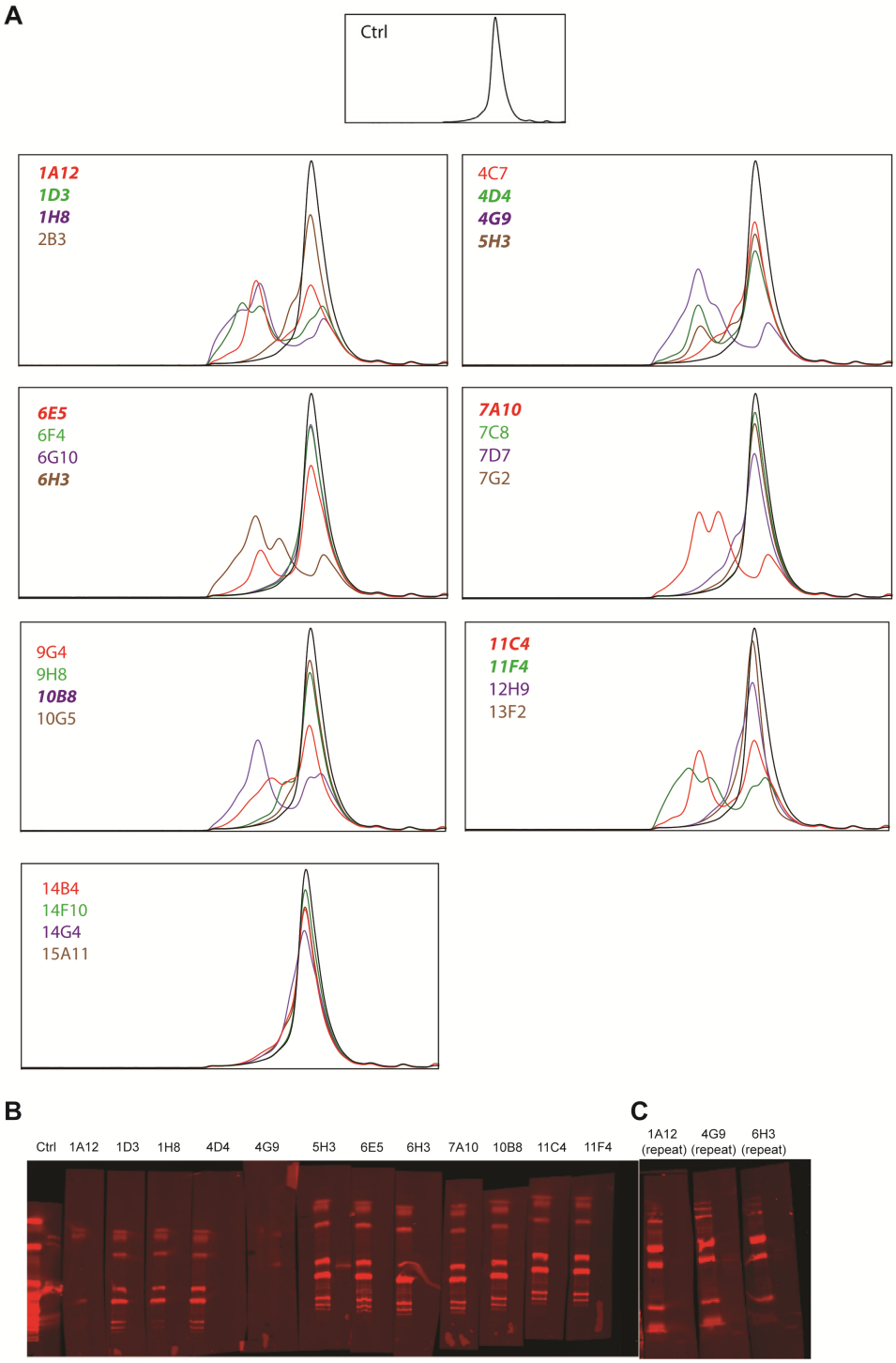

Fig. II.12 Antibody screening

(A) Monoclonal antibodies were first screened for a leftward shift in FSEC traces. Hits are bolded. (B) Positive hits were screened by western blotting to make sure antibodies did not recognize linear epitopes. Inconclusive results were repeated in (C). Only 5H3 was positive.

After receiving these antibodies, I digested them with papain and purified the Fab fragments with a cation exchange column and confirmed that these fragments still bound to α3β4 by FSEC. The resulting FSEC traces showed monodisperse peaks that were left-shifted, indicating a protein-Fab complex (Fig. II.13A). I purified α3β4-Fab complexes by combining affinity-purified receptors and Fabs prior to size exclusion chromatography, and grids were frozen at final concentrations of roughly 1.5 (A280). Dr. Noviello helped me to collect 266 images of the receptor-Fab complex. I followed the same workflow for data processing as detailed in previously. 2D classes showed clear top, side, and diagonal views (Fig. II.13B), and following classification, I was left with only ~4000 particles. The final reconstruction clearly showed a pentameric receptor with Fab fragments bound to the top of the ECD (Fig. II.13C). Although initially appearing unimpressive, this reconstruction was significant in that it was the first evidence in the lab that the pseudosymmetry of heteromeric receptors could be broken with the inclusion of Fab fragments, paving the way for studies on α4β2 (Walsh et al., 2018) and $GABA_A$ receptors (Zhu et al., 2018).

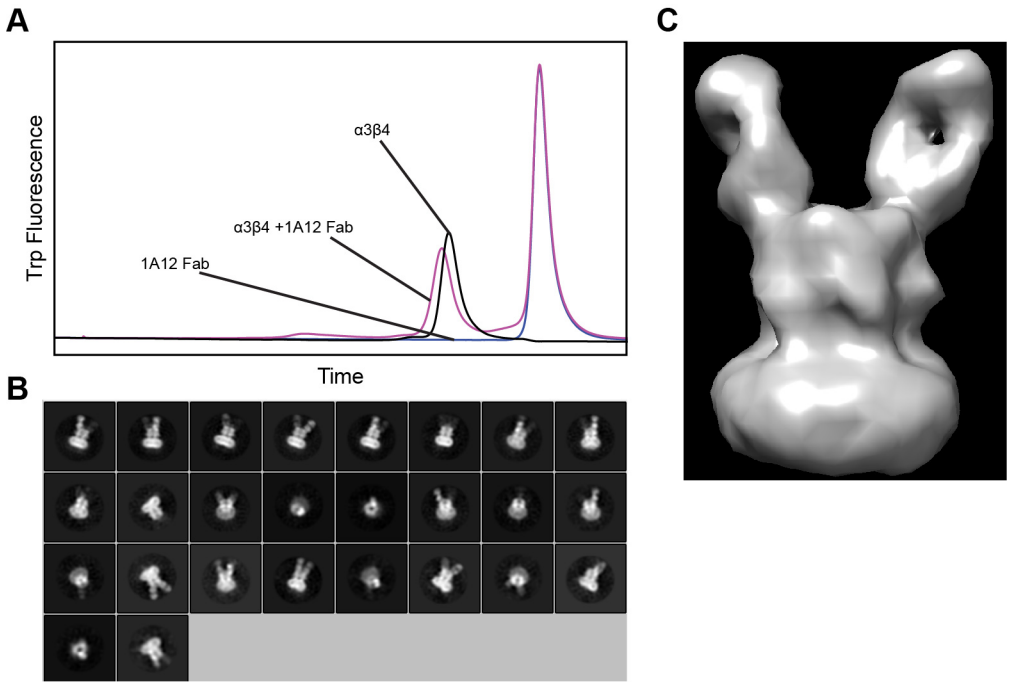

Fig. II.13 Preliminary α3β4-Fab EM dataset
(A) FSEC traces showing shift upon binding of 1A12 Fab. (B) 2D classes showing a variety of orientations. (C) Reconstruction showing pentamer bound to Fabs.

Having optimized Fab complex preps for α3β4 and 1A12 Fab, I set out to collect a larger dataset on this complex in DDM/CHS with nicotine as the ligand. By concentrating peak affinity fractions to an A280 of ~16 and then adding Fab, I was able to get SEC fractions with absorbance values of 2.5. The two best fractions were concentrated to ~5.8 and I used this sample to freeze grids. 2964 images were collected over the course of 72 hours. Autopicking selected 374,691 particles, and after manual curation of the images, I was left with 2095 images with 207,926 particles. Multiple iterations of 2D classification were used to further clean up the particle set. After selecting ideal 2D classes, I moved on to 3D

classification. Here, I found that 3D classification was extremely effective in separating out different occupancies/stoichiometries of pentamer:Fab. At this stage, I found no/few particles with no Fabs or one Fab bound (which would likely be useless for high-resolution reconstructions). There were good classes with three Fabs bound (Fig. II.14A-B), and two classes with two Fabs bound- one with Fabs on adjacent subunits (Fig. II.14C), and one with Fabs on non-neighboring subunits (Fig. II.14D). After 3D refinement on the three Fab bound particles, I was able to determine that the Fabs bound to the beta subunit based on differences in loop C sizes. I then concluded that the class with Fabs on adjacent subunit must also be of the 2α:3β stoichiometry (the only plausible way two β subunits would be next to each other is if there were three beta subunits in the pentamer) and included these particles in my refinement. After refining and post-processing on this set of 68,033 particles, I got a reconstruction with a 5.35 Å resolution (Fig. II.14E). Importantly, I could see clear features throughout the ECD, and while some of the peripheral TM helices cannot be resolved, clear turns in the helices were present. Even with this apparent TMD disorder, I was very excited when I saw this map, as it gave me the best look at α3β4 to this point.

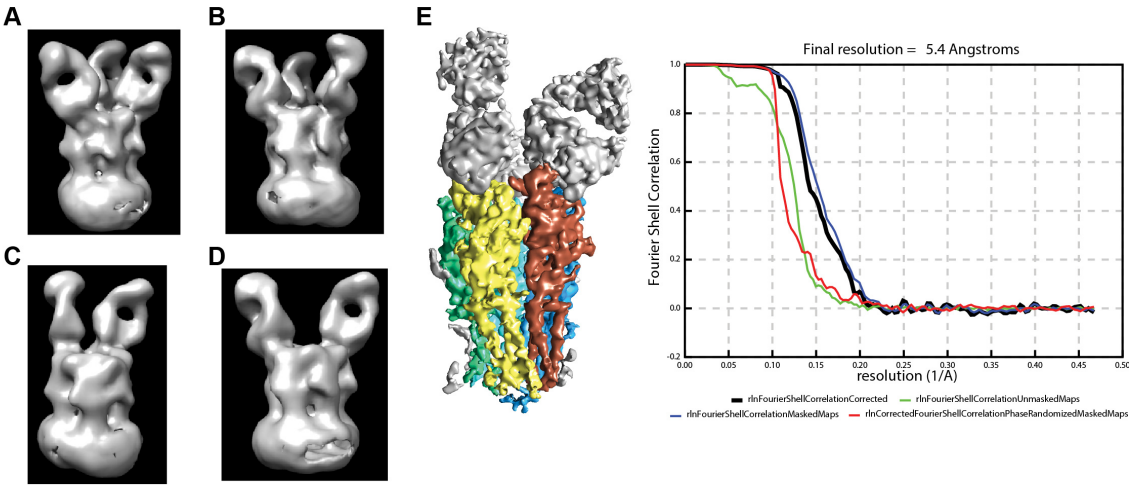

Fig. II.14 α3β4-1A12 dataset
(A-B) 3D classes with three Fabs bound to β4 subunits. (C) 3D class with Fabs bound to adjacent β4 subunits. (D) 3D class with Fabs bound to non-adjacent β4 subunits. (D) Final reconstruction colored by subunit and FSC curve from particles in classes in (A-C).

Although the differential Fab occupancy in the previous dataset was not necessarily problematic, it was not optimal. I decided to order another antibody (4G9) from Dan Cawley in hopes that it would be a higher-affinity binder. A rough titration FSEC experiment showed that 4G9 caused a saturated peak shift with less free Fab in the sample when compared with 1A12, providing some indication that this would be a better antibody (Fig. II.15A-B). I also wanted to confirm that these Fabs did not dramatically affect ligand binding through radioligand binding assays. The presence of 1 μM 4G9 Fabs did not cause a large change in measured EC50 values for an agonist (nicotine) (Fig.II.15C) and an antagonist (α-conotoxin TxID) (Fig. II.15D), indicating that 4G9 was not disrupting ligand binding, and also was not conformation specific.

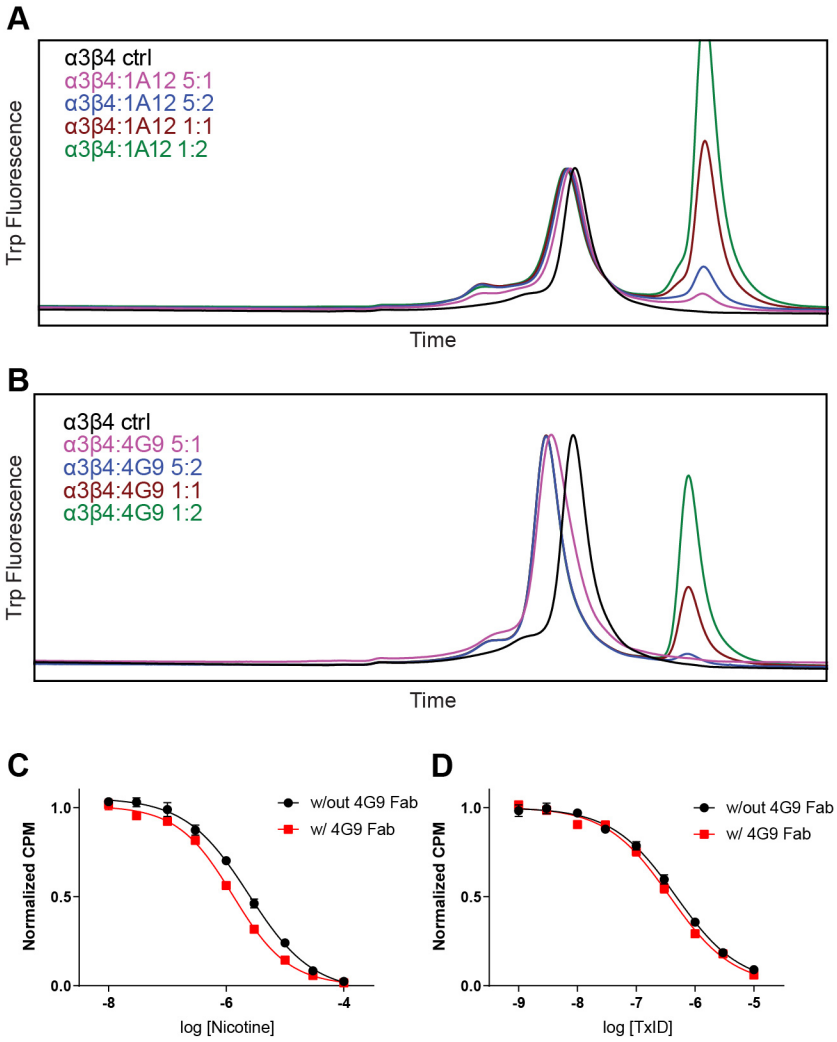

Fig. II.15 Characterization of 4G9 Fab

(A) Titration FSEC experiment for 1A12 Fab. Ratios are weight: weight. Full saturation of peak shift requires substantial excess Fab in the sample (brown trace), indicating low affinity. (B) Titration FSEC experiment for 4G9 Fav. Ratios are weight: weight. Full saturation of peak shift requires minimal excess Fab (blue trace), indicating higher affinity. (C) Competition radioligand binding assay with nicotine in the presence and absence of 4G9. IC_{50} without 4G9: 2.49 µM, with 4G9: 1.32 µM. (D) Competition radioligand binding assay with α-conotoxin TxID in the presence and absence of 4G9. IC_{50} without 4G9: 470 nM, with 4G9: 371 nM.

At this time, I also decided to optimize nanodisc reconstitution of these receptors in order to address the TMD disorder seen in the previous dataset. Nanodiscs would allow me to determine structures in lipids more closely resembling the native environments of nicotinic receptors rather than in detergent micelles. After several conversations with members of the Youxing Jiang lab and repeated attempts at optimizing protein: lipid: membrane scaffold protein (MSP) ratios as well as BioBead incubation times, I was able to form empty nanodiscs as well as nanodiscs with incorporated α3β4 (Fig. II.16A-B). I was able to freeze grids at a concentration of ~1 (A280) with and without a couple additives that may help with potential preferred orientation issues. The additives used were 3 mM fluorinated fos-choline 8 (Liu et al., 2017), and 0.05% NP-40 (Zhao et al., 2015). Initial observations from this experiment were that when no additive is used, the images had great contrast and good particle density at a concentration of 1 (A280) but appeared to contain mostly top views. With the additives, I could see more of what appeared to be side views, but the particle density and image quality suffered, and fos-choline looked better than NP-40.

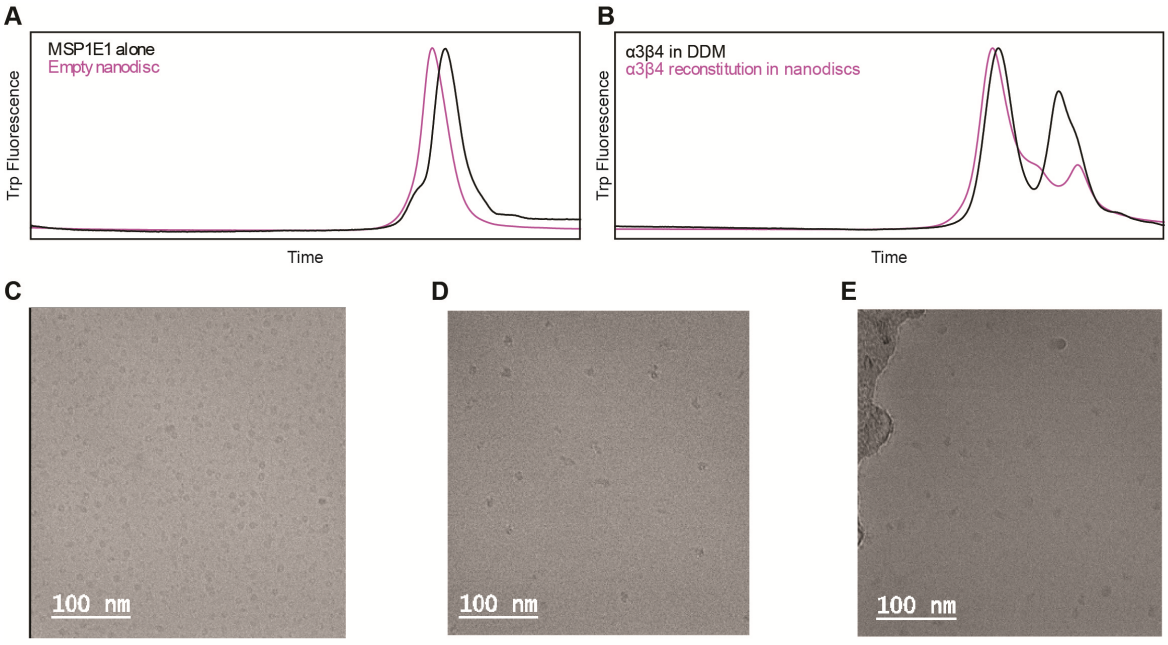

Fig. II.16 Nanodisc sample optimization
(A) FSEC traces of empty nanodiscs compared with MSP1E1 alone. (B) α3β4 incorporated in MSP1E1 nanodiscs. (C) Sample image of α3β4 in nanodiscs with no additive. Only top views are seen. (D) α3β4 in nanodiscs with 3 mM fluorinated fos-choline 8. Side views are visible, but particle density suffers. (E) α3β4 in nanodiscs with 0.05% NP-40. The same conclusions can be drawn as in (D).

Having optimized a protocol for nanodisc reconstitution, I wanted to collect a cryo-EM dataset of α3β4 in nanodiscs to see if the resulting reconstruction would be any better than what I saw in detergent. The main concern with detergent-solubilized protein (DDM) was that the signal from the micelles was strong compared to that of the TMD, leading to an obscured view of the transmembrane helices. Furthermore, there was a question as to whether or not detergent-solubilized membrane proteins actually adopt physiologically relevant conformations. By solving structures in the presence of lipids that are known support

proper receptor function, I could be more confident that the observed conformations (especially in the TMD) are part of the true gating cycles of these proteins. For this data collection, I purified α3β4 Del1-BRIL protein in MSP1E1 nanodiscs in complex with conotoxin TxID. The protein was left apo throughout the prep until after gel filtration, at which point I added the conotoxin to a final concentration of 100 μM. I froze the protein at an absorbance value of 5.8 after adding 1 mM fluorinated fos-choline to induce side views. 2900 images were collected over the course of 2 weekends on the Krios, however many of these images were unusable due to a problem with the energy filter. Still, I was able to autopick ~450k particles from this dataset, which was whittled down to 270k after 2D classification and 140k after 3D classification (Fig. II.17A). This was the largest number of particles I had collected from any dataset, and I was optimistic that the reconstruction would be significantly improved. Unfortunately, this was not the case. After post-processing, Relion estimated the resolution to be ~5.1 Å. Looking at the map itself, the ECD was better defined than I had seen before, with strong secondary structural features and a large globular density in the ligand binding pocket, but still not good enough to model side chains. The TMD still suffered from the same problem as before, with the helices shrouded by nanodisc density. Looking within the nanodisc revealed clear helices, but there only appeared to be three per subunit, and density for helices on alpha subunits was much weaker. Upon closer inspection, it appeared as though MSP1E1 nanodiscs might have been too small. Docking the α4β2 crystal structure into my map showed that the M4 helices would actually contact the MSP protein (Fig. II.17B). This was a problem, as the protein-protein contact between MSP and

M4 could potentially distort the structure. Thus, my conclusion from this dataset was that using a larger MSP or saposin would be necessary.

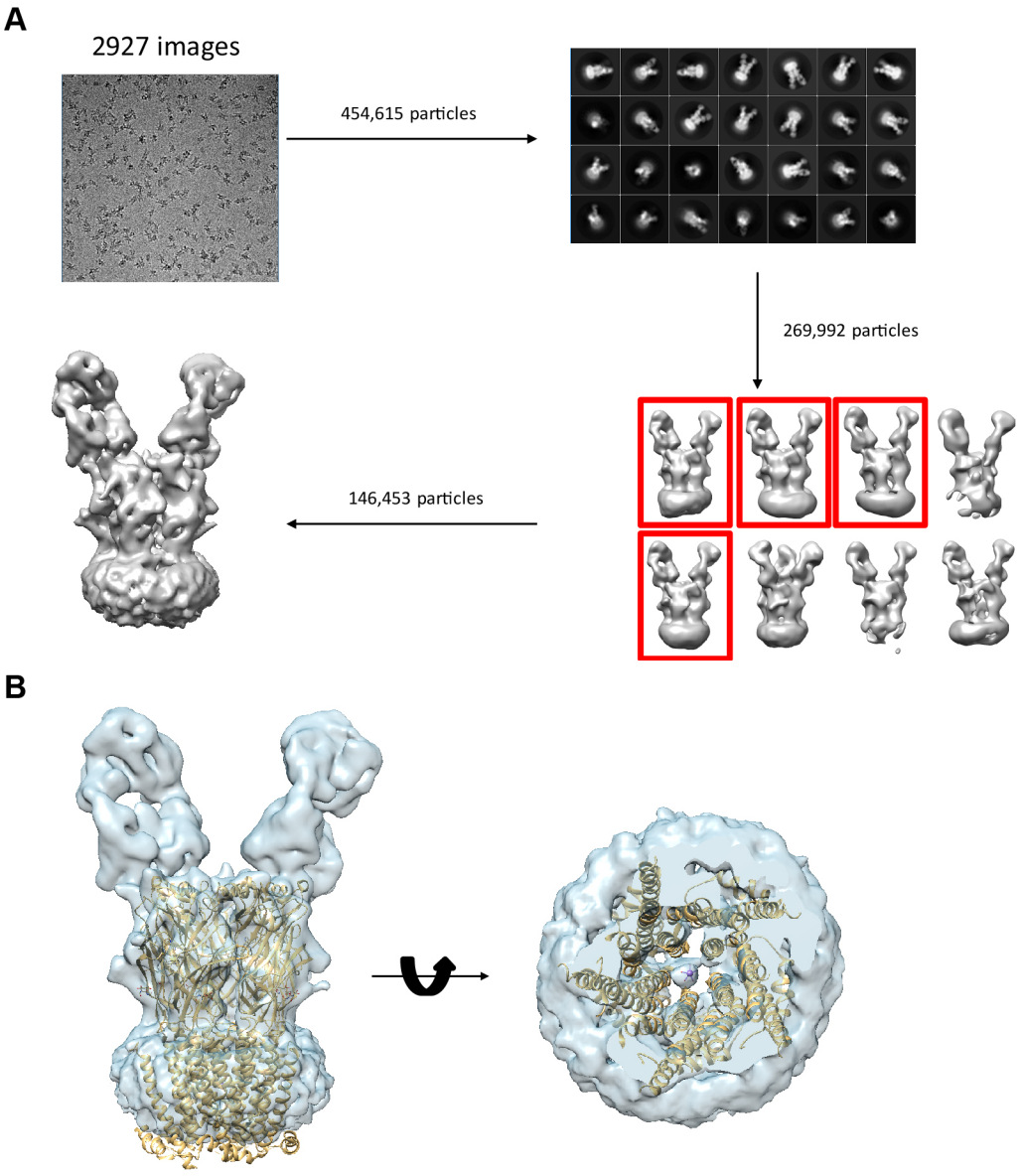

Fig. II.17 α3β4-TxID-4G9 dataset in MSP1E1 nanodiscs
(A) Data processing flowchart for the dataset resulting in 5.1 Å resolution map. (B) α4β2 crystal structure (PDB: 5KXI) docked into map. M4 helices appear to contact edge of the nanodisc.

I next optimized protein:saposin:lipid ratios for salipro reconstitution and found that a 1:5:50 ratio worked best. I was able to successfully purify the protein in the presence of nicotine and froze grids from this prep with an A280 of 3.7. Dr. Noviello collected ~1200 images over the course of a weekend on one of these grids on the Talos. From this dataset, I autopicked 270k particles, and was left with 99k particles after classification (Fig. II.18A). The 2D classes from this dataset looked sharper overall, and especially in the TMD, where signal for helices was stronger than in other datasets. 3D classes showed a larger "micelle" than I had seen for detergent and nanodiscs, which was encouraging. 3D refinement revealed that the TMD signal was stronger than the surroundings and I could clearly see TM helices. However, although the TMD was clearer in saposin, it was not necessarily better defined (Fig. II.18B). Again, there was only strong density for three helices per subunit with poor connectivity in α3 M2 helices. This result suggested to me that the construct may be flawed or α3β4 receptors may be intrinsically more disordered in the transmembrane region. To address these possibilities, I decided to design new constructs that might promote stability for the M4 helices.

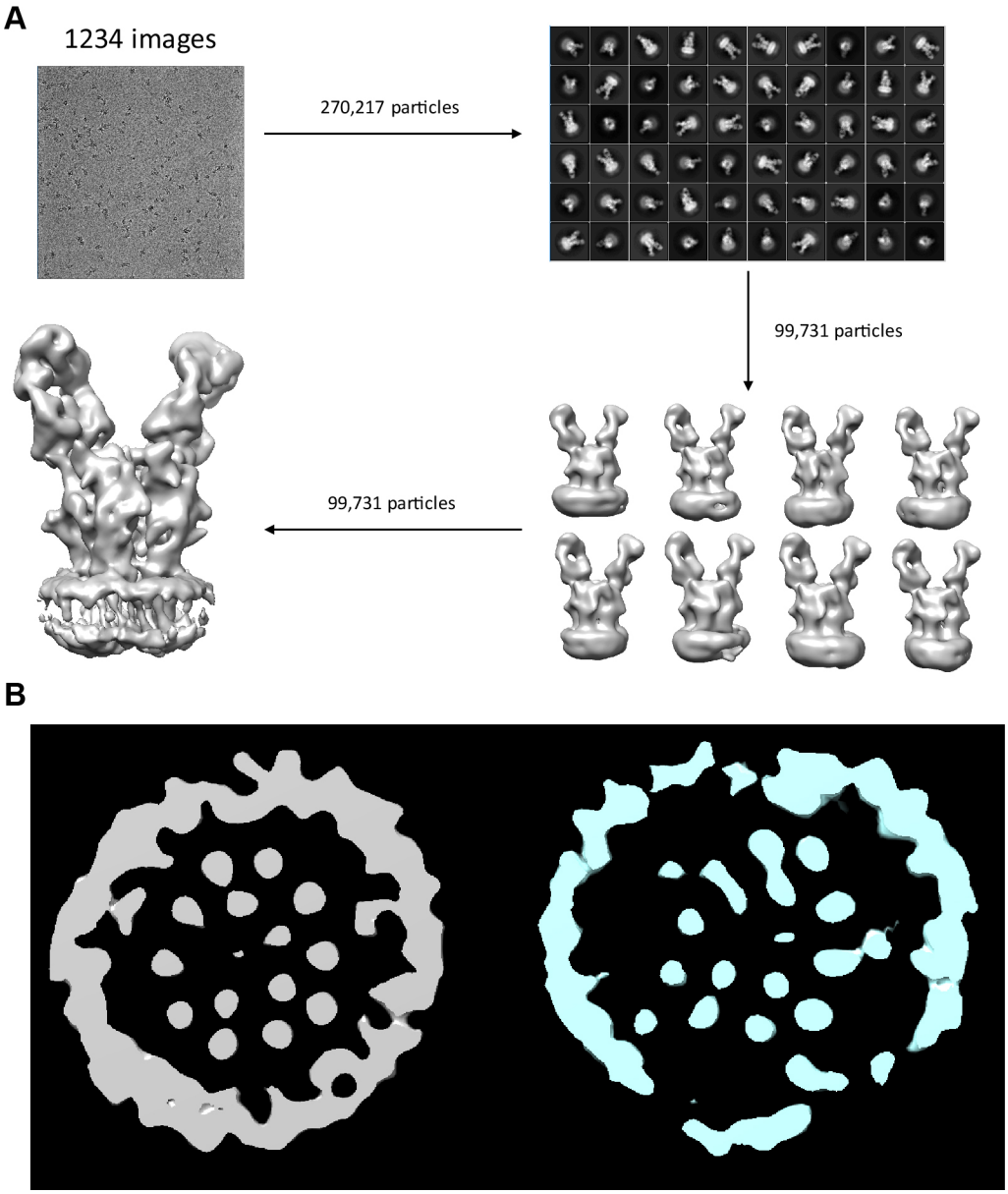

Fig. II.18 Saposin dataset

(A) Data processing flowchart for α3β4-nicotine-4G9 in saposin nanodiscs dataset. Final reconstruction shows better TMD clarity than in MSP1E1 nanodiscs. (B) Side-by-side comparison of slices through TMD of MSP1E1 map (gray) and salipro map (blue). Nanodisc shell is larger in saposin, however TM helices are still asymmetric and not fully ordered.

In the constructs I had been using, BRIL was inserted just a few residues before the predicted start of the M4 helix. This position is in the middle of the intracellular MA helix that leads into M4, with the first half of MA deleted. The insertion of BRIL in this location may have potentially been destabilizing the M4 helix as well as the TMD in general. For the new constructs, I inserted BRIL 5 residues prior to the predicted start of MA. I also designed a series of deletions (EB2-EB6, with EB6 being the longest construct) that would allow for more of the M3-M4 loop from the N-terminal side in case the previous M3-M4 linker had been too short and was pulling the M4 helix into instability. These constructs showed monodisperse pentamer peaks in initial FSEC analysis, including the EB full-length construct which was exciting (Fig. II.19A). However, after doing a small-scale batch purification on a handful of these (EB, EB4, and EB6), the full length did not purify well but the deletion constructs looked to be more amenable to purification (Fig. II.19B). I was also able to confirm that α3β4 EB4 is functional with whole-cell recordings (Fig. II.19C). In large-scale preps, I found that a combination of α3 EB6 and β4 EB4 constructs worked best, so all future structural studies were performed using these constructs, which will henceforth be referred to as α3β4 EM

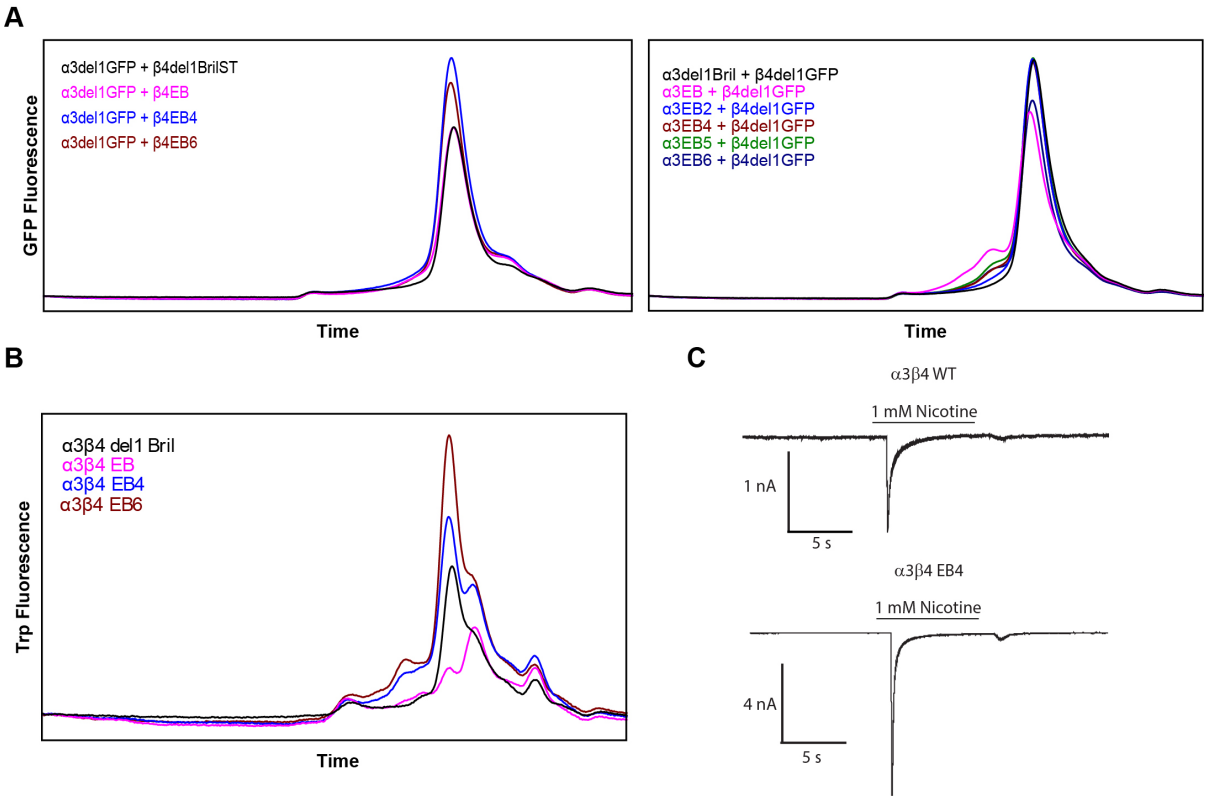

Fig. II.19 EB construct screening
(A) Initial GFP-tagged FSEC screening of EB constructs for β4 subunits (left) and α3 subunits (right). (B) Small-scale batch purification of several EB constructs. α3β4 EB does not purify as well as deletion constructs (EB4 and EB6). (C) Whole-cell patch clamp experiments demonstrating functionality of α3β4 EB4.

I first reconstituted these new constructs in MSP1E2 nanodiscs as opposed to saposin, as I believed these nanodiscs should be more rigid and require less optimization of molar ratios. I froze grids of this protein in complex with nicotine in MSP1E2 at an A280 of ~4.2. A weekend dataset was collected on the Talos (1150 images). From these images, I autopicked 373k particles, and was left with 110k particles after 2D and 3D classification. At the 2D classification step, the quality of classes immediately stood out to me (Fig. II.20A). Not only was the ICD apparent, but the TMD also looked much clearer with distinct helices

spanning the transmembrane region. This observation carried through to 3D refinement, where for the first time, I saw 20 well-ordered transmembrane helices (Fig. II.20B). The nanodisc density surrounding the TMD was very strong, which was a cause for concern, but I was happy with the overall reconstruction and felt the sample was ready for high-resolution Krios data collection.

However, based on Dr. Xiaochen Bai's recommendation, I tried to improve the TMD:nanodisc signal ratio by using saposin as the scaffolding protein. I tried a saposin reconstitution with a ratio of 1:20:100 and was able to successfully integrate my EM protein into nanodiscs. I purified protein with nicotine and froze grids at an A280 of 4.65 and a 24-hour dataset was collected on the Talos of about 500 images. I autopicked about 80k particles, and after classification, was left with 18k particles. This was a pretty low final particle count, especially considering that autopicking was rather conservative and did not include much carbon, but regardless, the resulting reconstruction was surprisingly good (Fig. II.20C). Even with so few particles, I was able to clearly see TM helices and density for the surrounding saposin shell was much weaker than that for protein. With these new constructs in saposin nanodiscs, it appeared as though I had finally found the right conditions for high-resolution structure determination.

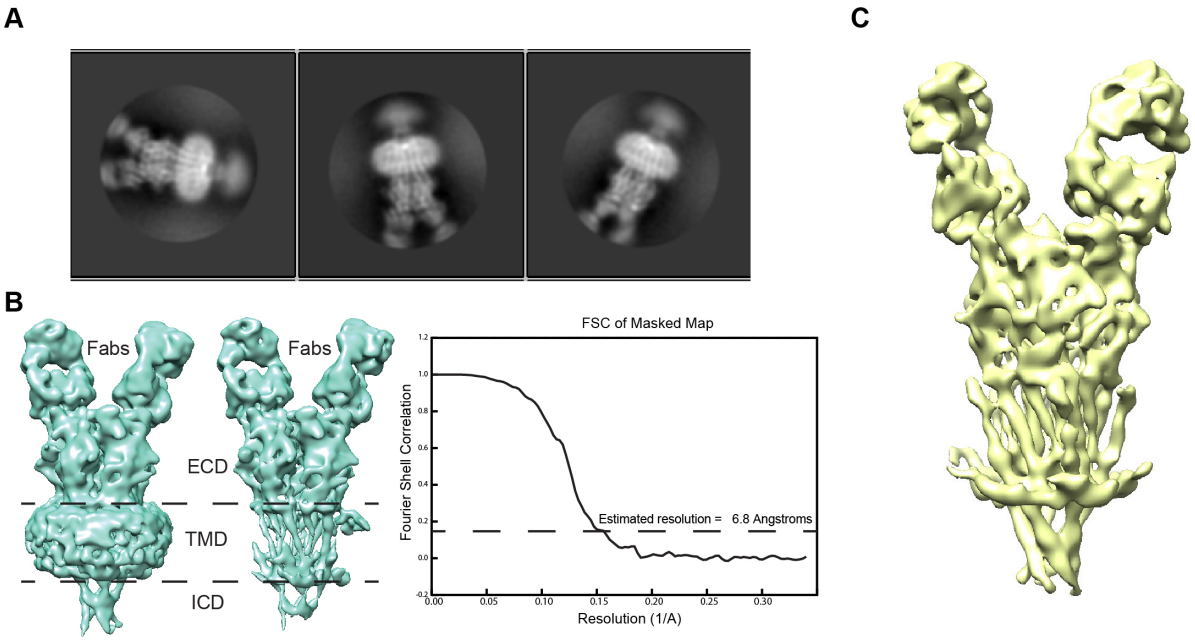

Fig. II.20 EM analysis of final α3β4 EM constructs
(A) 2D classes of α3β4 EM in MSP1E2 nanodiscs showing clear features in the ECD, and helical density in the TMD and ICD. (B) Final reconstruction from the dataset, approaching 7 Å and showing density for all 20 transmembrane helices. (C) Reconstruction from 18,000 particles of α3β4 EM in saposin nanodiscs, with even clearer TM density.

Methods

Molecular biology

Oligonucleotide primers were ordered from Sigma. Deletion constructs were produced by site-directed mutagenesis using PfuUltraII polymerase by Agilent in pEZT and pCDNA vectors. PCR samples were digested with DpnI and transformed into competent DH5α E. coli cells. Plasmids were purified from 5 mL overnight cultures using the various commercially available mini-prep kits. Confirmation of constructs was provided by the DNA Sequencing Core Facility at the McDermott Center for Human Growth and Development.

Transient transfections and FSEC analysis

12-well culture dishes were seeded with 1/40 of GnT1- adherent cells that were about 80-90% confluent and were allowed to incubate overnight. 1 mL fresh DMEM with 10% FBS was added to each well prior to transfection. 1.6 µL of Lipofectamine 2000 was added to 125 µL Optimem as a master mix. 1 µg (500 ng alpha subunit and 500 ng beta subunit) was added to 125 µL Optimem, and the two mixes were combined. These samples were left to incubate at room temperature for 20 min then were added to the wells in a dropwise fashion. Dishes were incubated at 30°C, 5% CO_2 for 72 hours. Cells were harvested after 72 hours by resuspending in 1 mL TBS (20 mM Tris pH 7.4, 150 mM NaCl) on ice. The resuspended cells were centrifuged at 15,000 rpm for 2 minutes and the supernatant was aspirated off. PMSF was added to aliquots of DDM in TBS immediately prior to use to create 40mM DDM + 1 mM PMSF in TBS. 150 µL of this solution was used to resuspend the pellet. This suspension was nutated at 4°C for 40 min and then spun at 40,000 rpm for 40 min at 4°C in an ultracentrifuge. The supernatant was transferred to a fresh 1.5 mL centrifuge tube and 10 µL of each sample was injected over the SRT column. The column was run with TBS + 1 mM DDM.

Bacmid DNA production

Desired constructs were transformed into DH10Bac cells using 5 ng purified DNA from DH5α and were grown for 48 hours on bacmid plates (with kanamycin, gentamicin, and tetracycline). White colonies wer selected and grown overnight in a 5 mL culture containing

kanamycin, gentamicin, and tetracycline. DNA was purified from these cultures using isopropanol precipitation and a final wash with 70% ethanol.

Baculovirus production

6-well culture dishes were plated with 2 mL of Sf9 cells at a density of 0.9 x 10^6 cells/mL. Fresh SF900III SFM media was added to each well prior to transfection. 5 µL bacmid DNA was added to 100 µL Sf900 medium. 100 µL Sf900 was also added to 8 µL Cellfectin II reagent. These two mixtures were mixed, left to incubate for 30 min, and then added drop by drop to the wells. Dishes were incubated at 27°C until ~100% cells were glowing. The medium was harvested using a needle and syringe and P1 virus was dispensed with 0.22 µm sterile syringe filter. P2 virus was produced by adding 1 mL P1 virus to 1 L suspension culture of Sf9 at a density of 1 x 10^6 cells / mL. P2 virus was harvested when about 100% cells were glowing by centrifuging at 5000 rpm for 25 min and sterile filtered into a sterile bottle. P2 virus was concentrated by centrifuging for 1 hourr in 45Ti rotor at 4°C. Pellets were resuspended with Freestyle293 medium and filtered through 0.22 µm syringe filter. Filtered P2 virus was wrapped in aluminum foil and kept at 4°C.

Protein purification and crystallization

Suspension cultures of GnT1- cells were transduced with baculovirus and left at 30°C for 72 hours. Cells were pelleted, washed with TBS and then lysed by running through the Avestin Emulsiflex. Membranes were isolated with a 2 hour spin at 40k rpm and then stored at -80°C. Membranes were later homogenized in TBS with a Dounce homogenizer and

solubilized in 40 mM DDM. Protein was run over Streptactin resin and eluted with 5 mM desthiobiotin. Peak elution fractions were pooled, concentrated, and treated with EndoH for overnight digestion at 4°C. Sample was run over a Superose 6 column for further purification. Peak fractions were analyzed by FSEC and concentrated. Pure protein was used to set up crystallization trays using MemGold 1 and 2, JCSG 1-4, and Wizard screens, as well as custom-made optimization screens.

mAb screening

For FSEC experiments, 30 mL of suspension GnT1- cells were transduced with baculovirus of α3β4-GFP containing constructs. Cells were pelleted after 72 hours and solubilized in 5 mL of 40 mM DDM + 1mM PMSF in TBS for 3 hours in 1.5 mL microcentrifuge tubes. After a hard spin, 10 µL of mAbs in the form of hybridoma supernatants was added to 100 µL of solubilized protein and left to rotate in the cold room for 10 min. After another hard spin, 10 µL of each sample was injected over the SRT column.

For western blot analysis, 500 ng of protein was run on a 12% polyacrylamide gel. This was transferred to PVDF membrane using the semi-dry transfer rig. Membrane was rinsed with water and blocked with TBS + 0.5% Tween20 + 3% bovine serum albumin for 1 hour. After three 10 min washes with TBST, membranes were incubated with mAbs (diluted 1:10) and left rocking overnight in the cold room. The next day, the membranes were washed again three times and incubated with secondary antibody for 1 hour at room temperature. Membranes were washed again and imaged on the Li-Cor Odyssey imager.

Negative stain EM

Purified protein was diluted to an A280 of 0.05 in SEC buffer. 5 uL of sample was added to carbon or formvar coated grids and left sitting for 1 min before being blotted off. 5 uL of 2% uranyl acetate was then added to these grids before being blotted off. Grids were imaged on the Tecnai Spirit electron microscope.

Whole-cell electrophysiology

Adherent cells were transfected with α3, β4, and GFP plasmids and incubated for 24 hours at 30°C to allow for protein expression. Cells were re-plated onto 35 mm culture dishes and incubated for 24 more hours. On the day of recording, cells were washed with and incubated with bath solution (2.4 mM KCl, 140 mM NaCl, 4 mM CaCl2, 4 mM MgCl2, 10 mM Glucose, 10 mM HEPES 7.3). Cells that were GFP positive were patched with seals of at least several hundred megaohms. Current was measured following application of 100 μM acetylcholine in bath solution. The pipette solution contained 150 mM CsF, 10 mM NaCl, 10 mM EGTA, 20 mM HEPES 7.3 and cells were clamped at a membrane potential of -90 mV.

Nanodisc reconstitution

Protein was purified as described above up through affinity chromatography. Protein was concentrated to A280 of ~10 (around 20 μM). A 500 μL reaction was set up with 10 μM protein, 25 μM MSP1E1, 100 μM soy polar lipids (1:2.5:10 molar ratio). A final concentration of 14 mM DDM was used in the initial reaction. TBS, DDM, MSPs, and lipids

were mixed and allowed to rotate for 1 hour at 4°C. α3β4 was then added and allowed to rotate for an additional 30 min. Finally, 100 mg Biobeads were added and the sample was left to rotate overnight. The next day, the sample was analyzed by FSEC (in TBS). For MSP1E2 nanodiscs, I used a 1:2.5:25 molar ratio, and for saposin, I used a 1:5:50 molar ratio, but the general protocol was the same.

Cryo-EM grid preparation

Grids were frozen using the Vitrobot. 3 μL of protein sample was applied to glow-discharged quantifoil grids or non-glow discharged C-flat grids. Typical blotting conditions include: 100% humidity, 4°C temp, 0.5-1 sec blot (for C-flats) or 3-4 sec blot (for quantifoils). Typical glow discharge conditions were 21 mA for 60 seconds or 30 mA for 80 seconds. For protein samples with lower concentrations, sample was repeatedly applied and manually wicked off of a grid before the grid was loaded into the Vitrobot.

CHAPTER THREE

Agonist selectivity and ion permeation in the α3β4 nicotinic receptor

(Modified from Gharpure A, Teng J, Zhuang Y, Noviello CM, Walsh RM, Cabuco R, Howard RJ, Zaveri NT, Lindahl E, Hibbs RE. "Agonist Selectivity and Ion Permeation in the α3β4 Ganglionic Nicotinic Receptor." *Neuron* 2019:104(3):501-511.)

Introduction

The autonomic nervous system comprises sympathetic and parasympathetic pathways and facilitates all involuntary control of visceral organs. The sympathetic branch classically mediates "fight or flight" activity in response to acute stress, whereas the parasympathetic branch maintains peripheral homeostasis. Despite their antagonistic effects, the two branches share a generally conserved disynaptic architecture. Neurons in the autonomic ganglia that innervate downstream targets receive cholinergic input from the central nervous system (Wehrwein et al., 2016). The predominant neurotransmitter receptor in these neurons is the α3β4 nicotinic acetylcholine receptor, commonly referred to as the ganglionic nicotinic receptor (Conroy and Berg, 1995, Skok, 2002, Couturier et al., 1990).

While this receptor forms a critical relay in the autonomic nervous system, its expression is not limited to the periphery. The α3β4 receptor is also found in abundance in the habenulo-interpeduncular tract (Mulle et al., 1991, Quick et al., 1999, Grady et al., 2009), which modulates the mesolimbic dopamine system, the main reward pathway in the brain (Nishikawa et al., 1986, McCallum et al., 2012, Sutherland, 1982). Functional antagonists of α3β4, such as 18-methoxycoronaridine and AT-1001, have been shown to decrease self-

administration of a wide range of drugs, including morphine, cocaine, alcohol, and nicotine in rodent models (Glick et al., 1996, Rezvani et al., 1997, Glick et al., 2000, Toll et al., 2012). Consequently, this subtype has received considerable interest as a potential target for anti-addiction therapeutics (Glick et al., 2002).

The nicotinic receptor family consists of many different subtypes, each with distinct physiological functions and biophysical properties (Albuquerque et al., 2009). Prior to this study, high-resolution information has been restricted to structures of the α4β2 subtype (Morales-Perez et al., 2016b, Walsh et al., 2018), limiting understanding of the diversity in this family. Moreover, the α4β2 structures were determined in the presence of detergent and were missing much of the intracellular domain (ICD). In this study, I went beyond previous structural studies of nicotinic receptors by determining agonist-bound complexes of the human α3β4 nicotinic receptor reconstituted in a functionally supportive lipidic environment. This work reveals molecular mechanisms underlying ligand selectivity, as well as ion permeation through the ICD.

Results

Biochemistry, structure determination, and receptor architecture

I optimized biochemical stability of the human α3 and β4 genes by replacing a portion of the intracellular M3-M4 loop that was predicted to be disordered with BRIL, a thermostable fusion partner (EM construct; see Methods). The EM construct retains function qualitatively equivalent to that of wild-type α3β4 (Fig. III.1A). To better simulate the native environment of nicotinic receptors, I reconstituted receptors into lipid nanodiscs using

saposin (Frauenfeld et al., 2016), soy lipids, and cholesteryl hemisuccinate (CHS), a soluble cholesterol derivative and functional proxy (Addona et al., 1998). This lipid mixture was selected for its ability to support channel activity, as demonstrated by proteoliposome patch-clamp experiments using receptor purified as for structural analysis (Fig. III.1B-C). I raised monoclonal antibodies to the α3β4 receptor and purified receptor-Fab complexes to break the pseudo-symmetry of the heteromeric protein and facilitate particle alignment in cryo-EM studies (Walsh et al., 2018). The Fab had a small positive effect on ligand binding (Fig. III.2C-F), but little to no effect on the functional response to nicotine (Fig. III.2B).

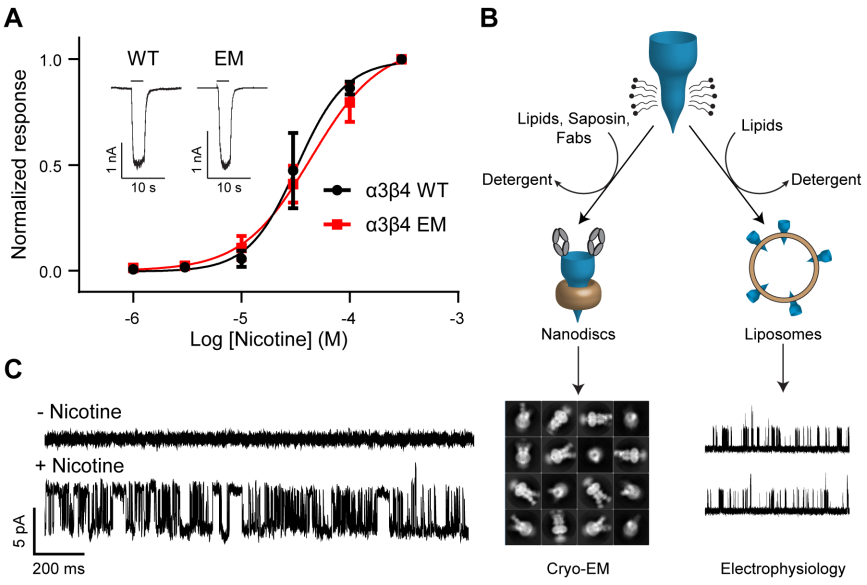

Fig. III.1 Construct modification and functional reconstitution
(A) Whole-cell electrophysiology dose-response experiments comparing WT and EM constructs. WT EC_{50} = 32.7 μM (95% CI: 25.6-44.8 μM; n = 3). EM EC_{50} = 43.9 μM (95% CI: 35.7-57.7 μM; n = 5). Inset shows representative responses of WT and EM constructs to 30 μM nicotine. (B) Flowchart describing reconstitution for electrophysiology and cryo-EM sample preparation. (C) Proteoliposome patch-clamp recording shows single channel currents from a representative patch (n = 3) before and after application of nicotine to the bath solution.

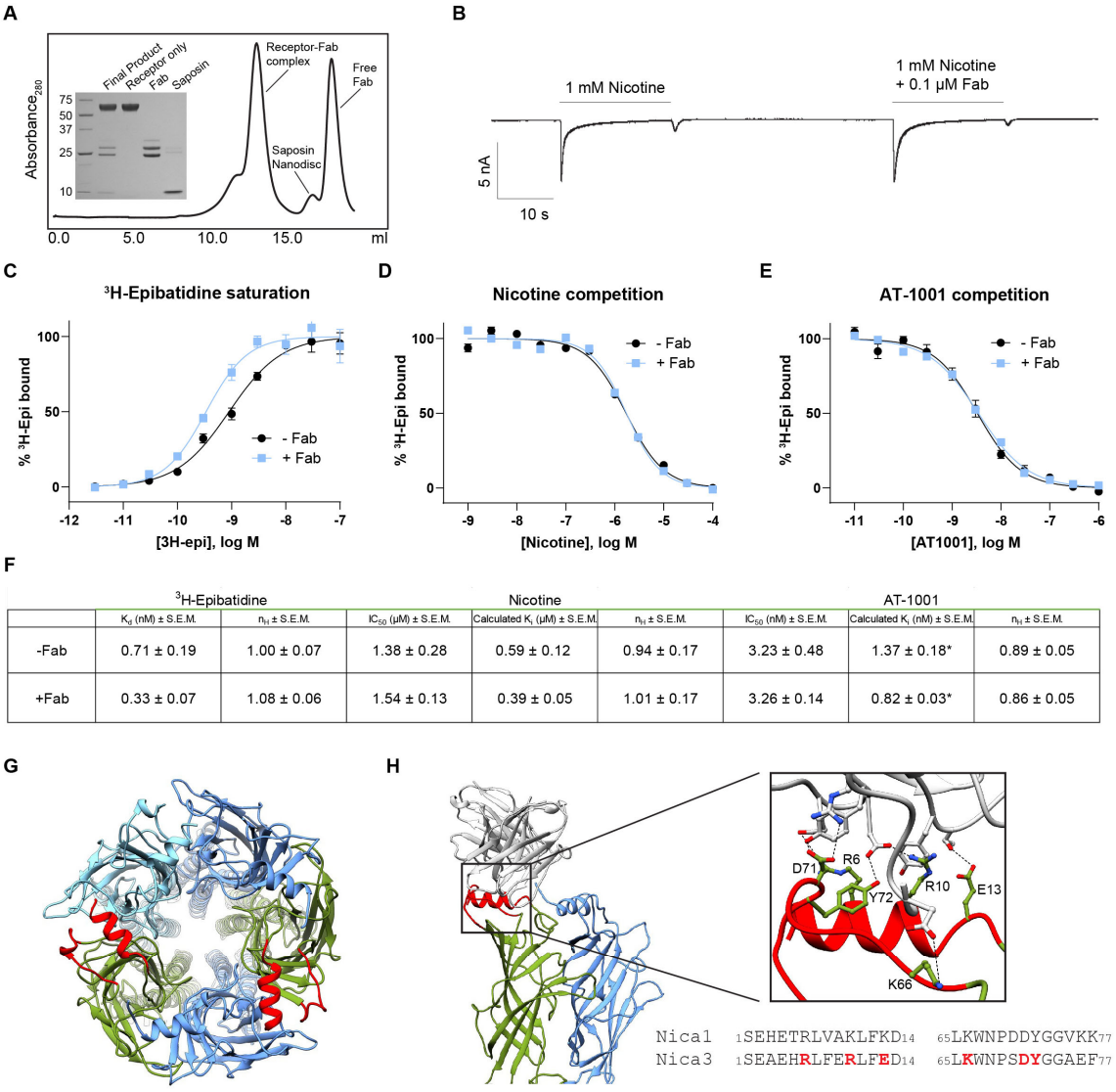

F

	^{3}H-Epibatidine		Nicotine			AT-1001		
	K_d (nM) ± S.E.M.	n_H ± S.E.M.	IC_{50} (µM) ± S.E.M.	Calculated K_i (µM) ± S.E.M.	n_H ± S.E.M.	IC_{50} (nM) ± S.E.M.	Calculated K_i (nM) ± S.E.M.	n_H ± S.E.M.
-Fab	0.71 ± 0.19	1.00 ± 0.07	1.38 ± 0.28	0.59 ± 0.12	0.94 ± 0.17	3.23 ± 0.48	1.37 ± 0.18*	0.89 ± 0.05
+Fab	0.33 ± 0.07	1.08 ± 0.06	1.54 ± 0.13	0.39 ± 0.05	1.01 ± 0.17	3.26 ± 0.14	0.82 ± 0.03*	0.86 ± 0.05

Fig. III.2 Effects of Fab binding

(A) Gel-filtration and SDS-PAGE of receptor-Fab-nanodisc complex. (B) Whole-cell patch-clamp recording showing effects of Fab on currents elicited from 1 mM nicotine. (C) Saturation binding of ^{3}H-epibatidine with and without 1 µM Fab. (D) Competition of 1 nM ^{3}H-epibatidine with nicotine with and without Fab. (E) Competition of 1 nM ^{3}H-epibatidine with AT-1001 with and without Fab. (F) Table of K_d's for ^{3}H-epibatidine, and IC_{50}'s and calculated K_i's for nicotine and AT-1001. Significant differences between + and – Fab ($p < 0.05$) are indicated by *. (G) Top view of the α3β4 receptor. Regions homologous to the MIR of α1 are indicated in red. (H) Side view of Fab binding site colored as before. Inset shows interactions between region homologous to MIR and Fab and sequence alignment of α1 MIR and α3. Interacting residues are shown as sticks. Four out of six residues directly involved in Fab binding on α3 are conserved between the two subunits.

Single particle analysis of the receptor-Fab-nanodisc complex in the presence of nicotine revealed an assembly with two Fabs bound to the top of the receptor (Fig. III.3A). The final reconstruction was resolved to approximately 3.3 Å (Table III.1), allowing me to build a model for the receptor and the variable domains of the Fab fragments. I determined that the Fabs bind to α3 subunits, indicating a 2α:3β stoichiometry. Interestingly, the structural epitopes recognized by these Fabs are homologous to the main immunogenic region (MIR) of α1 subunits in muscle-type receptors, the target of the majority of autoantibodies that cause myasthenia gravis (Luo et al., 2009) (Fig. III.2G-H). The α3β4 receptor itself resembles a cone with α3 (chains A and D) and β4 (chains B, C, and E) subunits arranged pseudo-symmetrically about the channel axis in an alternating manner (Fig. III.3B). Each subunit adopts a fold characteristic of the Cys-loop receptor superfamily, which includes the cationic nicotinic acetylcholine and 5-HT_3 receptors, as well as the anionic glycine and $GABA_A$ receptors (Nemecz et al., 2016). All subunits contain an extracellular N-terminal domain composed of a β-sandwich followed by four transmembrane helices (M1-M4) with M2 helices lining the ion-conducting pore. The ICD of cationic members of the superfamily is primarily composed of the membrane-associated (MA) helices, which form the tip of the cone. In addition to density for the receptor, I observed nicotine and water at the orthosteric binding sites, CHS at the periphery of the transmembrane domain, and waters and ions in the pore (Fig. III.3). Density for BRIL was notably absent in all cryo-EM maps.

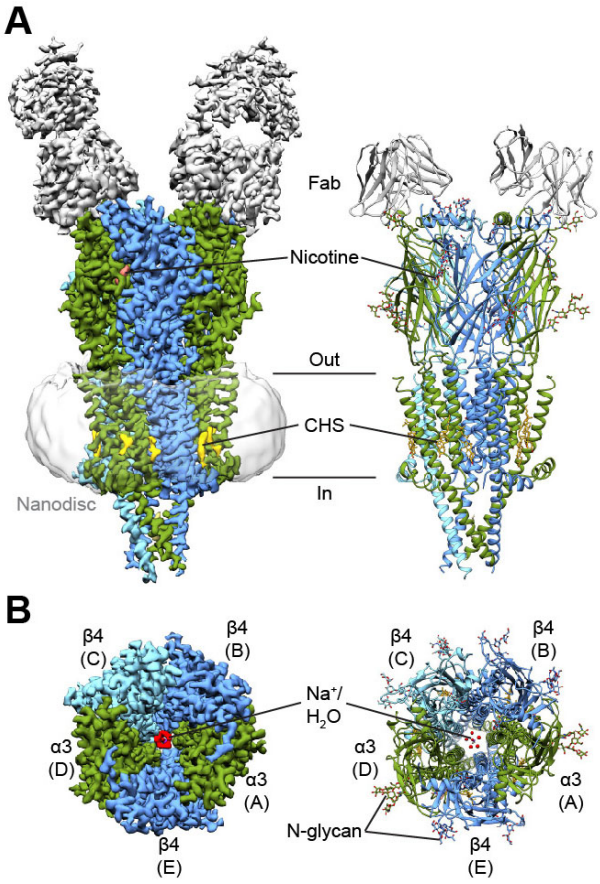

Fig. III.3 Architecture of the α3β4 receptor
(A) Side views of cryo-EM map and atomic model of α3β4-nicotine complex. α3 subunits are colored in green, β4 subunits in blue, Fabs in gray, nicotine in salmon, and CHS in yellow. (B) Top views of cryo-EM map and atomic model. Coloring is as indicated before. Water is in red; sodium is in purple.

In the presence of AT-1001, the sample suffered from profound aggregation in nanodiscs, evident in both gel filtration and in micrographs (Fig. III.4A-D). This dataset produced a density map with an overall resolution of 4.6 Å (Fig. III.5D, Table III.1). When purified in detergent, the sample displayed markedly improved biochemical behavior and yielded a 3.9 Å map (Table III.1). Local resolution in the orthosteric pocket approached 3.0 Å with clear density for sidechains and the ligand, allowing me to confidently model this region (Fig. III.5B, III.6B). Importantly, I was able to compare this structure to the lower-

resolution lipid-reconstituted map and did not observe conformational differences that could be attributed to detergent artifacts (Fig. III.4E-F). The general architecture of the AT-1001-bound structure is consistent with the nicotine complex (r.m.s.d. = 0.75 Å; Fig. III.7A).

Dataset	Nicotine	AT-1001 in DDM	Nicotine w/out CHS	AT-1001 in nanodiscs
Data collection				
Microscope	FEI Titan Krios	FEI Titan Krios	FEI Talos Arctica	FEI Titan Krios
Magnification	46,730	59,523	57,013	59,523
Voltage (ke$^-$V)	300	300	200	300
Exposure time (s)	10	8	2	8
Number of frames	40	20	40	20
Electron exposure (e$^-$/Å^{-2})	47	48	64	48
Detector	Gatan K2 Summit with GIF	Gatan K2 Summit with GIF	Gatan K3	Gatan K2 Summit with GIF
Pixel size (Å/pixel)	1.07	0.84	0.89	0.84
Micrographs	5053	3008	1020	3993
Reconstruction				
Initial number of particles	705,401	548,045	231,484	471,274
Final number of particles for reconstruction	112,737	93,080	74,820	40,686
Symmetry imposed	C1	C1	C1	C1
Box size (pixels)	300	300	300	320
Map Resolution (Å)	3.34	3.87	4.70	4.55
FSC threshold	0.143	0.143	0.143	0.143
Map-sharpening B-factor (Å^2)	-114	-200	-234	-172
Refinement				
Number of non-H atoms	20,048	20,051	-	-
Protein residues	2,379	2,379	-	-
Molprobity score	1.63 (100th percentile)	1.61 (100th percentile)	-	-
Clashscore	5.24 (100th percentile)	5.02 (100th percentile)	-	-
Poor rotamers (%)	0.64	0.69	-	-
R.M.S.D. values				
Bond lengths (Å)	0.006	0.006	-	-
Bond angles (°)	1.056	1.008	-	-
Ramachandran analysis				
Favored (%)	95.0	95.1	-	-
Outliers (%)	0	0	-	-

Table III.1 Data collection and refinement statistics.

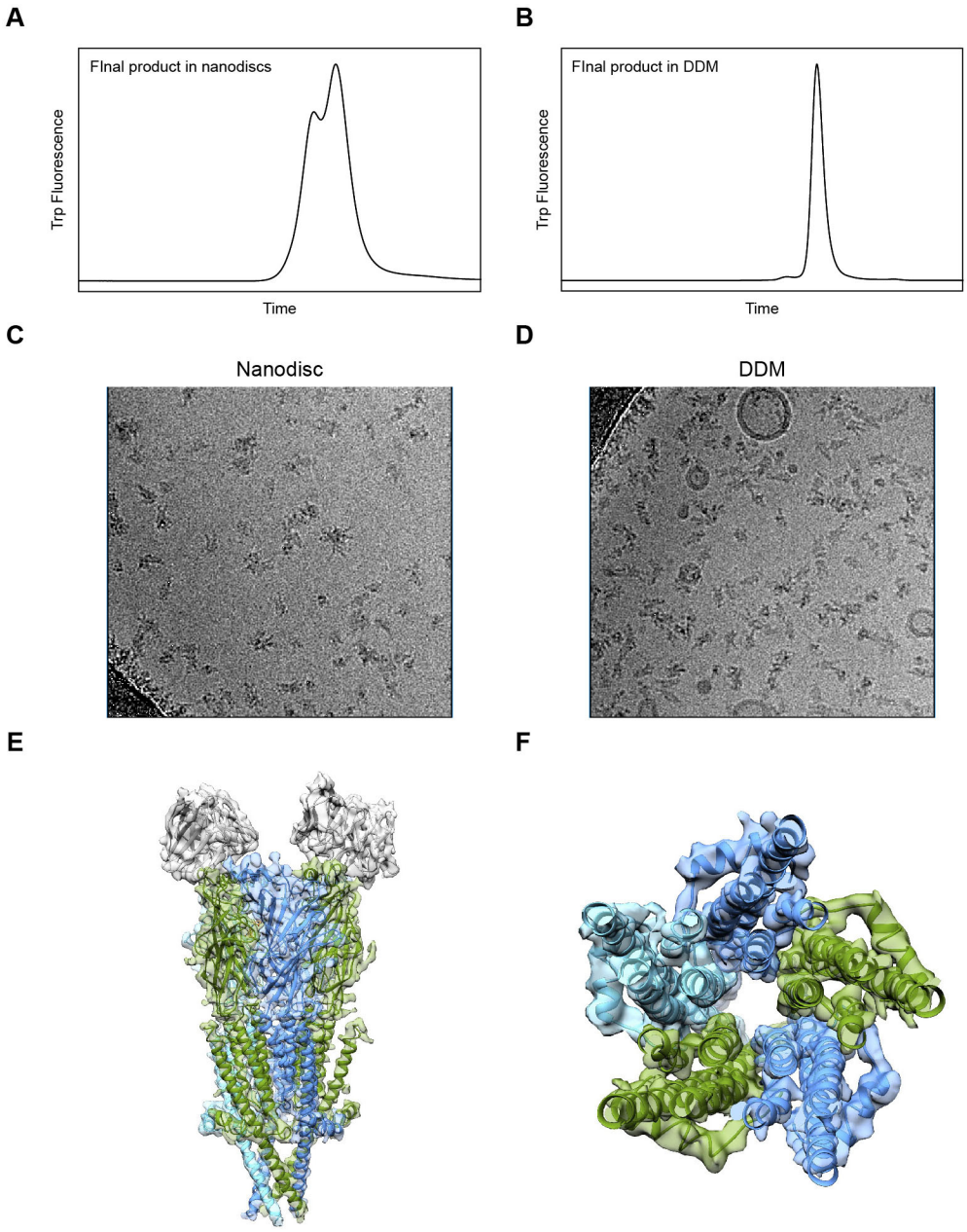

Fig. III.4 Comparisons of AT-1001 sample in nanodisc and detergent.
(A-B) Comparison of final product FSEC traces. Sample shows substantial aggregation in nanodiscs but is monodisperse in detergent. (C-D) Representative micrographs of two samples. Particles appear aggregated in nanodisc sample. (E) AT-1001 complex model in detergent fitted into lower-resolution nanodisc-sample density map. No clear differences are distinguishable. (F) Closeup of transmembrane region shows that the detergent-sample model fits well into nanodisc map.

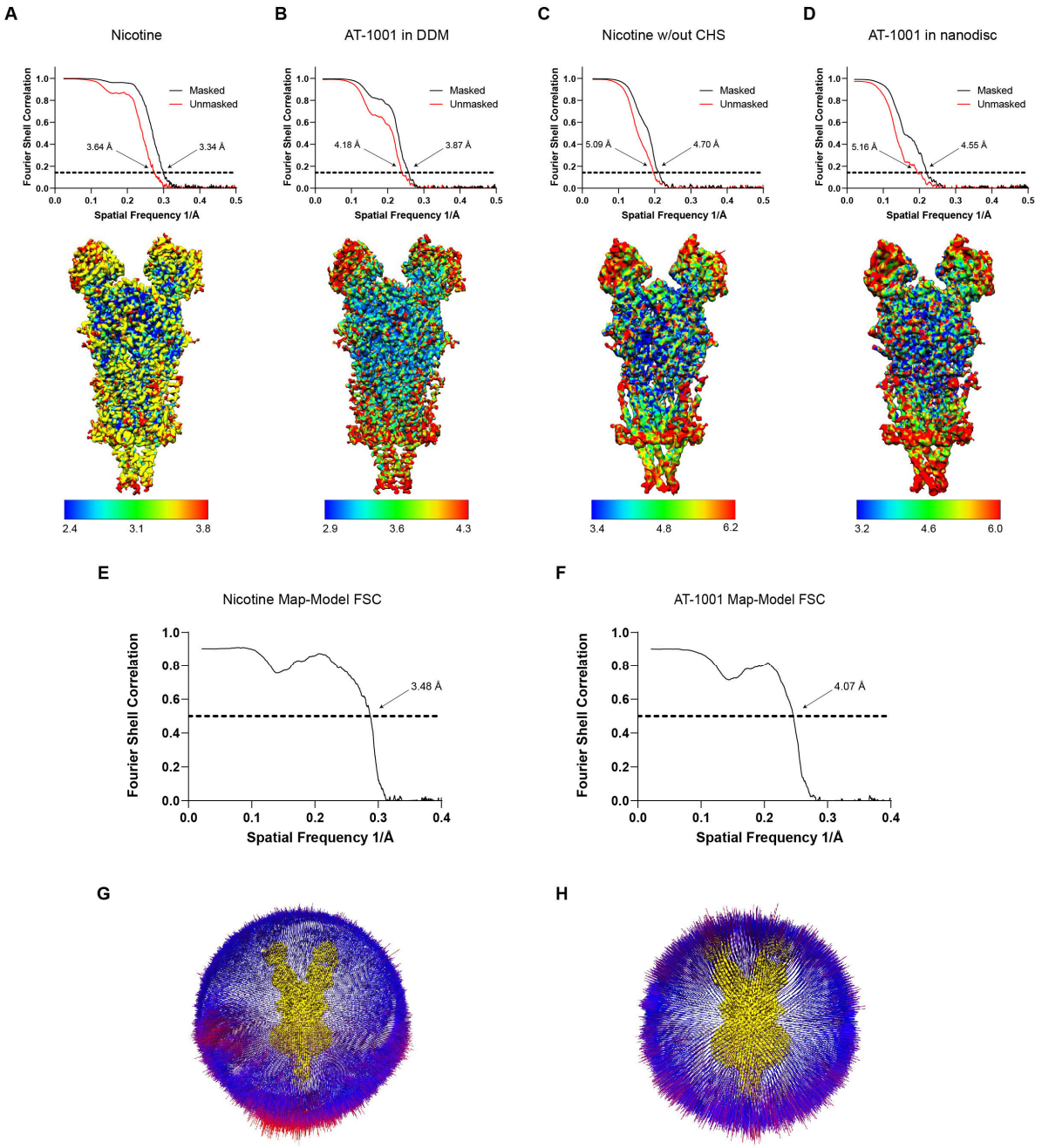

Fig. III.5 Map and model statistics

(A) FSC curve and local resolution map of α3β4-nicotine complex. (B) FSC curve and local resolution map of α3β4-AT-1001 complex in detergent. (C) FSC curve and local resolution map of CHS-free dataset. (D) FSC curve and local resolution map of α3β4-AT-1001 complex in saposin nanodiscs. (E) Map-model FSC of nicotine structure. (F) Map-model FSC of AT-1001 structure. (G) Angular distribution histogram of nicotine structure. (H) Angular distribution histogram of AT-1001 structure.

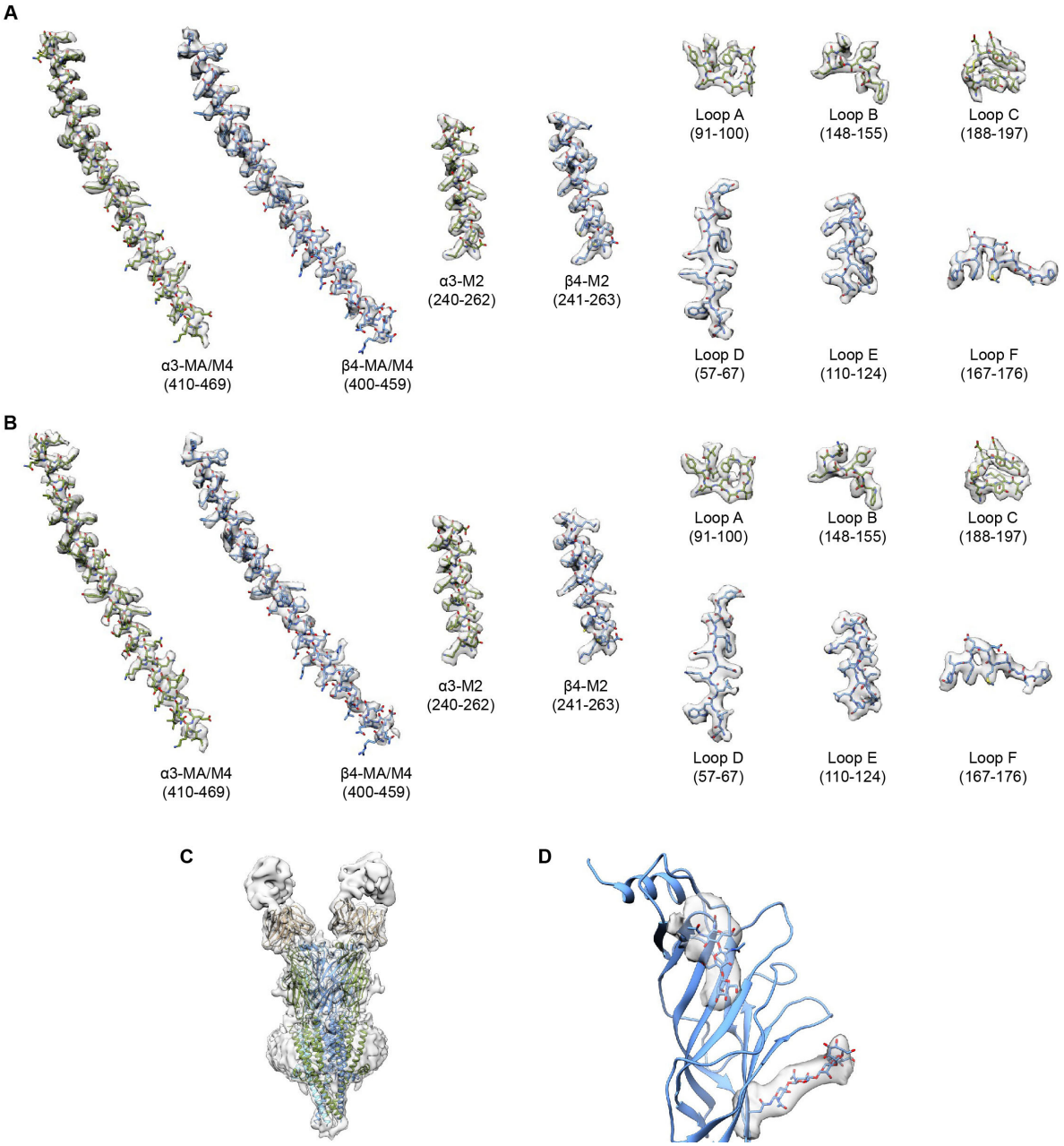

Fig. III.6 Density maps

(A) Density maps of key features in the α3β4-nicotine complex. Maps were rendered in Chimera at threshold levels of 0.02. (B) Density maps of key features in the α3β4-AT-1001 complex. Maps are displayed at threshold levels of 0.01. (C) 6 Å low-pass filtered map from nicotine dataset. (D) The low-pass filtered map showed clear density for and assisted building of N-linked glycans. Density for glycans originating from N117 and N145 on β4 are shown. The map is displayed at a threshold level of 0.01.

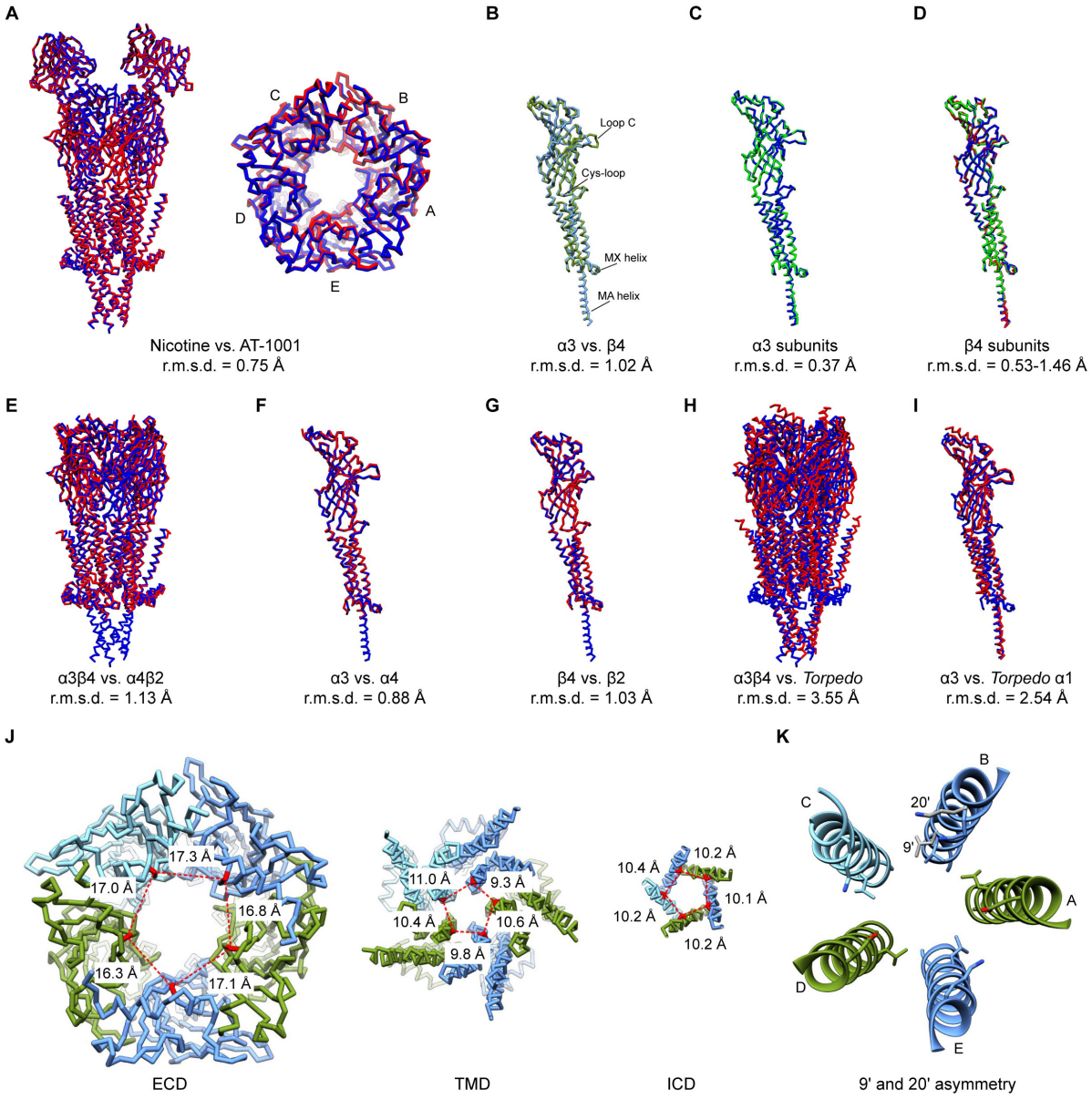

	α3	α4	β4	β2
α3	-	-	-	-
α4	67%	-	-	-
β4	46%	55%	-	-
β2	47%	59%	66%	-

Fig. III.7 Superpositions and pentagonal symmetry

(A) Superposition of α3β4-nicotine complex (blue) and α3β4-AT-1001 complex (red). (B) Superposition of α3 (green) and β4 (blue). (C) Superposition of α3 subunits. (D) Superposition of β4 subunits. (E) Superposition of α3β4 (nicotine complex; blue) and α4β2

(PDB ID: 6CNJ; red). (F) Superposition of α3 (blue) and α4 (red). (G) Superposition of β4 (blue) and β2 (red). (H) Superposition of α3β4 (nicotine complex; blue) and Torpedo receptor (PDB ID: 2BG9; red). (I) Superposition of α3 (blue) and Torpedo α1 (red). (J) Symmetry of equivalent positions in the nicotine complex in the ECD (α3 K84 and β4 R88), TMD (α3 L250 and β4 L251), and ICD (α3 M424 and β4 M417). (K) Breakdown in side chain symmetry at the 20′ and 9′ positions. Viewed from the top, sidechains at these positions in chains A, C, D, and E point in a counterclockwise direction. Sidechains from chain B are oriented in a more clockwise manner (shown in blue), creating a chasm at the only β-β interface of the pentamer. For reference, sidechains for L9′ and K20′ from chain E are superposed on chain B and shown in gray. The functional consequence of this asymmetry, if any, is not immediately clear; however, it is interesting to note that the symmetry breakdown occurs at functionally relevant positions. The 20′ position has been shown to be important for channel conductance and calcium permeability (Imoto et al., 1988; Tapia et al., 2007) and the 9′ position has been implicated in forming a hydrophobic gate near the midpoint of the pore (Beckstein and Sansom, 2006; Labarca et al., 1995). (L) Table of sequence identities between α3, α4, β4, and β2.

Ligand binding and selectivity

The neurotransmitter-binding sites of heteromeric neuronal nicotinic acetylcholine receptors are found extracellularly at α-β interfaces, with the α subunit forming the principal face and the β subunit forming the complementary face. Each face contributes three loops to the binding site: loops A-C from the principal side and loops D-F from the complementary side. α3β4 and α4β2 receptor subtypes share high sequence identity at these binding sites, yet affinities for many classical nicotinic receptor agonists, such as nicotine, acetylcholine, and epibatidine are ~10-100 fold lower for α3β4 than for α4β2 (Eaton et al., 2003, Xiao et al., 1998). Previous studies investigating the low affinity of these ligands to other subtypes, such as the α7 and muscle-type nicotinic receptors, identified an intrasubunit hydrogen bond between loops B and C that conferred high affinity (Grutter et al., 2003, Xiu et al., 2009).

However, the residues involved in this interaction are conserved between α4 and α3, leaving the cause of the differential affinities unclear.

To gain insight into this question, I determined a structure of the α3β4 receptor bound to nicotine. I observed clear density corresponding to the ligand at both α-β interfaces: the A-B interface (subsequently referred to as site 1), and the D-E interface (site 2) (Fig. III.8A, Fig. III.9A). The orientation of nicotine is equivalent at both sites and is analogous to that seen in structures of the α4β2 receptor and the acetylcholine binding protein (AChBP) (Morales-Perez et al., 2016b, Walsh et al., 2018, Celie et al., 2004). Nicotine is enveloped in a nest of highly conserved aromatic residues, namely Y93 from loop A, W149 from loop B, Y190 and Y197 from loop C, and W59 from loop D (Fig. III.8C). The basic nitrogen in the pyrrolidine ring is oriented such that it can form a hydrogen bond with the backbone carbonyl of W149, as well as a cation-π interaction with the aromatic sidechain of this residue. As expected in the presence of an agonist, loop C is in a closed conformation, occluding the binding pocket from solvent and allowing the vicinal disulfide to form hydrophobic interactions with the ligand. Consistent with the structure of the AChBP-nicotine complex (Celie et al., 2004), I observed density for an ordered water bridging the pyridine nitrogen and the backbone carbonyl oxygen of N111, S150 sidechain, and L123 amide nitrogen (Fig. III.8C, III.9A). Collaborators in Sweden further investigated the stability of these binding sites during triplicate 500-ns molecular dynamics simulations, during which both nicotine molecules remained within 2 Å of their initial positions (Fig. III.9I).

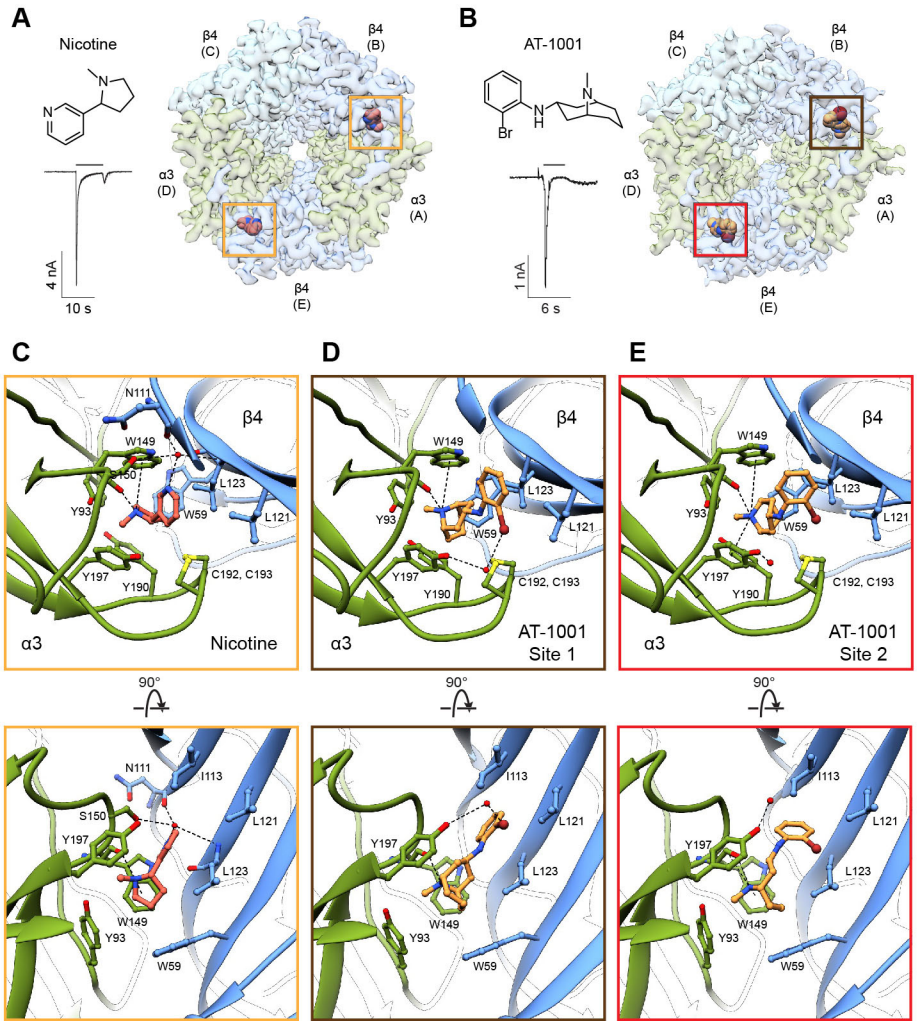

Fig. III.8 Ligand-binding sites

(A) Structure of nicotine, whole-cell response to 1 mM nicotine (concentration used for EM sample preparation), and top view of the α3β4-nicotine complex. Yellow boxes indicate nicotine binding sites. (B) Structure of AT-1001, whole-cell response to 50 μM (concentration used for EM sample preparation), and top view of the α3β4-AT-1001 complex. The brown box indicates site 1 and the red box indicates site 2. (C) Top and side views of nicotine binding site. For clarity, loop C has been removed in the side view. Putative hydrogen bonding and cation–π interactions are represented as dashed lines. (D) Top and side view of binding site 1 for AT-1001. (E) Top and side views for binding site 2 for AT-1001.

Next, I sought to understand mechanisms underlying agonist selectivity by determining a structure of α3β4 in complex with AT-1001. AT-1001 is a partial agonist that acts functionally as an antagonist by causing rapid desensitization (Cippitelli et al., 2015) (Fig. III.8B). This compound displays sub-nanomolar affinity to the human α3β4 receptor and is ~200-fold selective for this subtype over α4β2 (Tuan et al., 2015). Our structure revealed that AT-1001 binds at the orthosteric sites (Fig. III.8B). Although density for the bromine atom was underrepresented, I was able to confidently model the ligand due to clear signal from the large bicyclic ring and the smaller halo-phenyl group (Fig. III.9B-C). To my surprise, I found that AT-1001 unambiguously adopts different poses at the two binding sites. At site 1, the halo-phenyl moiety is oriented roughly parallel to the long axis of the bicyclic ring (Fig. III.8D). The bromine points outwards, away from the channel axis, coordinating a water in conjunction with the hydroxyl group of Y197, and the phenyl ring is slotted in between I113 and L121 on loop E. The positively-charged bridging nitrogen of the bicyclic ring (pKa 9.35) mimics the basic nitrogen of nicotine, forming a hydrogen bond and a cation-π interaction with W149. At site 2, AT-1001 assumes a distinctly kinked pose, with the halo-phenyl ring bent and rotated toward the complementary face (Fig. III.8E). Here, the bromine positions in between L121 and L123 on loop E, disrupting the hydrogen bond with the water, which moves closer to Y197. This orientation of the top ring forces an outward rotation of the bicyclic ring, positioning the tertiary nitrogen to form a cation-π interaction with Y197 in addition to W149. At both sites, the aromatic nest remains intact, with constituent residues oriented similarly as in the nicotine structure, with loop C in the closed conformation (Fig.

III.8C-E). Similar to nicotine, AT-1001 remained bound within 2 Å of its initial position in simulations (Fig. III.9J).

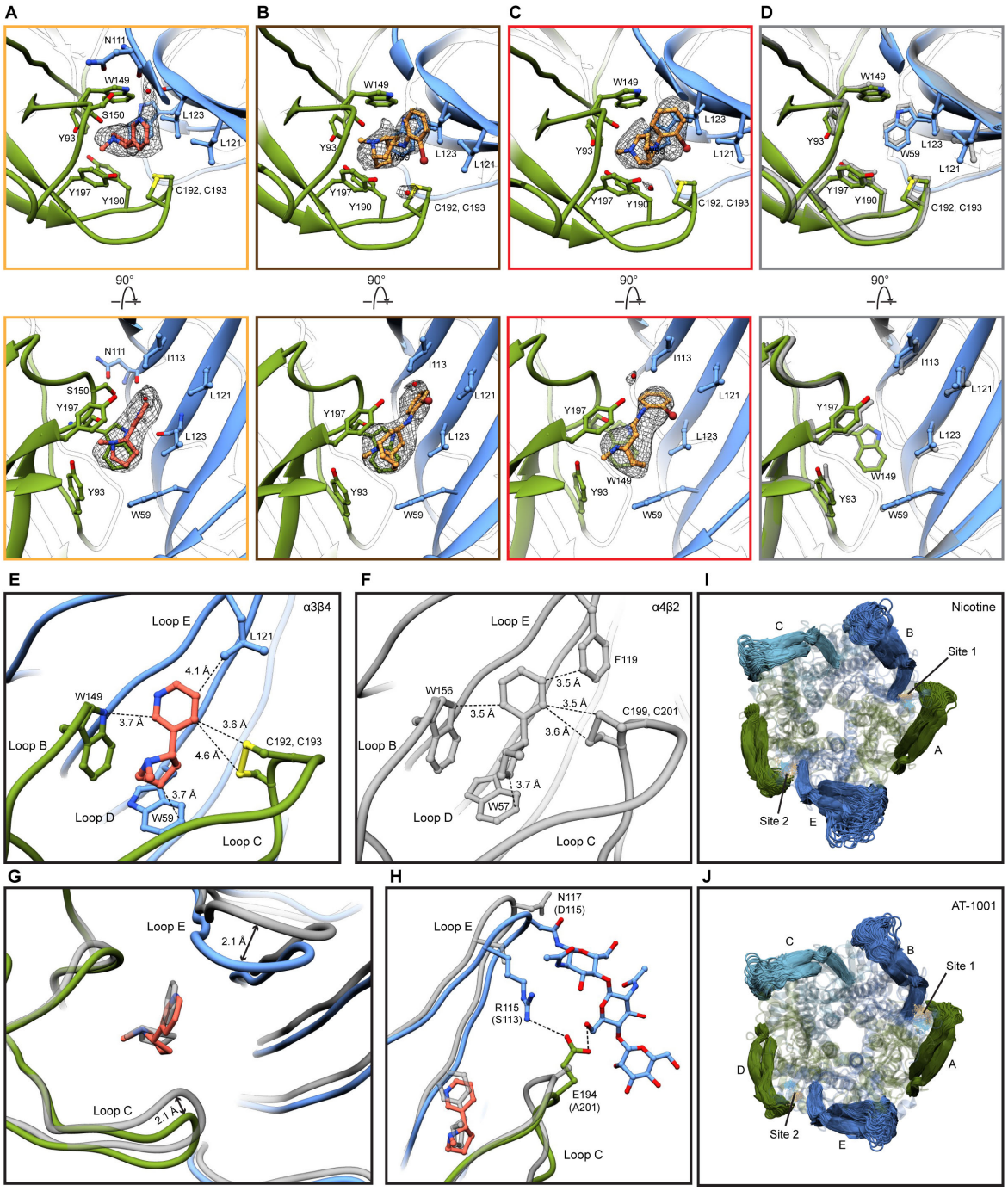

Fig. III.9 Ligand density and binding pocket details
(A) Density for nicotine and water in ligand-binding pocket. Density is shown at a threshold level of 0.02 in Chimera. (B) Density for AT-1001 and water at site 1. Density is shown at a threshold level of 0.018 in Chimera. (C) Density for AT-1001 and water at site 2. Density is shown at a threshold level of 0.018 in Chimera. All orientations are as shown in Fig. III.8. (D) Overlay of sites 1 (color) and 2 (gray) in the AT-1001 complex. The backbone and sidechain positions at the two binding sites are nearly identical, leaving the cause of the different poses of AT-1001 unclear. (E) Distances between nicotine and surrounding residues in α3β4. (F) Distances between nicotine and surrounding residues in α4β2. The binding pocket of α4β2 is more compact, as loop C forms closer contacts with nicotine and pushes it further back towards loop B. (G) Backbone differences in loops C and E between α3β4 and α4β2. Although the top of loop E is outwardly displaced in α3β4, its orientation is comparable to that of α4β2 at the level of the ligand-binding site. (H) Putative electrostatic interactions between loops C and E in α3β4. Interactions between E194 and R115 as well as a glycan chain originating from N117 pull loop E forward while scaffolding loop C in a distal position. These interactions are not possible in α4β2, as E194 and R115 are substituted with much smaller residues (alanine and serine), and N117 is replaced with an aspartate, and thus not glycosylated. (I) Representative frames, viewed from the extracellular side, taken at 5-ns intervals from triplicate 500-ns molecular dynamics simulations of the nicotine complex, examining stability of loop C and agonists. Dots indicate snapshot positions of pyridine (brown) and pyrrolidine (blue) nitrogen atoms. (J) Representative frames as in panel I from simulations of the AT-1001 complex. Dots indicate snapshot positions of bromine (brown) and bridged-ring nitrogen (blue) atoms. Nicotine and AT1001 atoms deviate less than 2 Å from their initial positions. Panels I-J thus illustrate stability of small-molecule agonists over the simulation time course, and relatively high mobility of loop C in β subunits (blue) compared to α subunits (green).

These studies allowed me to address questions regarding ligand selectivity between nicotinic receptor subtypes. By comparing the nicotine-bound structure to previous structures of the α4β2 receptor (Walsh et al., 2018, Morales-Perez et al., 2016b), I sought to understand the relatively low affinity of non-selective agonists for the α3β4 receptor. Superposition of the α4β2 and α3β4 binding sites revealed that not only are the majority of residues contacting nicotine conserved, but they are also similarly oriented (Fig. III.10A). The only two substitutions directly in the binding pocket are I113 (V111 in β2) and L121 (F119) on loop E. Of these two, the L121F substitution is of greater interest, as the aromatic sidechain of

phenylalanine could engage in a π-π interaction with the pyridine of nicotine. I also noticed an outward displacement of ~2.1 Å in loop C when compared to α4β2 (Fig. III.9G, Fig. III.10A). These shifts result in a less compact binding pocket in α3β4 (Fig. III.9E-F), potentially leading to a loss in affinity for nicotine by weakening Van der Waals contacts with surrounding residues. I found key differences between α3β4 and α4β2 that may account for the divergence in loop C positioning. The residue immediately prior to the vicinal cysteines on loop C is an asparagine in α3 and a glutamate in α4. Both residues appear poised to interact with a conserved aspartate on loop F. While N191 in α3 can hydrogen bond with the aspartate, pulling loop C downward, the negative charge of E198 in α4 is repelled away, potentially pushing loop C toward the ligand binding site (Fig. III.10B). K61 on loop D is positioned to form a hydrogen bond with the backbone carbonyl of C192 in α3β4, propping open loop C. This hydrogen bond cannot form in α4β2, as the lysine is replaced by a threonine, whose sidechain is not long enough to interact with loop C (Fig. III.10B). Next, I looked to explain the selectivity of AT-1001 for α3β4. I can speculate that the more spacious binding pocket of α3β4 may better accommodate the larger ligand. Superpositions revealed potential clashes of the bromine on AT-1001 with F119 on β2 at both sites, and a clash of the water with loop C at site 1 (Fig. III.10C-D). These structural comparisons provide initial insights into the different ligand sensitivities of these subtypes; however, a thorough mutational analysis will be required to draw definitive conclusions.

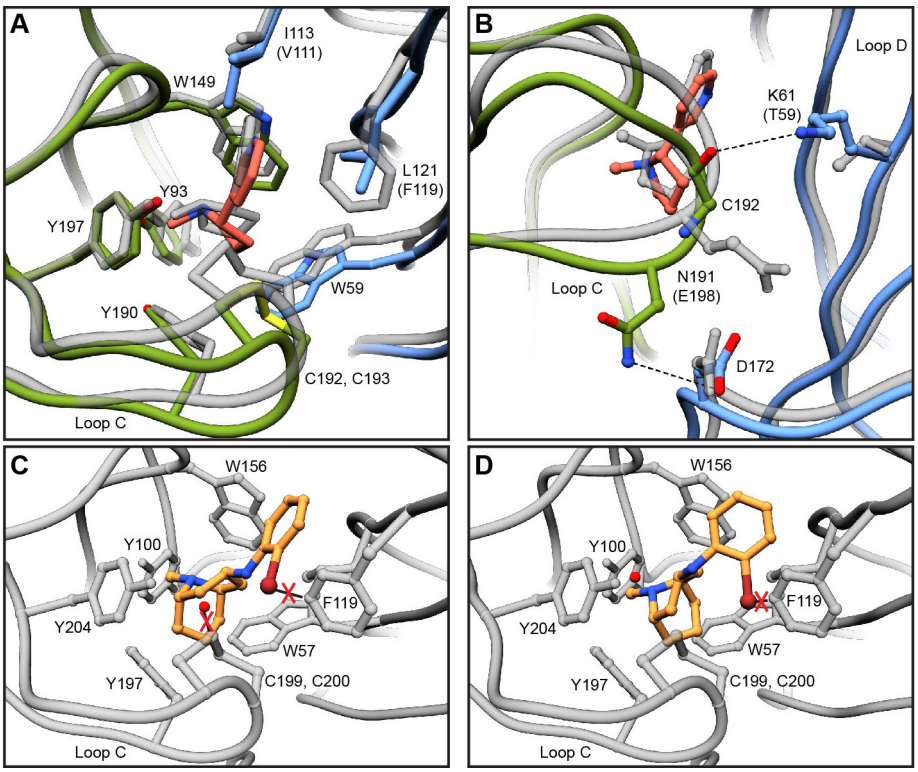

Fig. III.10 Comparisons of α3β4 and α4β2 binding pockets
(A) Overlay of α3β4 and α4β2 binding sites. α4β2 structure is shown in gray. Residue numbering is for α3β4 and substitutions between subtypes are indicated in parentheses. (B) Hydrogen bonds between α3 and β4 that may account for differential loop C structures and corresponding residues in α4β2. (C) Overlay of AT-1001 site 1 orientation in α4β2 binding site. Potential clashes are indicated with red X's. (D) Overlay of AT-1001 site 2 orientation in α4β2 binding site.

Permeation pathway

Recently, there has been considerable controversy surrounding structures of Cys-loop receptors in detergent micelles and whether or not they represent physiologically relevant conformations (Laverty et al., 2019, Cerdan et al., 2018). Decades of studies on the nicotinic receptor from the *Torpedo* ray electric organ highlight strong lipid dependence for function of this prototypical family member (daCosta and Baenziger, 2013, Chak and Karlin, 1992). Membranes lacking essential lipidic components may stabilize an uncoupled receptor conformation that is unable to undergo agonist-induced conformational changes (daCosta and Baenziger, 2009). Previous structures of the α4β2 receptor in complex with nicotine were characterized to be in non-conducting desensitized states but were determined in the absence of phospholipids. In this study, I determined the structure of a nicotine-bound receptor reconstituted into a bilayer that was shown to support channel function. I also solved a structure of the same protein bound to AT-1001 both in the presence of dodecylmaltoside (DDM) and in lipid nanodiscs, granting me the opportunity to directly compare the pore conformations of lipid-reconstituted and detergent-solubilized receptors. I found that the pore architectures for the two complexes are nearly identical and are congruent with previous structures of the α4β2 receptor (Walsh et al., 2018, Morales-Perez et al., 2016b) (Fig. III.11A-B). Because all of these structures were determined in the presence of desensitizing agonists, I suggest that this shared pore architecture represents a desensitized state.

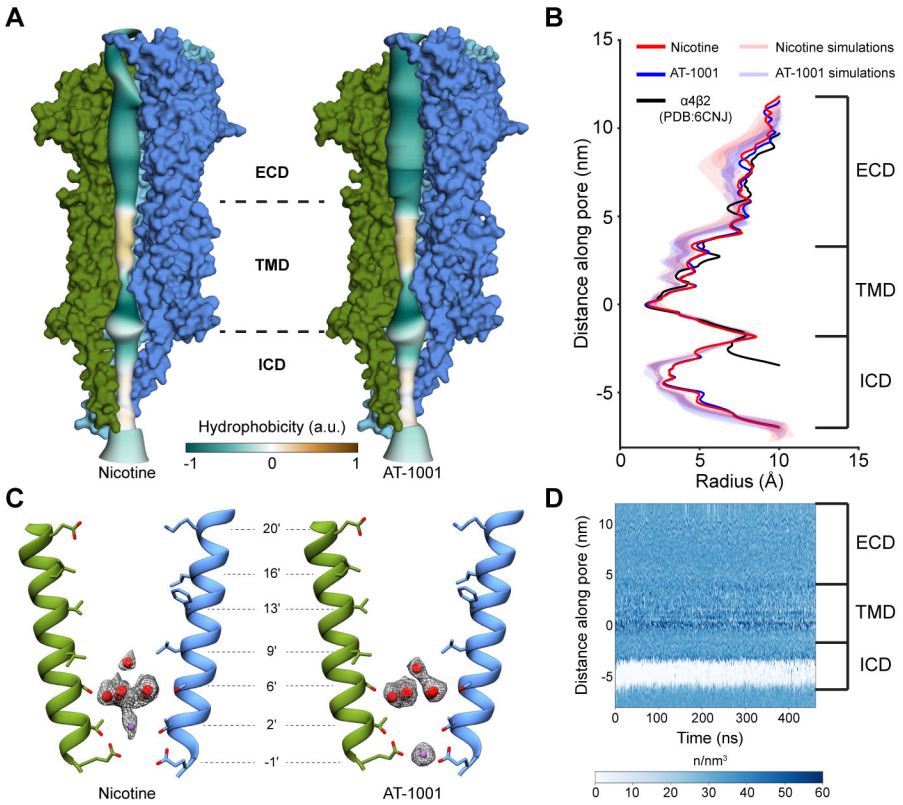

Fig. III.11 Channel axis and permeation
(A) Radius profiles of nicotine and AT-1001 structures colored by hydrophobicity. For clarity, chains A and E are not shown. (B) Pore radius profiles comparing nicotine, AT-1001, and α4β2 structures, and simulations in the presence of nicotine or AT-1001. (C) Positions of ordered waters and ions in the pore and corresponding density. Chains D and B are shown. (D) Water density profile along channel axis. In (B) and (D), zero point on y-axis corresponds to Glu-1′.

The transmembrane portion of the α3β4 channel resembles a funnel that narrows as it approaches the cytoplasm, consistent with structural and functional evidence that the desensitization gate lies toward the intracellular end (Gielen and Corringer, 2018). The pore ultimately reaches a constriction point formed by the sidechains of Glu-1′ with a radius of ~1.7 Å (Fig. III.11A-C). Density for acidic sidechains is typically underrepresented due to

inherent flexibility, radiation damage, and negative atomic scattering factors at low resolutions, but high-pass filtered maps have been used to resolve such sidechains (Yonekura et al., 2015). Using a 5 Å high-pass filtered map from the nicotine dataset, I observed clear density for these key residues and were able to confirm their orientation (Fig. III.12A, Fig. III.13A-B). The pore radius at the hydrophobic girdle, corresponding to the 9′ and 13′ positions, is ~3.8 Å, large enough to pass a hydrated sodium ion. Simulations of the *Torpedo* receptor have led to a proposed hydrophobic gating mechanism, in which the pore is not fully occluded (~3 Å radius) but a steep energetic barrier due to desolvation prevents ion flux in the resting state (Beckstein and Sansom, 2006, Ivanov et al., 2007). Throughout molecular dynamics simulations of the α3β4 channel, the pore radius profile remained stable, with a constriction point at the -1′ position (Fig. III.11B, Fig. III.13F); however, the entire transmembrane region of the pore remained solvated (Fig. III.11D). This result suggests that the observed pore conformation for α3β4 is inconsistent with consensus models of a resting state, further supporting our conclusion that these structures represent a desensitized state.

Within the pore, I observed density for a pentagonal ring of waters coplanar with the hydroxyl group of Ser6′ (Fig. III.11C, Fig. III.12B-D). Similar water pentagons have been found at this position in higher-resolution structures of GLIC (Sauguet et al., 2013), and the polar nature of 6′ residues is essential for channel conductance (Imoto et al., 1991). The pore diameter in our structures is wider in this region than in GLIC, and consequently I found that the water molecules form a looser ring (mean distance of 3.6 Å vs 2.8 Å (Sauguet et al., 2013)) (Fig. III.12B). I also observed densities along the pore axis above and below the pentagon. Without very high-resolution structural information or anomalous X-ray

crystallographic data, the assignments for these densities remain speculative. However, molecular dynamics simulations suggested water occupies the pore near Ser6′ more often than sodium ions (Fig. III.13C-D); thus, I modeled the upper axial density as a water. The more cytosolic axial density differs in height between the nicotine and AT-1001 complexes, but in both cases was modeled as sodium due to similarly identified cation binding sites in GLIC (Sauguet et al., 2013, Hilf et al., 2010) and proximity to Glu-1′ sidechains. The sodium ions potentially contribute to the stabilization of Glu-1′ sidechains in the observed "up" (mm) rotamer (Fig. III.12C-D). During 500 ns simulations, these sidechains predominantly remained in this conformation and sodium ions preferentially occupied nearby positions in the pore (Fig. III.13C-E). I thus speculate that sodium ions at these positions occupy structurally significant cation binding sites that enable the negatively charged carboxyl groups of Glu-1′ to orient inward toward the channel pore and form the desensitization gate.

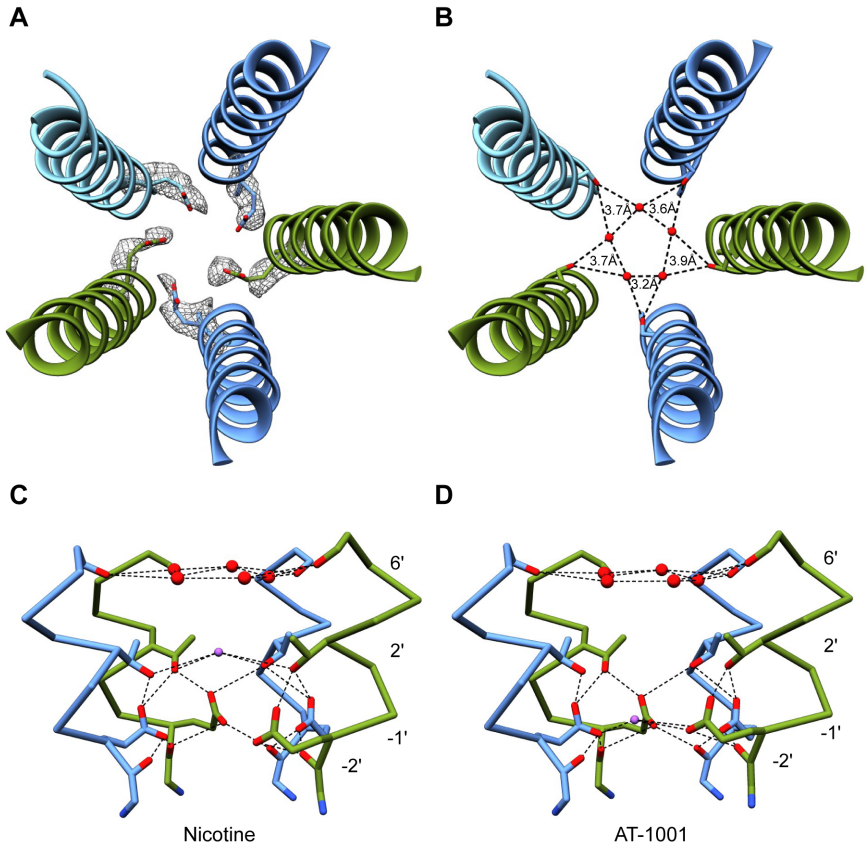

Fig. III.12 Pore features

(A) Density for Glu-1′ from 5 Å high-pass filtered map. (B) Coordination of pentagonal water ring from Ser6′. (C) Hydrogen bonding network showing interactions between pentagonal water ring, sodium ion, and surrounding residues in nicotine structure. Glu-1′ is stabilized by Thr2′ and Gly-2′. Chain C has been removed for clarity. Mean distances for dashed lines- Ser6′ hydroxyl/water: 4.3 Å, Na^+/Thr2′ hydroxyl: 4.4 Å, Thr2′ hydroxyl/Glu-1′ carboxyl: 3.6 Å, Glu-1′ carboxyl/Gly-2′ carbonyl: 3.0 Å. (D) Same as in panel C, but for AT-1001 structure. Sodium ion may help stabilize Glu-1′ in this position. Mean distances for dashed lines- Ser6′ hydroxyl/water: 4.4 Å, Thr2′ hydroxyl/Glu-1′ carboxyl: 3.5 Å, Na^+/Glu-1′ carboxyl: 3.8 Å, Glu-1′ carboxyl-Gly-2′ carbonyl: 3.1 Å.

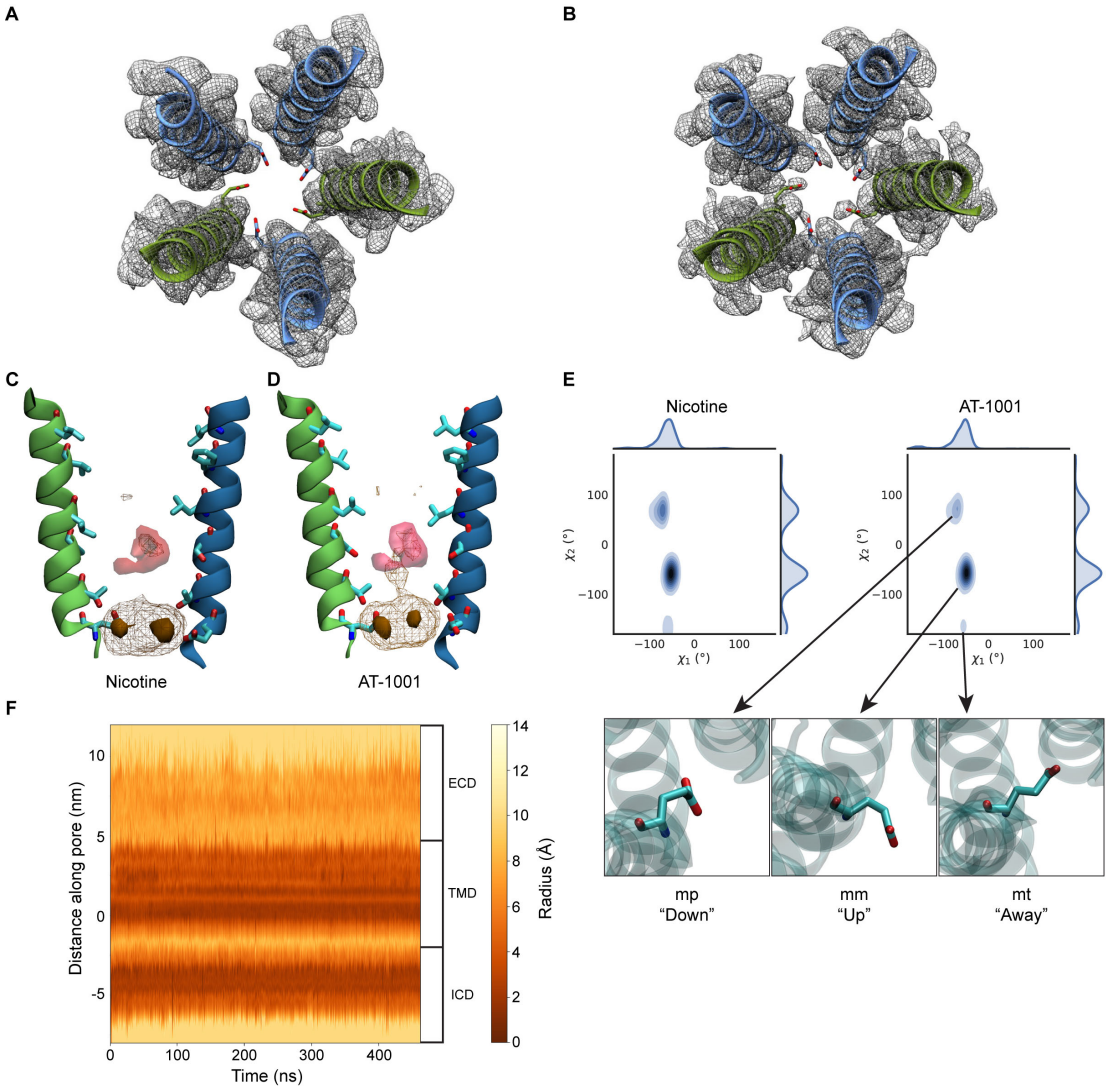

Fig. III.13 Pore details

(A) Map for M2 helices before high-pass filtering. Glu-1′ sidechains are shown as sticks. (B) Map for M2 helices after high-pass (5Å) filtering. Density for Glu-1′ is apparent without the introduction of substantial noise. (C) Model of the α3β4 pore during molecular dynamics simulations of the nicotine complex, showing two pore-lining helices with water (red) and sodium-ion (brown) densities. Ion probability densities are shown at both lower (mesh) and higher (solid) thresholds to reveal less-frequent explorations above Thr2′. (D) Model of the α3β4 pore, shown as in panel C, for simulations of the AT-1001 complex. (E) Conformation of Glu-1′ sidechains throughout nicotine (top left) and AT-1001 (top right) simulations. Three representative rotamers (below) are shown from the extracellular side of the pore. Sidechains primarily adopted the "up" (mm) conformation (Harpole and Grosman, 2014; Lovell et al., 2000). (F) Radius profile of the central channel over time. Zero point on y-axis corresponds to Glu-1′. The radius profile remains consistent over the course of triplicate 500-ns simulations, with the most constricted point at Glu-1′.

Structure and function of the intracellular domain

The ICD of nicotinic receptors plays crucial roles in cellular trafficking, gating kinetics, and channel conductance (St John, 2009, Bouzat et al., 1994, Hales et al., 2006). This domain consists of a short post-M3 loop, an amphipathic MX helix that lies parallel to the plane of the membrane, a poorly conserved and disordered cytoplasmic loop, and the MA helix. Previous structures of the α4β2 receptor utilized aggressive deletions in this region to promote crystallization and biochemical stability. Thus, comprehensive structural information on nicotinic ICDs has been limited to homologous domains of homomeric 5-HT_{3A} receptors (Basak et al., 2018a, Hassaine et al., 2014, Polovinkin et al., 2018) and lower-resolution reconstructions from the *Torpedo* receptor (Unwin, 2005). By retaining all ordered components of this domain in our EM construct, I was able to resolve a heteromeric assembly of the ICD and explore its role in ion permeation.

Most notably, this study allowed me to examine the structure and function of the MA helices. These helices are continuous extensions of M4, protruding ~40 Å into the cytosol and forming a conical intracellular vestibule at the bottom tip of the receptor. The helices diverge as they approach the membrane, forming five distinct portals that are predominantly lined by polar and acidic residues. Toward the constriction point at the bottom of the vestibule, I observed a strong oblong density along the central axis of the receptor, lined by several rings of conserved hydrophobic residues (Fig. III.14A-B). I was curious about the identity of this "hydrophobic plug," and initially suspected it to be CHS. To test this hypothesis, Dr. Noviello helped me collected an EM dataset from a sample that did not include CHS during the preparation (Fig. III.5C, Table III.1). Density for the plug was still

present in the reconstruction (Fig. III.15A-B), while densities attributed to CHS along the periphery of the transmembrane domain disappeared. Furthermore, MD simulations suggested a lipid molecule is needed at this site to promote stability of the ICD (Fig. III.15J). I thus speculate that the density represents the tail of a detergent molecule or a lipid and modeled this feature as a lipid hydrocarbon tail. This site may correspond to a promiscuous hydrophobic site also occupied physiologically. Noteworthy is that a subset of density maps from recent 5-HT_{3A} receptor structures contain unmodeled features in this region or close by (Polovinkin et al., 2018, Basak et al., 2018a). The presence of this hydrophobic plug affirms the current consensus that ions permeate through the lateral portals of the intracellular vestibule (Basak et al., 2018a, Miyazawa et al., 1999). Even without a direct physical obstruction, the narrow radius (~2.7 Å) and highly hydrophobic nature of the central axis of the ICD would likely prevent ion flux through this region. Simulations support this concept, showing continuous hydration pathways through the portals (Fig. III.14C).

To verify the importance of the portals in ion permeation, I explored the contribution of portal-lining residues to channel conductance. Guided by the structure, I identified negatively charged residues whose sidechains project into the lateral windows. I found two residues in α3, E432 and D435, and four in β4, D420, D421, D423, and E428 (Fig. III.14D-F). I flipped the charges of these amino acids by mutating them to lysines and made single-channel recordings from cells transfected with the mutated subunits. The “K mutant” exhibited significantly attenuated single-channel responses in comparison with the EM construct (Fig. III.14G-H). This work expands on seminal studies of 5-HT_{3A} homomers that identified three regularly spaced arginines that underlie this channel’s remarkably low

conductance (Kelley et al., 2003). These studies first highlighted the functional importance of charged residues in MA helices. Here, I used direct structural information to decrease the electronegativity in the intracellular portals and showed that this causes a substantial reduction in channel conductance.

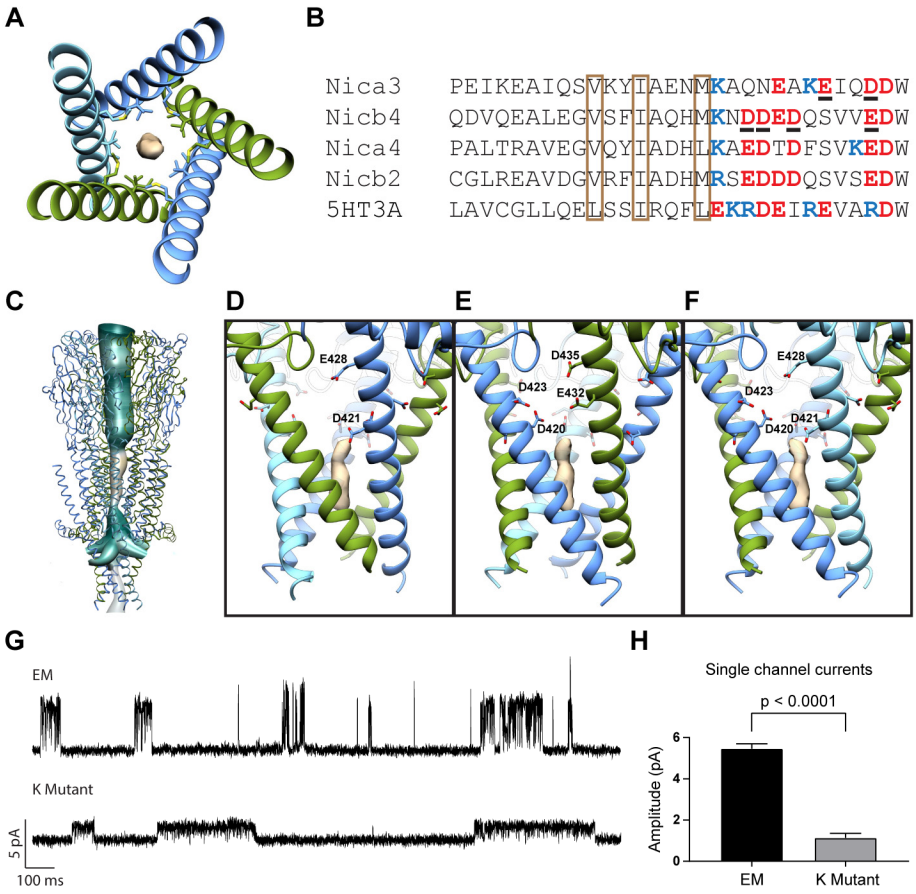

Fig. III.14 Intracellular domain
(A) Top view of ICD showing density of hydrophobic plug. Surrounding residues are shown as sticks. (B) Sequence alignment of ICD. Conserved hydrophobic residues are in brown boxes. Negatively-charged and positively-charged residues near portals are indicated in red and blue respectively. Residues mutated to lysines for the K mutant are underlined. (C) Continuous hydration pathway through the channel pore and five intracellular portals. (D) Side view of α-β portal. Mutated residues are shown as sticks. (E) Side view of β-α portal. (F) Side view of β-β portal. (G) Representative single channel recordings from EM construct and K mutant. (H) Comparison of single channel current amplitudes at 100 mV from EM construct and K mutant (n = 3 for each).

Finally, I investigated the positioning of the post-M3 loop and MA helix. Structures of the 5-HT_{3A} receptor suggest that channel gating involves conformational changes in these intracellular substructures (Basak et al., 2018a, Basak et al., 2018b). A putative open 5-HT_{3A} structure reveals an upward translation of MX, pulling the post-M3 loop away from the lateral portals (Fig. III.15C). This movement, along with a kinking of the MA-M4 helix, widens the proposed exit pathway for ions. In the α3β4 receptor, this region more closely resembles 5-HT_{3A} in the closed state. The MX helix lies along the membrane-cytoplasm interface and the post-M3 loop extends even further down into the lateral window (Fig. III.15C). The position of the post-M3 loop may be stabilized by a hydrogen bond between the hydroxyl group of T303 in α3 or S304 in β4 with the sidechain of an acidic residue on the neighboring MA helix (Fig. III.15D-F). However, this sunken orientation of the loop does not appear to fully obstruct ion permeation. Fenestrations of ~6 Å are present in portals at α-β and β-β interfaces (Fig. III.15G, Fig. III.15I). K431 of α3 partially occludes this opening at α-β interfaces (Fig. III.15H), although flexibility of this and surrounding sidechains may still permit ion passage. Further structural studies elucidating alternate conformational states of nicotinic receptors will provide additional insight into the role of this region in channel gating.

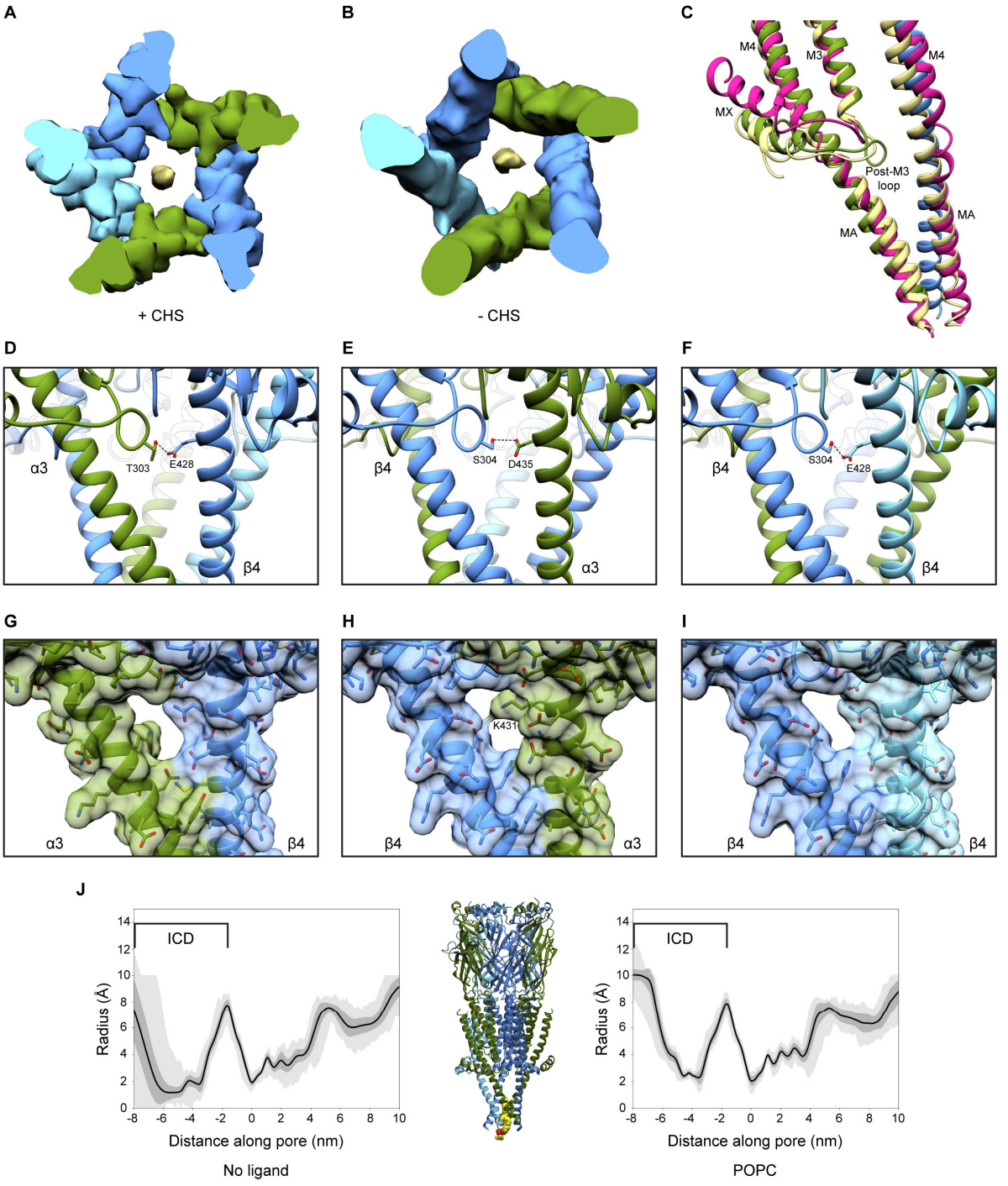

Fig. III.15 ICD details

(A) Top view of ICD of EM reconstruction from sample with included CHS. (B) Top view of ICD of EM reconstruction from sample without included CHS. (C) Comparison of post-M3 loop with 5-HT3A. Structures were superposed onto chain A of α3β4. Open 5-HT3A (6DG8) is shown in magenta, apo (6BE1) in yellow. (D-F) Potential hydrogen bond between post-M3

loop and MA helix of neighboring subunit shown in α-β, β-α, and β-β interfaces respectively. (G-I) Space-filling models show open portals between subunits at α-β, β-α, and β-β interfaces respectively. K431 may occlude the portal at the β-α interface. (J) Radius profile of the nicotine complex with either no ligand (left) or POPC (right) modeled into the intracellular-domain hydrophobic bundle. Distances along pore axes are calibrated as in Fig. III.11, with the zero-point at Glu-1′. Representative model (center) indicates initial position of POPC (yellow spheres, colored by heteroatom) in bound simulations. Shaded regions indicate maximum/minimum values (light gray) and standard deviation (dark gray) at each point along the pore axis during the simulation. Decreased deviations in the POPC complex indicate stabilization of the intracellular domain.

Conclusion

Here I present the first structures of the α3β4 ganglionic nicotinic acetylcholine receptor. A foundation of this work is the lipid reconstitution and electrophysiology experiments, which allowed me to obtain high resolution structural information in an environment that supports channel function; a first in the Cys-loop receptor family for recombinantly-produced protein. I analyzed structures of the receptor in complex with the non-selective agonist nicotine and the selective partial agonist AT-1001 to suggest that selectivity and overall lower agonist affinity at the ganglionic receptor stem from a less compact neurotransmitter site. These structures further reveal the architecture of the ICD and support conclusions from homologous protein structures that ions permeate through side portals and not through the hydrophobic axial pathway. Computational analyses complement all aspects of the structure-function study to examine pore hydration, ion permeation, and ligand site stability, building from the rigid structural snapshots toward a dynamic understanding of receptor mechanisms.

Methods

Construct design

Human α3 (UniProtKB P32297) and β4 (P30926) genes were codon optimized, synthesized, and cloned into the pEZT-BM expression vector (Morales-Perez et al., 2016a). Enhanced green fluorescent protein (EGFP) was inserted into the M3-M4 loop of both subunits and a Strep-tag was placed at the C-terminus of the β4 subunit. Constructs were initially screened via co-transfection of HEK293S GnTI$^-$ cells (ATCC CRL-3022) with combinations of EGFP-tagged and untagged subunits via Lipofectamine 2000 (Invitrogen). Cells were pelleted, solubilized with 20 mM Tris, pH 7.4, 150 mM NaCl (TBS buffer), 40 mM *n*-dodecyl-β-D-maltopyranoside (DDM; Anatrace), and 1 mM phenylmethanesulfonyl fluoride (PMSF; Sigma-Aldrich), and analyzed by fluorescence-detection size-exclusion chromatography (FSEC) (Kawate and Gouaux, 2006). Viable candidates without EGFP were then co-transfected in GnTI$^-$ cells in small-scale purification experiments (1-2 mL culture scale). Cells were pelleted, solubilized as before, and allowed to bind to high-capacity Strep-Tactin (IBA) affinity resin. Resin was washed with TBS containing 1 mM DDM, and protein was eluted with the same buffer supplemented with 5 mM desthiobiotin (Sigma-Aldrich) before being evaluated by FSEC monitoring tryptophan fluorescence. Screens revealed that robust expression and stable pentamer formation required deletions in the M3-M4 loop and were aided by the inclusion of soluble fusion partners in this region. Thus, in the final EM constructs, residues Asn348-Ser402 in α3 and Pro341-Ser395 in β4 were replaced with apocytochrome b(562)RIL (BRIL), a thermostabilized four-helical bundle that has been used to promote crystallization in G protein-coupled receptors (Chun et al., 2012).

Receptor expression and purification

Bacmam viruses for each subunit were produced as described for the α4β2 receptor (Morales-Perez et al., 2016a). Briefly, constructs in the pEZT-BM vector were transformed in DH10-Bac cells to produce recombinant bacmid. 2 mL of Sf9 cells (ATCC CRL-1711) were transfected with purified bacmid DNA to generate "P1" virus. 500 µL of this virus was then added to 1 L of Sf9 cells at a cell density of 1×10^6 cells/ml to produce a second generation of amplified virus ("P2"). Suspension cultures of GnTI$^-$ cells were grown at 37°C, 8% CO_2 and were transduced with α3 and β4 P2 viruses at a cell density of 4×10^6 cells/ml. At the time of transduction, 1 mM sodium butyrate (Sigma-Aldrich) was added to the culture and temperature was dropped to 30°C to boost protein expression. After 72 hours, cells were harvested by centrifugation, resuspended in TBS and 1 mM PMSF, and disrupted using an Avestin Emulsiflex. Lysed cells were centrifuged for 20 minutes at 10,000 g, and the resulting supernatants were centrifuged for 2 hours at 186,000 g to isolate membranes. Membrane pellets were mechanically homogenized and solubilized for 1 hour at 4°C with 40 mM DDM in TBS. Solubilized membranes were centrifuged for 40 minutes at 186,000 g then passed over high capacity Strep-Tactin resin. The resin was washed with TBS, 1 mM DDM, 0.2 mM cholesteryl hemisuccinate (CHS, Anatrace), and 1 mM TCEP (Thermo Fisher Scientific), and protein was eluted in the same buffer containing 5 mM desthiobiotin. For the nicotine-bound structure, 1 mM nicotine (Sigma) was included during affinity purification and for the AT-1001-bound structure, 10 µM AT-1001 (generous gift from Astrea Therapeutics) was included.

α3β4 receptors have been proposed to assemble in multiple subunit stoichiometries: $(\alpha3)_2(\beta4)_3$ and $(\alpha3)_3(\beta4)_2$ (Covernton et al., 1994, Krashia et al., 2010, Grishin et al., 2010). To bias expression towards one stoichiometry, a fluorescence-based assay was used, as described previously for the α4β2 nicotinic receptor (Morales-Perez et al., 2016a). Briefly, bacmam viruses were made and titered for α3-mCherry and β4-EGFP constructs. Viruses were used to transduce one liter of GnTI- cells. Protein was purified as described above, and molar concentrations of each subunit were calculated by measuring absorbance at the maxima for the two fluorophores (GFP, 488 nm; mCherry, 587 nm) and dividing by their respective extinction coefficients (GFP, 56,000 M^{-1} cm^{-1}; mCherry, 72,000 M^{-1} cm^{-1}). Protein was analyzed by FSEC measuring GFP and mCherry fluorescence, allowing scale factors to be calculated relating known molar concentrations to fluorescence signal. This medium-scale purification was followed by small-scale experiments where different viral ratios were used to transduce 1 mL of GnTI- cells. Cells were solubilized and analyzed by FSEC, and previously calculated scale factors were used to determine molar ratios of α3 and β4 subunits. A 1:1 ratio of α3 and β4 viruses was found to produce a homogenous population of pentamers containing two α3 and three β4 subunits, and thus this ratio of viruses was used to produce protein for structural studies, reconstitutions for electrophysiology, and for binding assays.

Saposin nanodisc reconstitution

The Saposin A expression plasmid was provided by Salipro Biotech AB. Reconstitution of α3β4 into saposin nanoparticles was modified from Nguyen et al. (Nguyen

et al., 2018) The reaction contained a 1:20:100 molar ratio of α3β4: saposin: soy polar lipid extract (Avanti). Lipids and saposin were mixed in TBS and 14 mM DDM and allowed to rotate at 4°C for 1 hour. Affinity-purified α3β4 was concentrated to ~20 μM, added to the saposin/lipid mixture, and rotated for 30 min at 4°C. 200 mg/mL Bio-Beads SM-2 (BioRad) were added to the mixture and rotation was continued overnight. The following morning, Bio-Beads were removed and replaced with 150 mg/mL fresh Bio-Beads for 2 hours.

Generation of monoclonal antibodies and Fab fragments

The 4G9 monoclonal antibody (mAb) (IgG2b, κ) was raised using standard methods following immunization of mice with α3β4 in detergent (Monoclonal Core, Vaccine and Gene Therapy Institute, Oregon Health & Science University). High affinity and specificity of the antibody for properly folded receptor was assayed by FSEC with EGFP-tagged receptor (shift in elution volume) and western blot (no binding). Fab fragments were generated by papain cleavage of whole antibody at a final concentration of 0.5 mg/ml for 2 hours at 37°C in 50 mM $NaPO_4$, pH 7.0, 1 mM EDTA, 10 mM cysteine and 1:10 (w/w) papain. Digestion was quenched using 30 mM iodoacetamide at 25°C for 30 min. Fab was purified by anion exchange using a HiTrap Q HP (GE Healthcare) column in 10 mM Tris, pH 8.0 and a NaCl gradient elution. Cloning and sequencing of Fab antibody regions were performed from mouse hybridoma cells.

Cryo-EM sample preparation and data collection

Affinity-purified α3β4 receptors reconstituted in nanodiscs were mixed with 4G9 Fab in a 1:1 (w/w) ratio and injected over a Superose 6 Increase 10/300 GL column (GE Healthcare) equilibrated in TBS, 1 mM TCEP, and ligand (1 mM nicotine or 50 μM AT-1001). Receptors purified in detergent followed the same protocol, but the buffer included 1 mM DDM and 0.2 mM CHS. Peak fractions were evaluated by analytical SEC, monitoring tryptophan fluorescence, and concentrated to an A280 of ~6. Samples in nanodiscs were supplemented with 1 mM Fos-Choline-8, fluorinated (Anatrace) immediately prior to freezing to induce random orientations in the grid holes. Protein sample (3 μL) was applied to glow-discharged gold R1.2/1.3 300 mesh holey carbon grids (Quantifoil) and immediately blotted for 4 s at 100% humidity and 4°C before being plunge-frozen into liquid ethane cooled by liquid nitrogen using a Vitrobot Mark IV (FEI).

Cryo-EM data were collected on a 300 kV Titan Krios microscope (FEI) equipped with a K2 Summit direct electron detector (Gatan) and a GIF quantum energy filter (20 eV) (Gatan) using EPU (FEI) and a 200 kV Talos Arctica (FEI) equipped with a K3 direct electron detector (Gatan) using Serial EM (Mastronarde, 2005). Sample-specific details are included in Table III.1.

Cryo-EM data processing

All datasets were processed using the same general workflow in RELION 3.0 (Zivanov et al., 2018). Dose-fractionated images were gain normalized, 2 x Fourier binned, aligned, dose-weighted, and summed with MotionCor2 (Zheng et al., 2017). Contrast transfer function correction and defocus value estimation were done with GCTF (Zhang, 2016).

Several hundred particles were manually picked and subjected to 2D classification to generate templates for auto-picking. Auto-picked particles were subjected to 2D classification to remove false positives. Ab initio models were generated in RELION and used for 3D classification. 3D classes with strong ICD density were selected for 3D refinement. An initial round of 3D refinement using the best 3D class as an initial model (low-pass filtered to 60 Å) was followed by a second round with finer angular sampling using the map from the first refinement low-pass filtered to 10 Å as the initial model. Next, per-particle CTF refinement and beam tilt estimation were performed before another round of 3D classification with no image alignment/angular searches. Particles from the best classes were selected, polished, and used for 3D refinement to generate the final maps. In the AT-1001 detergent dataset, particles with defocus values greater than -3.0 µm were removed from the final reconstruction to improve resolution. Local resolution was estimated with ResMap (Kucukelbir et al., 2014).

Model building, refinement, and validation

A homology model for the α3β4 receptor was generated from the cryo-EM structure of the 2α:3β assembly of the α4β2 nicotinic acetylcholine receptor (PDB ID:6CNJ) (Walsh et al., 2018) via Swiss-Model (Schwede et al., 2003). A homology model for the Fab fragment was made using PDB entry 4WFE (Brohawn et al., 2014) for the light chain and 3MXV (Maun et al., 2010) for the heavy chain. The receptor and one copy of the Fab were docked into the density map using UCSF-Chimera (Pettersen et al., 2004). Manual adjustments of the models were then done in Coot (Emsley et al., 2010). The ECD and TMD of each individual

subunit, as well as the variable domain of the Fab fragment were rigid body fitted into the density map. The density in the region of the constant domain of the Fab was not sufficiently ordered to allow accurate building of an atomic model; therefore, only the variable domain was included in the final model. Once the variable domain was rebuilt into the density, it was copied into the second site and manually adjusted. MA helices, which were not included in the α4β2 structure, were built *de novo*, and M4 helices, which are continuous with MA, were rebuilt into the map. Well-ordered N-linked glycans were built along the surface of the ECD. In many cases, density for these glycans was clearer in a 6 Å low-pass filtered map (Fig. III.6C-D), and this map was used to assist building. Likewise, the water molecule in the ligand-binding pocket was apparent in the full map but showed stronger density in a 5 Å high-pass filtered map, which was used for accurate placement of this water. A portion of the M3-M4 loop (including the BRI: fusion protein) in both subunits was unresolved and the following residues were not modeled: 328-409 in α3 and 329-399 in β4. Additionally, residues 1-3 were not modeled in chain C (β4) due to weak density. After manual building in Coot, global real space coordinate and B-factor refinement were performed in Phenix (Adams et al., 2010).

Sequences used in alignments were retrieved from the UnitProtKB database (UniProt Consortium, 2018). Sequence alignments were made using PROMALS3D (Pei et al., 2008). Pore radius profiles and hydrophobicity plots were made using CHAP (Klesse et al., 2019). Structural figures were made using UCSF-Chimera and PyMOL (Schrodinger, LLC). Structural biology software packages were compiled by SBGrid (Morin et al., 2013).

Electrophysiology

Whole cell voltage-clamp recordings were made from cells transiently transfected with the constructs used in structural analysis. For the patch-clamp experiments, adherent HEK293S GnTI- cells were transiently transfected with pEZT-based plasmids 2-3 days before recording. Each 35 mm dish of cells was transfected with the DNA of α3 and β4 subunits in a 1:1 ratio. Upon transfection, cells were moved to 30°C. On the day of recording, cells were washed with bath solution, which contained (in mM): 140 NaCl, 2.4 KCl, 4 $MgCl_2$, 4 $CaCl_2$, 10 HEPES pH 7.3, and 10 glucose. Borosilicate pipettes were pulled and polished to a resistance of 2-4 MΩ. The pipette solution contained (in mM): 150 CsCl, 10 NaCl, 10 EGTA, and 20 HEPES pH 7.3. Cells were clamped at -75 mV. The recordings were made with an Axopatch 200B amplifier, sampled at 5 kHz, and low-pass filtered at 2 kHz using a Digidata 1440A (Molecular Devices) and analyzed with pClamp 10 software (Molecular Devices). The nicotine and AT-1001 solutions were prepared in bath solution from concentrated stocks. A stock solution of 1 M nicotine was prepared in water and the stock solution of 100 mM AT-1001 was prepared in DMSO. Solution exchange was achieved using a gravity driven RSC-200 rapid solution changer (Bio-Logic).

Cell-attached single channel recordings were made from cells 1-2 days post-transient transfection, following the same procedure for transfection as above. On the day of recording, cells were washed with bath solution containing (in mM): 142 KCl, 5.4 NaCl, 1.8 $CaCl_2$, 1.7 $MgCl_2$, and 10 HEPES pH 7.4 (adjusted with KOH) (Mukhtasimova et al., 2016). Borosilicate pipettes were pulled and polished to initial resistances of 8-12 MΩ. The pipette solution contained (in mM): 80 KF, 20 KCl, 40 potassium aspartate, 2 $MgCl_2$, 1 EGTA, 10

HEPES 7.4 (adjusted with KOH), and 0.05 nicotine (Mukhtasimova et al., 2016). Currents were recorded at 100 mV, sampled at 50 kHz, and filtered at 10 kHz.

For proteoliposome patch-clamp experiments, receptors were first affinity-purified in DDM/CHS, as described above. Soy polar lipids in chloroform (Avanti) were dried in a test tube under a stream of argon while rotating the tube to make a homogeneous lipid film. The lipid film was further dried under vacuum for 2 hours and resuspended to 10 mg/mL with TBS. To make uniform lipid vesicles, the lipid resuspension solution was sonicated for 15 min. Purified receptors (4 μg) were added into lipid vesicles in a protein to lipid mass ratio of 1:500 (w/w). The mixture was rotated at room temperature for 1 hour to allow the protein to incorporate into lipid vesicles. Detergent was removed by incubating with Bio-Beads SM-2 and the resultant liposomes were collected by ultracentrifugation, 4°C, 30 min at 186,000 g. The pellet was resuspended in 6 μL TBS buffer. 2 μL of the suspension was spotted on a glass coverslip, and then desiccated overnight under vacuum at 4°C. Desiccated liposomes were rehydrated with 5 μL of buffer (320 mM sucrose, 10 mM KCl, and 2 mM $MgCl_2$, 5 mM Hepes pH 8.0) for at least 2 hours at 4°C, and then used for patch-clamp recording. Channel activity of α3β4 was examined in excised liposome patches. Data were acquired at 70 mV at a sampling rate of 50 kHz with a 10 kHz filter. The bath solution contained (in mM): 200 KCl, 40 $MgCl_2$, 2 $CaCl_2$, and 5 HEPES pH 7.3. Pipettes were filled with the same bath solution and initial pipette resistances ranged from 4-8 MΩ. After a stable baseline was observed, 10 mM nicotine in bath solution was added to the bath to achieve a final concentration of ~0.5 mM.

Radioligand binding

Experiments to measure binding of [^{3}H]-epibatidine (PerkinElmer) to the α3β4 receptor were performed with protein purified in TBS with 1 mM DDM, 0.2 mM CHS, and 1 mM TCEP in the absence of agonists. The concentration of binding sites was 0.3 nM. For the binding experiments in the presence of Fab, Fab was added in large excess (1 μM). In addition to the receptor, the binding assay conditions included 20 mM Tris pH 7.4, 150 mM NaCl, 1 mM DDM, and 1 mg/mL streptavidin-YiSi scintillation proximity assay beads (SPA; GE Healthcare Life Sciences). Non-specific signal was determined in the presence of 1 mM [^{1}H]-nicotine. All data shown are from background-subtracted measurements. For radioligand competition experiments, binding site concentration was also 0.3 nM and the concentration of [^{3}H]-epibatidine was 1 nM.

Molecular dynamics simulations

Deposited coordinates for the cryo-electron microscopy structure of the α3β4 receptor bound to nicotine in nanodiscs were used as a starting model for molecular dynamics simulations. Nicotine and AT-1001 parameters were generated using STaGE (Lundborg and Lindahl, 2015), and virtual sites were added. Nicotine, CHS, and ions and water resolved in the channel pore were placed as in the deposited structure. To resolve instabilities observed in the partially resolved intracellular domain, 1-palmitoyl 2-oleoyl phosphatidylcholine (POPC) was docked using AutoDock Vina (Trott and Olson, 2010) in a 37.5 Å x 36 Å x 39.75 Å box surrounding the MA helical bundle. For simulations with AT-1001, the partial agonist was substituted for nicotine at both binding sites. The Amber99sb-ildn force field

(Lindorff-Larsen et al., 2010) was used to describe each protein, which was embedded in a bilayer of 300 POPC molecules modeled with Slipids-extended force field parameters (Jämbeck and Lyubartsev, 2012, Jämbeck and Lyubartsev, 2013). Each system was solvated in a cubic box using CHARMM-GUI (Jo et al., 2008, Wu et al., 2014) and the TIP3P water model (Jorgensen et al., 1983), and NaCl was added to bring the system to neutral charge and an ionic strength of 0.15 M.

All simulations were performed with GROMACS 2018 (Abraham et al., 2015). Each system was energy-minimized with a velocity rescaling thermostat (Bussi et al., 2007) set to 300 K, then equilibrated for 50 ps, both with a constant number of particles, volume, and temperature. Virtual interaction sites were used for hydrogens to enable 5-fs time steps. Each was then equilibrated with a constant number of particles, pressure, and temperature for at least 60 ns, during which the position restraints on the protein were gradually released. Agonists, CHS, and resolved ions and water in the channel pore were restrained until the final 15 ns of equilibration. For each equilibrated system containing POPC in the intracellular domain, three replicates of 500-ns unrestrained simulations were generated. An additional 200-ns unrestrained simulation was performed for the nicotine-bound model in the absence of intracellular POPC. Parrinello-Rahman pressure coupling (Parrinello and Rahman, 1980) ensured constant pressure, the particle mesh Ewald algorithm (Essmann et al., 1995) was used for long-range electrostatic interactions, and bond lengths were constrained using the LINCS algorithm (Hess, 2008). Analyses were performed using VMD (Humphrey et al., 1996), CHAP, and MDTraj (McGibbon et al., 2015).

Quantification and statistical analysis

Statistical analyses were performed using Prism 8 (GraphPad). To quantify differences in single channel currents between EM and mutant constructs, mean and standard deviations were calculated from three independent patches for each group. Statistical significance was determined with an unpaired t-test. To quantify differences in binding affinities and hill slopes, each set of binding reaction experiments was performed three to five times. For each independent experiment, measurements were taken in triplicate. From these triplicate measurements, mean and standard error were calculated, and K_d and n_H values were determined by nonlinear regression. For competition experiments, IC_{50} and n_H values were determined by nonlinear regression and K_i values were calculated using experimental K_d values for [^{3}H]-epibatidine. Statistical significance between +Fab and -Fab groups was determined with unpaired t-tests.

Data and code availability

The structures and EM density maps generated in this study are available in the PDB and EMDB respectively. The accession numbers for the reported data are PDB: 6PV7, EMDB: EMD-20487 ($\alpha3\beta4_{EM}$-Nicotine complex); PDB: 6PV8, EMDB: EMD-20488 ($\alpha3\beta4_{EM}$-AT-1001 complex in DDM); EMDB: EMD-20489 ($\alpha3\beta4_{EM}$-Nicotine complex without CHS); EMDB: EMD-20490 ($\alpha3\beta4_{EM}$-AT-1001 complex in nanodiscs).

CHAPTER FOUR

Discussion of available nicotinic receptor structures

(Modified from Gharpure A, Noviello CM, Hibbs RE. "Progress in nicotinic receptor structural biology." *Neuropharmacology* 2020:171:108086.)

With the determination of the aforementioned structures of the α3β4 subtype, there is now high-resolution structural information available for three distinct species of neuronal nicotinic receptors, including the two stoichiometries of α4β2. Together, these structures allow for an initial examination of shared characteristics of the nicotinic receptor family, as well as the idiosyncratic features that give individual subtypes their unique functional properties. In this chapter, I will discuss these commonalities and differences, as well as invoke studies on other Cys-loop receptors in an attempt to fill in the gaps left by the available nicotinic receptor structures.

Global architecture of heteromeric assemblies

The overall topology of nicotinic receptor subunits is consistent with that of other Cys-loop receptors (Fig. IV.1). Following an N-terminal α-helix, the extracellular domain folds as a β-sandwich comprising ten β-strands (β1-β10). Between strands β6 and β7 lies the Cys-loop, from which the superfamily derives its name. This loop, which has been implicated in transducing the signal from agonist binding to channel opening, comprises 13 amino acids flanked by a pair of disulfide-bonded cysteine residues. These cysteines are absent in the

prokaryotic orthologs, but the architecture of the loop is the same. The transmembrane domain consists of four α-helices (M1-M4) arranged in a pseudo-rhombic bundle. The M2 helices are situated proximally to the central axis and line the channel pore, while the M4 helices are most distal and lipid-exposed, leading to a proposed role as a lipid sensor (Henault et al., 2015). The M3 and M4 helices are connected by a cytoplasmic substructure that constitutes the intracellular domain. This domain contains a stretch of ~10 residues known as the post-M3 loop, an amphipathic helix, MX, that rests at the interface between the plasma membrane and cytosol, and an intracellular helix, MA, that feeds directly into M4. The MX and MA helices are connected by a poorly conserved and disordered loop, ranging in length from 78-259 amino acids. Receptor constructs used for structure determination of both α4β2 and α3β4 subtypes utilized deletions in this region to promote biochemical stability. However, these construct modifications did not significantly alter protein function and structures of related Cys-loop receptors (Basak et al., 2018a, Basak et al., 2018b, Polovinkin et al., 2018) show no clear density corresponding to this region, so these structures are not expected to deviate significantly from full-length proteins. Crystallization of the α4β2 receptor required a more aggressive deletion that removed most of the MA helix. Subsequent EM studies of this subtype used the same constructs; thus, high-resolution structural information on this portion of the intracellular domain is only available from the α3β4 receptor.

Despite these differences in the intracellular loop, nicotine-bound structures of α4β2 (Walsh et al., 2018) and α3β4 (Gharpure et al., 2019) are remarkably similar. Superposition of the two models reveals that the root mean square deviation (rmsd) for the Cα atoms in the

full pentamers is only 1.1 Å. Individual α subunits have rmsd values of about 0.9 Å, whereas values for β subunits range from 0.9 to 1.4 Å. This high conservation of backbone positioning is perhaps unsurprising as the two subtypes share high sequence identity (67% between α3 and α4, 65% between β2 and β4). The remaining two principal subunits in neuronal nicotinic receptors for which there is currently no structural information also share high sequence identity with α3 and α4 (α2:α3, 57%; α2:α4, 70%; α6:α3, 65%; α6:α4, 54%). It is therefore likely that they will also adopt a tertiary structure similar to the observed α subunits, suggesting that differences in functional properties between various subtypes may be governed by local differences in key regions of the protein, as will be discussed later, rather than by large-scale rearrangements.

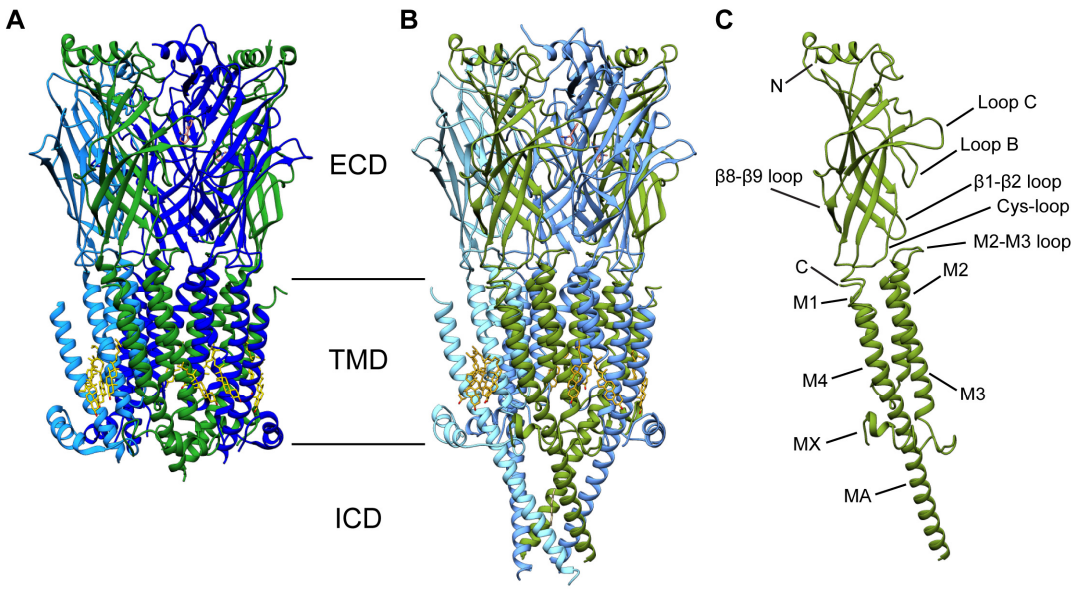

Fig. IV.1 Nicotinic receptor architecture
(A) Cryo-EM structure of the α4β2 subtype (PDB: 6CNJ). α4 subunits are in green, β2 subunits in blue, nicotine in salmon, and CHS in gold. (B) Cryo-EM structure of the α3β4 subtype (PDB:6PV7). α3 subunits are in green, β4 subunits in blue, nicotine in salmon, and CHS in gold. (C) Architecture of an α subunit, with key regions labeled.

The α4β2 and α3β4 subtype structures further helped probe the nature of heteromeric assemblies. The elucidation of both expected stoichiometries of the α4β2 receptor was particularly enlightening, as it provided direct structural information on all possible interface classes. Using this information, Walsh and Roh *et al*. sought to understand why formation of 2α:3β and 3α:2β receptors were more favorable than other possible stoichiometries. Analysis of these structures revealed that α-α interfaces buried the most protein surface area and β-β buried the least, with α-β and β-α intermediate. These differences resulted in varying interfacial angles between subunits and suggested that optimal packing in a pentamer only permitted the presence of one α-α or β-β interface. More specifically, hypothetical pentamers containing four or five α4 subunits would incur significant clashes, while pentamers containing four or five β4 subunits would result in an incomplete pentamer with a substantial gap. In reality, formation of these aberrant stoichiometric assemblies would likely involve some compensatory rearrangement in order to avoid such clashes or gaps. However, these structural changes may prove to be too energetically costly to allow for efficient production of these stoichiometries. Preferential formation of 2α:3β and 3α:2β assemblies is probably important physiologically as well, as it only allows for a receptor population with two high-affinity neurotransmitter binding sites per pentamer at either α-β interface.

Neurotransmitter-binding site

High-resolution structural information for the orthosteric binding site has been of interest from a basic-science perspective and as a rational framework for developing improved therapeutics for drug addiction, schizophrenia, and cognitive and

neurodegenerative disorders (Hogg and Bertrand, 2004, Lloyd and Williams, 2000). The considerable diversity of nicotinic receptors poses a conceptual challenge for drugability of this site, as different subtypes play diverse physiological roles throughout the nervous system, increasing the risk of potential side effects. Although residues lining the ligand-binding pocket are well conserved, differences in the pharmacological properties between subtypes suggest subtle structural changes, thus emphasizing the need for structures from numerous members of the family. Studies on agonist-bound complexes of α4β2 and α3β4 have begun to reveal the extensive similarities in different classes of ligand-binding sites, as well as the minor rearrangements that give rise to varying functional properties.

The neurotransmitter-binding site of nicotinic receptors is located in the extracellular domain at the interface between a principal (+) and a complementary (-) subunit and is encompassed by six canonical loops designated A-F (Fig. IV.2A). The principal face of the pocket, which must be contributed by an α subunit, contains loops A, B, and C, while the complementary face provides loops D, E, and F. In the available agonist-bound structures, residues on loops A-E directly contact the ligand whereas loop F potentially plays a scaffolding role in shaping the pocket. The hallmark feature of the binding site is loop C with its characteristic vicinal disulfide at the tip. This loop undergoes a large conformational change upon agonist binding, wherein it tightly caps the neurotransmitter site and makes direct interactions with agonists (Hansen et al., 2005). The core of the pocket is defined by a cage of five highly conserved aromatic residues on loops A-D, which stabilize agonists through hydrophobic and cation-π interactions. Notable among these is the tryptophan on loop B. This residue lines the back wall of the binding pocket and makes essential cation-π

and hydrogen bonding interactions with a basic nitrogen on the ligand (Xiu et al., 2009), a nearly strictly-conserved pharmacophore of nicotinic receptor agonists (Beers and Reich, 1970, Glennon and Dukat, 2000, Camacho-Hernandez et al., 2019). Another common, although less essential pharmacophore, is a hydrogen bond acceptor (Blum et al., 2010) that interacts with mainchain atoms on loop E at the top of the binding site. In nicotine complexes, this interaction is indirect and mediated by a water molecule that serves as a hydrogen bonding bridge. Density for this water is likely resolution-limited and thus only seen in the highest-resolution α3β4 structure, but related structures of AChBP (Celie et al., 2004) and mutagenesis studies in α4β2 (Blum et al., 2010) suggest its presence in this subtype as well. Residues on loop E whose sidechains are in close proximity to the ligand are not well conserved, and this variability may contribute to affinity differences at various interface classes (Fig. IV.2E).

Structures of both stoichiometries of α4β2 and the 2α:3β stoichiometry of α3β4 in complex with the same agonist (nicotine), allow for direct comparison of three distinct ligand-binding sites: α4-β2, α4-α4, and α3-β4. Among these, the α4-β2 site has the highest affinity for nicotine (Eaton et al., 2003, Xiao et al., 1998, Harpsoe et al., 2011, Mazzaferro et al., 2011). Structural deviations in the other two sites may provide insights into their lowered sensitivity to this and other classical nicotinic receptor agonists such as acetylcholine and epibatidine. The α4-α4 site shares its principal face with α4-β2 so substitutions on the complementary face are likely responsible for its weaker affinity (Harpsoe et al., 2011). Three hydrophobic residues on loop E of β2- V111, F119, and L121, are replaced with a histidine, glutamine, and threonine respectively in α4 (Shahsavar et al., 2015, Ahring et al.,

2015). The longer phenylalanine and leucine residues in β2 may optimally orient nicotine in the aromatic cage by providing a hydrophobic scaffold of van der Waals contacts. In contrast, the shorter and polar residues in these positions of α4 allow the pyridine ring of nicotine to tilt away from the core of the pocket toward the complementary face, in what may be a less favorable pose (Fig. IV.2B). Analysis of sequences of loop E in all subunits suggest that this difference in polarity may be a conserved distinction between α-β and α-α interfaces, as the hydrophobic nature of these residues in all β subunits is conserved, while most α subunits, including homomer-forming α7 and α9, contain at least one polar residue at these positions.

Consistent with this observation, the nicotine-binding site of α3-β4 looks similar to that of α4-β2, with nicotine assuming a similar orientation. The only two differences directly in the agonist-binding pocket are V111I and F119L substitutions. While hydrophobicity at these positions is maintained, the loss of the aromatic group of F119 may contribute to the lower affinity in the α3-β4 pocket by removing a potential π-stacking interaction with the pyridine ring of nicotine (Fig. IV.2C). Another intriguing hypothesis for the weaker sensitivity at this site relates to restructuring of loop C. In α3β4, this loop is located about 2.1 Å farther away from nicotine, potentially weakening van der Waals contacts with the ligand. This rearrangement may be explained by differences in loops C (E198N and A201E), D (T59K), and E (S113R and D115N) between the two subtypes. Together, these substitutions create a network of hydrogen bonds in α3β4 that cannot form in α4β2, potentially supporting loop C in the observed retracted position. The more spacious binding pocket of α3β4 may also explain the higher affinity of this subtype to larger agonists such as AT-1001 (Tuan et al., 2015). Importantly, these observations suggest that residues not in direct proximity to the

ligand may influence binding by structurally rearranging the pocket. This discovery further highlights the need for structures of more subtypes, as changes like these distinct conformations of loop C would not be easily predicted from sequence alignments.

These heteromeric structures also clarified why orthosteric ligands do not bind at β-α and β-β interfaces (Fig. IV.2D). Unique to canonical β subunits (β2 and β4) is an arginine in loop B, which is a glycine in all other neuronal nicotinic subunits. The bulkier sidechain of arginine settles at the bottom of the pocket, forcing a rearrangement of the surrounding aromatic cage. Two tyrosine residues on loops A and C rotate downward and upward respectively to accommodate and form cation-π interactions with the guanidinium group of arginine. The movement of the tyrosine on loop A forces the aforementioned tryptophan on loop B back and out of the binding pocket. This disruption of the aromatic cage, along with the shorter loop C of β subunits that would be unable to fully cap a putative ligand, likely explain why interfaces with β2 or β4 as the principal face are not conducive to neurotransmitter binding. Interfaces where β2 or β4 are the principal subunits remain of interest in development of allosteric modulators, with the strikingly different chemistry at these interfaces explaining why efforts building off the classical basic nitrogen pharmacophore have failed to hit these potential sites.

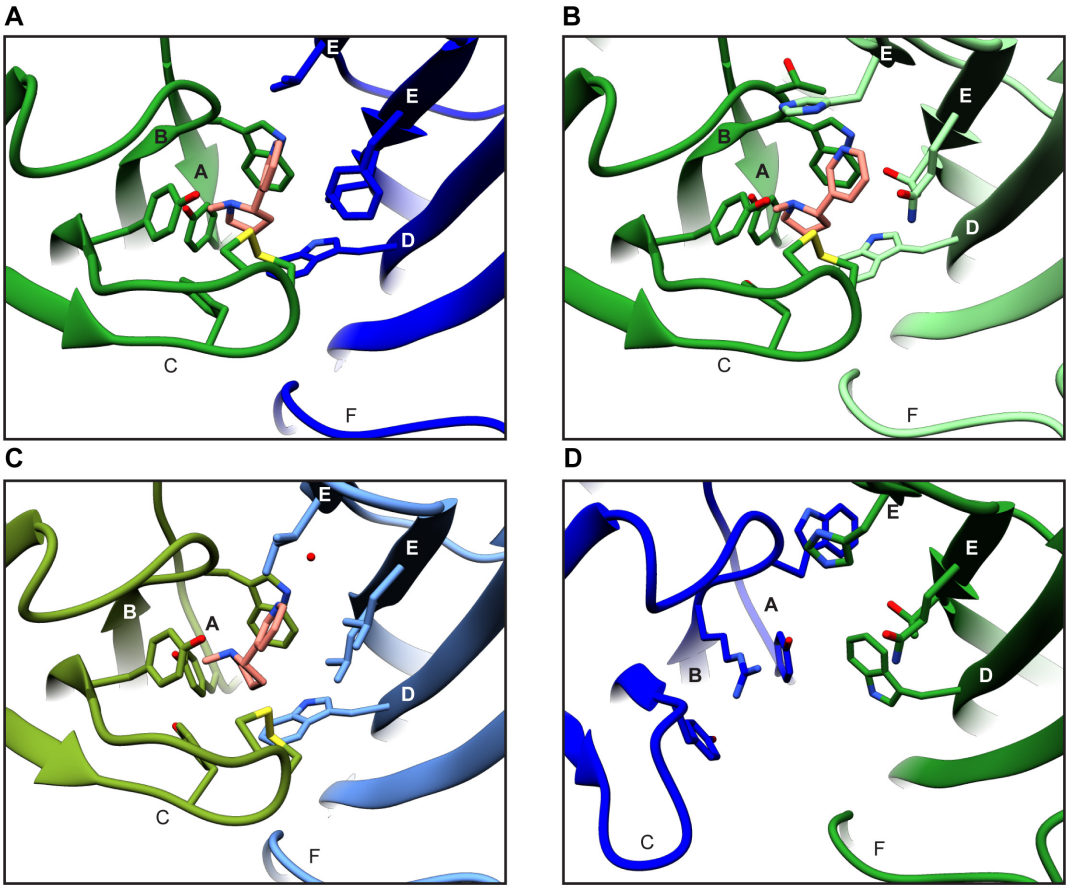

Fig. IV.2 Neurotransmitter-binding site of neuronal nicotinic receptors
(A) Binding of nicotine at the α4-β2 interface (PDB: 6CNJ). Loops A-F are labeled and residues contacting the ligand are shown as sticks. (B) Binding of nicotine at the α4-α4 interface (PDB: 6CNK). (C) Binding of nicotine at the α3-β4 interface (PDB: 6PV7). (D) Pseudo-agonist binding site at the β2-α4 interface (PDB: 6CNJ). (E) Sequence alignments of loops A-F in all human neuronal nicotinic receptor subunits. Bolded residues are shown as sticks in panels A-D. Residues comprising the aromatic cage and vicinal disulfide are highlighted in yellow. Variable residues in close proximity to the ligand on loop E are highlighted in magenta. Residues in β subunits that may preclude agonist binding on loop B are highlighted in orange.

Channel gating and pore conformation

The binding of agonists to orthosteric sites is coupled to a conformational change in the transmembrane domain ~50 Å away, resulting in the opening of an ion permeable pore and allowing for flux of cations across the membrane. A functional chimera of AChBP and the 5-HT_3 TMD (Bouzat et al., 2004), as well as structures of other Cys-loop receptors in multiple conformations (Du et al., 2015, Althoff et al., 2014, Sauguet et al., 2014, Basak et al., 2018a, Polovinkin et al., 2018) have implicated several key loops at the ECD-TMD interface to be important in this signal transduction. These include the β1-β2 loop, the β8-β9 loop, and the Cys-loop on the extracellular side and the pre-M1 linker and the M2-M3 loop in the transmembrane domain. From these other Cys-loop receptor structures, a potential mechanism for activation has begun to emerge. Binding of an agonist at the orthosteric site leads to the capping of loop C, as well as an "un-blooming" and counterclockwise twisting motion in the ECD. This tertiary change is accompanied by an outward movement of the M2-M3 loop which results in an outward twisting motion of the M2 helices and an iris-like opening of the pore (Nemecz et al., 2016).

The existing neuronal nicotinic receptor structures are all bound to agonists and adopt similar conformational states, presumably representing desensitized receptors, thus limiting insights into the specific molecular details of this process. However, they do show that key residues identified by functional studies are poised to communicate signals from the ECD to pore domain. These include an arginine on the pre-M1 loop (Lee and Sine, 2005, Purohit and Auerbach, 2007) and a proline on the M2-M3 loop (Lee et al., 2008) which interact with residues on the β1-β2 and Cys-loops, and a conserved "FPF" motif on the Cys-loop (Lee et

al., 2009, Alcaino et al., 2017) that forms substantial contacts with the pre-M1 loop and the extracellular end of the M1 helix (Fig. IV.3B).

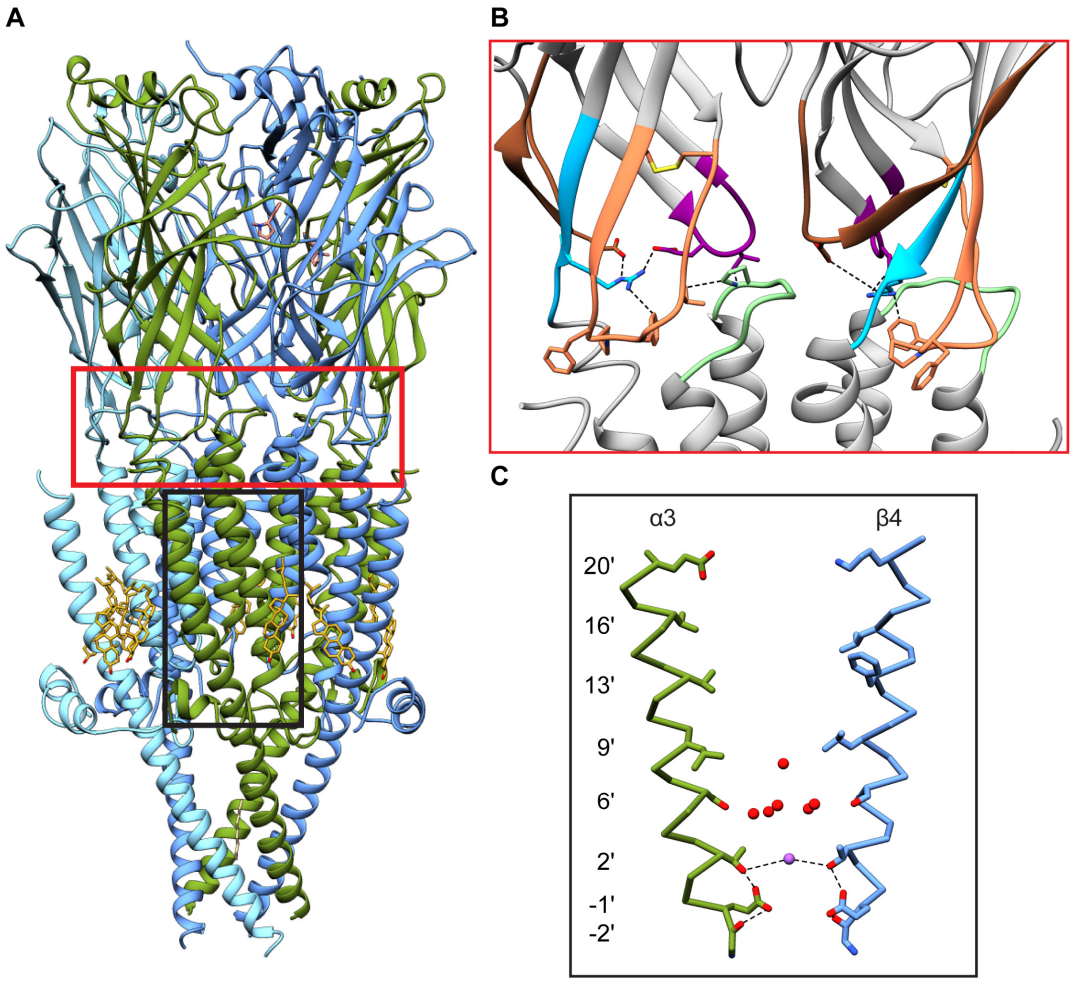

Fig. IV.3 Gating regions of the desensitized nicotinic receptor
(A) Overview of the α3β4 receptor in a putatively desensitized state. The red box highlights the hinge region, and the black box highlights the channel pore. (B) Closeup of the hinge region. The β1-β2 loop is shown in magenta, β8-β9 loop in brown, Cys-loop in orange, pre-M1 linker in blue, and M2-M3 linker in green. Key residues are shown as sticks. (C) Pore architecture. Representative M2 helices from an α3 and a β4 subunit are shown. Waters and sodium ions are shown as red and purple spheres respectively. Dashed lines indicate putative electrostatic interactions.

Upon prolonged exposure to agonists, nicotinic receptors will desensitize and enter one or more classes of non-conducting states (Katz and Thesleff, 1957, Feltz and Trautmann, 1982, Karlin, 2002). Decades of functional, biochemical, and structural data support the notion that the slow desensitized state is structurally distinct from the resting, or antagonist-bound state (Auerbach and Akk, 1998, Unwin et al., 1988, Purohit and Grosman, 2006, Wilson and Karlin, 2001, Keramidas and Lynch, 2013, Gielen and Corringer, 2018). In the resting state, the primary gate is formed by a hydrophobic constriction at the 9′ position on the pore-forming M2 helix near the midpoint of the membrane (Rahman et al., 2020). Mutation of the conserved leucine at this position to a polar residue alters fundamental channel properties of nicotinic receptors (Revah et al., 1991, Filatov and White, 1995, Labarca et al., 1995). Furthermore, structures of other Cys-loop receptors in conditions that would presumably favor the resting state show an impermeable constriction at 9′ (Basak et al., 2018b, Du et al., 2015, Masiulis et al., 2019, Polovinkin et al., 2018, Huang et al., 2015, Pan et al., 2012). In contrast, the consensus location for the desensitization gate is at the intracellular end of the pore (Gielen and Corringer, 2018). The available nicotinic receptor structures are consistent with this idea, with a minimum pore radius of ~1.7 Å formed by the sidechains of glutamates at the -1′ position (Fig. IV.3C).

It may be initially surprising to think of a gate for a cation-selective channel to be defined by acidic sidechains, as is suggested by the presumed desensitized-state nicotinic receptor structures. The negatively-charged carboxyl groups of the sidechains and their ability to adopt a variety of rotameric conformations (Cymes and Grosman, 2012, Harpole and Grosman, 2014) would appear to be conducive to ion flux, rather than forming a robust

obstruction. A gate formed by charged residues also contrasts with familiar hydrophobic gating mechanisms in voltage-gated and glutamate-gated channels, and with the hydrophobic resting-state gate likely conserved across the Cys-loop receptor superfamily (Twomey et al., 2017, Aryal et al., 2015). The highest-resolution nicotinic receptor structure of the α3β4 subtype provides some clues into this hypothetical ionic desensitization gate. In the α3β4 nicotinic receptor structure bound to nicotine, clear density was observed for all five -1′ glutamates, confirming that they position their sidechains, on average, toward the central pore axis. At first glance, this orientation appears energetically unfavorable, however nearby structural features allow for dispersal of the electrostatic potential. Density for a putative cation was observed near the 2′ position. This ion, modeled as Na^+, in conjunction with the hydroxyl groups on Thr2′ sidechains and backbone carbonyls of Gly-2′, may form a network of electrostatic interactions that stabilize the constriction-forming orientation of the -1′ sidechains (Fig. IV.3C). The positive charge of the sodium ion is likely important to counterbalance the concentrated negative charges from the glutamates and thus a divalent cation, such as calcium, may be even more effective in this role

I would be remiss to discuss the pore conformation of an ion channel without mentioning the membrane mimetic used for structural studies. Historically, purification and crystallization of membrane proteins typically required the use of detergents. Detergent micelles are capable of stabilizing transmembrane regions while maintaining solubility but are far from perfect substitutes for the natural lipid bilayer that encompasses membrane proteins. The advent of cryo-EM has allowed for structural studies in more native-like lipidic environments through the use of nanodisc technology. Nanodiscs are ~100-200 Å diameter

lipid bilayers that are rendered soluble through the use of amphipathic protein or polymer belts, (Denisov and Sligar, 2016, Frauenfeld et al., 2016, Knowles et al., 2009). Reconstitution into such lipidic environments is particularly important for nicotinic receptors, which have been shown to have a strong functional dependence on the surrounding lipid composition (Fong and McNamee, 1986, Epstein and Racker, 1978, Nelson et al., 1980, Lindstrom et al., 1980, McNamee et al., 1975). The absence of essential components, such as anionic lipids (daCosta et al., 2002) and cholesterol (Criado et al., 1982), can force nicotinic receptors into an uncoupled state where agonist binding is no longer coupled to conformational changes in the pore (daCosta and Baenziger, 2009).

To address the lipid issue, the study on the α3β4 subtype utilized a functional reconstitution approach where a lipid mixture that was shown to support channel activity was used for structure determination. Importantly, the selected lipids included phosphatidic acid, a common anionic lipid, and the sample was supplemented with cholesteryl hemisuccinate (CHS), a soluble cholesterol analog. In this study, another agonist-bound complex was determined in detergent (dodecylmaltoside) micelles, also supplemented with CHS, allowing for direct comparison of detergent- and nanodisc- bound structures. The pore architectures of the two complexes are remarkably similar, resembling the observed conformations of the α4β2 structures, also in detergent. Furthermore, there are not substantial structural differences in M4, which has been proposed to play a role as a lipid sensor through putative interactions with surrounding lipids and the Cys-loop (Henault et al., 2015). Densities corresponding to CHS are seen along the periphery of the TMD in both detergent and nanodisc structures, supporting and more clearly defining the presence of cholesterol binding

sites (Hamouda et al., 2006, Corbin et al., 1998), but do not clearly explain the lipid dependence of nicotinic receptors. It is possible that lipids may be more influential in stabilizing the open state, and structural information on an open channel may reveal other important lipid-binding sites. Obtaining nicotinic receptor structures in additional conformational states is essential in understanding the mechanism of allosteric gating and should shed light on how differences in lipid composition affect the gating process.

Intracellular domain

The cytoplasmic portion of nicotinic receptors provides an interface for communication with the cellular milieu. As such, this domain is the site of post-translational modifications and protein-protein interactions, which can modulate cellular trafficking and channel properties (Stokes et al., 2015, Paulo et al., 2009, Williams et al., 2005, Williams et al., 1998, Talwar and Lynch, 2014, Swope et al., 1999). Besides the amphipathic MX and intracellular MA helices, the M3-M4 substructure or "loop" is largely disordered, frustrating efforts to understand the structural bases underlying these processes. The intracellular domain also contributes to ion permeation by providing an exit pathway for cations in the cytosol. This function appears to be primarily facilitated by the MA helices, and structures of the α3β4 receptor have shed light on how the chemical environment of this region may affect channel conductance.

The five MA helices converge to form a narrow constriction at the bottom (cytosolic extremity) of the receptor (Fig. IV.4A). This constriction has a diameter of ~5.4 Å, which would be large enough to permit the passage of a hydrated sodium ion. However, this axial

pathway is highly hydrophobic in nature, with several conserved rings of aliphatic residues lining the central axis of the ICD. Interestingly, a strong density, probably corresponding to the hydrocarbon tail of a lipid or detergent molecule, was observed in this hydrophobic patch, indicating that a physical obstruction may also prevent ion flux through the bottom tip of the receptor. Instead, early structural studies from Unwin (Miyazawa et al., 1999), and work on the 5-HT_3 receptor (Kelley et al., 2003, Hales et al., 2006), suggested that cations are likely to diffuse into the cytosol through the five lateral portals located at the interface of MA helices. These portals contain fenestrations in the α3β4 receptor of about ~6 Å diameter and are primarily surrounded by acidic and other polar sidechains, making them ideal cation exit pathways (Fig. IV.4). The high concentration of negatively charged residues in this region has been shown to influence channel conductance. In the α3β4 study, acidic residues whose sidechains lined the portals were mutated to lysines, thereby decreasing the electronegativity of the fenestrations. The mutant receptor yielded significantly reduced single-channel currents than WT receptors, confirming that the electronegative nature of the portals plays a key role in ion permeation.

Structural studies on the 5-HT_3 receptor have suggested that the ICD may also contribute to pentameric assembly (Pandhare et al., 2019) as well as channel gating. Structures of this receptor in a putative open conformation suggest that the MA helices may develop a kink or even become disordered in the open state (Basak et al., 2018a, Polovinkin et al., 2018). It is not immediately clear why such drastic conformational changes would be necessary in a conductive state, as the fenestrations seen in the putative desensitized conformations are large enough to accommodate hydrated ions. Nevertheless, structures of

nicotinic receptors in alternative conformations will be helpful in visualizing potential roles of the ICD in channel gating.

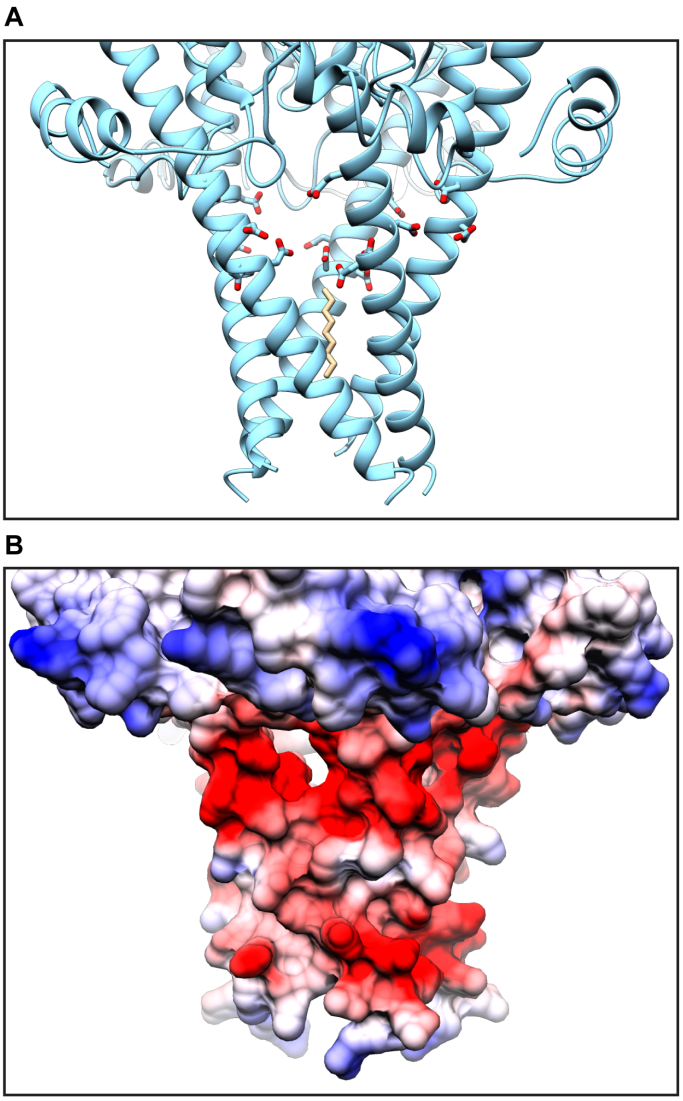

Fig. IV.4 Intracellular domain
(A) Side view of the α3β4 ICD. Acidic residues lining the portals are shown as sticks. The hydrophobic plug is shown in tan. (B) Side view shown as a surface colored by electrostatic potential.

Looking forward

Despite serving as the paradigm for ligand-gated ion channels for well over a century, the nicotinic acetylcholine receptor was one of the last families to be characterized structurally at high resolution. The recent series of structures of two neuronal nicotinic receptor subtypes have helped contextualize decades of functional and biochemical data and have laid groundwork for new insights into quaternary assembly, subtype-specific ligand selectivity, gating, and ion permeation. However, this work is merely the beginning of a new age of studies on nicotinic receptors- many unanswered questions remain that can be addressed structurally.

Structural information on other subtypes will be imperative in understanding the mechanisms governing their idiosyncratic properties. The muscle-type receptor and the homomeric α7 receptor are of utmost importance, considering their crucial roles in human physiology and disease (Kalamida et al., 2007, Lindstrom, 2000, Pohanka, 2012). The muscle-type receptor is perhaps the best characterized subtype and high-resolution structures of this receptor would allow for a direct interpretation of many historical studies. α7 displays several unique properties, including a high calcium permeability (Seguela et al., 1993, Castro and Albuquerque, 1995) and rapid desensitization (Peng et al., 1994). Other notable targets are subtypes containing accessory subunits, such as α5 and β3, as it is unclear whether or not these subunits contribute to neurotransmitter binding sites (Jain et al., 2016, Kuryatov et al., 2008, Groot-Kormelink et al., 2001). Structures of α5- and/or β3- containing pentamers would definitively clarify this issue and may also reveal a novel class of binding sites with potential for allosteric ligand binding akin to the benzodiazepine sites of $GABA_A$ receptors

(Sigel and Buhr, 1997, Kuryatov et al., 2008). Single-particle cryo-EM can also provide insights into the relative proportions of nicotinic receptor subtypes found in native tissues. Up until this point, the identification of receptor populations has relied on bulk measurement techniques such as in situ hybridization (Wada et al., 1989, Boulter et al., 1990), immunoprecipitation (Vernallis et al., 1993, Conroy and Berg, 1995), and immunohistochemistry (Graham et al., 2002). Isolation and cryo-EM analysis of receptors from native sources, as was done in a recent study on native AMPA receptors (Zhao et al., 2019), could help define the exact subunit composition and stoichiometries of native receptors. Finally, the pursuit of structures in other conformational states will be essential to fully understand the gating cycle of nicotinic receptors. While it is probable that the overall features of gating are likely broadly conserved throughout the Cys-loop receptor superfamily (Nemecz et al., 2016), many specific details are likely receptor-family and even subtype specific. Therefore, structures of nicotinic receptors in resting-like and open conformations will further help identify important regions involved in channel function.

CHAPTER FIVE

Concluding remarks- ongoing studies

Introduction

The determination of the structure of the α3β4 nicotinic acetylcholine receptor provided many insights into general and subtype-specific properties of nicotinic acetylcholine receptors, as detailed in chapters three and four. As is often the case in structural biology, this study also provided a blueprint to address further intriguing questions about this family of proteins. In this chapter, I will describe three projects that I have begun that are natural follow-up studies to my dissertation work. These projects seek to provide insight into the role of accessory subunits in α3β4-containing receptors, the effects of divalent cations on desensitization, and the contribution of the MA helices on cation selectivity and rectification in neuronal and muscle-type nicotinic receptors.

Results

Accessory subunits in α3β4-containing receptors

Accessory subunits, such as α5 and β3, are expected to co-assemble with α3 and β4 physiologically (Fig. V.1), although the extent to which this occurs is unclear (Conroy and Berg, 1995, Grady et al., 2009, Mao et al., 2006, Vernallis et al., 1993, Sheffield et al., 2000). The α5 subunit is of particular interest, as mutations in this subunit have been associated with increased risk of addiction (Saccone et al., 2007, Saccone et al., 2010, Sherva et al., 2010).

The functional influence of these subunits is also controversial, as in vitro studies on assemblies containing α5 and β3 have yielded conflicting results regarding effects on many functional properties, including maximal current, desensitization kinetics, calcium permeability, and ligand affinity (Frahm et al., 2011, Broadbent et al., 2006, Groot-Kormelink et al., 2001, George et al., 2012, Gerzanich et al., 1998, Boorman et al., 2003). Furthermore, it is uncertain whether these subunits can contribute to an orthosteric binding site or play a role in a modulatory allosteric site in the extracellular domain (Groot-Kormelink et al., 2001, Jain et al., 2016, Kuryatov et al., 2008). To provide some clarity to these outstanding questions concerning the α5 and β3 subunits, I wanted to purify a homogenous population of α3β4α5 and α3β4β3 receptors to study structurally and functionally. The data presented in this section was either carried out by myself, or by a summer high school student, Rahul Pentaparthi, and two junior graduate students, Dagimhiwat Legesse and Umang Goswami, under my supervision.

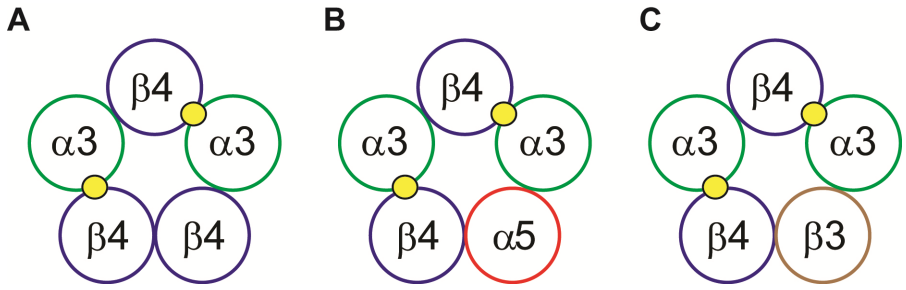

Fig. V.1 Accessory subunit incorporation
(A) α3β4 receptor with a 2α:3β stoichiometry (as in the previously determined receptor structure). Orthosteric ligand-binding sites are indicated as yellow circles. (B) α3β4α5 receptor with predicted subunit arrangement and stoichiometry. (C) α3β4β3 receptor with predicted subunit arrangement and stoichiometry.

To initially test for incorporation of α5 and β3 into α3β4-containing pentamers, I created α5-BFP and β3-BFP fusion constructs. Having already made α3-mCherry and β4-GFP fusion constructs, I now had three different fluorescent markers for the three subunits that would form accessory subunit-containing pentamers (α3β4α5 or α3β4β3). Using these constructs, I co-transfected α3 and β4 with either α5 or β3 in HEK293 cells. I already knew that α3 and β4 would preferentially form heteromers from earlier experiments and wanted to see if α5 and β3 would do the same, so I included controls of α5-BFP and β3-BFP transfected individually. After allowing 72 hours for expression and harvesting and solubilizing the cells, I tested the samples by FSEC. I found that α5 and β3 did appear to co-elute with α3 and β4, as a monodisperse peak in the BFP channel was seen at the same elution time as GFP and mCherry (Fig. V.2A-B). However, the individually transfected α5-BFP and β3-BFP genes also showed strong peaks in the pentamer region (Fig. V.2C-D), suggesting that there may be some homopentamer formation. This also raised the possibility that the peak seen in the BFP channel in the co-transfected samples may have been α5 or β3 homomers that were just the same size as α3-mCherry + β4-GFP heteromers.

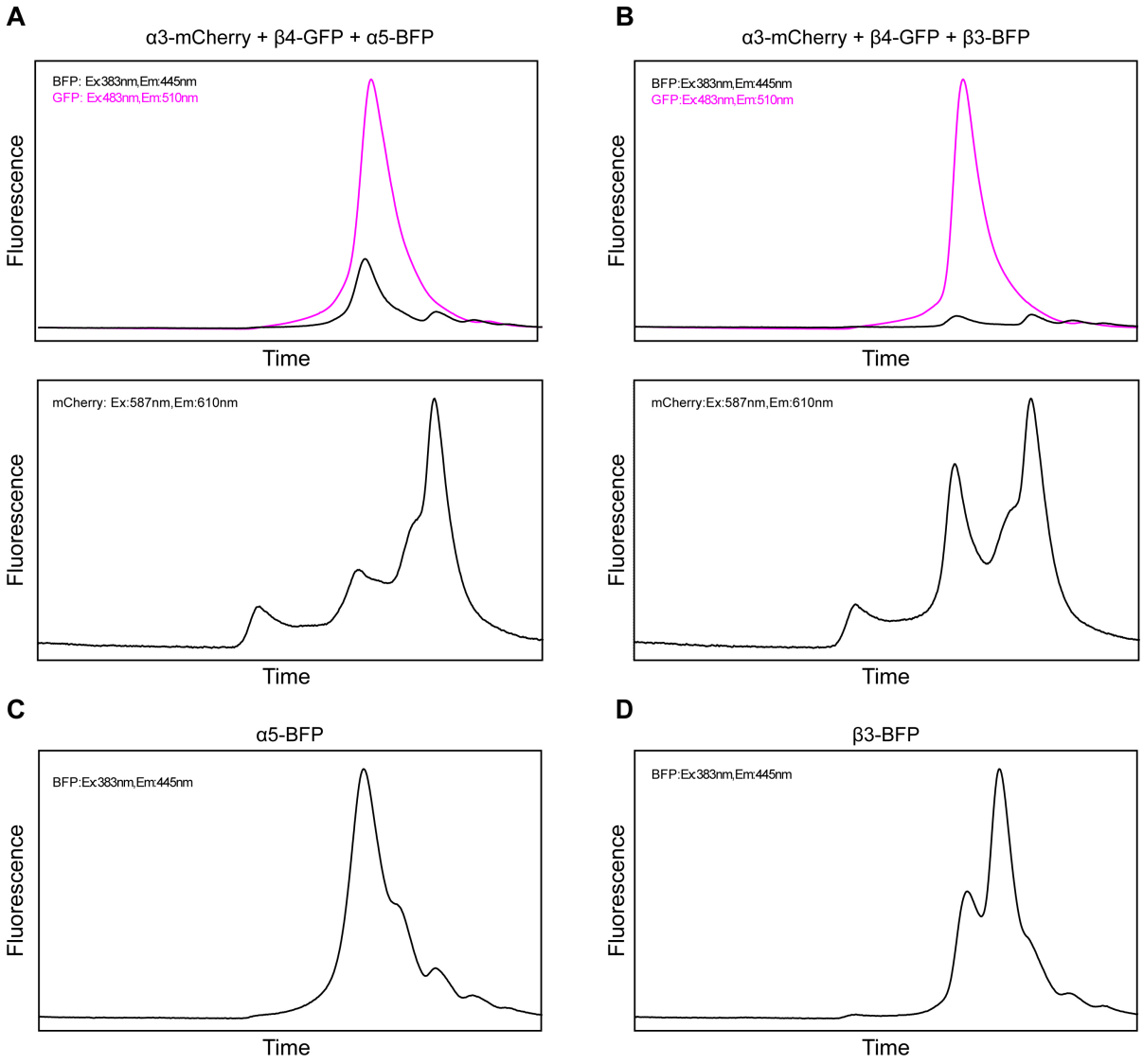

Fig. V.2 FSEC screening of α3β4α5 and α3β4β3

(A) FSEC traces of α3β4α5 co-transfection. Top graph shows BFP (α5) and GFP (β4) fluorescence; bottom graph shows mCherry (α3) fluorescence. (B) FSEC traces of α3β4β3 co-transfection. Top graph shows BFP (β3) and GFP (β4) fluorescence; bottom graph shows mCherry (α3) fluorescence. (C) FSEC trace of α5-BFP transfected alone. A pentamer-sized peak is clearly seen. (D) FSEC trace of β3-BFP transfected alone. The pentamer peak is less strong, but still present.

I had initially suspected that in a co-transfection of α3, β4, and α5/β3 subunits, there would be a significant population of just α3β4 receptors in addition to those containing accessory subunits. So, I had planned on putting an affinity tag on the accessory subunits, so that I could preferentially pull down α3β4α5 or α3β4β3 pentamers in affinity purification. The possibility of α5 and β3 homomers complicated the issue, as having an affinity tag on these subunits would result in purification of the triheteromeric assembly and any potential homomers of these subunits. This would have been problematic for crystallization and also potentially for radioligand-binding assays, so I devised a purification strategy that would utilize two affinity tags- one on β4, as was done for the α3β4 project, and a second tag on α5/β3. Since I had already put a strep-tag on β4, I added a His-tag to the accessory subunits. My plan was to first use a nickel-NTA column to enrich the sample for accessory subunit-containing receptors, and then do a second round of affinity purification to isolate the heteromeric assemblies containing β4 (and presumably α3 as well). However, the yields from these initial purifications were very low, suggesting that this was not an effective strategy for structural studies. The tradeoff between good yields and homogeneity of the sample would have made it difficult to pursue a crystal structure of one of these assemblies. Fortunately, the emergence of cryo-EM made this project more feasible. Sample heterogeneity can be computationally resolved through classification procedures, so any potential α5 or β3 homomers would be less problematic. Furthermore, I had already identified α3 recognizing antibodies, which could help separate heteromeric assemblies in size-exclusion steps.

Before I could move on to large-scale purifications, I had to modify the constructs for the accessory subunits to optimize biochemical behavior. In α3 and β4, I had to truncate the

M3-M4 loop and add an additional fusion partner into this region. The M3-M4 loops of α5 and β3 were much shorter than those of α3 and β4 and were of a similar length to the EM constructs I had generated. So, I decided to not make any deletions and instead just inserted BRIL into a similar place as was done for α3 and β4. Small-scale affinity purifications using an α5 subunit with BRIL inserted and a strep-tag at the C-terminus yielded a peak at the same elution time as α3β4, although the fluorescence intensity was substantially lower, and it was less monodisperse (Fig. V.3A). Additionally, after incubating the sample with the 4G9 Fab fragment I had used for structural studies of α3β4 (Fig. V.3B), I saw a substantial peak shift, indicating that the purified protein also contained α3 (and likely β4 as well) (Fig. V.3C).

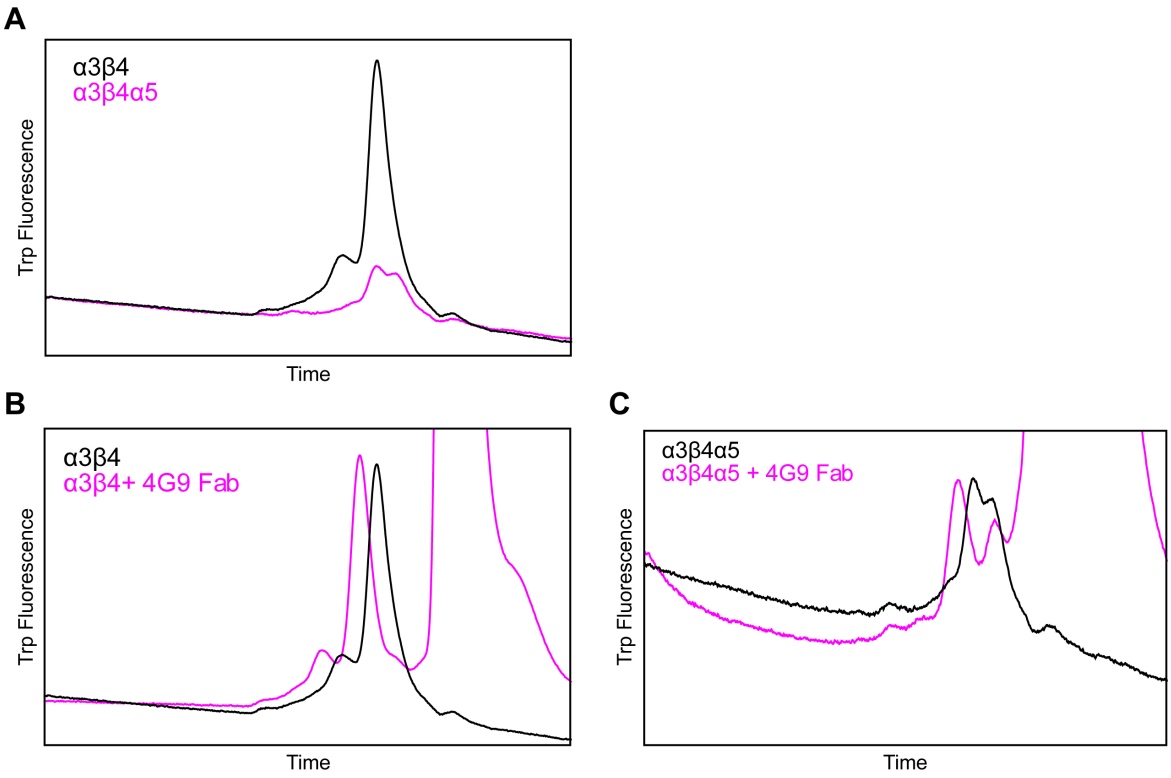

Fig. V.3 α3β4α5 small-scale purification and Fab test
(A) FSEC traces of purified α3β4 and α3β4α5. (B) FSEC trace of purified α3β4 before and after addition of 4G9 Fab. Pentamer peak shifts leftward after addition of Fab. (C) FSEC trace of purified α3β4α5 before and after addition of 4G9 Fab. Pentamer peak shifts leftward after addition of Fab.

I first wanted to collect a dataset of on the α3β4α5 assembly in detergent to get an initial sense of how the protein would look structurally. I was able to freeze grids of the protein in detergent and Dr. Noviello collected a small dataset on the Talos at UTSW. Initial data processing was not so promising, as the 2D classes did not show very clear density for the MA helices (Fig. V.4A), as seen in α3β4. This was reflected in the final 3D reconstruction, with just a ball of density for the ICD rather than clearly ordered helices (Fig. V.4B). As seen in α3β4 as well, the disordered ICD also resulted in an unclear TMD. The reconstruction had two Fabs bound (as would be expected in an assembly with a stoichiometry of (α3)2(β4)2(α5)1), and differences in loop C structure suggested that there was α5 incorporation into the pentamer. Loop C of α5 is shorter than that of α3 and also contains a predicted glycosylation site, which is what was seen in the location of the fifth subunit. Thus, although the sample was not as well-resolved as I would have hoped, the silver lining was that I was confident that I was expressing and purifying the correct stoichiometry.

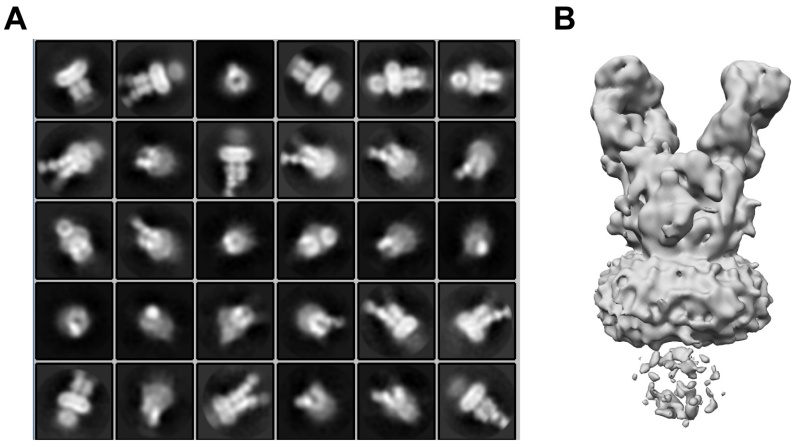

Fig. V.4 α3β4α5 EM dataset in detergent
(A) 2D classes of α3β4α5 in detergent. (B) 3D reconstruction from this dataset with disordered ICD.

One possible explanation for the disordered TMD/ICD could be the lack of lipids. Lipids have been shown to be essential for stabilization of heteromeric $GABA_A$ receptors (Zhu et al., 2018, Laverty et al., 2019, Masiulis et al., 2019), and α3β4α5 could have a similar dependency on the surrounding environment. So, I next decided to collect an EM dataset on this subtype in nanodiscs. Surprisingly, 2D classes from this dataset showed even weaker signal for the ICD (Fig. V.5A), and little density was observed in this region in the final 6.8 Å-resolution 3D reconstruction (Fig. V.5B). I was once again able to confirm that α5 was in the protein due to the different loop C size and shape (Fig. V.5C-F).

Moving forward, it may be necessary to go back to construct modification. It is possible that BRIL may be disturbing MA helix formation of α5 in a way that it did not for α3 or β4. Another possibility is that α5 subunits do not form well-ordered MA helices. This is very unlikely, however, due to the high sequence similarity in this region for nicotinic acetylcholine receptor subunits. Working with β3 may also prove to be more fruitful. Overall, this is a promising start to the project, as the α3β4α5 subtype looks to have good expression levels and purifies well, but further optimization will be required to get a high-resolution structure that will lend insights into the biophysical consequences of accessory subunit incorporation.

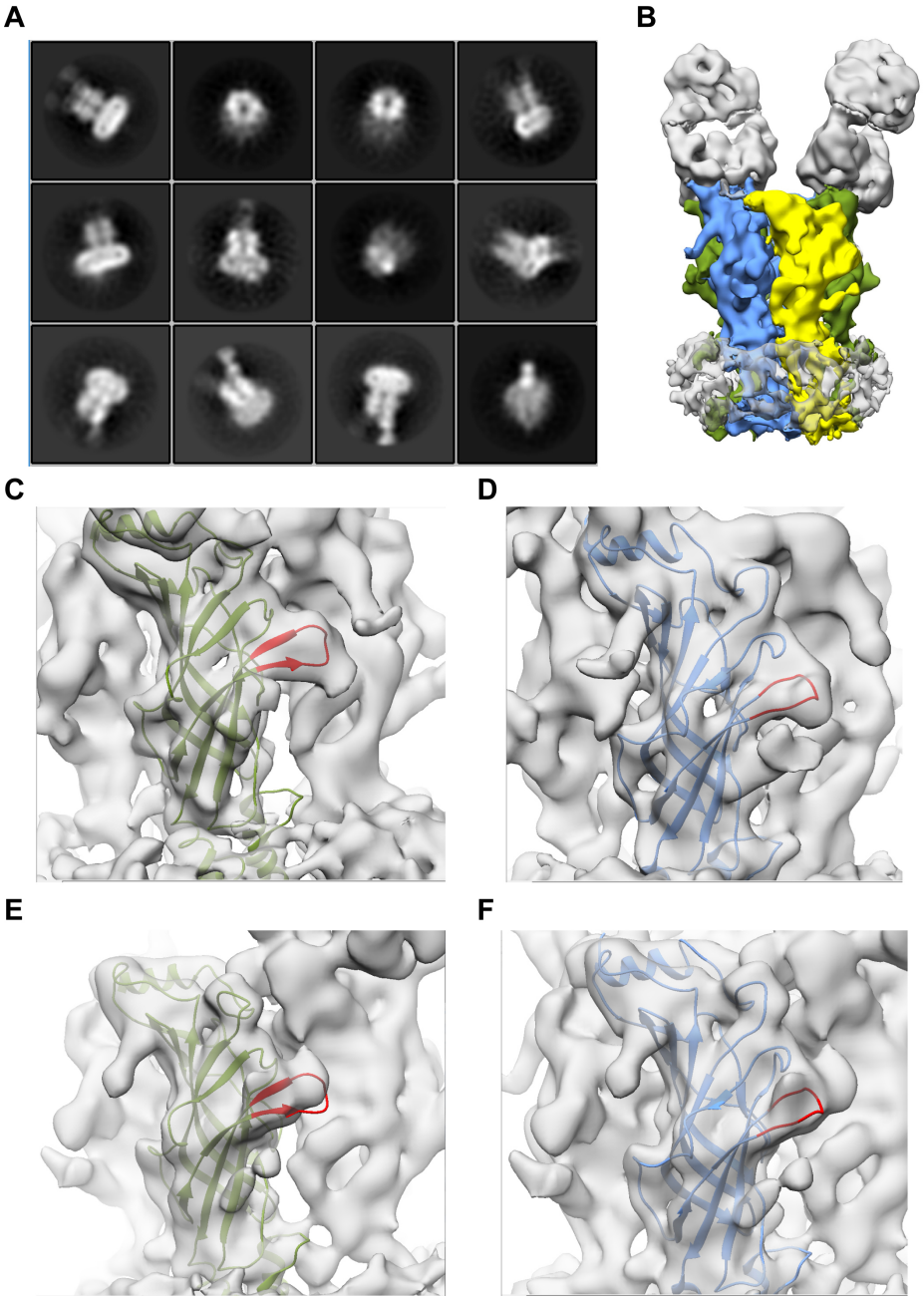

Fig. V.5 α3β4α5 EM dataset in nanodiscs

(A) 2D classes showing of α3β4α5 in nanodiscs. (B) 3D reconstruction colored by predicted subunit position. α3 is green, β4 is blue, and α5 is yellow. Density for the ICD is conspicuously absent. (C) α3 model (PDB:6PV7) docked into predicted α3 position. Loop C (shown in red) fits density well. (D) β4 model (PDB:6PV7) docked into predicted β4 position. Loop C (shown in red) fits density well. (E) α3 model (PDB:6PV7) docked into predicted α5 position. Loop C (shown in red) does not fit density well. (F) β4 model (PDB:6PV7) docked into predicted α5 position. Loop C (shown in red) does not fit density well.

Effects of calcium on desensitization

The structures of α3β4 provided some interesting insights into the pore conformation of desensitized nicotinic receptors. The desensitization gate of α3β4 was shown to be formed by the sidechains of glutamate residues at the -1′ position at the cytoplasmic end of the M2 helix. All of these glutamate residues are believed to be deprotonated at physiological pH's (Cymes and Grosman, 2012), creating a very high concentration of negative charges at this gate. A nearby axial density was modeled as a sodium ion and was used to explain the stabilization of the glutamate sidechains in this seemingly energetically unfavorable conformation. Because of the strong negative charge in this region, I wondered if multivalent cations might be better at stabilizing the desensitization gate. In support of this hypothesis, functional studies in the 60's and 70's on the neuromuscular junction showed that increasing concentrations of divalent and trivalent cations increased the desensitization rates of nicotinic receptors (Manthey, 1966, Magazanik and Vyskocil, 1970). It is also possible that this density may actually correspond to calcium in the experimental map. Trace amounts of calcium in buffers or contamination from blotting paper may have provided up to millimolar concentrations of calcium in the final sample and on the grid. To see if there were any distinguishable structural differences in the presence and absence of divalent cations and to rule out the possibility of the 2′ axial density corresponding to calcium in the original structure, I determined structures of α3β4 in the same conditions as the nicotine complex with added calcium or ethylene glycol tetraacetic acid (EGTA).

I first purified α3β4 in the presence of extra calcium in hopes of seeing additional or stronger densities in the pore corresponding to the divalent cation. The purification was

carried out using the same methods as detailed before, except I added 10 mM to the size-exclusion chromatography buffer. I was able to freeze grids at a final A280 of 8.3 and these grids were sent to the Pacific Northwest Center for Cryo-EM (PNCC) for data collection on a Titan Krios microscope equipped with a Falcon 3 direct electron detector. Over the course of 48 hours, 3559 images were collected. After processing this data, I produced a 4.0 Å map (Fig. V.6A-B). Although the resolution of this reconstruction was not exceptional, it did provide insights into differences in the pore. All densities that had previously been seen in the nicotine-complex were still clearly present in this map, including the putative cation density near the 2′ position (Fig. V.6C). There was another strong density seen below the selectivity filter glutamates that can almost certainly be attributed to calcium (Fig. V.6D). This density is probably not physiologically relevant, as it is located below the main constriction point of the channel. In the context of a cell, there would be a negative membrane potential pulling the calcium ion into the cytoplasm. Additionally, 10 mM calcium, specifically on the intracellular side, is an extremely high concentration that would not be seen in a cell. However, the presence of this density did lend some insight into the identity of the 2′ density. The main concern with potentially assigning that density as calcium was that it did not resemble a canonical calcium-binding site. Calcium-binding sites typically have a coordination number of 6-8, mostly from sidechain carboxylates and waters within 3 Å of the calcium atom (Pidcock and Moore, 2001). The 2′ density was surrounded by the hydroxyls of threonines that were all >4 Å away from the ion. The bottom density, which almost certainly represented a calcium ion was closest to the backbone carbonyls of Gly-2′, which were also >4 Å away. This suggested that non-canonical calcium binding sites were

possibly present in this region of the protein, and so the 2′ axial density could still correspond to a calcium ion.

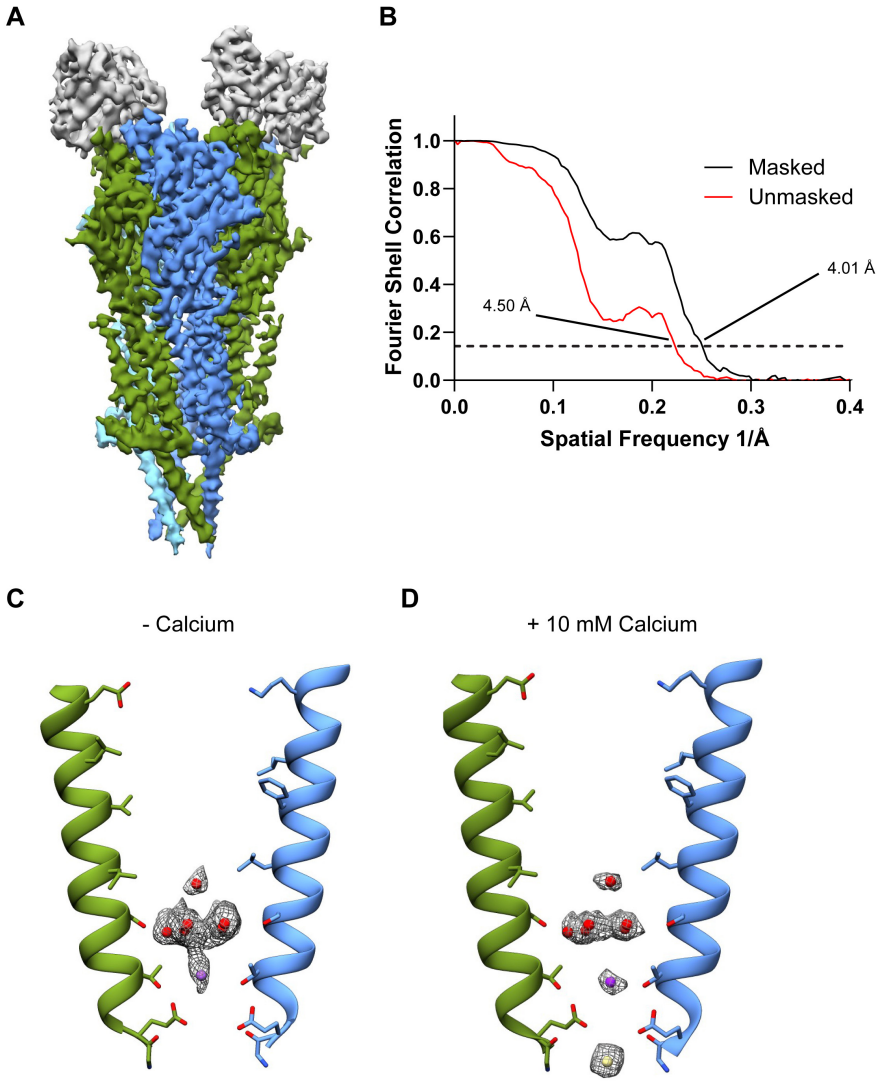

Fig. V.6 α3β4 map with 10 mM $CaCl_2$
(A) Map of α3β4 in saposin nanodiscs bound to nicotine with 10 mM $CaCl_2$ added to the sample colored by subunit. α3 is in green, β4 in blue, and Fab fragments are gray. (B) FSC plot of the final map, indicating a 4.01 Å resolution. (C) Densities corresponding to ions and waters in pore from 6PV7 (sample without added calcium). (D) Densities corresponding to ions and waters in pore in structure with added calcium.

To gain further insight into the possible presence of calcium in the original nicotine-complex structure, I collected a dataset in the presence of EGTA. In order to ensure that there would not be any contamination from calcium, I included 5 mM EGTA throughout the protein purification and also soaked the blotting papers for grid preparation in 2 mM EGTA (Miller et al., 2019). For this sample, I froze grids at an A280 of 7.4. 7308 images were collected from these grids at the PNCC on a Titan Krios equipped with a K3 camera and produced a 3.1 Å map (Fig. V.7A-B), allowing for an in-depth look at the densities within the pore. Interestingly, the axial density at the 2′ position was substantially weaker than had been seen in the original structure and in the structure with 10 mM calcium added (Fig. V.7C). However, density for the -1′ glutamate sidechains were still seen, even in a non-high-pass filtered map, in the same position as before. This result suggested that maybe a cation in this position is not necessary for stabilization of the glutamate sidechains in the "up" conformation to form the desensitization gate.

Overall, these structural experiments raise some doubts about the identity of the 2′ axial density and its role in stabilizing the desensitization gate. The fact that this density was less strong in the presence of EGTA suggests that it may at least partially be occupied by calcium. However, the weakening of this density did not result in a change in the sidechain conformation of the gate-forming glutamate sidechains. It would be nice to complement this structural work with functional experiments. Specifically, I would have like to have pulled outside-out patches from cells expressing α3β4 and looked at desensitization kinetics in the presence of varying concentrations of different divalent cations, effectively repeating the

initial experiments on the neuromuscular junction from a half-century ago in a more controlled, quantitative manner.

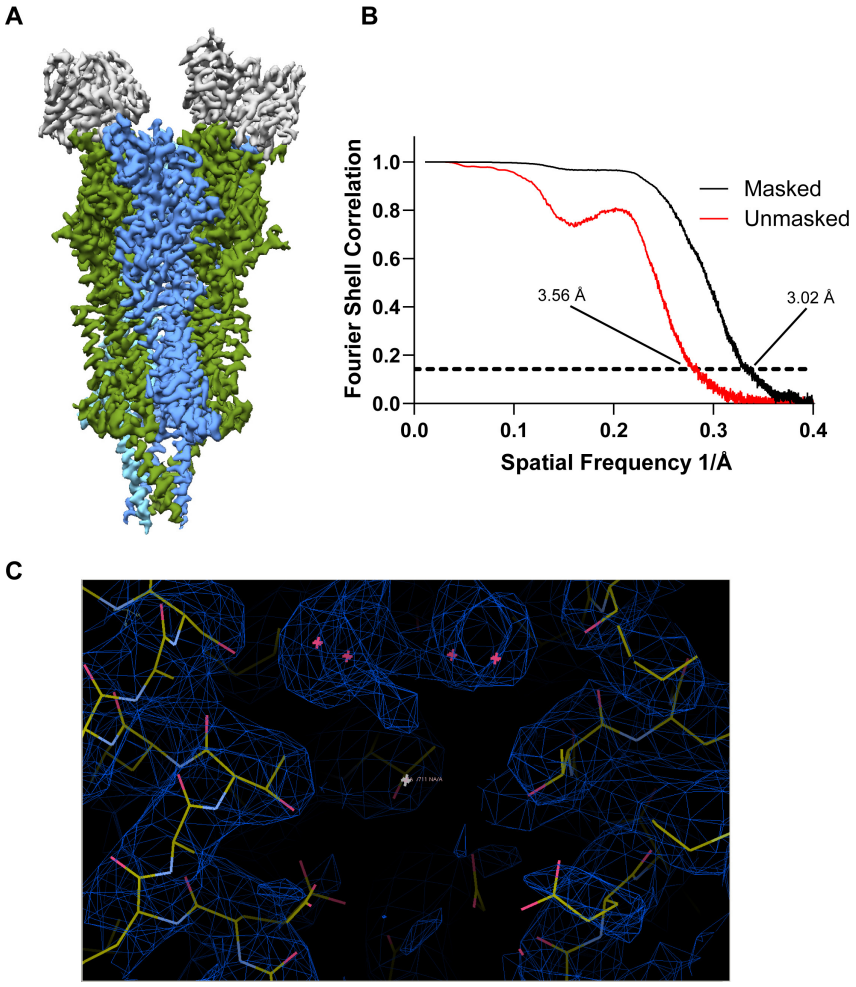

Fig. V.7 α3β4 map with EGTA
(A) Map of α3β4 in saposin nanodiscs bound to nicotine with 5 mM EGTA added to the sample colored by subunit. α3 is in green, β4 in blue, and Fab fragments are gray. (B) FSC plot of the final map, indicating a 3.02 Å resolution. (C) Density for the pore region and n6PV7 fitted into the map. Clear density is seen for pentagonal ring of waters (pink dots at top), and 2′ threonine sidechains (middle), but no density for bottom ion (gray) is visible.

Functional properties of the intracellular domain

As the exit pathway for cations entering the cell following activation of nicotinic receptors, the portals between the MA helices have the potential to modulate many functional properties of nicotinic receptors. Given the profound effect that the electronegativity of the MA helices was found to have on single-channel conductance in the initial study on α3β4, I also wondered if the chemical environment of this region would contribute to other channel properties. Specifically, I was interested in looking at the effects of mutations in portal-lining residues on cation vs. anion selectivity and inward rectification of nicotinic receptors.

Nicotinic acetylcholine receptors belong to the Cys-loop receptor superfamily, which is comprised of both cation-selective and anion-selective ion channels. Interestingly, the molecular determinants of this differential selectivity are not immediately obvious (Galzi et al., 1992, Keramidas et al., 2000, Hansen et al., 2008, Corringer et al., 1999, Cymes and Grosman, 2016). Although there are some trends in primary sequence for cation-selective and anion-selective channels, such as negatively charged residues at the -1′ position for excitatory channels, and an extra amino acid in the M1-M2 linker for inhibitory channels, these are not strictly conserved. Furthermore, mutations in these regions, such as the neutralization of -1′ glutamates in muscle-type nicotinic receptors, do not necessarily flip the selectivity of these receptors (Cymes and Grosman, 2016, Cymes and Grosman, 2012). Instead, a study on a number of different Cys-loop receptors showed that the effects of mutations on selectivity was context dependent and influenced by structural elements throughout the protein (Cymes and Grosman, 2016). In this study, it was shown that the presence of arginines in the MA helices of 5-HT_{3A} receptors rendered this channel very

sensitive to mutations at the -1′ position. I wondered if the “K mutant” I had made in the original α3β4 study would be more susceptible to anion-flux compared to α3β4 EM constructs in the context of wild-type and neutralized -1′ residues.

Another channel property that could potentially be influenced by a change in the chemical environment of the intracellular domain is rectification. I hypothesized that if the intracellular vestibule was less electronegative, as in the case of the “K mutant” (Fig. V.8), there would be a lower local concentration of cations in this region, thus decreasing outward cation flux at membrane potentials greater than the reversal potential for a given set of ionic conditions and resulting in inward rectification. Neuronal nicotinic receptors, such as α3β4 and α4β2, have been shown to inwardly rectify in whole-cell configurations (Haghighi and Cooper, 2000, Haghighi and Cooper, 1998). This is not believed to be an intrinsic property of the receptors themselves, but rather due to an intracellular voltage-dependent channel block from intracellular polyamines, such as spermine. I wanted to test whether or not the channels would become intrinsically rectifying in the case of the ICD mutant.

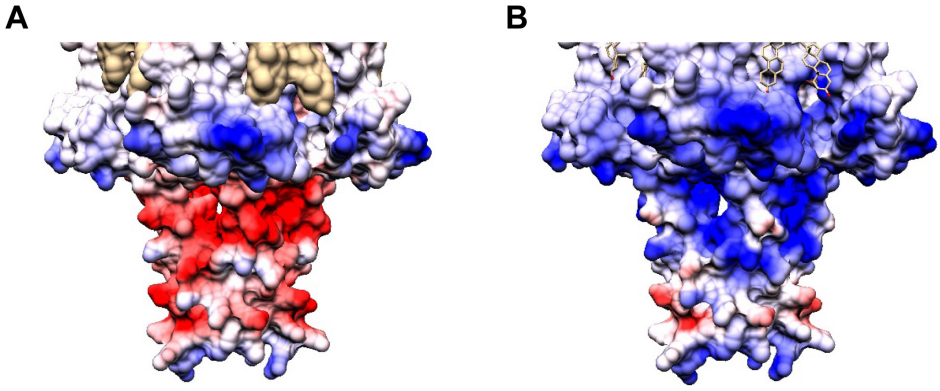

Fig. V.8 ICD electrostatic potential
Side views of the ordered portions of the ICD of α3β4 EM (A) and the K mutant (B) colored by electrostatic potential.

To answer both of these questions, I used whole-cell electrophysiology to measure current-voltage (I-V) relationships. In these experiments, the reversal potential would tell me about relative ion permeabilities by fitting to the Goldman-Hodgkin-Katz (GHK) equation ($V_{rev} = \frac{RT}{F} \ln(\frac{p_K [K^+]_o + p_{Cl} [Cl^-]_i}{p_K [K^+]_i + p_{Cl} [Cl^-]_o})$), and I would also be able to measure inward and outward currents, providing insight into any potential rectification. In order to avoid complications due to preferential selectivity of one cation over another, I decided to use intracellular and extracellular solutions consisting of only potassium and chloride. I set up a dilution experiment with 150 mM KCl in the pipet (intracellular) solution and 15 mM KCl in the bath (extracellular) solution, which would set the reversal potential for K^+ at -58 mV and the reversal potential for Cl^- at +58 mV, as determined by the GHK equation. I thought this would sidestep the issue of voltage-dependent polyamine block, as cation-selective channels would have very negative reversal potentials and thus, all recordings could be done at negative voltages. Initial experiments using these solutions were very frustrating, as it was very difficult to get good seals that would last throughout the long voltage-step recordings. After consulting the literature, I found that the inclusion of intracellular fluoride could help with seal formation in the absence of divalent cations, as was the case in these experiments. Thus, I replaced 40 mM of the intracellular KCl with KF under the assumption that fluoride was impermeable in pentameric ligand-gated ion channels (Cymes and Grosman, 2016, Fatima-Shad and Barry, 1993). With this new set of solutions (which consistently provided good gigaohm seals), the new reversal potential for chloride would be +50 mV, but the same principle would hold for determining selectivity- any deviation in the reversal potential for

the modified construct in the positive direction would suggest a relative increase in anion permeability.

With this experimental setup, I first tested α3β4 EM. I chose to work with EM constructs as opposed to wild type because I had created the "K mutants" in the context of the modified constructs, so these would allow me to make the most direct comparison. For each cell patched, I recorded at 10 different voltages starting at -100 mV with increasing voltage steps of 10 mV. In order to account for differences in cell size, ion channel expression, I normalized the maximal current values at each voltage to the maximal current at -100 mV for that cell. To my surprise, I found that even at negative voltages, there was substantial inward rectification, as the maximal outward current at -10 mV was only ~6% of the maximal inward current at -100 mV (Fig. V.9A). The resultant I-V curve was distinctly non-linear, thus making it difficult to accurately fit a line and determine a reversal potential (Fig. V.9B). My initial explanation for this phenomenon was that maybe the construct modifications, specifically the inclusion of BRIL near the intracellular vestibule created by the MA helices, may be blocking cations from exiting the cell. So, I decided to test wild type α3β4 as well. Again, I found that there was considerable rectification with the maximal outward current at only ~3% of the maximal inward current (Fig. V.10).

This rectification was therefore not an issue related to construct modification, but a general property of the intracellular polyamine block. I had originally predicted that this block would be strongly voltage dependent. Since spermine is expected to be positively charged at physiological pH, I assumed that at negative voltages, there would not be a strong driving force pulling the molecule through the channel of nicotinic receptors, causing the

channel block. What I failed to account for was the large concentration gradient. Because there is no extracellular spermine, the reversal potential for this molecule would be at -∞ and there would be outward "current" from spermine at any finite voltage. Because of this, working with α3β4 in a whole-cell configuration would not be ideal for the experiments I had planned.

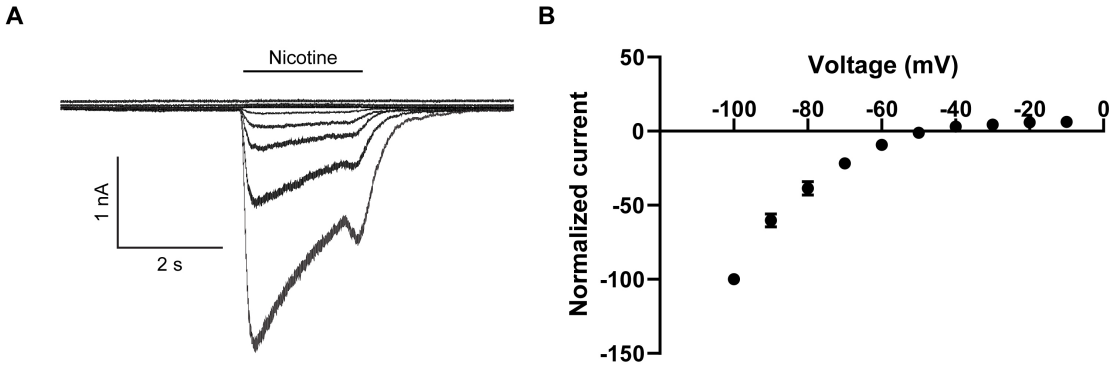

Fig. V.9 α3β4 EM current-voltage relationship
(A) Whole-cell responses at multiple voltages (-100 mV to -10 mV) for a representative cell transfected with α3β4 EM constructs. Little outward current is seen in comparison to inward current. (B) Current-voltage (I-V) relationship for all α3β4 EM data (n = 7).

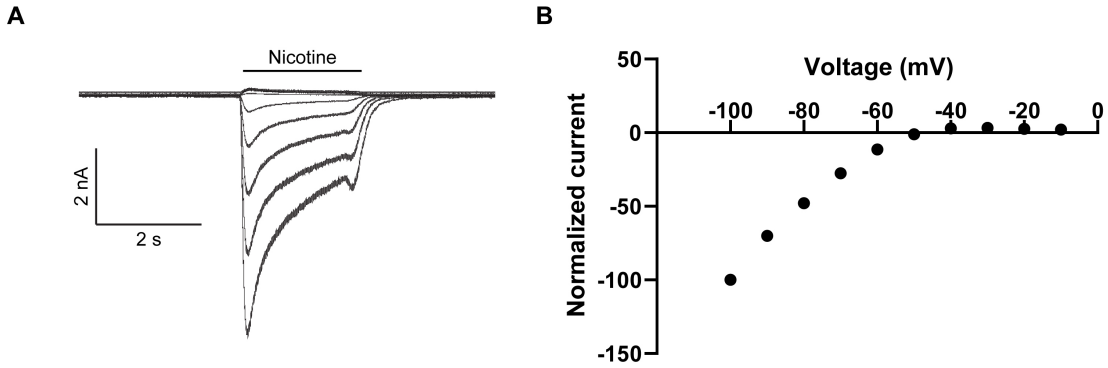

Fig. V.10 α3β4 WT current-voltage relationship
(A) Whole-cell responses at multiple voltages (-100 mV to -10 mV) for a representative cell transfected with α3β4 WT constructs. Little outward current is seen in comparison to inward current. (B) Current-voltage (I-V) relationship for all α3β4 WT data (n = 8).

Interestingly, it has been shown that muscle-type receptors do not show the same inward rectification due to polyamine block displayed by neuronal nicotinic receptors (Haghighi and Cooper, 2000). This might make muscle-type nicotinic receptors more useful for these potential experiments, as I would be able to calculate more accurate reversal potentials from these receptors. To confirm this property, I repeated the same experiments detailed before on mouse muscle receptors with a predicted subunit composition of $(\alpha 1)_2\beta 1\varepsilon\delta$. Here, I saw robust outward currents at voltages greater than -40 mV (Fig. V.11A). From this initial set of experiments, I was able to fit a linear regression and found that the reversal potential was roughly -42 mV (Fig. V.11B). Plugging this value and the known intracellular and extracellular ion concentrations into the GHK equation, I determined that the relative permeability of potassium to chloride (P_K/P_{Cl}) was about 8. This seemed exceptionally low, with reported values near 100 (Cymes and Grosman, 2016); however, these experiments were all done on the same day, so slight errors in salt concentrations in the solutions may have caused this abnormal value.

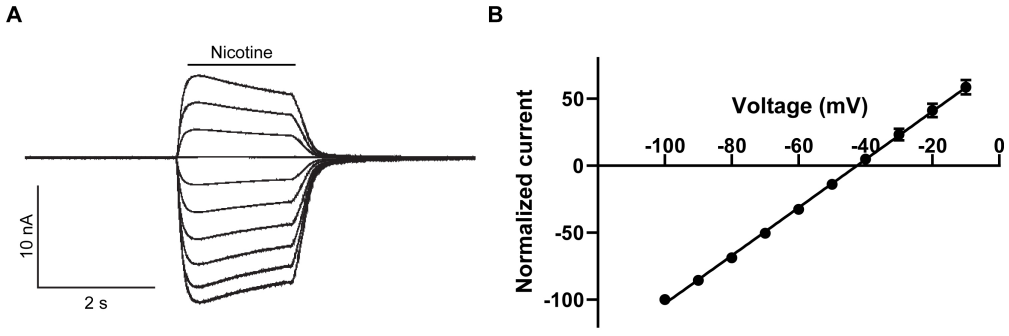

Fig. V.11 Mouse muscle-type receptor current-voltage relationship
(A) Whole-cell responses at multiple voltages (-100 mV to -10 mV) for a representative cell transfected with mouse muscle-type constructs. Large outward currents are seen in addition to inward currents. (B) Current-voltage (I-V) relationship for all mouse muscle data (n = 4).

Moving forward, I would probably want to repeat these experiments to increase the number of data points and account for errors in the solutions. However, muscle-type receptors would serve as a better model for these experiments due to the absence of polyamine-related intracellular block. To this end, I could use the recently determined structure of the Torpedo receptor (Rahman et al., 2020) as a template to design a "K mutant" for the muscle-type receptor. Otherwise, I could repeat the same experiments in outside-out patches using α3β4 under the assumption that these patches would have a greatly reduced (nearly 0) concentration of polyamines compared with the whole-cell configuration. An interesting note is that the molecular determinant for the inward rectification in neuronal receptors is the selectivity filter -1′ glutamates (Haghighi and Cooper, 2000). These were the same residues I had proposed to neutralize through a mutation to glutamine. With this neutralized mutation, I might still be able to test the effect of the ICD portals on selectivity if these mutants do not rectify. Another interesting note is that muscle-type receptors, in contrast to neuronal-type, have only four glutamates at the -1′ position, with the ε subunit having a glutamine in that position. This may potentially account for the lack of rectification in this subtype. It would also be interesting to see if a -1′ Q to E mutation in ε would result in polyamine block, suggesting that five glutamates are required at the selectivity filter to produce this effect.

Methods

Construct design

Human α5 (UniProtKB P30532) and β3 (Q05901) genes were codon optimized, synthesized, and cloned into the pEZT-BM expression vector (Morales-Perez et al., 2016a). Blue fluorescent protein (BFP) was inserted into the M3-M4 loop of both subunits. Constructs were initially screened via co-transfection of HEK293S GnTI$^-$ cells (ATCC CRL-3022) with combinations of fluorescently tagged α3 and β4 via Lipofectamine 2000 (Invitrogen). Cells were pelleted, solubilized with 20 mM Tris, pH 7.4, 150 mM NaCl (TBS buffer), 40 mM *n*-dodecyl-β-D-maltopyranoside (DDM; Anatrace), and 1 mM phenylmethanesulfonyl fluoride (PMSF; Sigma-Aldrich), and analyzed by fluorescence-detection size-exclusion chromatography (FSEC) (Kawate and Gouaux, 2006). Viable candidates without fluorescent fusion partners were then co-transfected in GnTI$^-$ cells in small-scale purification experiments (1-2 mL culture scale). Cells were pelleted, solubilized as before, and allowed to bind to high-capacity Strep-Tactin (IBA) affinity resin. Resin was washed with TBS containing 1 mM DDM, and protein was eluted with the same buffer supplemented with 5 mM desthiobiotin (Sigma-Aldrich) before being evaluated by FSEC monitoring tryptophan fluorescence.

Receptor expression and purification

Bacmam viruses for each subunit were produced as described above. Suspension cultures of GnTI$^-$ cells were grown at 37°C, 8% CO_2 and were transduced with requisite P2 viruses at a cell density of 4×10^6 cells/ml. At the time of transduction, 1 mM sodium

butyrate (Sigma-Aldrich) was added to the culture and temperature was dropped to 30°C to boost protein expression. After 72 hours, cells were harvested by centrifugation, resuspended in TBS and 1 mM PMSF, and disrupted using an Avestin Emulsiflex. Lysed cells were centrifuged for 20 minutes at 10,000 g, and the resulting supernatants were centrifuged for 2 hours at 186,000 g to isolate membranes. Membrane pellets were mechanically homogenized and solubilized for 1 hour at 4°C with 40 mM DDM in TBS. Solubilized membranes were centrifuged for 40 minutes at 186,000 g then passed over high capacity Strep-Tactin resin. The resin was washed with TBS, 1 mM DDM, 0.2 mM cholesteryl hemisuccinate (CHS, Anatrace), and 1 mM TCEP (Thermo Fisher Scientific), and protein was eluted in the same buffer containing 5 mM desthiobiotin. For the high calcium structure, 10 mM $CaCl_2$ was included throughout the preparation, and for the EGTA structure, 5 mM EGTA was included.

Saposin nanodisc reconstitution

Reconstitution of α3β4 into saposin nanodiscs was done as described above. The reaction contained a 1:20:100 molar ratio of α3β4: saposin: soy polar lipid extract (Avanti). Lipids and saposin were mixed in TBS and 14 mM DDM and allowed to rotate at 4°C for 1 hour. Affinity-purified α3β4 or α3βα5 was concentrated to ~20 μM, added to the saposin/lipid mixture, and rotated for 30 min at 4°C. 200 mg/mL Bio-Beads SM-2 (BioRad) were added to the mixture and rotation was continued overnight. The following morning, Bio-Beads were removed and replaced with 150 mg/mL fresh Bio-Beads for 2 hours.

Cryo-EM sample preparation and data collection

Affinity-purified α3β4 or α3β4α5 receptors reconstituted in nanodiscs were mixed with 4G9 Fab in a 1:1 (w/w) ratio and injected over a Superose 6 Increase 10/300 GL column (GE Healthcare) equilibrated in TBS, 1 mM TCEP, and 1 mM nicotine. In some cases, as described above, 10 mM $CaCl_2$ or 5 mM EGTA were also included in the SEC buffers. Receptors purified in detergent followed the same protocol, but the buffer included 1 mM DDM and 0.2 mM CHS. Peak fractions were evaluated by analytical SEC, monitoring tryptophan fluorescence, and concentrated to an A280 of ~6. Samples in nanodiscs were supplemented with 1 mM Fos-Choline-8, fluorinated (Anatrace) immediately prior to freezing to induce random orientations in the grid holes. Protein sample (3 μL) was applied to glow-discharged gold R1.2/1.3 300 mesh holey carbon grids (Quantifoil) and immediately blotted for 4 s at 100% humidity and 4°C before being plunge-frozen into liquid ethane cooled by liquid nitrogen using a Vitrobot Mark IV (FEI).

Cryo-EM data were collected on a 300 kV Titan Krios microscope (FEI) equipped with a K2 Summit direct electron detector (Gatan) and a GIF quantum energy filter (20 eV) (Gatan) using EPU (FEI) and a 200 kV Talos Arctica (FEI) equipped with a K3 direct electron detector (Gatan) using Serial EM (Mastronarde, 2005).

Cryo-EM data processing

All datasets were processed using the same general workflow in RELION 3.0 (Zivanov et al., 2018). Dose-fractionated images were gain normalized, 2 x Fourier binned, aligned, dose-weighted, and summed with MotionCor2 (Zheng et al., 2017). Contrast transfer

function correction and defocus value estimation were done with GCTF (Zhang, 2016). Several hundred particles were manually picked and subjected to 2D classification to generate templates for auto-picking. Auto-picked particles were subjected to 2D classification to remove false positives. Ab initio models were generated in RELION and used for 3D classification. 3D classes with strong ICD density were selected for 3D refinement. An initial round of 3D refinement using the best 3D class as an initial model (low-pass filtered to 60 Å) was followed by a second round with finer angular sampling using the map from the first refinement low-pass filtered to 10 Å as the initial model. Next, per-particle CTF refinement and beam tilt estimation were performed before another round of 3D classification with no image alignment/angular searches. Particles from the best classes were selected, polished, and used for 3D refinement to generate the final maps.

Electrophysiology

Whole cell voltage-clamp recordings were made from cells transiently transfected with the constructs described. For the patch-clamp experiments, adherent HEK293S GnTI- cells were transiently transfected with pEZT-based plasmids 2-3 days before recording. Each 35 mm dish of cells was transfected with the DNA of α3 and β4 subunits in a 1:1 ratio or with mouse muscle-type subunits (α1, β1, ε, and δ) in a 2:1:1:1 ratio. Upon transfection, cells were moved to 30°C. On the day of recording, cells were washed with bath solution, which contained 15 mM KCl, 10 mM HEPES pH 7.3, and 280 mM mannitol. Borosilicate pipettes were pulled and polished to a resistance of 2-4 MΩ. The pipette solution contained 110 mM KCl, 40 mM KF, 10 mM EGTA, and 20 mM HEPES pH 7.3. Cells were initially clamped at

-110 mV. The recordings were made with an Axopatch 200B amplifier, sampled at 5 kHz, and low-pass filtered at 2 kHz using a Digidata 1440A (Molecular Devices) and analyzed with pClamp 10 software (Molecular Devices). Currents were recorded in response to 40 μM nicotine. Solution exchange was achieved using a gravity driven RSC-200 rapid solution changer (Bio-Logic). Data was normalized to the -100 mV current value for each cell.

APPENDIX A

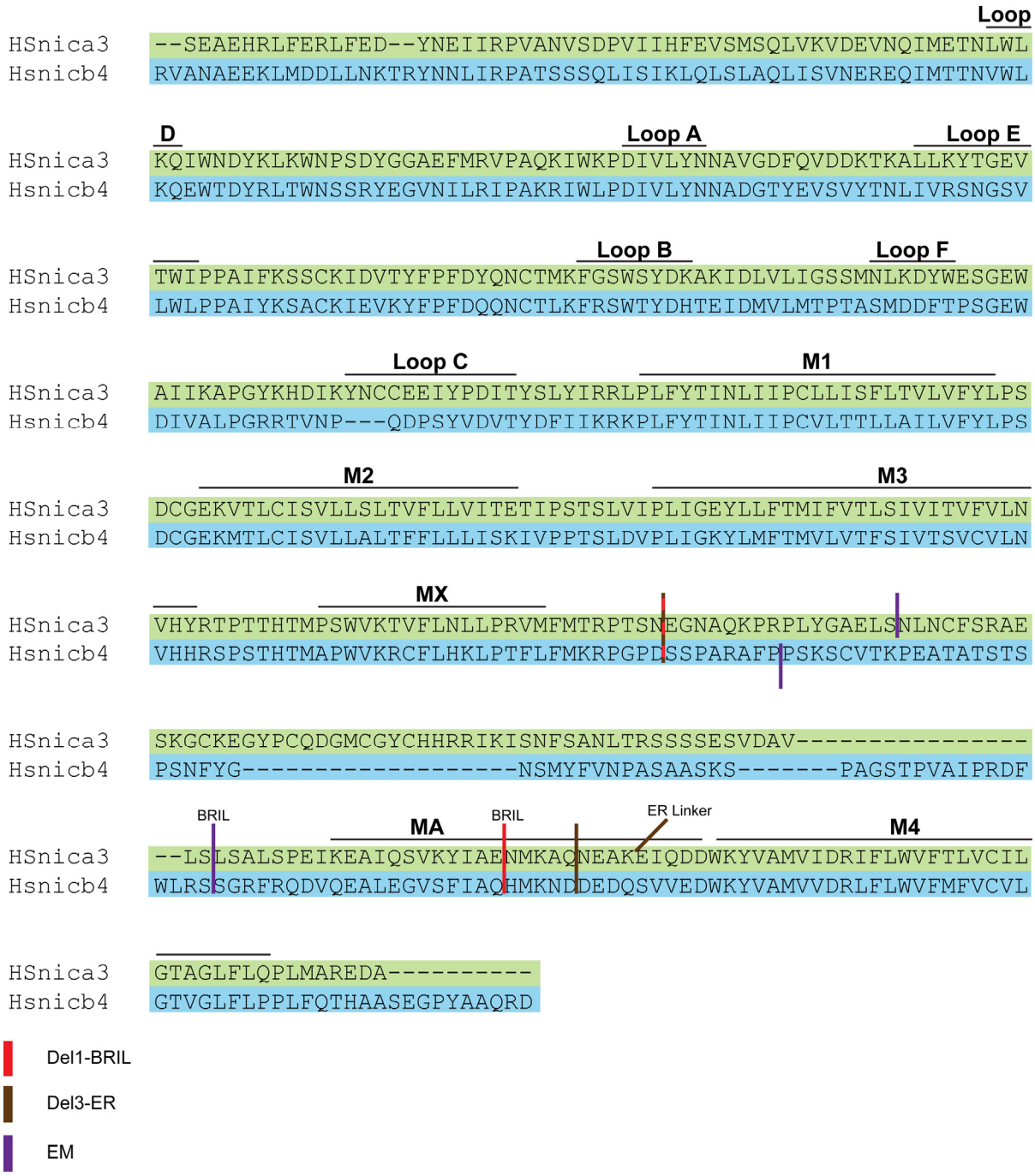
Loop
HSnica3 --SEAEHRLFERLFED--YNEIIRPVANVSDPVIIHFEVSMSQLVKVDEVNQIMETNLWL
Hsnicb4 RVANAEEKLMDDLLNKTRYNNLIRPATSSSQLISIKLQLSLAQLISVNEREQIMTTNVWL
D
Loop A
Loop E
HSnica3 KQIWNDYKLKWNPSDYGGAEFMRVPAQKIWKPDIVLYNNAVGDFQVDDKTKALLKYTGEV
Hsnicb4 KQEWTDYRLTWNSSRYEGVNILRIPAKRIWLPDIVLYNNADGTYEVSVYTNLIVRSNGSV
Loop B
Loop F
HSnica3 TWIPPAIFKSSCKIDVTYFPFDYQNCTMKFGSWSYDKAKIDLVLIGSSMNLKDYWESGEW
Hsnicb4 LWLPPAIYKSACKIEVKYFPFDQQNCTLKFRSWTYDHTEIDMVLMTPTASMDDFTPSGEW
Loop C
M1
HSnica3 AIIKAPGYKHDIKYNCCEEIYPDITYSLYIRRLPLFYTINLIIPCLLISFLTVLVFYLPS
Hsnicb4 DIVALPGRRTVNP---QDPSYVDVTYDFIIKRKPLFYTINLIIPCVLTTLLAILVFYLPS
M2
M3
HSnica3 DCGEKVTLCISVLLSLTVFLLVITETIPSTSLVIPLIGEYLLFTMIFVTLSIVITVFVLN
Hsnicb4 DCGEKMTLCISVLLALTFFLLLISKIVPPTSLDVPLIGKYLMFTMVLVTFSIVTSVCVLN
MX
HSnica3 VHYRTPTTHTMPSWVKTVFLNLLPRVMFMTRPTSNEGNAQKPRPLYGAELSNLNCFSRAE
Hsnicb4 VHHRSPSTHTMAPWVKRCFLHKLPTFLFMKRPGPDSSPARAFPPSKSCVTKPEATATSTS
HSnica3 SKGCKEGYPCQDGMCGYCHHRRIKISNFSANLTRSSSSESVDAV----------
Hsnicb4 PSNFYG----------NSMYFVNPASAASKS-------PAGSTPVAIPRDF
BRIL
MA
BRIL
ER Linker
M4
HSnica3 --LSLLSALSPEIKEAIQSVKYIAENMKAQNEAKEIQDDWKYVAMVIDRIFLWVFTLVCIL
Hsnicb4 WLRSSGRFRQDVQEALEGVSFIAQHMKNDDEDQSVVEDWKYVAMVVDRLFLWVFMFVCVL
HSnica3 GTAGLFLQPLMAREDA----------
Hsnicb4 GTVGLFLPPLFQTHAASEGPYAAQRD
Del1-BRIL
Del3-ER
EM

BIBLIOGRAPHY

ABRAHAM, M. J., MURTOLA, T., SCHULZ, R., PÁLL, S., SMITH, J. C., HESS, B. & LINDAHL, E. 2015. GROMACS: High performance molecular simulations through multi-level parallelism from laptops to supercomputers. *SoftwareX,* 1-2**,** 19-25.

ADAMS, P. D., AFONINE, P. V., BUNKOCZI, G., CHEN, V. B., DAVIS, I. W., ECHOLS, N., HEADD, J. J., HUNG, L. W., KAPRAL, G. J., GROSSE-KUNSTLEVE, R. W., MCCOY, A. J., MORIARTY, N. W., OEFFNER, R., READ, R. J., RICHARDSON, D. C., RICHARDSON, J. S., TERWILLIGER, T. C. & ZWART, P. H. 2010. PHENIX: a comprehensive Python-based system for macromolecular structure solution. *Acta Crystallogr D Biol Crystallogr,* 66**,** 213-21.

ADDONA, G. H., SANDERMANN, H., JR., KLOCZEWIAK, M. A., HUSAIN, S. S. & MILLER, K. W. 1998. Where does cholesterol act during activation of the nicotinic acetylcholine receptor? *Biochim Biophys Acta,* 1370**,** 299-309.

AHRING, P. K., OLSEN, J. A., NIELSEN, E. O., PETERS, D., PEDERSEN, M. H., ROHDE, L. A., KASTRUP, J. S., SHAHSAVAR, A., INDURTHI, D. C., CHEBIB, M., GAJHEDE, M. & BALLE, T. 2015. Engineered alpha4beta2 nicotinic acetylcholine receptors as models for measuring agonist binding and effect at the orthosteric low-affinity alpha4-alpha4 interface. *Neuropharmacology,* 92**,** 135-45.

ALBUQUERQUE, E. X., PEREIRA, E. F., ALKONDON, M. & ROGERS, S. W. 2009. Mammalian nicotinic acetylcholine receptors: from structure to function. *Physiol Rev,* 89**,** 73-120.

ALCAINO, C., MUSGAARD, M., MINGUEZ, T., MAZZAFERRO, S., FAUNDEZ, M., ITURRIAGA-VASQUEZ, P., BIGGIN, P. C. & BERMUDEZ, I. 2017. Role of

the Cys Loop and Transmembrane Domain in the Allosteric Modulation of alpha4beta2 Nicotinic Acetylcholine Receptors. *J Biol Chem,* 292**,** 551-562.

ALTHOFF, T., HIBBS, R. E., BANERJEE, S. & GOUAUX, E. 2014. X-ray structures of GluCl in apo states reveal a gating mechanism of Cys-loop receptors. *Nature,* 512**,** 333-7.

ARYAL, P., SANSOM, M. S. & TUCKER, S. J. 2015. Hydrophobic gating in ion channels. *J Mol Biol,* 427**,** 121-30.

AUERBACH, A. & AKK, G. 1998. Desensitization of mouse nicotinic acetylcholine receptor channels. A two-gate mechanism. *J Gen Physiol,* 112**,** 181-97.

AZAM, L., WINZER-SERHAN, U. H., CHEN, Y. & LESLIE, F. M. 2002. Expression of neuronal nicotinic acetylcholine receptor subunit mRNAs within midbrain dopamine neurons. *J Comp Neurol,* 444**,** 260-74.

BASAK, S., GICHERU, Y., RAO, S., SANSOM, M. S. P. & CHAKRAPANI, S. 2018a. Cryo-EM reveals two distinct serotonin-bound conformations of full-length 5-HT3A receptor. *Nature,* 563**,** 270-274.

BASAK, S., GICHERU, Y., SAMANTA, A., MOLUGU, S. K., HUANG, W., FUENTE, M., HUGHES, T., TAYLOR, D. J., NIEMAN, M. T., MOISEENKOVA-BELL, V. & CHAKRAPANI, S. 2018b. Cryo-EM structure of 5-HT3A receptor in its resting conformation. *Nat Commun,* 9**,** 514.

BECKSTEIN, O. & SANSOM, M. S. 2006. A hydrophobic gate in an ion channel: the closed state of the nicotinic acetylcholine receptor. *Phys Biol,* 3**,** 147-59.

BEERS, W. H. & REICH, E. 1970. Structure and activity of acetylcholine. *Nature,* 228**,** 917-22.

BEROUKHIM, R. & UNWIN, N. 1997. Distortion correction of tubular crystals: improvements in the acetylcholine receptor structure. *Ultramicroscopy,* 70**,** 57-81.

BERRETTINI, W., YUAN, X., TOZZI, F., SONG, K., FRANCKS, C., CHILCOAT, H., WATERWORTH, D., MUGLIA, P. & MOOSER, V. 2008. Alpha-5/alpha-3 nicotinic receptor subunit alleles increase risk for heavy smoking. *Mol Psychiatry,* 13**,** 368-73.

BLACK, J. 1999. Claude bernard on the action of curare. *BMJ,* 319**,** 622.

BLUM, A. P., LESTER, H. A. & DOUGHERTY, D. A. 2010. Nicotinic pharmacophore: the pyridine N of nicotine and carbonyl of acetylcholine hydrogen bond across a subunit interface to a backbone NH. *Proc Natl Acad Sci U S A,* 107**,** 13206-11.

BOCQUET, N., NURY, H., BAADEN, M., LE POUPON, C., CHANGEUX, J. P., DELARUE, M. & CORRINGER, P. J. 2009. X-ray structure of a pentameric ligand-gated ion channel in an apparently open conformation. *Nature,* 457**,** 111-4.

BOORMAN, J. P., BEATO, M., GROOT-KORMELINK, P. J., BROADBENT, S. D. & SIVILOTTI, L. G. 2003. The effects of beta 3 subunit incorporation on the pharmacology and single channel properties of oocyte-expressed human alpha 3 beta 4 neuronal nicotinic receptors. *Journal of Biological Chemistry,* 278**,** 44033-44040.

BOULTER, J., O'SHEA-GREENFIELD, A., DUVOISIN, R. M., CONNOLLY, J. G., WADA, E., JENSEN, A., GARDNER, P. D., BALLIVET, M., DENERIS, E. S., MCKINNON, D. & ET AL. 1990. Alpha 3, alpha 5, and beta 4: three members of the rat neuronal nicotinic acetylcholine receptor-related gene family form a gene cluster. *J Biol Chem,* 265**,** 4472-82.

BOURNE, Y., TALLEY, T. T., HANSEN, S. B., TAYLOR, P. & MARCHOT, P. 2005. Crystal structure of a Cbtx-AChBP complex reveals essential interactions between snake alpha-neurotoxins and nicotinic receptors. *EMBO J,* 24**,** 1512-22.

BOUZAT, C., BREN, N. & SINE, S. M. 1994. Structural basis of the different gating kinetics of fetal and adult acetylcholine receptors. *Neuron,* 13**,** 1395-402.

BOUZAT, C., GUMILAR, F., SPITZMAUL, G., WANG, H. L., RAYES, D., HANSEN, S. B., TAYLOR, P. & SINE, S. M. 2004. Coupling of agonist binding to channel gating in an ACh-binding protein linked to an ion channel. *Nature,* 430**,** 896-900.

BOWERY, N. G. & SMART, T. G. 2006. GABA and glycine as neurotransmitters: a brief history. *Br J Pharmacol,* 147 Suppl 1**,** S109-19.

BREJC, K., VAN DIJK, W. J., KLAASSEN, R. V., SCHUURMANS, M., VAN DER OOST, J., SMIT, A. B. & SIXMA, T. K. 2001. Crystal structure of an ACh-

binding protein reveals the ligand-binding domain of nicotinic receptors. *Nature,* 411**,** 269-76.

BRISSON, A. & UNWIN, P. N. 1984. Tubular crystals of acetylcholine receptor. *J Cell Biol,* 99**,** 1202-11.

BRISSON, A. & UNWIN, P. N. 1985. Quaternary structure of the acetylcholine receptor. *Nature,* 315**,** 474-7.

BROADBENT, S., GROOT-KORMELINK, P. J., KRASHIA, P. A., HARKNESS, P. C., MILLAR, N. S., BEATO, M. & SIVILOTTI, L. G. 2006. Incorporation of the beta3 subunit has a dominant-negative effect on the function of recombinant central-type neuronal nicotinic receptors. *Mol Pharmacol,* 70**,** 1350-7.

BROHAWN, S. G., CAMPBELL, E. B. & MACKINNON, R. 2014. Physical mechanism for gating and mechanosensitivity of the human TRAAK K+ channel. *Nature,* 516**,** 126-30.

BROWNING, K. N. 2015. Role of central vagal 5-HT3 receptors in gastrointestinal physiology and pathophysiology. *Front Neurosci,* 9**,** 413.

BUSSI, G., DONADIO, D. & PARRINELLO, M. 2007. Canonical sampling through velocity rescaling. *The Journal of Chemical Physics,* 126**,** 014101.

CACHELIN, A. B. & JAGGI, R. 1991. Beta subunits determine the time course of desensitization in rat alpha 3 neuronal nicotinic acetylcholine receptors. *Pflugers Arch,* 419**,** 579-82.

CAMACHO-HERNANDEZ, G. A., STOKES, C., DUGGAN, B. M., KACZANOWSKA, K., BRANDAO-ARAIZA, S., DOAN, L., PAPKE, R. L. & TAYLOR, P. 2019. Synthesis, Pharmacological Characterization, and Structure-Activity Relationships of Noncanonical Selective Agonists for alpha7 nAChRs. *J Med Chem,* 62**,** 10376-10390.

CAMPOS-CARO, A., SMILLIE, F. I., DOMINGUEZ DEL TORO, E., ROVIRA, J. C., VICENTE-AGULLO, F., CHAPULI, J., JUIZ, J. M., SALA, S., SALA, F., BALLESTA, J. J. & CRIADO, M. 1997. Neuronal nicotinic acetylcholine

receptors on bovine chromaffin cells: cloning, expression, and genomic organization of receptor subunits. *J Neurochem,* 68**,** 488-97.

CAO, E. 2020. Structural mechanisms of transient receptor potential ion channels. *J Gen Physiol,* 152.

CARTAUD, J., BENEDETTI, E. L., COHEN, J. B., MEUNIER, J. C. & CHANGEUX, J. P. 1973. Presence of a lattice structure in membrane fragments rich in nicotinic receptor protein from the electric organ of Torpedo marmorata. *FEBS Lett,* 33**,** 109-13.

CARTAUD, J., POPOT, J. L. & CHANGEUX, J. P. 1980. Light and heavy forms of the acetylcholine receptor from Torpedo marmorata electric organ: morphological identification using reconstituted vesicles. *FEBS Lett,* 121**,** 327-32.

CASTRO, N. G. & ALBUQUERQUE, E. X. 1995. alpha-Bungarotoxin-sensitive hippocampal nicotinic receptor channel has a high calcium permeability. *Biophys J,* 68**,** 516-24.

CELIE, P. H., VAN ROSSUM-FIKKERT, S. E., VAN DIJK, W. J., BREJC, K., SMIT, A. B. & SIXMA, T. K. 2004. Nicotine and carbamylcholine binding to nicotinic acetylcholine receptors as studied in AChBP crystal structures. *Neuron,* 41**,** 907-14.

CERDAN, A. H., MARTIN, N. E. & CECCHINI, M. 2018. An Ion-Permeable State of the Glycine Receptor Captured by Molecular Dynamics. *Structure,* 26**,** 1555-1562 e4.

CHAK, A. & KARLIN, A. 1992. Purification and reconstitution of nicotinic acetylcholine receptor. *Methods Enzymol,* 207**,** 546-55.

CHANGEUX, J. P. 2012. The nicotinic acetylcholine receptor: the founding father of the pentameric ligand-gated ion channel superfamily. *J Biol Chem,* 287**,** 40207-15.

CHANGEUX, J. P., KASAI, M., HUCHET, M. & MEUNIER, J. C. 1970. [Extraction from electric tissue of gymnotus of a protein presenting several typical properties characteristic of the physiological receptor of acetylcholine]. *C R Acad Hebd Seances Acad Sci D,* 270**,** 2864-7.

CHENG, Y. 2015. Single-Particle Cryo-EM at Crystallographic Resolution. *Cell,* 161**,** 450-457.

CHENG, Y., GRIGORIEFF, N., PENCZEK, P. A. & WALZ, T. 2015. A primer to single-particle cryo-electron microscopy. *Cell,* 161**,** 438-449.

CHUN, E., THOMPSON, A. A., LIU, W., ROTH, C. B., GRIFFITH, M. T., KATRITCH, V., KUNKEN, J., XU, F., CHEREZOV, V., HANSON, M. A. & STEVENS, R. C. 2012. Fusion partner toolchest for the stabilization and crystallization of G protein-coupled receptors. *Structure,* 20**,** 967-76.

CIPPITELLI, A., WU, J., GAIOLINI, K. A., MERCATELLI, D., SCHOCH, J., GORMAN, M., RAMIREZ, A., CICCOCIOPPO, R., KHROYAN, T. V., YASUDA, D., ZAVERI, N. T., PASCUAL, C., XIE, X. S. & TOLL, L. 2015. AT-1001: a high-affinity alpha3beta4 nAChR ligand with novel nicotine-suppressive pharmacology. *Br J Pharmacol,* 172**,** 1834-45.

CLAUDIO, T., BALLIVET, M., PATRICK, J. & HEINEMANN, S. 1983. Nucleotide and deduced amino acid sequences of Torpedo californica acetylcholine receptor gamma subunit. *Proc Natl Acad Sci U S A,* 80**,** 1111-5.

CONROY, W. G. & BERG, D. K. 1995. Neurons can maintain multiple classes of nicotinic acetylcholine receptors distinguished by different subunit compositions. *J Biol Chem,* 270**,** 4424-31.

CONROY, W. G., VERNALLIS, A. B. & BERG, D. K. 1992. The alpha 5 gene product assembles with multiple acetylcholine receptor subunits to form distinctive receptor subtypes in brain. *Neuron,* 9**,** 679-91.

CORBIN, J., WANG, H. H. & BLANTON, M. P. 1998. Identifying the cholesterol binding domain in the nicotinic acetylcholine receptor with [125I]azido-cholesterol. *Biochim Biophys Acta,* 1414**,** 65-74.

CORRINGER, P. J., BERTRAND, S., GALZI, J. L., DEVILLERS-THIERY, A., CHANGEUX, J. P. & BERTRAND, D. 1999. Mutational analysis of the charge selectivity filter of the alpha 7 nicotinic acetylcholine receptor. *Neuron,* 22**,** 831-843.

COUTURIER, S., ERKMAN, L., VALERA, S., RUNGGER, D., BERTRAND, S., BOULTER, J., BALLIVET, M. & BERTRAND, D. 1990. Alpha 5, alpha 3, and non-alpha 3. Three clustered avian genes encoding neuronal nicotinic acetylcholine receptor-related subunits. *J Biol Chem,* 265**,** 17560-7.

COVERNTON, P. J., KOJIMA, H., SIVILOTTI, L. G., GIBB, A. J. & COLQUHOUN, D. 1994. Comparison of neuronal nicotinic receptors in rat sympathetic neurones with subunit pairs expressed in Xenopus oocytes. *J Physiol,* 481 (Pt 1)**,** 27-34.

CRIADO, M., EIBL, H. & BARRANTES, F. J. 1982. Effects of lipids on acetylcholine receptor. Essential need of cholesterol for maintenance of agonist-induced state transitions in lipid vesicles. *Biochemistry,* 21**,** 3622-9.

CYMES, G. D. & GROSMAN, C. 2012. The unanticipated complexity of the selectivity-filter glutamates of nicotinic receptors. *Nat Chem Biol,* 8**,** 975-81.

CYMES, G. D. & GROSMAN, C. 2016. Identifying the elusive link between amino acid sequence and charge selectivity in pentameric ligand-gated ion channels. *Proc Natl Acad Sci U S A,* 113**,** E7106-E7115.

DACOSTA, C. J. & BAENZIGER, J. E. 2009. A lipid-dependent uncoupled conformation of the acetylcholine receptor. *J Biol Chem,* 284**,** 17819-25.

DACOSTA, C. J. & BAENZIGER, J. E. 2013. Gating of pentameric ligand-gated ion channels: structural insights and ambiguities. *Structure,* 21**,** 1271-83.

DACOSTA, C. J., OGREL, A. A., MCCARDY, E. A., BLANTON, M. P. & BAENZIGER, J. E. 2002. Lipid-protein interactions at the nicotinic acetylcholine receptor. A functional coupling between nicotinic receptors and phosphatidic acid-containing lipid bilayers. *J Biol Chem,* 277**,** 201-8.

DALE, H. H. 1914. THE ACTION OF CERTAIN ESTERS AND ETHERS OF CHOLINE, AND THEIR RELATION TO MUSCARINE. *Journal of Pharmacology and Experimental Therapeutics,* 6**,** 147.

DAMLE, V. N. & KARLIN, A. 1980. Effects of agonists and antagonists on the reactivity of the binding site disulfide in acetylcholine receptor from Torpedo californica. *Biochemistry,* 19**,** 3924-32.

DANI, J. A. & BERTRAND, D. 2007. Nicotinic acetylcholine receptors and nicotinic cholinergic mechanisms of the central nervous system. *Annu Rev Pharmacol Toxicol,* 47**,** 699-729.

DELBART, F., BRAMS, M., GRUSS, F., NOPPEN, S., PEIGNEUR, S., BOLAND, S., CHALTIN, P., BRANDAO-NETO, J., VON DELFT, F., TOUW, W. G., JOOSTEN, R. P., LIEKENS, S., TYTGAT, J. & ULENS, C. 2018. An allosteric binding site of the alpha7 nicotinic acetylcholine receptor revealed in a humanized acetylcholine-binding protein. *J Biol Chem,* 293**,** 2534-2545.

DELLISANTI, C. D., YAO, Y., STROUD, J. C., WANG, Z. Z. & CHEN, L. 2007. Crystal structure of the extracellular domain of nAChR alpha1 bound to alpha-bungarotoxin at 1.94 A resolution. *Nat Neurosci,* 10**,** 953-62.

DENISOV, I. G. & SLIGAR, S. G. 2016. Nanodiscs for structural and functional studies of membrane proteins. *Nat Struct Mol Biol,* 23**,** 481-6.

DEVILLERS-THIERY, A., GIRAUDAT, J., BENTABOULET, M. & CHANGEUX, J. P. 1983. Complete mRNA coding sequence of the acetylcholine binding alpha-subunit of Torpedo marmorata acetylcholine receptor: a model for the transmembrane organization of the polypeptide chain. *Proc Natl Acad Sci U S A,* 80**,** 2067-71.

DU, J., LU, W., WU, S., CHENG, Y. & GOUAUX, E. 2015. Glycine receptor mechanism elucidated by electron cryo-microscopy. *Nature,* 526**,** 224-9.

DUKKIPATI, A., PARK, H. H., WAGHRAY, D., FISCHER, S. & GARCIA, K. C. 2008. BacMam system for high-level expression of recombinant soluble and membrane glycoproteins for structural studies. *Protein Expr Purif,* 62**,** 160-70.

EATON, J. B., PENG, J. H., SCHROEDER, K. M., GEORGE, A. A., FRYER, J. D., KRISHNAN, C., BUHLMAN, L., KUO, Y. P., STEINLEIN, O. & LUKAS, R. J. 2003. Characterization of human alpha 4 beta 2-nicotinic acetylcholine receptors stably and heterologously expressed in native nicotinic receptor-null SH-EP1 human epithelial cells. *Mol Pharmacol,* 64**,** 1283-94.

ECCLES, J. C., KATZ, B. & KUFFLER, S. W. 1941. NATURE OF THE "ENDPLATE POTENTIAL" IN CURARIZED MUSCLE. *Journal of Neurophysiology,* 4**,** 362-387.

ECCLES, J. C. & O'CONNOR, W. J. 1939. Responses which nerve impulses evoke in mammalian striated muscles. *The Journal of Physiology,* 97**,** 44-102.

ELGOYHEN, A. B., JOHNSON, D. S., BOULTER, J., VETTER, D. E. & HEINEMANN, S. 1994. Alpha 9: an acetylcholine receptor with novel pharmacological properties expressed in rat cochlear hair cells. *Cell,* 79**,** 705-15.

ELGOYHEN, A. B., VETTER, D. E., KATZ, E., ROTHLIN, C. V., HEINEMANN, S. F. & BOULTER, J. 2001. alpha10: a determinant of nicotinic cholinergic receptor function in mammalian vestibular and cochlear mechanosensory hair cells. *Proc Natl Acad Sci U S A,* 98**,** 3501-6.

EMSLEY, P., LOHKAMP, B., SCOTT, W. G. & COWTAN, K. 2010. Features and development of Coot. *Acta Crystallogr D Biol Crystallogr,* 66**,** 486-501.

EPSTEIN, M. & RACKER, E. 1978. Reconstitution of carbamylcholine-dependent sodium ion flux and desensitization of the acetylcholine receptor from Torpedo californica. *J Biol Chem,* 253**,** 6660-2.

ESSMANN, U., PERERA, L., BERKOWITZ, M. L., DARDEN, T., LEE, H. & PEDERSEN, L. G. 1995. A smooth particle mesh Ewald method. *J. Chem. Phys.,* 103**,** 8577.

EWINS, A. J. 1914. Acetylcholine, a New Active Principle of Ergot. *Biochem J,* 8**,** 44-9.

FATIMA-SHAD, K. & BARRY, P. H. 1993. Anion permeation in GABA- and glycine-gated channels of mammalian cultured hippocampal neurons. *Proc Biol Sci,* 253**,** 69-75.

FATT, P. & KATZ, B. 1950. Membrane potentials at the motor end-plate. *J Physiol,* 111**,** 46p-7p.

FELTZ, A. & TRAUTMANN, A. 1982. Desensitization at the frog neuromuscular junction: a biphasic process. *The Journal of Physiology,* 322**,** 257-272.

FENSTER, C. P., RAINS, M. F., NOERAGER, B., QUICK, M. W. & LESTER, R. A. 1997. Influence of subunit composition on desensitization of neuronal acetylcholine receptors at low concentrations of nicotine. *J Neurosci,* 17**,** 5747-59.

FILATOV, G. N. & WHITE, M. M. 1995. The role of conserved leucines in the M2 domain of the acetylcholine receptor in channel gating. *Mol Pharmacol,* 48**,** 379-84.

FLORES, C. M., ROGERS, S. W., PABREZA, L. A., WOLFE, B. B. & KELLAR, K. J. 1992. A subtype of nicotinic cholinergic receptor in rat brain is composed of alpha 4 and beta 2 subunits and is up-regulated by chronic nicotine treatment. *Mol Pharmacol,* 41**,** 31-7.

FONG, T. M. & MCNAMEE, M. G. 1986. Correlation between acetylcholine receptor function and structural properties of membranes. *Biochemistry,* 25**,** 830-40.

FRAHM, S., SLIMAK, M. A., FERRARESE, L., SANTOS-TORRES, J., ANTOLIN-FONTES, B., AUER, S., FILKIN, S., PONS, S., FONTAINE, J. F., TSETLIN, V., MASKOS, U. & IBANEZ-TALLON, I. 2011. Aversion to Nicotine Is Regulated by the Balanced Activity of beta 4 and alpha 5 Nicotinic Receptor Subunits in the Medial Habenula. *Neuron,* 70**,** 522-535.

FRAUENFELD, J., LOVING, R., ARMACHE, J. P., SONNEN, A. F., GUETTOU, F., MOBERG, P., ZHU, L., JEGERSCHOLD, C., FLAYHAN, A., BRIGGS, J. A., GAROFF, H., LOW, C., CHENG, Y. & NORDLUND, P. 2016. A saposin-lipoprotein nanoparticle system for membrane proteins. *Nat Methods,* 13**,** 345-51.

FREE, R. B., BRYANT, D. L., MCKAY, S. B., KASER, D. J. & MCKAY, D. B. 2002. [3H]Epibatidine binding to bovine adrenal medulla: evidence for alpha3beta4* nicotinic receptors. *Neurosci Lett,* 318**,** 98-102.

FUCILE, S. 2004. Ca2+ permeability of nicotinic acetylcholine receptors. *Cell Calcium,* 35**,** 1-8.

GALZI, J. L., DEVILLERSTHIERY, A., HUSSY, N., BERTRAND, S., CHANGEUX, J. P. & BERTRAND, D. 1992. Mutations in the Channel Domain of a Neuronal

Nicotinic Receptor Convert Ion Selectivity from Cationic to Anionic. *Nature,* 359**,** 500-505.

GEORGE, A. A., LUCERO, L. M., DAMAJ, M. I., LUKAS, R. J., CHEN, X. N. & WHITEAKER, P. 2012. Function of Human alpha 3 beta 4 alpha 5 Nicotinic Acetylcholine Receptors Is Reduced by the alpha 5(D398N) Variant. *Journal of Biological Chemistry,* 287**,** 25151-25162.

GERZANICH, V., WANG, F., KURYATOV, A. & LINDSTROM, J. 1998. alpha 5 subunit alters desensitization, pharmacology, Ca++ permeability and Ca++ modulation of human neuronal alpha 3 nicotinic receptors. *Journal of Pharmacology and Experimental Therapeutics,* 286**,** 311-320.

GHARPURE, A., TENG, J., ZHUANG, Y., NOVIELLO, C. M., WALSH, R. M., JR., CABUCO, R., HOWARD, R. J., ZAVERI, N. T., LINDAHL, E. & HIBBS, R. E. 2019. Agonist Selectivity and Ion Permeation in the alpha3beta4 Ganglionic Nicotinic Receptor. *Neuron,* 104**,** 501-511 e6.

GIELEN, M. & CORRINGER, P. J. 2018. The dual-gate model for pentameric ligand-gated ion channels activation and desensitization. *J Physiol,* 596**,** 1873-1902.

GLENNON, R. A. & DUKAT, M. 2000. Central nicotinic receptor ligands and pharmacophores. *Pharm Acta Helv,* 74**,** 103-14.

GLICK, S. D., KUEHNE, M. E., MAISONNEUVE, I. M., BANDARAGE, U. K. & MOLINARI, H. H. 1996. 18-Methoxycoronaridine, a non-toxic iboga alkaloid congener: effects on morphine and cocaine self-administration and on mesolimbic dopamine release in rats. *Brain Res,* 719**,** 29-35.

GLICK, S. D., MAISONNEUVE, I. M. & DICKINSON, H. A. 2000. 18-MC reduces methamphetamine and nicotine self-administration in rats. *Neuroreport,* 11**,** 2013-5.

GLICK, S. D., MAISONNEUVE, I. M., KITCHEN, B. A. & FLECK, M. W. 2002. Antagonism of alpha 3 beta 4 nicotinic receptors as a strategy to reduce opioid and stimulant self-administration. *Eur J Pharmacol,* 438**,** 99-105.

GOEHRING, A., LEE, C. H., WANG, K. H., MICHEL, J. C., CLAXTON, D. P., BACONGUIS, I., ALTHOFF, T., FISCHER, S., GARCIA, K. C. & GOUAUX, E. 2014. Screening and large-scale expression of membrane proteins in mammalian cells for structural studies. *Nat Protoc,* 9**,** 2574-85.

GÖPFERT, H. & SCHAEFER, H. 1938. Über den direkt und indirekt erregten Aktionsstrom und die Funktion der motorischen Endplatte. *Pflüger's Archiv für die gesamte Physiologie des Menschen und der Tiere,* 239**,** 597-619.

GRADY, S. R., MORETTI, M., ZOLI, M., MARKS, M. J., ZANARDI, A., PUCCI, L., CLEMENTI, F. & GOTTI, C. 2009. Rodent habenulo-interpeduncular pathway expresses a large variety of uncommon nAChR subtypes, but only the alpha3beta4* and alpha3beta3beta4* subtypes mediate acetylcholine release. *J Neurosci,* 29**,** 2272-82.

GRAHAM, A., COURT, J. A., MARTIN-RUIZ, C. M., JAROS, E., PERRY, R., VOLSEN, S. G., BOSE, S., EVANS, N., INCE, P., KURYATOV, A., LINDSTROM, J., GOTTI, C. & PERRY, E. K. 2002. Immunohistochemical localisation of nicotinic acetylcholine receptor subunits in human cerebellum. *Neuroscience,* 113**,** 493-507.

GRISHIN, A. A., WANG, C. I., MUTTENTHALER, M., ALEWOOD, P. F., LEWIS, R. J. & ADAMS, D. J. 2010. Alpha-conotoxin AuIB isomers exhibit distinct inhibitory mechanisms and differential sensitivity to stoichiometry of alpha3beta4 nicotinic acetylcholine receptors. *J Biol Chem,* 285**,** 22254-63.

GROOT-KORMELINK, P. J., BOORMAN, J. P. & SIVILOTTI, L. G. 2001. Formation of functional α3β4α5 human neuronal nicotinic receptors in Xenopus oocytes: a reporter mutation approach. *British Journal of Pharmacology,* 134**,** 789-796.

GRUTTER, T., PRADO DE CARVALHO, L., LE NOVERE, N., CORRINGER, P. J., EDELSTEIN, S. & CHANGEUX, J. P. 2003. An H-bond between two residues from different loops of the acetylcholine binding site contributes to the activation mechanism of nicotinic receptors. *EMBO J,* 22**,** 1990-2003.

HAGHIGHI, A. P. & COOPER, E. 1998. Neuronal nicotinic acetylcholine receptors are blocked by intracellular spermine in a voltage-dependent manner. *Journal of Neuroscience,* 18**,** 4050-4062.

HAGHIGHI, A. P. & COOPER, E. 2000. A molecular link between inward rectification and calcium permeability of neuronal nicotinic acetylcholine alpha 3 beta 4 and alpha 4 beta 2 receptors. *Journal of Neuroscience,* 20**,** 529-541.

HALES, T. G., DUNLOP, J. I., DEEB, T. Z., CARLAND, J. E., KELLEY, S. P., LAMBERT, J. J. & PETERS, J. A. 2006. Common determinants of single channel conductance within the large cytoplasmic loop of 5-hydroxytryptamine type 3 and alpha4beta2 nicotinic acetylcholine receptors. *J Biol Chem,* 281**,** 8062-71.

HAMOUDA, A. K., CHIARA, D. C., SAULS, D., COHEN, J. B. & BLANTON, M. P. 2006. Cholesterol interacts with transmembrane alpha-helices M1, M3, and M4 of the Torpedo nicotinic acetylcholine receptor: photolabeling studies using [3H]Azicholesterol. *Biochemistry,* 45**,** 976-86.

HANSEN, S. B., SULZENBACHER, G., HUXFORD, T., MARCHOT, P., TAYLOR, P. & BOURNE, Y. 2005. Structures of Aplysia AChBP complexes with nicotinic agonists and antagonists reveal distinctive binding interfaces and conformations. *EMBO J,* 24**,** 3635-46.

HANSEN, S. B., WANG, H. L., TAYLOR, P. & SINE, S. M. 2008. An ion selectivity filter in the extracellular domain of Cys-loop receptors reveals determinants for ion conductance. *J Biol Chem,* 283**,** 36066-70.

HARPOLE, T. J. & GROSMAN, C. 2014. Side-chain conformation at the selectivity filter shapes the permeation free-energy landscape of an ion channel. *Proc Natl Acad Sci U S A,* 111**,** E3196-205.

HARPSOE, K., AHRING, P. K., CHRISTENSEN, J. K., JENSEN, M. L., PETERS, D. & BALLE, T. 2011. Unraveling the high- and low-sensitivity agonist responses of nicotinic acetylcholine receptors. *J Neurosci,* 31**,** 10759-66.

HASSAINE, G., DELUZ, C., GRASSO, L., WYSS, R., TOL, M. B., HOVIUS, R., GRAFF, A., STAHLBERG, H., TOMIZAKI, T., DESMYTER, A., MOREAU, C., LI, X. D., POITEVIN, F., VOGEL, H. & NURY, H. 2014. X-ray structure of the mouse serotonin 5-HT3 receptor. *Nature,* 512**,** 276-81.

HATTORI, M., HIBBS, R. E. & GOUAUX, E. 2012. A fluorescence-detection size-exclusion chromatography-based thermostability assay for membrane protein precrystallization screening. *Structure,* 20**,** 1293-9.

HENAULT, C. M., SUN, J., THERIEN, J. P., DACOSTA, C. J., CARSWELL, C. L., LABRIOLA, J. M., JURANKA, P. F. & BAENZIGER, J. E. 2015. The role of the M4 lipid-sensor in the folding, trafficking, and allosteric modulation of nicotinic acetylcholine receptors. *Neuropharmacology,* 96**,** 157-68.

HENDERSON, R., CHEN, S., CHEN, J. Z., GRIGORIEFF, N., PASSMORE, L. A., CICCARELLI, L., RUBINSTEIN, J. L., CROWTHER, R. A., STEWART, P. L. & ROSENTHAL, P. B. 2011. Tilt-pair analysis of images from a range of different specimens in single-particle electron cryomicroscopy. *J Mol Biol,* 413**,** 1028-46.

HESS, B. 2008. P-LINCS: A Parallel Linear Constraint Solver for Molecular Simulation. *Journal of Chemical Theory and Computation,* 4**,** 116-122.

HIBBS, R. E. & GOUAUX, E. 2011. Principles of activation and permeation in an anion-selective Cys-loop receptor. *Nature,* 474**,** 54-60.

HILF, R. J., BERTOZZI, C., ZIMMERMANN, I., REITER, A., TRAUNER, D. & DUTZLER, R. 2010. Structural basis of open channel block in a prokaryotic pentameric ligand-gated ion channel. *Nat Struct Mol Biol,* 17**,** 1330-6.

HILF, R. J. & DUTZLER, R. 2008. X-ray structure of a prokaryotic pentameric ligand-gated ion channel. *Nature,* 452**,** 375-9.

HILF, R. J. & DUTZLER, R. 2009. Structure of a potentially open state of a proton-activated pentameric ligand-gated ion channel. *Nature,* 457**,** 115-8.

HOGG, R. C. & BERTRAND, D. 2004. Nicotinic acetylcholine receptors as drug targets. *Curr Drug Targets CNS Neurol Disord,* 3**,** 123-30.

HUANG, X., CHEN, H., MICHELSEN, K., SCHNEIDER, S. & SHAFFER, P. L. 2015. Crystal structure of human glycine receptor-alpha3 bound to antagonist strychnine. *Nature,* 526**,** 277-80.

HUMPHREY, W., DALKE, A. & SCHULTEN, K. 1996. VMD: visual molecular dynamics. *Journal of molecular graphics,* 14**,** 33-8, 27.

IMOTO, K., KONNO, T., NAKAI, J., WANG, F., MISHINA, M. & NUMA, S. 1991. A ring of uncharged polar amino acids as a component of channel constriction in the nicotinic acetylcholine receptor. *FEBS Lett,* 289**,** 193-200.

IVANOV, I., CHENG, X., SINE, S. M. & MCCAMMON, J. A. 2007. Barriers to ion translocation in cationic and anionic receptors from the Cys-loop family. *J Am Chem Soc,* 129**,** 8217-24.

JAIN, A., KURYATOV, A., WANG, J., KAMENECKA, T. M. & LINDSTROM, J. 2016. Unorthodox Acetylcholine Binding Sites Formed by alpha5 and beta3 Accessory Subunits in alpha4beta2* Nicotinic Acetylcholine Receptors. *J Biol Chem,* 291**,** 23452-23463.

JÄMBECK, J. P. M. & LYUBARTSEV, A. P. 2012. An Extension and Further Validation of an All-Atomistic Force Field for Biological Membranes. *Journal of Chemical Theory and Computation,* 8**,** 2938-2948.

JÄMBECK, J. P. M. & LYUBARTSEV, A. P. 2013. Another piece of the membrane puzzle: extending slipids further. *Journal of Chemical Theory and Computation,* 9**,** 774-784.

JI, D., LAPE, R. & DANI, J. A. 2001. Timing and location of nicotinic activity enhances or depresses hippocampal synaptic plasticity. *Neuron,* 31**,** 131-41.

JO, S., KIM, T., IYER, V. G. & IM, W. 2008. CHARMM-GUI: a web-based graphical user interface for CHARMM. *Journal of Computational Chemistry,* 29**,** 1859-1865.

JORGENSEN, W. L., CHANDRASEKHAR, J., MADURA, J. D., IMPEY, R. W. & KLEIN, M. L. 1983. Comparison of simple potential functions for simulating liquid water. *J. Chem. Phys.,* 79**,** 926.

KALAMIDA, D., POULAS, K., AVRAMOPOULOU, V., FOSTIERI, E., LAGOUMINTZIS, G., LAZARIDIS, K., SIDERI, A., ZOURIDAKIS, M. & TZARTOS, S. J. 2007. Muscle and neuronal nicotinic acetylcholine receptors. Structure, function and pathogenicity. *FEBS J,* 274**,** 3799-845.

KARLIN, A. 1969. Chemical modification of the active site of the acetylcholine receptor. *J Gen Physiol,* 54**,** 245-64.

KARLIN, A. 2002. Emerging structure of the nicotinic acetylcholine receptors. *Nat Rev Neurosci,* 3**,** 102-14.

KARLIN, A., HOLTZMAN, E., YODH, N., LOBEL, P., WALL, J. & HAINFELD, J. 1983. The arrangement of the subunits of the acetylcholine receptor of Torpedo californica. *J Biol Chem,* 258**,** 6678-81.

KARLSSON, E., HEILBRONN, E. & WIDLUND, L. 1972. Isolation of the nicotinic acetylcholine receptor by biospecific chromatography on insolubilized Naja naja neurotoxin. *FEBS Lett,* 28**,** 107-11.

KATZ, B. & THESLEFF, S. 1957. A study of the desensitization produced by acetylcholine at the motor end-plate. *J Physiol,* 138**,** 63-80.

KAWATE, T. & GOUAUX, E. 2006. Fluorescence-detection size-exclusion chromatography for precrystallization screening of integral membrane proteins. *Structure,* 14**,** 673-81.

KELLEY, S. P., DUNLOP, J. I., KIRKNESS, E. F., LAMBERT, J. J. & PETERS, J. A. 2003. A cytoplasmic region determines single-channel conductance in 5-HT3 receptors. *Nature,* 424**,** 321-4.

KERAMIDAS, A. & LYNCH, J. W. 2013. An outline of desensitization in pentameric ligand-gated ion channel receptors. *Cell Mol Life Sci,* 70**,** 1241-53.

KERAMIDAS, A., MOORHOUSE, A. J., FRENCH, C. R., SCHOFIELD, P. R. & BARRY, P. H. 2000. M2 pore mutations convert the glycine receptor channel from being anion- to cation-selective. *Biophysical Journal,* 79**,** 247-259.

KLESSE, G., RAO, S., SANSOM, M. S. & TUCKER, S. J. 2019. CHAP: a versatile tool for the structural and functional annotation of ion channel pores. *bioRxiv***,** 527275.

KLETT, R. P., FULPIUS, B. W., COOPER, D., SMITH, M., REICH, E. & POSSANI, L. D. 1973. The acetylcholine receptor. I. Purification and characterization of a macromolecule isolated from Electrophorus electricus. *J Biol Chem,* 248**,** 6841-53.

KLYMKOWSKY, M. W. & STROUD, R. M. 1979. Immunospecific identification and three-dimensional structure of a membrane-bound acetylcholine receptor from Torpedo californica. *J Mol Biol,* 128**,** 319-34.

KNOWLES, T. J., FINKA, R., SMITH, C., LIN, Y. P., DAFFORN, T. & OVERDUIN, M. 2009. Membrane proteins solubilized intact in lipid containing nanoparticles bounded by styrene maleic acid copolymer. *J Am Chem Soc,* 131**,** 7484-5.

KOENEN, M., PETER, C., VILLARROEL, A., WITZEMANN, V. & SAKMANN, B. 2005. Acetylcholine receptor channel subtype directs the innervation pattern of skeletal muscle. *EMBO Rep,* 6**,** 570-6.

KOUVATSOS, N., GIASTAS, P., CHRONI-TZARTOU, D., POULOPOULOU, C. & TZARTOS, S. J. 2016. Crystal structure of a human neuronal nAChR extracellular domain in pentameric assembly: Ligand-bound alpha2 homopentamer. *Proc Natl Acad Sci U S A,* 113**,** 9635-40.

KRASHIA, P., MORONI, M., BROADBENT, S., HOFMANN, G., KRACUN, S., BEATO, M., GROOT-KORMELINK, P. J. & SIVILOTTI, L. G. 2010. Human alpha3beta4 neuronal nicotinic receptors show different stoichiometry if they are expressed in Xenopus oocytes or mammalian HEK293 cells. *PLoS One,* 5**,** e13611.

KUCUKELBIR, A., SIGWORTH, F. J. & TAGARE, H. D. 2014. Quantifying the local resolution of cryo-EM density maps. *Nat Methods,* 11**,** 63-5.

KURYATOV, A., ONKSEN, J. & LINDSTROM, J. 2008. Roles of accessory subunits in alpha4beta2(*) nicotinic receptors. *Mol Pharmacol,* 74**,** 132-43.

LABARCA, C., NOWAK, M. W., ZHANG, H., TANG, L., DESHPANDE, P. & LESTER, H. A. 1995. Channel gating governed symmetrically by conserved leucine residues in the M2 domain of nicotinic receptors. *Nature,* 376**,** 514-6.

LANGLEY, J. N. 1880. On the Antagonism of Poisons. *J Physiol,* 3**,** 11-21.

LANGLEY, J. N. 1905. On the reaction of cells and of nerve-endings to certain poisons, chiefly as regards the reaction of striated muscle to nicotine and to curari. *J Physiol,* 33**,** 374-413.

LAVERTY, D., DESAI, R., UCHANSKI, T., MASIULIS, S., STEC, W. J., MALINAUSKAS, T., ZIVANOV, J., PARDON, E., STEYAERT, J., MILLER, K. W. & ARICESCU, A. R. 2019. Cryo-EM structure of the human alpha1beta3gamma2 GABAA receptor in a lipid bilayer. *Nature,* 565**,** 516-520.

LE NOVERE, N., CORRINGER, P. J. & CHANGEUX, J. P. 2002. The diversity of subunit composition in nAChRs: evolutionary origins, physiologic and pharmacologic consequences. *J Neurobiol,* 53**,** 447-56.

LEE, W. Y., FREE, C. R. & SINE, S. M. 2008. Nicotinic receptor interloop proline anchors beta1-beta2 and Cys loops in coupling agonist binding to channel gating. *J Gen Physiol,* 132**,** 265-78.

LEE, W. Y., FREE, C. R. & SINE, S. M. 2009. Binding to gating transduction in nicotinic receptors: Cys-loop energetically couples to pre-M1 and M2-M3 regions. *J Neurosci,* 29**,** 3189-99.

LEE, W. Y. & SINE, S. M. 2005. Principal pathway coupling agonist binding to channel gating in nicotinic receptors. *Nature,* 438**,** 243-7.

LESLIE, F. M., MOJICA, C. Y. & REYNAGA, D. D. 2013. Nicotinic receptors in addiction pathways. *Mol Pharmacol,* 83**,** 753-8.

LEVIN, E. D. 2002. Nicotinic receptor subtypes and cognitive function. *J Neurobiol,* 53**,** 633-40.

LI, S. X., HUANG, S., BREN, N., NORIDOMI, K., DELLISANTI, C. D., SINE, S. M. & CHEN, L. 2011. Ligand-binding domain of an alpha7-nicotinic receptor chimera and its complex with agonist. *Nat Neurosci,* 14**,** 1253-9.

LINDORFF-LARSEN, K., PIANA, S., PALMO, K., MARAGAKIS, P., KLEPEIS, J. L., DROR, R. O. & SHAW, D. E. 2010. Improved side-chain torsion potentials for the Amber ff99SB protein force field. *Proteins,* 78**,** 1950-1958.

LINDSTROM, J., ANHOLT, R., EINARSON, B., ENGEL, A., OSAME, M. & MONTAL, M. 1980. Purification of acetylcholine receptors, reconstitution into lipid vesicles, and study of agonist-induced cation channel regulation. *J Biol Chem,* 255**,** 8340-50.

LINDSTROM, J. M. 2000. Acetylcholine receptors and myasthenia. *Muscle Nerve,* 23**,** 453-77.

LIU, F., ZHANG, Z., CSANADY, L., GADSBY, D. C. & CHEN, J. 2017. Molecular Structure of the Human CFTR Ion Channel. *Cell,* 169**,** 85-95 e8.

LIU, Q., HUANG, Y., XUE, F., SIMARD, A., DECHON, J., LI, G., ZHANG, J., LUCERO, L., WANG, M., SIERKS, M., HU, G., CHANG, Y., LUKAS, R. J. & WU, J. 2009. A novel nicotinic acetylcholine receptor subtype in basal forebrain cholinergic neurons with high sensitivity to amyloid peptides. *J Neurosci,* 29**,** 918-29.

LIU, Y., PADGETT, D., TAKAHASHI, M., LI, H., SAYEED, A., TEICHERT, R. W., OLIVERA, B. M., MCARDLE, J. J., GREEN, W. N. & LIN, W. 2008. Essential roles of the acetylcholine receptor gamma-subunit in neuromuscular synaptic patterning. *Development,* 135**,** 1957-67.

LLOYD, G. K. & WILLIAMS, M. 2000. Neuronal nicotinic acetylcholine receptors as novel drug targets. *J Pharmacol Exp Ther,* 292**,** 461-7.

LOEWI, O. 1921. Über humorale übertragbarkeit der Herznervenwirkung. *Pflüger's Archiv für die gesamte Physiologie des Menschen und der Tiere,* 189**,** 239-242.

LUMMIS, S. C. 2012. 5-HT(3) receptors. *J Biol Chem,* 287**,** 40239-45.

LUNDBORG, M. & LINDAHL, E. 2015. Automatic GROMACS topology generation and comparisons of force fields for solvation free energy calculations. *The Journal of Physical Chemistry. B,* 119**,** 810-823.

LUO, J., TAYLOR, P., LOSEN, M., DE BAETS, M. H., SHELTON, G. D. & LINDSTROM, J. 2009. Main immunogenic region structure promotes binding of conformation-dependent myasthenia gravis autoantibodies, nicotinic acetylcholine

receptor conformation maturation, and agonist sensitivity. *J Neurosci,* 29**,** 13898-908.

MAEHLE, A. H. 2004. "Receptive substances": John Newport Langley (1852-1925) and his path to a receptor theory of drug action. *Med Hist,* 48**,** 153-74.

MAGAZANIK, L. G. & VYSKOCIL, F. 1970. Dependence of acetylcholine desensitization on the membrane potential of frog muscle fibre and on the ionic changes in the medium. *J Physiol,* 210**,** 507-18.

MANTHEY, A. A. 1966. Effect of Calcium on Desensitization of Membrane Receptors at Neuromuscular Junction. *Journal of General Physiology,* 49**,** 963-&.

MAO, D., YASUDA, R. P., FAN, H., WOLFE, B. B. & KELLAR, K. J. 2006. Heterogeneity of nicotinic cholinergic receptors in rat superior cervical and nodose Ganglia. *Mol Pharmacol,* 70**,** 1693-9.

MASIULIS, S., DESAI, R., UCHANSKI, T., SERNA MARTIN, I., LAVERTY, D., KARIA, D., MALINAUSKAS, T., ZIVANOV, J., PARDON, E., KOTECHA, A., STEYAERT, J., MILLER, K. W. & ARICESCU, A. R. 2019. GABAA receptor signalling mechanisms revealed by structural pharmacology. *Nature,* 565**,** 454-459.

MASKOS, U., MOLLES, B. E., PONS, S., BESSON, M., GUIARD, B. P., GUILLOUX, J. P., EVRARD, A., CAZALA, P., CORMIER, A., MAMELI-ENGVALL, M., DUFOUR, N., CLOEZ-TAYARANI, I., BEMELMANS, A. P., MALLET, J., GARDIER, A. M., DAVID, V., FAURE, P., GRANON, S. & CHANGEUX, J. P. 2005. Nicotine reinforcement and cognition restored by targeted expression of nicotinic receptors. *Nature,* 436**,** 103-7.

MASTRONARDE, D. N. 2005. Automated electron microscope tomography using robust prediction of specimen movements. *J Struct Biol,* 152**,** 36-51.

MAUN, H. R., WEN, X., LINGEL, A., DE SAUVAGE, F. J., LAZARUS, R. A., SCALES, S. J. & HYMOWITZ, S. G. 2010. Hedgehog pathway antagonist 5E1 binds hedgehog at the pseudo-active site. *J Biol Chem,* 285**,** 26570-80.

MAZZAFERRO, S., BENALLEGUE, N., CARBONE, A., GASPARRI, F., VIJAYAN, R., BIGGIN, P. C., MORONI, M. & BERMUDEZ, I. 2011. Additional acetylcholine (ACh) binding site at alpha4/alpha4 interface of (alpha4beta2)2alpha4 nicotinic receptor influences agonist sensitivity. *J Biol Chem,* 286**,** 31043-54.

MCCALLUM, S. E., COWE, M. A., LEWIS, S. W. & GLICK, S. D. 2012. alpha3beta4 nicotinic acetylcholine receptors in the medial habenula modulate the mesolimbic dopaminergic response to acute nicotine in vivo. *Neuropharmacology,* 63**,** 434-40.

MCGIBBON, R. T., BEAUCHAMP, K. A., HARRIGAN, M. P., KLEIN, C., SWAILS, J. M., HERNÁNDEZ, C. X., SCHWANTES, C. R., WANG, L.-P., LANE, T. J. & PANDE, V. S. 2015. Mdtraj: A modern open library for the analysis of molecular dynamics trajectories. *Biophysical Journal,* 109**,** 1528-1532.

MCNAMEE, M. G., WEILL, C. L. & KARLIN, A. 1975. Purification of acetylcholine receptor from Torpedo californica and its incorporation into phospholipid vesicles. *Ann N Y Acad Sci,* 264**,** 175-82.

MEUNIER, J. C., HUCHET, M., BOQUET, P. & CHANGEUX, J. P. 1971. [Separation of the receptor protein of acetylcholine and acetylcholinesterase]. *C R Acad Hebd Seances Acad Sci D,* 272**,** 117-20.

MILEDI, R., MOLINOFF, P. & POTTER, L. T. 1971. Isolation of the cholinergic receptor protein of Torpedo electric tissue. *Nature,* 229**,** 554-7.

MILLER, A. N., VAISEY, G. & LONG, S. B. 2019. Molecular mechanisms of gating in the calcium-activated chloride channel bestrophin. *Elife,* 8.

MIQUEL, M. C., EMERIT, M. B., NOSJEAN, A., SIMON, A., RUMAJOGEE, P., BRISORGUEIL, M. J., DOUCET, E., HAMON, M. & VERGE, D. 2002. Differential subcellular localization of the 5-HT3-As receptor subunit in the rat central nervous system. *Eur J Neurosci,* 15**,** 449-57.

MISHINA, M., TAKAI, T., IMOTO, K., NODA, M., TAKAHASHI, T., NUMA, S., METHFESSEL, C. & SAKMANN, B. 1986. Molecular distinction between fetal and adult forms of muscle acetylcholine receptor. *Nature,* 321**,** 406-11.

MIYAZAWA, A., FUJIYOSHI, Y., STOWELL, M. & UNWIN, N. 1999. Nicotinic acetylcholine receptor at 4.6 A resolution: transverse tunnels in the channel wall. *J Mol Biol,* 288**,** 765-86.

MIYAZAWA, A., FUJIYOSHI, Y. & UNWIN, N. 2003. Structure and gating mechanism of the acetylcholine receptor pore. *Nature,* 423**,** 949-55.

MORALES-PEREZ, C. L., NOVIELLO, C. M. & HIBBS, R. E. 2016a. Manipulation of Subunit Stoichiometry in Heteromeric Membrane Proteins. *Structure,* 24**,** 797-805.

MORALES-PEREZ, C. L., NOVIELLO, C. M. & HIBBS, R. E. 2016b. X-ray structure of the human alpha4beta2 nicotinic receptor. *Nature,* 538**,** 411-415.

MORETTI, M., ZOLI, M., GEORGE, A. A., LUKAS, R. J., PISTILLO, F., MASKOS, U., WHITEAKER, P. & GOTTI, C. 2014. The novel alpha7beta2-nicotinic acetylcholine receptor subtype is expressed in mouse and human basal forebrain: biochemical and pharmacological characterization. *Mol Pharmacol,* 86**,** 306-17.

MORIN, A., EISENBRAUN, B., KEY, J., SANSCHAGRIN, P. C., TIMONY, M. A., OTTAVIANO, M. & SLIZ, P. 2013. Collaboration gets the most out of software. *Elife,* 2**,** e01456.

MUKHTASIMOVA, N., DACOSTA, C. J. & SINE, S. M. 2016. Improved resolution of single channel dwell times reveals mechanisms of binding, priming, and gating in muscle AChR. *J Gen Physiol,* 148**,** 43-63.

MULLE, C., VIDAL, C., BENOIT, P. & CHANGEUX, J. P. 1991. Existence of different subtypes of nicotinic acetylcholine receptors in the rat habenulo-interpeduncular system. *J Neurosci,* 11**,** 2588-97.

NACHMANSOHN, D., COATES, C. W. & COX, R. T. 1941. Electric Potential and Activity of Choline Esterase in the Electric Organ of Electrophorus Electricus (Linnaeus). *J Gen Physiol,* 25**,** 75-88.

NEHER, E. & SAKMANN, B. 1976. Single-channel currents recorded from membrane of denervated frog muscle fibres. *Nature,* 260**,** 799-802.

NELSON, M. E., KURYATOV, A., CHOI, C. H., ZHOU, Y. & LINDSTROM, J. 2003. Alternate stoichiometries of alpha4beta2 nicotinic acetylcholine receptors. *Mol Pharmacol,* 63**,** 332-41.

NELSON, N., ANHOLT, R., LINDSTROM, J. & MONTAL, M. 1980. Reconstitution of purified acetylcholine receptors with functional ion channels in planar lipid bilayers. *Proc Natl Acad Sci U S A,* 77**,** 3057-61.

NEMECZ, A., PREVOST, M. S., MENNY, A. & CORRINGER, P. J. 2016. Emerging Molecular Mechanisms of Signal Transduction in Pentameric Ligand-Gated Ion Channels. *Neuron,* 90**,** 452-70.

NEMECZ, A. & TAYLOR, P. 2011. Creating an alpha7 nicotinic acetylcholine recognition domain from the acetylcholine-binding protein: crystallographic and ligand selectivity analyses. *J Biol Chem,* 286**,** 42555-65.

NGUYEN, N. X., ARMACHE, J. P., LEE, C., YANG, Y., ZENG, W., MOOTHA, V. K., CHENG, Y., BAI, X. C. & JIANG, Y. 2018. Cryo-EM structure of a fungal mitochondrial calcium uniporter. *Nature,* 559**,** 570-574.

NISHIKAWA, T., FAGE, D. & SCATTON, B. 1986. Evidence for, and nature of, the tonic inhibitory influence of habenulointerpeduncular pathways upon cerebral dopaminergic transmission in the rat. *Brain Res,* 373**,** 324-36.

NODA, M., TAKAHASHI, H., TANABE, T., TOYOSATO, M., KIKYOTANI, S., FURUTANI, Y., HIROSE, T., TAKASHIMA, H., INAYAMA, S., MIYATA, T. & NUMA, S. 1983. Structural homology of Torpedo californica acetylcholine receptor subunits. *Nature,* 302**,** 528-32.

NORIDOMI, K., WATANABE, G., HANSEN, M. N., HAN, G. W. & CHEN, L. 2017. Structural insights into the molecular mechanisms of myasthenia gravis and their therapeutic implications. *Elife,* 6.

OHNO, M., YAMAMOTO, T. & WATANABE, S. 1993. Blockade of hippocampal nicotinic receptors impairs working memory but not reference memory in rats. *Pharmacol Biochem Behav,* 45**,** 89-93.

OLSEN, R. W., MEUNIER, J. C. & CHANGEUX, J. P. 1972. Progress in the purification of the cholinergic receptor protein from Electrophorus electricus by affinity chromatography. *FEBS Lett,* 28**,** 96-100.

PAN, J., CHEN, Q., WILLENBRING, D., YOSHIDA, K., TILLMAN, T., KASHLAN, O. B., COHEN, A., KONG, X. P., XU, Y. & TANG, P. 2012. Structure of the pentameric ligand-gated ion channel ELIC cocrystallized with its competitive antagonist acetylcholine. *Nat Commun,* 3**,** 714.

PANDHARE, A., PIRAYESH, E., STUEBLER, A. G. & JANSEN, M. 2019. Triple arginines as molecular determinants for pentameric assembly of the intracellular domain of 5-HT3A receptors. *J Gen Physiol,* 151**,** 1135-1145.

PARRINELLO, M. & RAHMAN, A. 1980. Crystal structure and pair potentials: A molecular-dynamics study. *Physical review letters,* 45**,** 1196-1199.

PAULO, J. A., BRUCKER, W. J. & HAWROT, E. 2009. Proteomic analysis of an alpha7 nicotinic acetylcholine receptor interactome. *J Proteome Res,* 8**,** 1849-58.

PEI, J., KIM, B. H. & GRISHIN, N. V. 2008. PROMALS3D: a tool for multiple protein sequence and structure alignments. *Nucleic Acids Res,* 36**,** 2295-300.

PENG, X., KATZ, M., GERZANICH, V., ANAND, R. & LINDSTROM, J. 1994. Human alpha 7 acetylcholine receptor: cloning of the alpha 7 subunit from the SH-SY5Y cell line and determination of pharmacological properties of native receptors and functional alpha 7 homomers expressed in Xenopus oocytes. *Mol Pharmacol,* 45**,** 546-54.

PETTERSEN, E. F., GODDARD, T. D., HUANG, C. C., COUCH, G. S., GREENBLATT, D. M., MENG, E. C. & FERRIN, T. E. 2004. UCSF Chimera--a visualization system for exploratory research and analysis. *J Comput Chem,* 25**,** 1605-12.

PICCIOTTO, M. R., HIGLEY, M. J. & MINEUR, Y. S. 2012. Acetylcholine as a neuromodulator: cholinergic signaling shapes nervous system function and behavior. *Neuron,* 76**,** 116-29.

PICCIOTTO, M. R., ZOLI, M., LENA, C., BESSIS, A., LALLEMAND, Y., LE NOVERE, N., VINCENT, P., PICH, E. M., BRULET, P. & CHANGEUX, J. P. 1995. Abnormal avoidance learning in mice lacking functional high-affinity nicotine receptor in the brain. *Nature,* 374**,** 65-7.

PICCIOTTO, M. R., ZOLI, M., RIMONDINI, R., LENA, C., MARUBIO, L. M., PICH, E. M., FUXE, K. & CHANGEUX, J. P. 1998. Acetylcholine receptors containing the beta2 subunit are involved in the reinforcing properties of nicotine. *Nature,* 391**,** 173-7.

PIDCOCK, E. & MOORE, G. R. 2001. Structural characteristics of protein binding sites for calcium and lanthanide ions. *Journal of Biological Inorganic Chemistry,* 6**,** 479-489.

POHANKA, M. 2012. Alpha7 nicotinic acetylcholine receptor is a target in pharmacology and toxicology. *Int J Mol Sci,* 13**,** 2219-38.

POLOVINKIN, L., HASSAINE, G., PEROT, J., NEUMANN, E., JENSEN, A. A., LEFEBVRE, S. N., CORRINGER, P. J., NEYTON, J., CHIPOT, C., DEHEZ, F., SCHOEHN, G. & NURY, H. 2018. Conformational transitions of the serotonin 5-HT3 receptor. *Nature,* 563**,** 275-279.

PUROHIT, P. & AUERBACH, A. 2007. Acetylcholine receptor gating at extracellular transmembrane domain interface: the "pre-M1" linker. *J Gen Physiol,* 130**,** 559-68.

PUROHIT, Y. & GROSMAN, C. 2006. Block of muscle nicotinic receptors by choline suggests that the activation and desensitization gates act as distinct molecular entities. *J Gen Physiol,* 127**,** 703-17.

QUICK, M. W., CEBALLOS, R. M., KASTEN, M., MCINTOSH, J. M. & LESTER, R. A. 1999. Alpha3beta4 subunit-containing nicotinic receptors dominate function in rat medial habenula neurons. *Neuropharmacology,* 38**,** 769-83.

QUICK, M. W. & LESTER, R. A. 2002. Desensitization of neuronal nicotinic receptors. *J Neurobiol,* 53**,** 457-78.

RAHMAN, M. M., TENG, J., WORRELL, B. T., NOVIELLO, C. M., LEE, M., KARLIN, A., STOWELL, M. H. B. & HIBBS, R. E. 2020. Structure of the Native Muscle-type Nicotinic Receptor and Inhibition by Snake Venom Toxins. *Neuron*.

RAMIREZ-LATORRE, J., YU, C. R., QU, X., PERIN, F., KARLIN, A. & ROLE, L. 1996. Functional contributions of alpha5 subunit to neuronal acetylcholine receptor channels. *Nature,* 380**,** 347-51.

REEVES, P. J., CALLEWAERT, N., CONTRERAS, R. & KHORANA, H. G. 2002. Structure and function in rhodopsin: high-level expression of rhodopsin with restricted and homogeneous N-glycosylation by a tetracycline-inducible N-acetylglucosaminyltransferase I-negative HEK293S stable mammalian cell line. *Proc Natl Acad Sci U S A,* 99**,** 13419-24.

REVAH, F., BERTRAND, D., GALZI, J. L., DEVILLERS-THIERY, A., MULLE, C., HUSSY, N., BERTRAND, S., BALLIVET, M. & CHANGEUX, J. P. 1991. Mutations in the channel domain alter desensitization of a neuronal nicotinic receptor. *Nature,* 353**,** 846-9.

REZVANI, A. H., OVERSTREET, D. H., YANG, Y., MAISONNEUVE, I. M., BANDARAGE, U. K., KUEHNE, M. E. & GLICK, S. D. 1997. Attenuation of alcohol consumption by a novel nontoxic ibogaine analogue (18-methoxycoronaridine) in alcohol-preferring rats. *Pharmacol Biochem Behav,* 58**,** 615-9.

RUCKTOOA, P., SMIT, A. B. & SIXMA, T. K. 2009. Insight in nAChR subtype selectivity from AChBP crystal structures. *Biochem Pharmacol,* 78**,** 777-87.

SACCONE, N. L., SCHWANTES-AN, T. H., WANG, J. C., GRUCZA, R. A., BRESLAU, N., HATSUKAMI, D., JOHNSON, E. O., RICE, J. P., GOATE, A. M. & BIERUT, L. J. 2010. Multiple cholinergic nicotinic receptor genes affect

nicotine dependence risk in African and European Americans. *Genes Brain Behav,* 9**,** 741-50.

SACCONE, S. F., HINRICHS, A. L., SACCONE, N. L., CHASE, G. A., KONVICKA, K., MADDEN, P. A., BRESLAU, N., JOHNSON, E. O., HATSUKAMI, D., POMERLEAU, O., SWAN, G. E., GOATE, A. M., RUTTER, J., BERTELSEN, S., FOX, L., FUGMAN, D., MARTIN, N. G., MONTGOMERY, G. W., WANG, J. C., BALLINGER, D. G., RICE, J. P. & BIERUT, L. J. 2007. Cholinergic nicotinic receptor genes implicated in a nicotine dependence association study targeting 348 candidate genes with 3713 SNPs. *Hum Mol Genet,* 16**,** 36-49.

SAKMANN, B. & BRENNER, H. R. 1978. Change in synaptic channel gating during neuromuscular development. *Nature,* 276**,** 401-2.

SAUGUET, L., POITEVIN, F., MURAIL, S., VAN RENTERGHEM, C., MORAGA-CID, G., MALHERBE, L., THOMPSON, A. W., KOEHL, P., CORRINGER, P. J., BAADEN, M. & DELARUE, M. 2013. Structural basis for ion permeation mechanism in pentameric ligand-gated ion channels. *EMBO J,* 32**,** 728-41.

SAUGUET, L., SHAHSAVAR, A., POITEVIN, F., HUON, C., MENNY, A., NEMECZ, A., HAOUZ, A., CHANGEUX, J. P., CORRINGER, P. J. & DELARUE, M. 2014. Crystal structures of a pentameric ligand-gated ion channel provide a mechanism for activation. *Proc Natl Acad Sci U S A,* 111**,** 966-71.

SCHERES, S. H. 2016. Processing of Structurally Heterogeneous Cryo-EM Data in RELION. *Methods Enzymol,* 579**,** 125-57.

SCHMIDT, T. G. & SKERRA, A. 2007. The Strep-tag system for one-step purification and high-affinity detection or capturing of proteins. *Nat Protoc,* 2**,** 1528-35.

SCHWEDE, T., KOPP, J., GUEX, N. & PEITSCH, M. C. 2003. SWISS-MODEL: An automated protein homology-modeling server. *Nucleic Acids Res,* 31**,** 3381-5.

SEGUELA, P., WADICHE, J., DINELEY-MILLER, K., DANI, J. A. & PATRICK, J. W. 1993. Molecular cloning, functional properties, and distribution of rat brain alpha 7: a nicotinic cation channel highly permeable to calcium. *J Neurosci,* 13**,** 596-604.

SGARD, F., CHARPANTIER, E., BERTRAND, S., WALKER, N., CAPUT, D., GRAHAM, D., BERTRAND, D. & BESNARD, F. 2002. A novel human nicotinic receptor subunit, alpha10, that confers functionality to the alpha9-subunit. *Mol Pharmacol,* 61**,** 150-9.

SHAHSAVAR, A., AHRING, P. K., OLSEN, J. A., KRINTEL, C., KASTRUP, J. S., BALLE, T. & GAJHEDE, M. 2015. Acetylcholine-Binding Protein Engineered to Mimic the alpha4-alpha4 Binding Pocket in alpha4beta2 Nicotinic Acetylcholine Receptors Reveals Interface Specific Interactions Important for Binding and Activity. *Mol Pharmacol,* 88**,** 697-707.

SHAHSAVAR, A., GAJHEDE, M., KASTRUP, J. S. & BALLE, T. 2016. Structural Studies of Nicotinic Acetylcholine Receptors: Using Acetylcholine-Binding Protein as a Structural Surrogate. *Basic Clin Pharmacol Toxicol,* 118**,** 399-407.

SHEFFIELD, E. B., QUICK, M. W. & LESTER, R. A. 2000. Nicotinic acetylcholine receptor subunit mRNA expression and channel function in medial habenula neurons. *Neuropharmacology,* 39**,** 2591-603.

SHERVA, R., KRANZLER, H. R., YU, Y., LOGUE, M. W., POLING, J., ARIAS, A. J., ANTON, R. F., OSLIN, D., FARRER, L. A. & GELERNTER, J. 2010. Variation in Nicotinic Acetylcholine Receptor Genes is Associated with Multiple Substance Dependence Phenotypes. *Neuropsychopharmacology,* 35**,** 1921-1931.

SIGEL, E. & BUHR, A. 1997. The benzodiazepine binding site of GABAA receptors. *Trends Pharmacol Sci,* 18**,** 425-9.

SKOK, V. I. 2002. Nicotinic acetylcholine receptors in autonomic ganglia. *Auton Neurosci,* 97**,** 1-11.

SMIT, A. B., SYED, N. I., SCHAAP, D., VAN MINNEN, J., KLUMPERMAN, J., KITS, K. S., LODDER, H., VAN DER SCHORS, R. C., VAN ELK, R., SORGEDRAGER, B., BREJC, K., SIXMA, T. K. & GERAERTS, W. P. 2001. A glia-derived acetylcholine-binding protein that modulates synaptic transmission. *Nature,* 411**,** 261-8.

ST JOHN, P. A. 2009. Cellular trafficking of nicotinic acetylcholine receptors. *Acta Pharmacol Sin,* 30**,** 656-62.

STOKES, C., TREININ, M. & PAPKE, R. L. 2015. Looking below the surface of nicotinic acetylcholine receptors. *Trends Pharmacol Sci,* 36**,** 514-23.

SUTHERLAND, R. J. 1982. The dorsal diencephalic conduction system: a review of the anatomy and functions of the habenular complex. *Neurosci Biobehav Rev,* 6**,** 1-13.

SWOPE, S. L., MOSS, S. J., RAYMOND, L. A. & HUGANIR, R. L. 1999. Regulation of ligand-gated ion channels by protein phosphorylation. *Adv Second Messenger Phosphoprotein Res,* 33**,** 49-78.

TAKAHASHI, M., KUBO, T., MIZOGUCHI, A., CARLSON, C. G., ENDO, K. & OHNISHI, K. 2002. Spontaneous muscle action potentials fail to develop without fetal-type acetylcholine receptors. *EMBO Rep,* 3**,** 674-81.

TALWAR, S. & LYNCH, J. W. 2014. Phosphorylation mediated structural and functional changes in pentameric ligand-gated ion channels: implications for drug discovery. *Int J Biochem Cell Biol,* 53**,** 218-23.

TANSEY, E. M. 1991. Chemical neurotransmission in the autonomic nervous system: Sir Henry Dale and acetylcholine. *Clin Auton Res,* 1**,** 63-72.

TAPIA, L., KURYATOV, A. & LINDSTROM, J. 2007. Ca2+ permeability of the (alpha4)3(beta2)2 stoichiometry greatly exceeds that of (alpha4)2(beta2)3 human acetylcholine receptors. *Mol Pharmacol,* 71**,** 769-76.

TASNEEM, A., IYER, L. M., JAKOBSSON, E. & ARAVIND, L. 2005. Identification of the prokaryotic ligand-gated ion channels and their implications for the mechanisms and origins of animal Cys-loop ion channels. *Genome Biol,* 6**,** R4.

THOMPSON, A. J., LESTER, H. A. & LUMMIS, S. C. 2010. The structural basis of function in Cys-loop receptors. *Q Rev Biophys,* 43**,** 449-99.

TOLL, L., ZAVERI, N. T., POLGAR, W. E., JIANG, F., KHROYAN, T. V., ZHOU, W., XIE, X. S., STAUBER, G. B., COSTELLO, M. R. & LESLIE, F. M. 2012. AT-1001: a high affinity and selective alpha3beta4 nicotinic acetylcholine receptor

antagonist blocks nicotine self-administration in rats. *Neuropsychopharmacology,* 37**,** 1367-76.

TOYOSHIMA, C. & UNWIN, N. 1988. Ion channel of acetylcholine receptor reconstructed from images of postsynaptic membranes. *Nature,* 336**,** 247-50.

TOYOSHIMA, C. & UNWIN, N. 1990. Three-dimensional structure of the acetylcholine receptor by cryoelectron microscopy and helical image reconstruction. *J Cell Biol,* 111**,** 2623-35.

TROTT, O. & OLSON, A. J. 2010. AutoDock Vina: improving the speed and accuracy of docking with a new scoring function, efficient optimization, and multithreading. *Journal of Computational Chemistry,* 31**,** 455-461.

TUAN, E. W., HORTI, A. G., OLSON, T. T., GAO, Y., STOCKMEIER, C. A., AL-MUHTASIB, N., BOWMAN DALLEY, C., LEWIN, A. E., WOLFE, B. B., SAHIBZADA, N., XIAO, Y. & KELLAR, K. J. 2015. AT-1001 Is a Partial Agonist with High Affinity and Selectivity at Human and Rat alpha3beta4 Nicotinic Cholinergic Receptors. *Mol Pharmacol,* 88**,** 640-9.

TWOMEY, E. C., YELSHANSKAYA, M. V., GRASSUCCI, R. A., FRANK, J. & SOBOLEVSKY, A. I. 2017. Channel opening and gating mechanism in AMPA-subtype glutamate receptors. *Nature,* 549**,** 60-65.

UNIPROT CONSORTIUM, T. 2018. UniProt: the universal protein knowledgebase. *Nucleic Acids Res,* 46**,** 2699.

UNWIN, N. 1993. Nicotinic acetylcholine receptor at 9 A resolution. *J Mol Biol,* 229**,** 1101-24.

UNWIN, N. 2005. Refined structure of the nicotinic acetylcholine receptor at 4A resolution. *J Mol Biol,* 346**,** 967-89.

UNWIN, N. 2013. Nicotinic acetylcholine receptor and the structural basis of neuromuscular transmission: insights from Torpedo postsynaptic membranes. *Q Rev Biophys,* 46**,** 283-322.

UNWIN, N., TOYOSHIMA, C. & KUBALEK, E. 1988. Arrangement of the acetylcholine receptor subunits in the resting and desensitized states, determined

by cryoelectron microscopy of crystallized Torpedo postsynaptic membranes. *J Cell Biol,* 107**,** 1123-38.

VERNALLIS, A. B., CONROY, W. G. & BERG, D. K. 1993. Neurons assemble acetylcholine receptors with as many as three kinds of subunits while maintaining subunit segregation among receptor subtypes. *Neuron,* 10**,** 451-64.

WADA, E., WADA, K., BOULTER, J., DENERIS, E., HEINEMANN, S., PATRICK, J. & SWANSON, L. W. 1989. Distribution of alpha 2, alpha 3, alpha 4, and beta 2 neuronal nicotinic receptor subunit mRNAs in the central nervous system: a hybridization histochemical study in the rat. *J Comp Neurol,* 284**,** 314-35.

WALSH, R. M., JR., ROH, S. H., GHARPURE, A., MORALES-PEREZ, C. L., TENG, J. & HIBBS, R. E. 2018. Structural principles of distinct assemblies of the human alpha4beta2 nicotinic receptor. *Nature,* 557**,** 261-265.

WEHRWEIN, E. A., ORER, H. S. & BARMAN, S. M. 2016. Overview of the Anatomy, Physiology, and Pharmacology of the Autonomic Nervous System. *Compr Physiol,* 6**,** 1239-78.

WHITING, P. J. & LINDSTROM, J. M. 1988. Characterization of bovine and human neuronal nicotinic acetylcholine receptors using monoclonal antibodies. *J Neurosci,* 8**,** 3395-404.

WILLIAMS, B. M., TEMBURNI, M. K., LEVEY, M. S., BERTRAND, S., BERTRAND, D. & JACOB, M. H. 1998. The long internal loop of the alpha 3 subunit targets nAChRs to subdomains within individual synapses on neurons in vivo. *Nat Neurosci,* 1**,** 557-62.

WILLIAMS, M. E., BURTON, B., URRUTIA, A., SHCHERBATKO, A., CHAVEZ-NORIEGA, L. E., COHEN, C. J. & AIYAR, J. 2005. Ric-3 promotes functional expression of the nicotinic acetylcholine receptor alpha7 subunit in mammalian cells. *J Biol Chem,* 280**,** 1257-63.

WILSON, G. & KARLIN, A. 2001. Acetylcholine receptor channel structure in the resting, open, and desensitized states probed with the substituted-cysteine-accessibility method. *Proc Natl Acad Sci U S A,* 98**,** 1241-8.

WITZEMANN, V., SCHWARZ, H., KOENEN, M., BERBERICH, C., VILLARROEL, A., WERNIG, A., BRENNER, H. R. & SAKMANN, B. 1996. Acetylcholine receptor epsilon-subunit deletion causes muscle weakness and atrophy in juvenile and adult mice. *Proc Natl Acad Sci U S A,* 93**,** 13286-91.

WONNACOTT, S. 1997. Presynaptic nicotinic ACh receptors. *Trends Neurosci,* 20**,** 92-8.

WU, E. L., CHENG, X., JO, S., RUI, H., SONG, K. C., DÁVILA-CONTRERAS, E. M., QI, Y., LEE, J., MONJE-GALVAN, V., VENABLE, R. M., KLAUDA, J. B. & IM, W. 2014. CHARMM-GUI Membrane Builder toward realistic biological membrane simulations. *Journal of Computational Chemistry,* 35**,** 1997-2004.

XIAO, Y., MEYER, E. L., THOMPSON, J. M., SURIN, A., WROBLEWSKI, J. & KELLAR, K. J. 1998. Rat alpha3/beta4 subtype of neuronal nicotinic acetylcholine receptor stably expressed in a transfected cell line: pharmacology of ligand binding and function. *Mol Pharmacol,* 54**,** 322-33.

XIU, X., PUSKAR, N. L., SHANATA, J. A., LESTER, H. A. & DOUGHERTY, D. A. 2009. Nicotine binding to brain receptors requires a strong cation-pi interaction. *Nature,* 458**,** 534-7.

YONEKURA, K., KATO, K., OGASAWARA, M., TOMITA, M. & TOYOSHIMA, C. 2015. Electron crystallography of ultrathin 3D protein crystals: atomic model with charges. *Proc Natl Acad Sci U S A,* 112**,** 3368-73.

ZHANG, K. 2016. Gctf: Real-time CTF determination and correction. *J Struct Biol,* 193**,** 1-12.

ZHAO, M., WU, S., ZHOU, Q., VIVONA, S., CIPRIANO, D. J., CHENG, Y. & BRUNGER, A. T. 2015. Mechanistic insights into the recycling machine of the SNARE complex. *Nature,* 518**,** 61-7.

ZHAO, Y., CHEN, S., SWENSEN, A. C., QIAN, W. J. & GOUAUX, E. 2019. Architecture and subunit arrangement of native AMPA receptors elucidated by cryo-EM. *Science,* 364**,** 355-362.

ZHENG, S. Q., PALOVCAK, E., ARMACHE, J. P., VERBA, K. A., CHENG, Y. & AGARD, D. A. 2017. MotionCor2: anisotropic correction of beam-induced motion for improved cryo-electron microscopy. *Nat Methods,* 14**,** 331-332.

ZHU, S., NOVIELLO, C. M., TENG, J., WALSH, R. M., JR., KIM, J. J. & HIBBS, R. E. 2018. Structure of a human synaptic GABAA receptor. *Nature,* 559**,** 67-72.

ZIVANOV, J., NAKANE, T., FORSBERG, B. O., KIMANIUS, D., HAGEN, W. J., LINDAHL, E. & SCHERES, S. H. 2018. New tools for automated high-resolution cryo-EM structure determination in RELION-3. *Elife,* 7.

ZOLI, M., PISTILLO, F. & GOTTI, C. 2015. Diversity of native nicotinic receptor subtypes in mammalian brain. *Neuropharmacology,* 96**,** 302-11.

ZOURIDAKIS, M., GIASTAS, P., ZARKADAS, E., CHRONI-TZARTOU, D., BREGESTOVSKI, P. & TZARTOS, S. J. 2014. Crystal structures of free and antagonist-bound states of human alpha9 nicotinic receptor extracellular domain. *Nat Struct Mol Biol,* 21**,** 976-80.

ZOURIDAKIS, M., PAPAKYRIAKOU, A., IVANOV, I. A., KASHEVEROV, I. E., TSETLIN, V., TZARTOS, S. & GIASTAS, P. 2019. Crystal Structure of the Monomeric Extracellular Domain of alpha9 Nicotinic Receptor Subunit in Complex With alpha-Conotoxin RgIA: Molecular Dynamics Insights Into RgIA Binding to alpha9alpha10 Nicotinic Receptors. *Front Pharmacol,* 10**,** 474.